Satellite passive microwave surface moisture monitoring

A case–study on the impact of climatic variability and land use change on the regional hydrogeology of the West La Mancha region in semi–arid central Spain

B.T. Gouweleeuw

Satellite passive microwave surface moisture monitoring

A case–study on the impact of climate variability and
land use change on the regional hydrogeology of the
West La Mancha region in semi–arid central Spain

B.T. Gouweleeuw

2000

Front cover: Dry bed of the Záncara river in the Llanura Manchega plain above its confluence with the Córcoles river, August 1999.
(Photo: B.T. Gouweleeuw)

VRIJE UNIVERSITEIT

Satellite passive microwave
surface moisture monitoring

A case–study on the impact of climatic variability and
land use change on the regional hydrogeology of the
West La Mancha region in semi–arid central Spain

ACADEMISCH PROEFSCHRIFT

ter verkrijging van de graad van doctor aan
de Vrije Universiteit te Amsterdam,
op gezag van de rector magnificus
prof.dr. T. Sminia,
in het openbaar te verdedigen
ten overstaan van de promotiecommissie
van de faculteit der aardwetenschappen
op donderdag 20 januari 2000 om 15.45 uur
in het hoofdgebouw van de universiteit,
De Boelelaan 1105

door

Bernardus Theodorus Gouweleeuw

geboren te Delft

Promotor : prof.dr. H.F. Vugts

Het geval wilde dat de wolken dat jaar hun vocht aan de aarde hadden ontzegd en in alle dorpen in de omtrek werden processies, biddagen en boetedoeningen gehouden om God te smeken de handen van Zijn goedertierenheid te openen en de regen te laten komen, en met dat doel waren de inwoners van een nabij gelegen dorp in processie op weg naar een gewijde kluis, die op een valleihelling was gelegen.

Don Quichot, die de vreemde kleren van de boetelingen zag zonder dat hem te binnen schoot hoe vaak hij ze eerder gezien moest hebben, rook een nieuw avontuur dat uitsluitend hem, als dolend ridder, was voorbehouden; en in die veronderstelling werd hij gesterkt door de gedachte dat het met rouwgewaad bedekte beeld dat zij meedroegen een voorname dame was die die blaaskaken en onbeschofte rakkers met geweld meevoerden; en niet zodra had hij dit bedacht, of hij schoot pijlsnel naar de grazende Rocinant, nam de toom en het schild van de zadelboog, en had hem in een mum van tijd opgetuigd; en terwijl hij Sancho om zijn zwaard vroeg, besteeg hij het beest, schoof het schild aan zijn arm en zei luidkeels tegen alle omstanders: 'Thans, heldhaftig gezelschap, zult u zien hoe belangrijk het is dat er ridders op de wereld bestaan die de orde van het dolende ridderschap aanhangen; thans, zeg ik u, zult u via de bevrijding van die brave dame, die daar in gevangen staat wordt meegevoerd, zien of dolende ridders al dan niet achting verdienen.'

En terwijl hij dit zei, drukte hij, daar hij geen sporen droeg, zijn dijen tegen Rocinant en in volle galop, want in deze hele ware historie leest men nooit dat hij Rocinant tot een gestrekte draf liet overgaan, reed hij de boetelingen tegemoet, al renden de pastoor en de kanunnik en de barbier achter hem aan om hem tegen te houden; dat lukte hun echter niet, en dat lukte ook Sancho niet, die riep: 'Waar gaat u heen, heer Don Quichot? Welke duivels huizen er in u dat ze u ingeven ons katholieke geloof te lijf te gaan? Wee mij, luister toch, dat is de processie van boetelingen en die dame op die baar is het zeer gebenedijde beeld van de onbevlekte Maagd; kijk uit, heer, wat u doet; deze keer kun je wel zeggen dat u dat niet weet.'

Contents

Chapter 1

Introduction

1.1 Background and problem definition

1.1.1 Euro–mediterranean land degradation

An ecologically sustainable development of the biosphere has in recent years become a matter of growing concern as an increased economic, political, scientific and public awareness of the impacts of climate variability and human activity on environmental conditions of the landscape has become apparent. The application of remote sensing techniques as a tool to monitor the impacts of climate and/or man–induced changes on land–surface characteristics at various spatial and temporal scales has increased proportionally.

In the Mediterranean area, the study of spatial and temporal changes in land–surface character deals primarily with the identification of desertification processes. Although considerable debate continues regarding an appropriate definition of desertification in a Euro–Mediterranean context, land degradation resulting in a reduction of production potential and the inability to support an indigenous population appear to be the primary elements in most characterizations [*Perez–Trejo*, 1994]. A possible definition of desertification in causal terms appears to be even more complicated. Human activity is however generally recognized as a principal cause, aggravated subsequently by natural climatic conditions [*UNEP*, 1992]. The former involves overcultivation, deforestation, tourism, and depletion of water resources. The latter includes physical factors such as topography, soil erodability and effects of climate variability.

Natural land degradation and desertification processes in the Mediterranean region relate to Global Climate Change problems and, as such, are addressed in the land–surface oriented International Geosphere–Biosphere Program (IGBP) Core Projects on the Biospheric Aspects of the Hydrological Cycle (BAHC). While many detailed studies have been performed and are currently ongoing in different locations throughout the Mediterranean region, observations from space provide for a large–scale overview. While these enable the study of changes
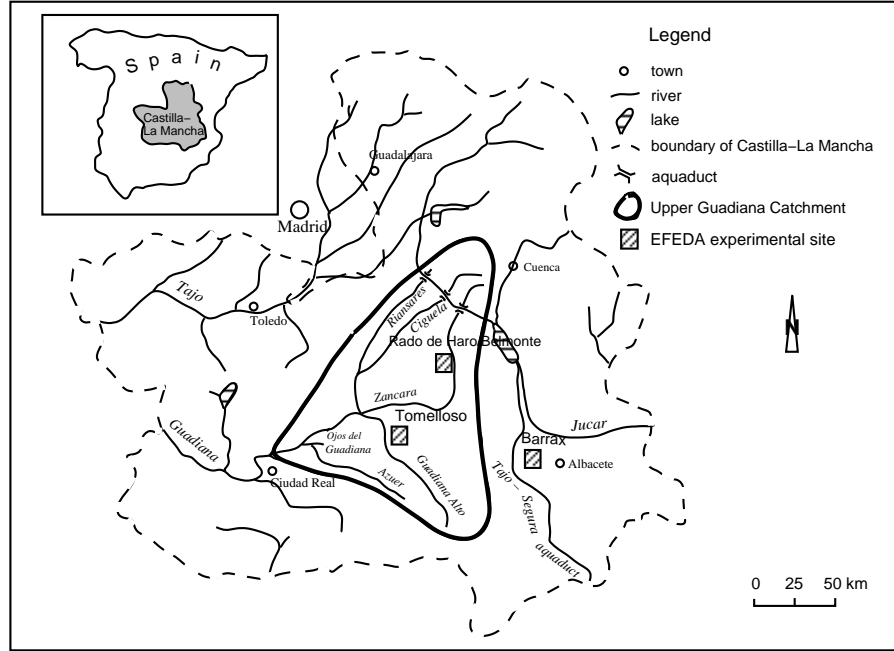
Figure 1.1: *Location of the EFEDA experimental sites relative to the Upper Guadiana Catchment. The Upper Guadiana Catchment coincides with the West La Mancha region.*

in land–surface characteristics at both the regional and global scale, they may permit one to extend the results to climate variability and global change problems.

1.1.2 The EFEDA project

In the above mentioned context and within the framework of the European International Project on Climatic and Hydrological Interactions between Vegetation, Atmosphere and Land–surfaces (ECHIVAL), a detailed study of land–surface changes in the La Mancha region of central Spain was conducted [*Bolle et al.*, 1993].

Within the ECHIVAL Field Experiment in Desertification–threatened Areas (EFEDA), processes responsible for moisture and energy exchange at the land surface–atmosphere interface were studied. Experiments were conducted to measure vegetation-, soil-, and (micro)meteorological parameters and to assess their role in so called 'Soil–Vegetation–Atmosphere–Transfer' (SVAT) models. These models describe soil–atmosphere interactions, and form the basis for representation and application of water- and energy transfer processes in global climate models.

To reduce the complexity of this task and to provide for comparison with observations from space, the relatively flat area of La Mancha in central Spain was selected for a pilot experiment (see Fig 1.1). Three representative sites were selected for detailed measurements: a partially irrigated agricultural site in the east near the village of Barrax; a dry cultivation site with mostly vineyards in the West La Mancha region near Tomelloso; and an area with a large fraction of uncultivated semi–natural vegetation in the north near Rado de Haro/Belmonte. All three experimental sites were instrumented with a variety of measuring devices for continuous monitoring of soil, plant, and atmospheric conditions.

1.1.3   Aridification in the West La Mancha region

The area of West La Mancha, named after the Moorish term *manxa*, i.e. dry land, has been characterized throughout history by poor economic development founded on agriculture and associated industries. This region has also experienced a significant decrease of the population during this century, largely the result of emigration to the cities. Economic stimulation of the region through increased investment by the banking and manufacturing industry has been recommended by a report of the Spanish Office of Industry and Energy [*IGME*, 1980a]. This report also recommended a change from overabundant and unprofitable traditional agricultural production, i.e. cereals, grapes and olives, to more profitable crops such as fruits and vegetables.

During this century, the region has gone from a predominantly rain–fed agricultural system to an irrigation–based system, since the availability of groundwater resources was not considered limiting. The reality of the situation indicates, though, that groundwater resources have been depleted to dangerously low levels and yet continue to be exploited at rates which far exceed the recharge capability. The continued demand for this resource has resulted in a highly complex situation, with scientific, economic and political ramifications.

Although a market–based water use strategy has been implemented in this region, such a policy tends to overlook the many social, cultural and ecological implications. When the allocation of water resources is based on the ability to pay, those who require it most desperately for basic subsistence, often must do without. Such a policy is clearly not in the best interest of the majority.

A direct ecological consequence of the market–based approach has been the overpumping of the main aquifer in the West La Mancha area and the subsequent effect on the National Park of the Tablas de Daimiel (see Fig. 2.1). This internationally famous ecosystem and refuge for various fauna and flora, altered from an extensive wetland into a dry barren site maintained by an artificial water supply from an adjacent river catchment and, rather ironically, from the underlying West La Mancha aquifer.
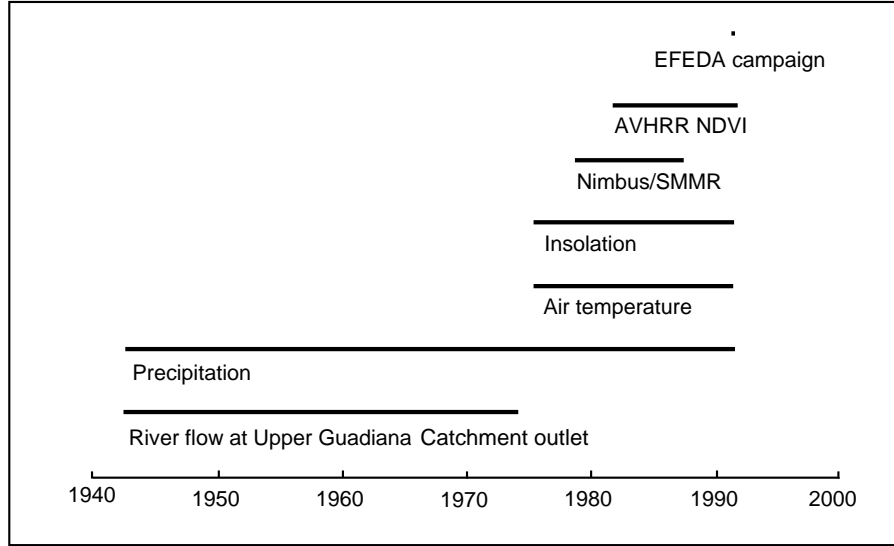
Figure 1.2: *The time series of available data used in the present study.*

1.2 Study objective and approach

Soil moisture is the temporary storage of precipitation within a layer of shallow depth at the land surface–atmosphere interface. In general, this layer is limited to the zone of aeration and approximately coincides with the root zone. For the purposes of the present study, surface moisture or topsoil moisture is defined as the water content of the very upper part or top of the soil profile, corresponding to a 5 cm soil depth or as otherwise indicated.

Surface moisture is an important integrating parameter in the processes responsible for the exchange of water and energy at the soil–atmosphere interface. Accordingly, it plays a significant role in large–scale atmospheric circulation processes [e.g. *Beljaars et al.*, 1993; *Betts et al.*, 1994]. Changes in these processes through time are reflected in the surface moisture and, as such, it may be used as an indicator of climatic variability and/or land use change.

Soil moisture is extremely difficult to measure in time and space, especially at large spatial scales. It changes constantly as a result of precipitation events, evaporation processes (which include extraction by vegetation) and redistribution within the soil. Soil moisture is highly variable on both small and large spatial scales, due to the variability of precipitation and the heterogeneity of the land surface (e.g. vegetation, soil physical properties, topography, etc.). While point sampling is for the most part reliable, areal averaging of these measurements, especially at spatial scales of $10^2 - 10^3$ km^2, will often introduce large errors.

Satellite microwave remote sensing has been shown to be an adequate technique to perform such large–scale surface moisture monitoring. *Owe et al.* [1992],
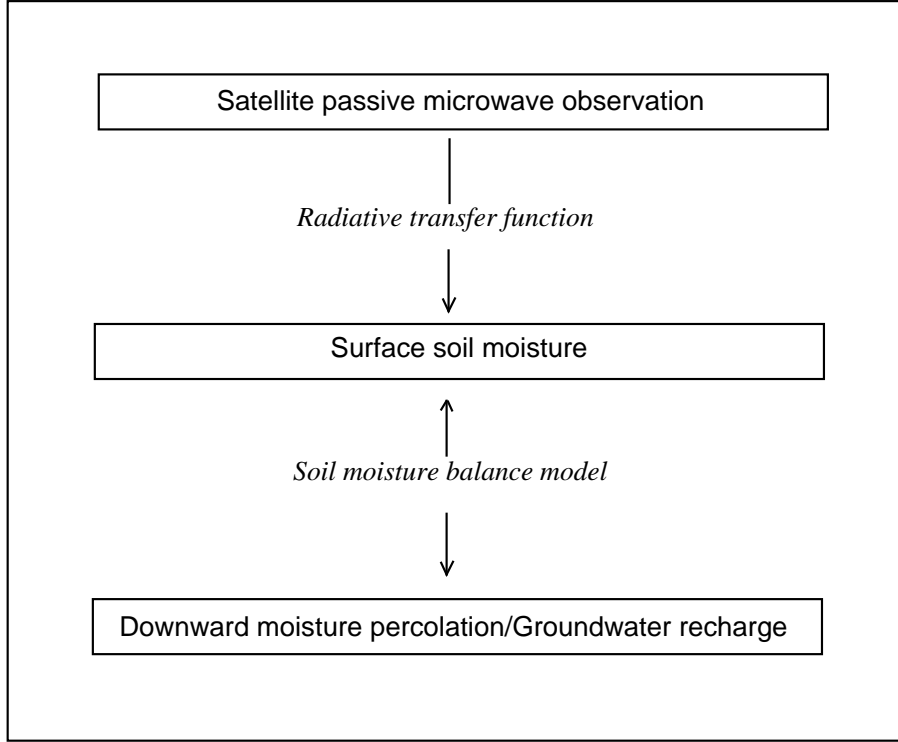
Figure 1.3: *Schematic representation of individual elements of the retrospective analysis carried out in the present study.*

Van de Griend and Owe [1994a] and *Van de Griend and Owe* [1994b] effectively related spatially averaged surface moisture estimates to satellite passive microwave observations collected over a semi–arid area in Botswana.

Space based remote sensing offers a potential for improved large–scale monito–ring of the Earth's surface. Since remotely sensed land surface measurements provide for spatially averaged or areally integrated values, they are a logical input to regional or larger–scale models. If properly utilized, satellite systems will yield data at the spatial, temporal and spectral scales required for consistent and continuous coverage of many aspects of the whole Earth and its atmosphere. Such detailed observations are necessary to monitor the often subtle environmental changes that frequently occur. Microwave sensing is unique, in that it is the only technology which is able to provide a consistent and physically based direct reading of the amount of water at the Earth's surface, while being minimally affected by the atmosphere.

The primary objective of the present study is to investiagte the potential of passive microwave surface moisture monitoring as a tool for the detection and evaluation of both regional scale climate variability and land use change. If successful, it may enable one to evaluate the impact of these changes on the

regional soil moisture balance and other apparent changes in the environmental conditions. The hypothesis is tested in the West La Mancha area.

The study is approached as a retrospective analysis of long–term time series of meteorological, hydrological and remote sensing data (see Fig. 1.2). The analysis of these time series is based on the derivation of regional surface moisture from passive microwave satellite data and the regional application of a soil moisture balance model. The time series of hydrological data are used as a control on the soil moisture balance model results. The individual elements of the analysis are depicted in Fig. 1.3 and further introduced below.

Nimbus–7/SMMR 6.6 GHz passive microwave observations   The lifetime of the Scanning Multichannel Microwave Radiometer (SMMR) on board the Nimbus–7 satellite extends from October 1978 to August 1987. Time series of regional surface moisture are derived from the satellite data, based on solving a radiative transfer equation for vegetation covered areas. Two approaches are used to solve the equation, which differ in the way the contribution of the vegetation to the microwave signal is corrected for. Vegetation radiative transfer properties derived from a ground–based microwave experiment are implemented in the radiative transfer equation to assist in the interpretation of the satellite data. A complete description of the analysis of satellite observations is presented in Chapter 3.

Soil moisture balance modelling   Time series of topsoil moisture content are modeled using a regional scale moisture balance approach. A modified *Priestley–Taylor PET* concept is applied to compute the evaporative loss from the topsoil. In this modified concept an evaporative fraction curve relates evapotranspiration to the topsoil moisture content. Experimental data of the EFEDA campaign are used to derive an area–averaged evaporative fraction curve and to apply the soil moisture balance model to the West La Mancha region. Once implemented, the soil moisture balance model is able to run with an input of routinely measured meteorological data. Chapter 4 describes the soil moisture balance model and its application to the study area.

Downward vertical moisture percolation   The average annual modeled downward vertical moisture percolation computed with the soil moisture balance model, is compared to the long–term average annual recharge estimate from river flow at the Upper Guadiana Catchment outlet. As such, the recharge estimate is used as a control on the time series of modeled topsoil moisture. A description of the analysis is presented in Chapter 5.

A summary of the analyses and conclusions arising from the present study are presented in Chapter 6. Prior to the retrospective analysis, a description of the study area is given in Chapter 2.

Chapter 2

Study area

2.1 Physiography

The West La Mancha region is located in the Southern Castillian Submeseta of central Spain. As illustrated in Fig. 1.1, it coincides with the Upper Guadiana Catchment. Fig. 2.1 presents the area at an enlarged scale. The region covers 16130 km^2, of which approximately one third is occupied by a gently undulating central plain, La Llanura Manchega. Elevation ranges from 600 m in the west to 750 m in the east. The northern part of the catchment, La Sierra de Altomira and La Mancha de Toledo, is characterized by gentle NW–SE oriented hills, ranging in elevation from 700–800 m. To the north the altitude increases to 1100 m. In the southeastern part of the catchment, the tabular–shaped relief of El Campo de Montiel is located with elevations ranging from 800–1000 m. The eastern boundary of the Upper Guadiana Catchment is formed by the N–S oriented drainage divide with the Jucar Catchment. At the outlet in the west, i.e. the reservoir of El Vicario, the watershed is bounded by the extensions of los Montes de Toledo.

The climate is classified as continental Mediterranean; dry and moderate. The average annual air temperature varies between 11.5–14.5ºC with extremes in December (4–6ºC) and July (23–26ºC) [*IGME*, 1980a]. The ferocity of the climate is illustrated by a 63ºC maximum range in the air temperature, ranging from 46ºC to –17ºC (1931–1980). This originates the characterization of La Mancha's climate as *nueve meses de invierno y tres meses de infierno*, i.e. nine months of winter and three months of hell [*Cervantes Saavedra*, 1605]. The maximum duration of the frost–free period is four months.

The long–term average annual precipitation varies between 415 mm in the centre of the catchment to 450–500 mm in the elevated boundary zone [*IGME*, 1980b]. This places the region among the driest in Europe. Precipitation is highly variable with large interannual variation and also considerable spatial variation within any one year. Fig. 2.2 shows the cumulative departure from mean precipitation in the central Llanura Manchega plain for the period 1943–
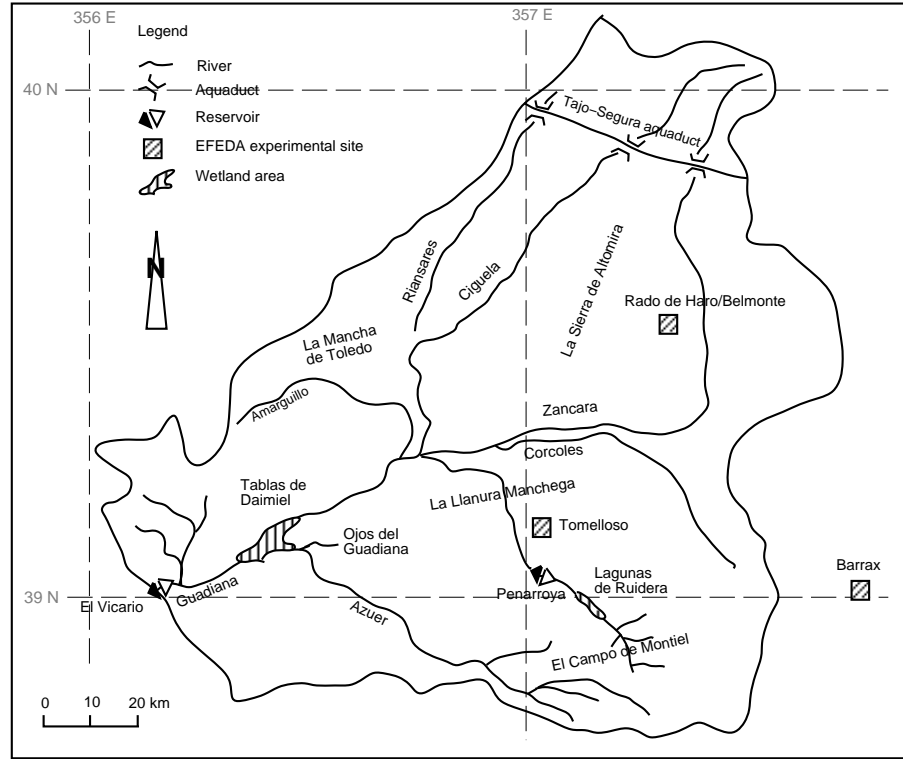
Figure 2.1: *The Upper Guadiana Catchment.*

1987, clearly demonstrating large variation and periodicity of alternating humid and dry periods with respect to the average [*SGDGOH*, 1988]. Precipitation is largely seasonal, with the spring and autumn seasons being the wettest.

Estimated annual potential evapotranspiration is in the order of 800 mm by Thornthwaite's method [*Thornthwaite*, 1944]. The evaporative demand thus exceeds precipitation except during the period November–March [*IGME*, 1980a]. High evapotranspiration rates and low rainfall cause surface flows to be small. Under natural conditions the long–term annual discharge of the Upper Guadiana river at the outlet of the catchment averaged 25 mm or only 5% of annual precipitation. Under these conditions the flow in most rivers was largely maintained by subsurface flow. Long–term river discharge therefore provides an indication of long–term recharge. Estimated long–term actual evapotranspiration balances the remaining 95%. Cloud–free or partly clouded conditions predominate over fully clouded conditions resulting in an average annual insolation of 2600–2900 hours [*IGME*, 1980a]. The dry character of the climate is also confirmed by an average annual relative humidity of 65%.
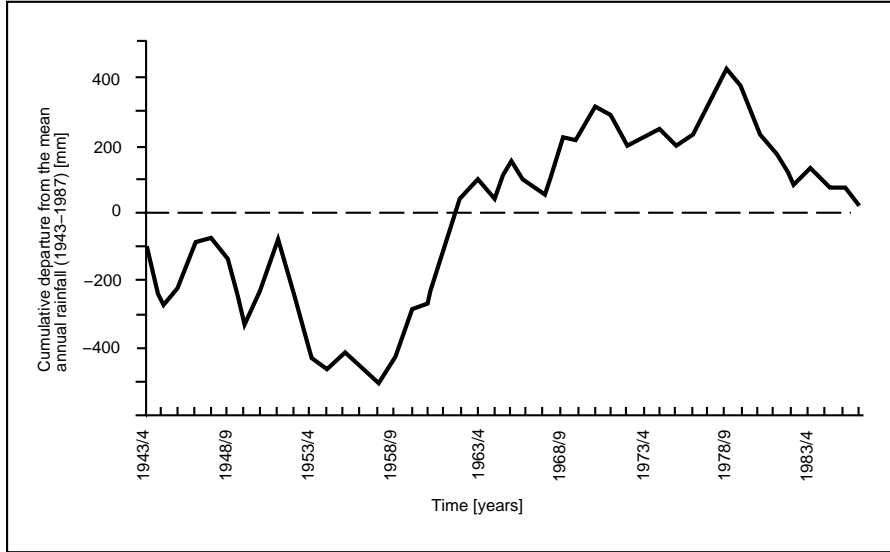
Figure 2.2: *Average annual rainfall in the Llanura Manchega (1943–1987): Cumulative departure from the mean (Source: SGDGOH [1988]; Young [1996]).*

2.2 Land use and socio–economic aspects

As introduced briefly in Section 1.1.3, until some two or three decades ago land use in La Llanura Manchega was mostly restricted to dry land farming of vineyards, olives and cereal crops. Irrigation of vegetable and fruit crops was practiced on a small scale in the vicinity of the 'La Mancha Wetlands', a UNESCO Biosphere Reserve composed of lakes and swamps in karst zones and along river courses, with a total area of approximately 250 km^2. Located within this zone is the National Park of the Tablas de Daimiel. In its original state this wetland of approximately 20 km^2 was maintained by surface flow from the Cigüela river and by subsurface flow from the West La Mancha aquifer via the Upper Guadiana river (see Fig. 2.6). Under previous natural conditions groundwater had always maintained a base level in the wetland, particularly during dry periods e.g. during the drought period in the 1950s (see Fig. 2.2).

A semi–natural grass, shrubs (rosemary, lavender, immortelle, sage) and tree vegetation i.e. oaks (*ilex, kermes*) are found in the basin boundary hills. Land use in this area has been historically restricted to firewood collection and grazing by sheep and goats.

A second ecosystem, the National Park of the Lagunas de Ruidera, is located in the bordering relief of El Campo de Montiel. The Upper Guadiana spring coincides with a cascade of lakes maintained by subsurface flow draining the Campo de Montiel aquifer. This aquifer is considered to provide a significant input to the West La Mancha aquifer. Under natural conditions prior to construction of

the Peñarroya dam, this was illustrated by the progressive disappearance of the Upper Guadiana river entering the Llanura Manchega plain from the southeast followed by a subsequent reoccurrence at the Ojos del Guadiana springs (see Fig. 2.1).

A decline in the agricultural economy in the 1950s and the 1960s was reflected in a marked decrease in local per capita income and subsequent standard of living, resulting in a significant population movement out of the area. From the late 1960s, the irrigation system infrastructure was significantly extended from the wetlands in the central Llanura Manchega plain to provide for the cultivation of profitable crops. Although the development of groundwater resources within La Llanura Manchega has not been controlled by quantitative licensing, which makes any assessment of the extent of exploitation very approximate [*Young*, 1996], it is estimated that irrigated land has increased from less than 300 km^2 to well over 1300 km^2 between 1974–1990. The annual water demand has subsequently increased from approximately 10 mm to some 40 mm and has been supplied largely by the West La Mancha aquifer, which underlies the central Llanura Manchega plain. Investment in the agricultural industry was highly encouraged as a result of the relatively low cost at which water was available. Irrigated cultivation in the basin boundary hills did not begin until the late 1970s. Water in this area is being supplied by local aquifers bordering the catchment (see Section 2.4). The amount of water abstracted from these bordering aquifers is about 10% of the total abstraction in the entire catchment [*Bromley et al.*, 1996].

The more profitable irrigation–based agriculture significantly increased production of crops such as cereal, maize, alfalfa, melon and grapes, resulting in a highly improved local economy. The regional economy received an additional boost by the entry of Spain to the European Union (EU) in 1986, since its status as a poorly developed agricultural region created a source of subsidies for the area. This resulted in a significant expansion of the market for local products, and encouraged 'cash crop' cultivation driven by market forces and price agreements within the EU. This philosophy was highly inconsistent with the regional hydrogeology, ultimately resulting in overuse and possibly permanent damage to the hydrogeological systems.

Coupled with the severe drought which occurred during the 1980s (see Fig. 2.2), the excessive groundwater use began to manifest itself in dramatic fashion. An annual decline of the West La Mancha aquifer groundwater level of 1–2 m, with a total decline of approximately 30 m, caused the Ojos del Guadiana springs to fall dry in 1984. Other rivers and wetlands in the central LLanura Manchega plain fell dry during the same period; the National Park of las Tablas de Daimiel changed from an extensive wetland into a mere puddle. In February 1987 the West La Mancha aquifer was provisionally declared overexploited; economic interests delayed the formal declaration until December 1995. Following a sharp water level decline in the National Park of the Lagunas de Ruidera in 1987, the Campo de Montiel aquifer was formally declared overexploited in June 1989, creating increased tension between farmers and government authorities. Since water abstraction from the Campo de Montiel aquifer is relatively small, water
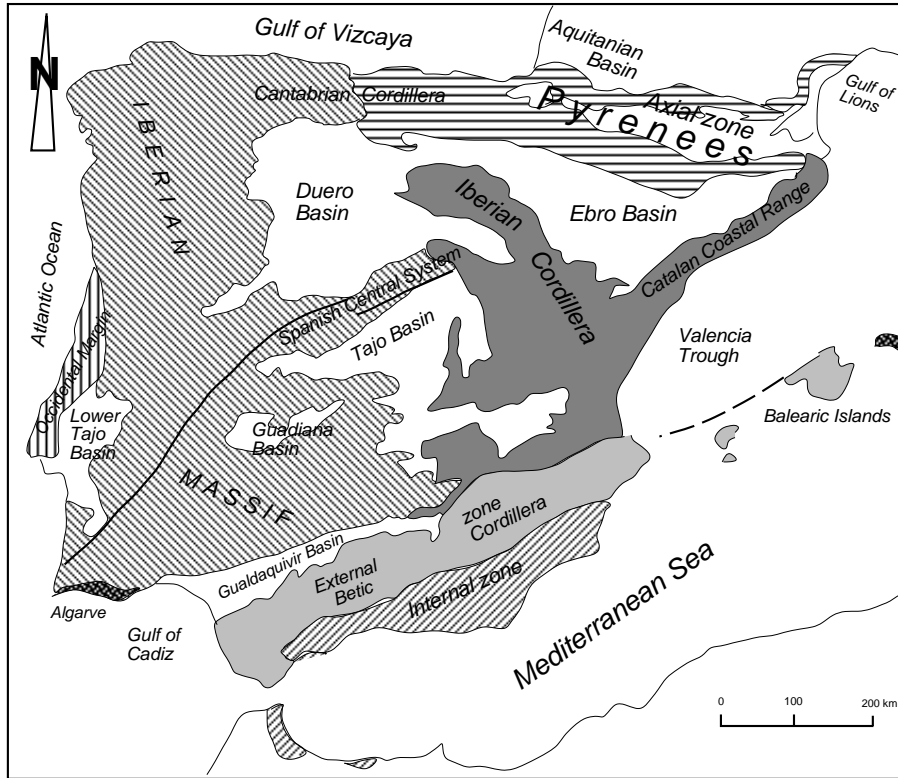
Figure 2.3: *Location of the Guadiana Basin in a simplified geological scheme of the principal domains in the Iberian Peninsula. (simplified and modified from IGME [1972]).*

levels probably declined as a result of the post–1980 drought period. A drought period during the 1950s had already caused the Lagunas to dry out on this previous occasion. Following the wet winter of 1995/1996 the water level in the Campo de Montiel aquifer recovered, while water levels in the West La Mancha aquifer continued to decline.

Current efforts directed towards achieving a more sustainable development of the region are aimed at reducing the rate of groundwater abstraction to the rate of recharge. Recent EU subsidies have been paid to landowners in compensation for not irrigating their land. While this financial arrangement improved relations between farmers and authorities and encouraged development of alternative cultivation techniques which use less water, it has also had a negative impact on employment [*Llamas et al.*, 1996a]. Since much of the land traditionally has been in the hands of large property owners, vast tracts are being left idle, resulting in increased unemployment within the agricultural sector and associated industries.

2.3   Geology

The study area forms a Tertiary basin located in the southern Iberian Massif (Fig. 2.3). The regional stratigraphy and the geological structure are summarized in the following sections. A more detailed description of the regional geology is given in several reports by the Instituto Geologico y Minero de España, e.g. *IGME* [1975]; *IGME* [1976a]; *IGME* [1976b]; *IGME* [1976c]; *IGME* [1988].

2.3.1   Stratigraphy

Fig. 2.4 presents the regional stratigraphy. Paleozoic sediment is of Cambrian, Ordovicium and Silurian age and primarily consists of quartzite and slate.
The Mesozoic is represented by sediment of the Triassic, the Jurassic and the Cretaceous. The Triassic sediment consists of red detritic series of sand–conglomerate and clay of the Buntsandstein and (hyper)saline deposits of marly gypsum of the Keuper. The estimated thickness of the Triassic series is 150 m. The Jurassic deposits comprise sediment of the Liassic, Dogger and Malm. The Lower Liassic sediment consists of limestone (calcarenites and bioclasts). Middle Liassic sediment comprises dolomite, limestone (lime mud) and clay. Upper Liassic and Lower Dogger sediment consists of limestone (calcarenite). Deposits of the Middle/Upper Dogger and Malm are present only in the northern part of the study area. The sediment consists of (oolitic) limestone, dolomite and *carniolas*: a dark red partly dissolved brittle limestone. The total thickness of the Jurassic deposits is estimated to vary between 50–200 m, accumulating from west to east.
The Lower/Upper Cretaceous (Albian–Cenomanian) sediment comprises sandy deposits of the Utrillas facies. The Upper Cretaceous (Turonian–Senonian) deposits consist of (marly) limestone and dolomite. Maximum thickness is approximately 150 m.
The Cenozoic deposits are represented by Tertiary sediment of Paleogene and Neogene (Miocene–Pliocene) age and by Quaternary sediment. The Paleogene sediment is found in the northern part of the study area and consists of conglomerate of limestone and quartzite pebbles in a sandy matrix. The conglomerate alternates with (lacustrine) limestone and marl. Maximum thickness is 150–200 m.
Late Miocene (Pontien) deposits consist of sand–conglomerate and clay. A maximum sediment thickness of 20–40 m is found in the Záncara river depression. On top of the sediment a series of Miocene–Pliocene (marly) limestone is deposited. The marl content increases towards the Pliocene top of the series. The Miocene–Pliocene series occupy the surface of most of the western part of the Llanura Manchega. Here, the sediment reaches a maximum thickness of 200 m. The average thickness is 35 m.
In the southern part of the basin deposits of Pliocene age consist of conglomerate of quartzite pebbles in a (sandy) clay matrix. The maximum thickness is 30–40 m. In the northern part of the basin Pliocene deposits consist of conglomerate of limestone pebbles in a sandy (clay) matrix. The average thickness is 3 m.
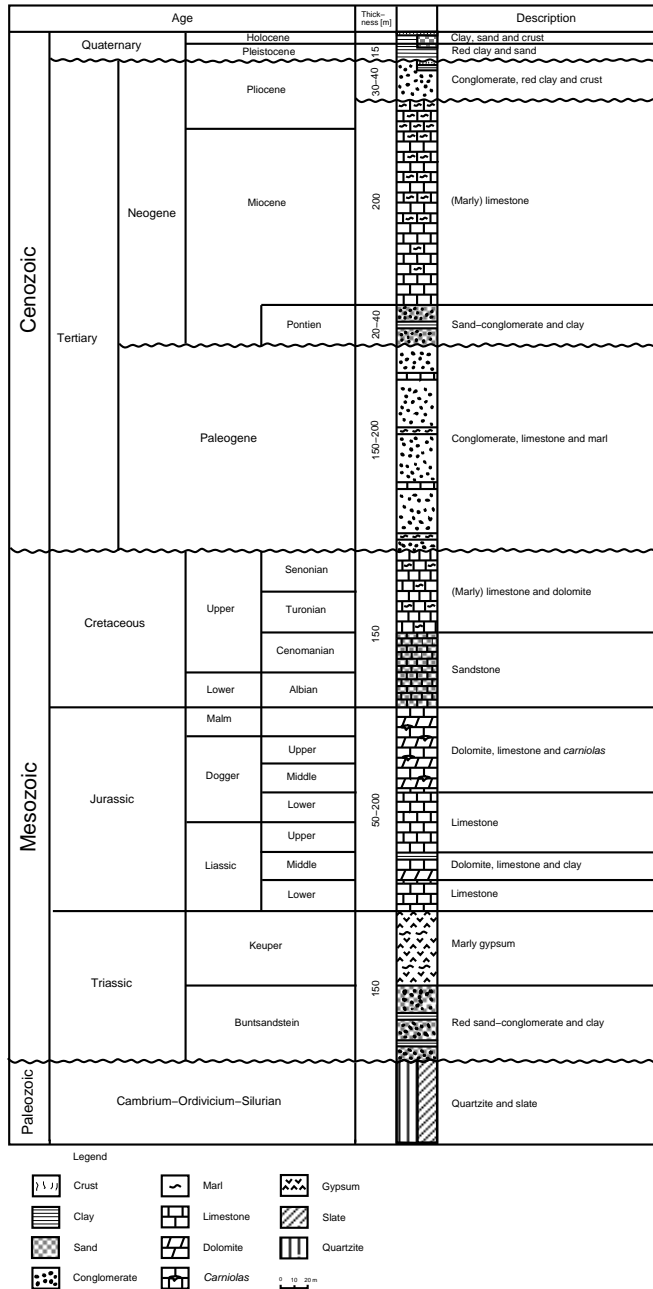
Figure 2.4: *Generalized lithostratigraphic section of the Upper Guadiana Basin (Source: IGME [1975]; IGME [1976a]; IGME [1976b]; IGME [1976c]; IGME [1988]).*

Upper Pliocene material consists of red clay soils and calcicrusts (*caliches*). The maximum thickness is 4 m.

Quaternary sediment comprises deposits of Pleistocene and Holocene age. The Pleistocene sediment is composed of red clay, which contains pebbles of limestone and quartzite and *caliche* fragments. The size of the included pebbles and fragments decreases towards the centre of the basin. The maximum thickness is 15 m. Pleistocene sediment in the Záncara river depression consists of sand and pebbles of limestone and quartzite. Holocene deposits consist of calcicrusts and alluvial sediment of clay, sand and organic material.
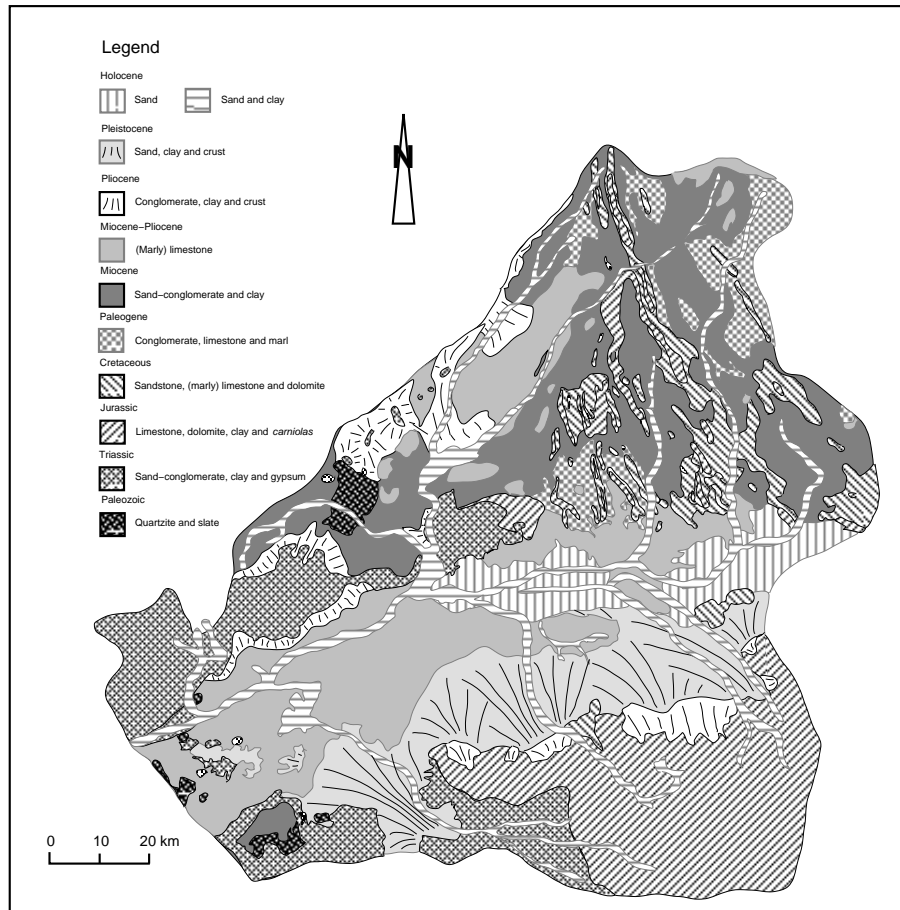
Figure 2.5: *Geological map of the Upper Guadiana Basin (simplified and redrawn after IGME [1985]).*

2.3.2 Geological setting and structure

The basement of the Iberian Massif consists of rocks affected by the Hercynian orogeny. The rocks are folded in a NW–SE direction. In the basement a stepwise block series is considered to be present descending towards the Záncara river depression in the central part of the Upper Guadiana Basin [*IGME*, 1976c]. Some of the faults separating these blocks have been reactivated, e.g. during post–Miocene isostatic movements. In general however, the basement provided a rigid substratum on which the Mesozoic series are folded.

During post–Hercynian uplift, the elevated blocks were subjected to intense erosion, resulting in a nearly complete peneplanation. Subsequently, during the Buntsandstein a fluvio–lacustrine regime was initiated.

The Keuper is characterized by a lagoon type of sedimentation. The sediment is found directly above the Buntsandstein deposits; a lack of Middle Triassic (Muschelkalk) indicates marginal, near–shore sedimentation conditions.

During the Lower Liassic a transgressive cycle began over an open subhorizontal platform. The Lower Liassic sediment was subsequently subjected to dolomitization during the Middle Liassic. This period is characterized by conditions of limited shallow sedimentation and intense evaporation. The deposits indicate the presence of fresh water flows. During the Upper Liassic (and possibly Lower Dogger) a new transgressive cycle occurred with a return to open shelf conditions. Sediments deposited during the Middle- and Upper Dogger and Malm indicate (sub)littoral near–shore conditions. A prolonged regression in the southern part of the basin from the Middle Dogger to the Lower Cretaceous (Albian) resulted in the marine coastline falling outside the region. Continental erosion led to dolomitization and recrystallization of the Upper Liassic sediment producing *carniolas*.

Sedimentation resumed during the Lower/Upper Cretaceous (Albian–Cenomanian) in a restricted transgressive cycle: the Utrillas facies. During the Upper Cretaceous (Turonian–Senonian) sedimentation was followed by several stages of dolomitization under marginal coastal conditions.

In the following time period a paleogeographic change was created by uplift of the Iberian Massif (see Fig. 2.3). The uplift caused a marine regression in a southeast direction and a final change to continental sedimentation conditions for the region. The Mesozoic sediment was intensely fractured and gently folded in an isolated synclinal basin structure during several compressive phases in the period from Upper Cretaceous to Early Miocene.

A line running through the Záncara river depression parallel to the fault direction in the Iberian Massif basement separates the southern and northern flank of the synclinal basin. The sediment of the southern flank is moderately inclined ($15 - 30°$) and intersected by (sub)vertical faults in NW and NE direction. NW–SE oriented folds intersected by parallel faults are present on the northern synclinal flank.

During the period of compressional phases (Upper Cretaceous–Early Miocene) all of the Cretaceous and part of the Jurassic sediment was eliminated on the southern synclinal flank. The Jurasssic and Cretaceous deposits on the northern

synclinal flank were fossilized by sedimentation during the Tertiary (Paleogene). The sediment indicates the presence of small, isolated basins.

During the Miocene (Pontien) sedimentation resumed in the central part of the synclinal basin with a fluvial type of deposition. The sedimentation was continued with a lacustrine type of deposition (Miocene–Pliocene).

After sedimentation ceased in the central basin, tectonic movement resulted in gentle folding and intense fracturing of the Miocene–Pliocene series. This movement is considered to correspond with an imbalance in the basement and Mesozoic series resulting from Tertiary sedimentation overload (see above, this section).

In the southern part of the synclinal basin, pediments (*rañas*) formed during a subsequent erosive cycle. These pediments were deposited by debris flows, coming from the Paleozoic relief at the exterior of the basin. In the northern part local pediments originated from nearby hills. During the Upper Pliocene red clay soils and calcareous crusts (*caliches*) formed on the pediments and Mesozoic strata. These materials indicate arid to semi–arid climate conditions.

The arid Upper Pliocene period was followed by a relatively humid period during the Pleistocene. The Pliocene pediments were eroded to form pediments in the southern part of the central basin. On the pediment surfaces a N–S oriented fluvial network formed draining towards the Záncara river depression. Although this network is partly fossilized and degenerated by tapping the underlying Mesozoic limestone, it is still functional at present (see Fig. 2.5).

During the humid period of the Pleistocene chemical weathering occurred in the central part of the basin. This resulted in planation and in karstification processes, which seized upon the extensive fracture pattern in the Miocene–Pliocene (marly) limestone series.

The present course of the Upper Guadiana river and its tributaries parallel to the E–W stretch of the central Llanura Manchega plain is established in karst depressions. In some of these depressions groundwater is discharged to form wetlands (see also Section 2.4).

Alluvial deposits correspond to a calm flow regime. Upward capillary flow of soil moisture containing dissolved calcium–carbonates followed by subsequent evaporation, causes continuing formation of calcicrusts.

2.4   Hydrogeology

Four aquifer systems are distinguished in the Upper Guadiana Catchment. These are the West La Mancha aquifer, the Campo de Montiel aquifer, the Sierra de Altomira aquifer and the Mancha de Toledo aquifer. This section describes the main aquifer characteristics. A more detailed description of the regional hydrogeology is given in *IGME* [1980a]; *IGME* [1980b]; *IGME* [1985]. The West La Mancha aquifer underlies the Manchega plain and is the largest and most productive (Fig. 2.6). The aquifer is built up of (marly) limestone of Miocene–Pliocene age and occupies the entire surface of the 5500 km^2 central Llanura Manchega plain. Average depth is 35 m with a maximum of 200 m
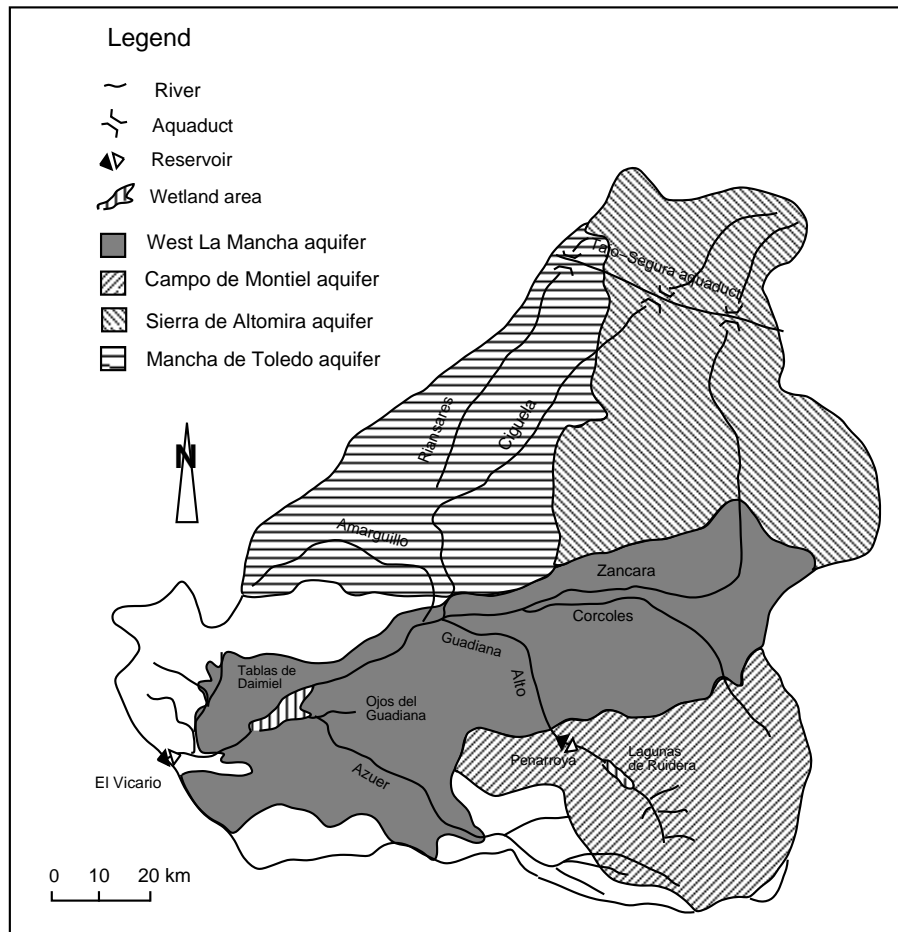
Figure 2.6: *Hydrogeological map of the Upper Guadiana Catchment (simplified and redrawn after IGME [1985]).*

in the central parts of the Llanura Manchega. The West La Mancha aquifer extends across the catchment divide to the East La Mancha aquifer, where it underlies the Jucar Catchment (see Fig. 1.1).

The West La Mancha aquifer is an unconfined aquifer. It is recharged by infiltration from rain water and intermittent rivers and by groundwater flow from adjacent aquifers. Under undisturbed natural conditions the aquifer was drained by the Upper Guadiana river and by evapotranspiration from wetlands formed by exfiltration of groundwater in karst depressions (see also Section 2.3.2). Over the last 20 years a progressive decline in groundwater level due to overpumping has caused rivers and wetlands to dry. Hence, a self–perpetuating system has ceased to function [*Cruces et al.*, 1992]. A rising groundwater level during humid periods resulted in an increase of wetland area and a consequent increase in evapotranspiration from these areas. At the same time, the contribution to rivers draining the aquifer increased. Dry periods resulted in the opposite effect. Combined with the multi–annual storage capacity of the aquifer, this mechanism maintained surface flow and flooded areas throughout the year. Under the present conditions the aquifer is primarily drained by groundwater abstraction. In the western part of the Llanura Manchega, the West La Mancha aquifer is underlain by impervious Paleozoic and Triassic sediment (see Fig. 2.5). In the eastern part, it is underlain by extensions of the Campo de Montiel aquifer and the Sierra de Altomira aquifer. It is separated from the latter aquifers by (semi–)impervious Miocene detritic deposits.

The Campo de Montiel aquifer is situated in the south of the Upper Guadiana Catchment and covers an area of 2700 km^2. Thickness varies between 50–200 m from west to east. It consists of karstified Jurassic limestone and dolomite, which are underlain by impervious Triassic sediment. Within the aquifer three levels may be distinguished: the upper level is unconfined and recharged by infiltrating rain water; the lower levels are (semi–)confined. To the north, the aquifer is overlain by the Tertiary sediment of the Llanura Manchega plain, where it connects to the West La Mancha aquifer. Thus it provides a significant amount of subsurface flow into the latter aquifer. Surface drainage occurs towards the rivers Azuer, Córcoles and Upper Guadiana; the latter originates from the National Park of the Lagunas de Ruidera and was dammed in 1959 to create the Peñarroya reservoir (see Fig. 2.6). Flowing over the Llanura Manchega, the rivers drain all or part of their water and, as such, they form an input source for the West La Mancha aquifer. Constant discharge rates within these rivers, indicate a high storage capacity of the Campo de Montiel aquifer.

The Sierra de Altomira aquifer is situated in the northeastern part of the Upper Guadiana Catchment and measures 4200 km^2. It is composed of several local Jurassic and Cretaceous limestone and dolomite aquifers separated by impervious marl and marl–limestone. The local aquifers are connected by faults of NW–SE direction. The strata are folded parallel to the faulting direction and underlain by impervious Triassic deposits. The aquifer is mainly recharged by infiltration of rain water. Part of the aquifer is covered by (semi–)impervious Tertiary deposits. Percolation from these deposits creates another source of recharge. In the covered parts the aquifer is (semi–)confined. It is drained by

subsurface flow to the West La Mancha aquifer and by the Záncara, Cigüela and Riansares rivers. The discharge rates of these rivers are highly variable and closely related to precipitation, indicating a lower storage capacity for the Sierra de Altomira aquifer. Under natural undisturbed conditions these rivers drained the West La Mancha aquifer from the point that they flow on to the Manchega plain. Under present conditions, water is lost from these rivers through induced recharge to the Sierra de Altomira and the West La Mancha aquifers.

The Mancha de Toledo aquifer is situated in the northwestern part of the Upper Guadiana basin and covers 3400 km^2. It is composed of folded alternating bands of pervious and impervious sediment of Paleozoic, Triassic and Tertiary age, resulting in a number of local aquifers with limited potential. It is recharged by rain water and drained by the Cigüela and Riansares rivers.

Chapter 3

Satellite surface moisture monitoring

3.1 Introduction

As discussed in Section 1.2, surface moisture is considered an important integrating parameter in the processes responsible for the exchange of water and energy at the land–surface interface. Its significance, therefore, as an indicator of changes in these exchange processes is apparent.

The advantages of satellite remote sensing in the context of monitoring regional surface moisture are two–fold. The first lies in its ability to provide information which is spatially integrated or averaged over a large area, generally the dimension of the pixel. The second advantage is the ability to provide repeated observations over a given area at regular time intervals.

Satellite passive microwave remote sensing has been shown to be an adequate technique for monitoring surface moisture at regional scales. *Owe et al.* [1992], *Van de Griend and Owe* [1994a] and *Van de Griend and Owe* [1994b] effectively related Nimbus–7 SMMR passive microwave data collected over Botswana, Africa to regional surface moisture, using two different approaches. These two approaches differed in the way the satellite microwave signal was corrected for the effect of vegetation. The first method was known as the synergistic approach, and used NDVI to parameterize the optical thickness of the vegetation. The second method was known as the dual polarization approach, and used constant ratios of horizontal and vertical polarization vegetation radiative transfer properties. In both approaches surface moisture estimates were used, derived from a regional 3–year weekly surface moisture data base, which served to calibrate a daily surface moisture model driven by meteorological data [*Owe and Van de Griend*, 1990].

This chapter presents the application of satellite passive microwave remote sensing within the present study. Section 3.2 introduces relevant microwave theory, which will help in understanding the principles of passive microwave remote

21

sensing. Section 3.3 describes the collection and processing of the satellite passive microwave data over the West La Mancha area. Section 3.4 presents the analysis of ground–based microwave measurements, which were conducted to assist in the interpretation and calibration of the retrospective satellite data. Section 3.5 describes the derivation of surface moisture from the collected satellite data.

3.2   Microwave theory

A detailed discussion of the theoretical basis and principles of passive microwave techniques can be found in a number of reference [e.g. *Njoku and Kong*, 1977; *Ulaby et al.*, 1981, 1982, 1986]. This section provides a brief overview of the microwave theory relevant to the present study.

3.2.1   Bare soil emissivity

Bare soil microwave emissivity is a measure of the natural thermal emission from the soil in the microwave region of the electromagnetic spectrum. Emissivity is an inverse function of a medium's dielectric properties, which are expressed in terms of the complex dielectric constant. This quantity is an electrical property of matter and measures the response of the medium to an applied electrical field. It is a complex number, containing a real and an imaginary part. The real part is a measure of the energy stored by the dipoles aligned in an applied electromagnetic field and the imaginary part is a measure of the energy dissipation rate in the medium. The absolute value of the dielectric constant is the index of refraction of the medium. Soil is a largely heterogeneous medium and its dielectric properties result from the combined permittivities of its constituents (i.e. air, rock, water, etc.). At low frequencies, the real part of the dielectric for a dry soil is low (less than $5\mathrm{Fm}^{-1}$), while for water the value is comparatively high ($\sim 80\mathrm{Fm}^{-1}$). This large difference in the dielectric properties between soil and water results in a measurable range in the emissivity (ranging from less than 0.5 to almost 1.0 at 6.6 GHz frequency), and provides the basis for microwave sensing of soil moisture.

The intensity of the microwave emission is usually referred to as its brightness temperature, T_b, and, neglecting atmospheric effects, may be expressed as:

$$T_\mathrm{b} = (1 - r_\mathrm{s})T_\mathrm{s} = e_\mathrm{s}T_\mathrm{s} \qquad (3.1)$$

where $e_\mathrm{s} = 1 - r_\mathrm{s}$ is soil surface emissivity; T_s is temperature of the emitting layer [K]. Soil surface reflectance, r_s, may be determined from the Fresnel equations, which describe the behaviour of an electromagnetic wave at a smooth dielectric boundary. For horizontally and vertically polarized radiation it may be expressed as:

$$r_{sH} = \left[\frac{\cos\mu - \sqrt{K - \sin^2\mu}}{\cos\mu + \sqrt{K - \sin^2\mu}}\right]^2 \tag{3.2}$$

$$r_{sV} = \left[\frac{K\cos\mu - \sqrt{K - \sin^2\mu}}{K\cos\mu + \sqrt{K - \sin^2\mu}}\right]^2 \tag{3.3}$$

where subscripts H and V refer to horizontal and vertical polarization respectively; μ is incidence angle; K is the absolute value of the complex dielectric constant.

The complex dielectric constant of a soil sample is difficult to measure in the laboratory, and even more so in the field. Due to the complexity of these measurements, a number of dielectric mixing models have been developed to calculate the complex dielectric constant [*Wang and Schmugge*, 1980; *Wang*, 1980; *Jackson and O'Neill*, 1986; *Dobson et al.*, 1985]. Most of these models perform reasonably well for a range of soil–water mixtures and are largely based on soil textural composition.

Although the relationship between soil moisture and soil emissivity is unambiguous, a number of external influences must generally be taken into consideration. These include surface roughness, vegetation effects and wavelength effects. Each of these are discussed in greater detail below.

3.2.2 Surface roughness

Surface roughness, as it pertains to microwave radiometry, is relative to and dependent on wavelength. A smooth surface for a relatively long wavelength, i.e. 21 cm (1.4 GHz), may not be smooth for a relatively short wavelength, i.e. 6 cm (4.9 GHz). In general, increasing surface roughness increases the emitting surface area, thus causing an increase in emissivity. Sensitivity to changes in soil moisture content also changes with roughness. As surface roughness increases, the range in emissivity from dry to wet conditions decreases substantially. Bare soil emissivity of a rough surface, e_{rs}, may be expressed as [*Choudhury et al.*, 1979]:

$$e_{rs} = 1 + (e_s - 1)\exp(-h\cos^2\mu) \tag{3.4}$$

where h is a dimensionless empirical parameter, related to the Root Mean Square (RMS) height variation of the surface. Values for h are reported to range from 0 for a smooth surface to 0.5 for a roughly ploughed surface [*Choudhury et al.*, 1979].

3.2.3 Vegetation effects

Vegetation both absorbs and scatters the emitted soil radiation, while also emitting its own microwave radiation. Vegetation radiative transfer characteristics

are commonly described in terms of its transmissivity, Γ , and scattering albedo, ω. Transmissivity may be expressed as a function of vegetation optical depth, τ, by:

$$\Gamma = \exp(\frac{-\tau}{\cos \mu}) \tag{3.5}$$

Optical depth is in turn related to the vegetation or canopy density. As vegetation density increases, the emitted signal from the soil surface is increasingly attenuated. Moreover, the intensity of the microwave signal emitted from the vegetation also increases with optical depth, thus saturating the microwave signal as observed above above the canopy. The result is a decrease in sensor sensitivity to changes in soil moisture.

Passive microwave emission intensity for a vegetation covered soil surface may be expressed by [*Kirdiashev et al.*, 1979; *Mo et al.*, 1982]; [for derivation see: *Van de Griend et al.*, 1996]:

$$T_\mathrm{b} = T_\mathrm{s}e_\mathrm{rs}\Gamma + (1 - \omega)T_\mathrm{c}(1 - \Gamma) + (1 - e_\mathrm{rs})(1 - \omega)T_\mathrm{c}(1 - \Gamma)\Gamma \tag{3.6}$$

where T_s and T_c are the temperature of the soil surface and vegetation canopy [K], respectively. The first term in the right–hand part of the equation describes the soil emitted microwave radiation. The second term represents the vegetation emitted radiation, e_c, while the third term describes the downward vegetation emitted radiation reflected by the soil.

The single scattering albedo, ω, describes the scattering of soil emitted radiation by vegetation. Its value may vary with species, plant associations, and vegetation density. It is reported to range between 0.04 and 0.12 for different crops [*Brunfeldt and Ulaby*, 1984; *Jackson and O'Neill*, 1990]. While an increase in ω results in a decrease in emissivity, both theoretical and experimental evidence has shown that the effect of the scattering albedo is relatively constant from dry to wet soil conditions [*Owe et al.*, 1992].

3.2.4   Wavelength effects

The effect of wavelength on microwave remote sensing is two–fold. First, longer wavelength radiation emanates from a greater soil depth, and thus is a reflection of moisture conditions throughout a deeper surface profile. While the contributing soil depth decreases slightly with increasing moisture content, penetration depth is thought not to exceed a few tenths of a wavelength under even the most optimum conditions [*Wilheit*, 1978; *Newton et al.*, 1982]. Second, longer wavelength radiation provides an increased ability to penetrate vegetation canopies. It is widely accepted that the optimum wavelength, λ, for microwave remote sensing of soil moisture is about 21 cm [*Schmugge*, 1985].

Figure 3.1: *Nimbus–7/SMMR 6.6 GHz passive microwave footprint T_b, collected over the West La Mancha area; period 1978/79 to 1980/81.*
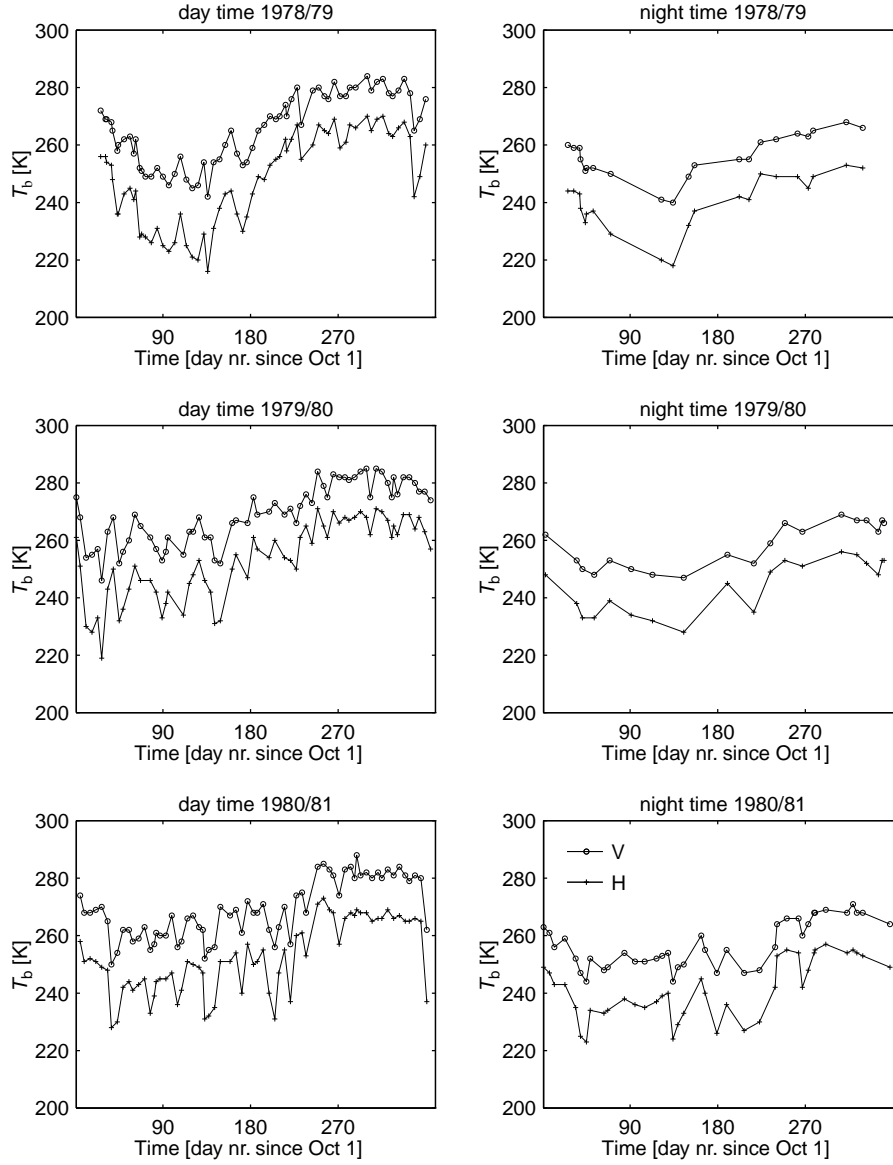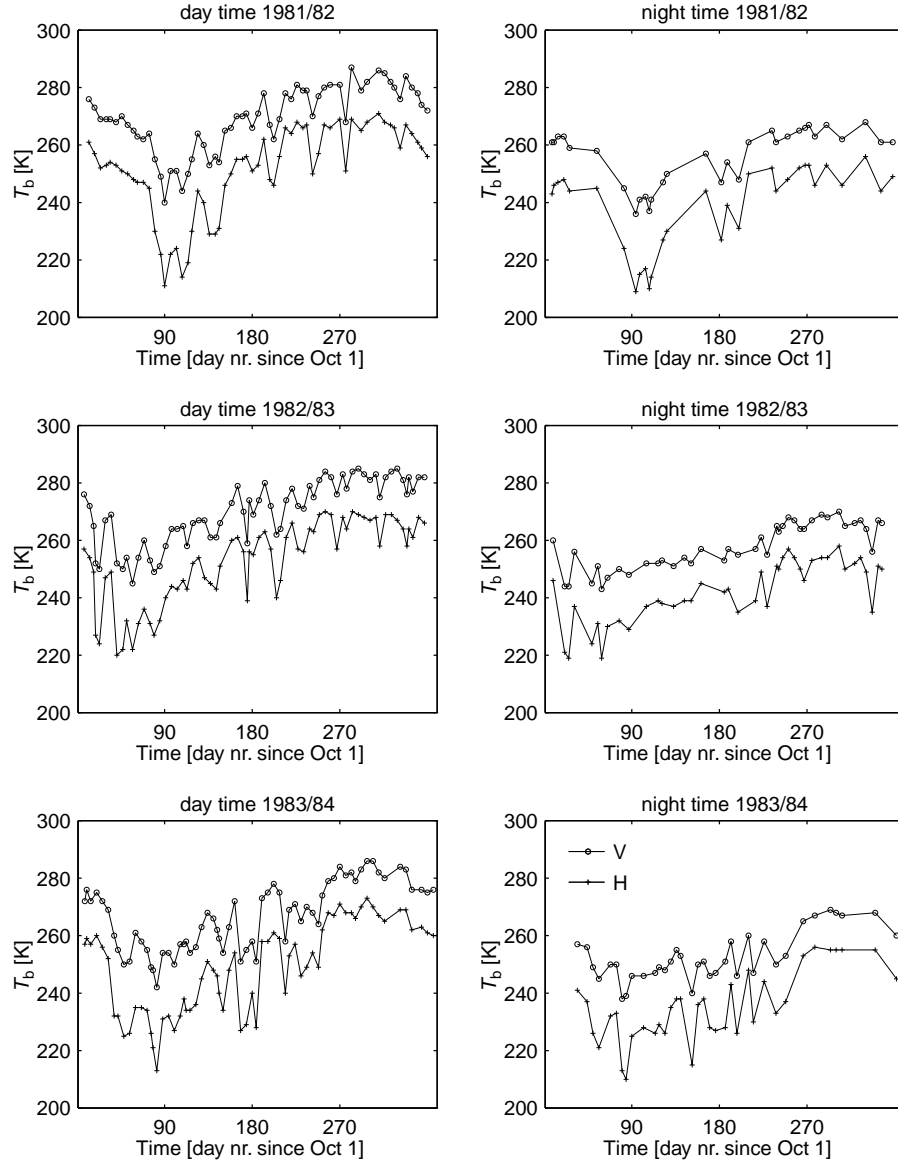
Figure 3.2: *Nimbus–7/SMMR 6.6 GHz passive microwave footprint T_b, collected over the West La Mancha area; period 1981/82 to 1983/84.*
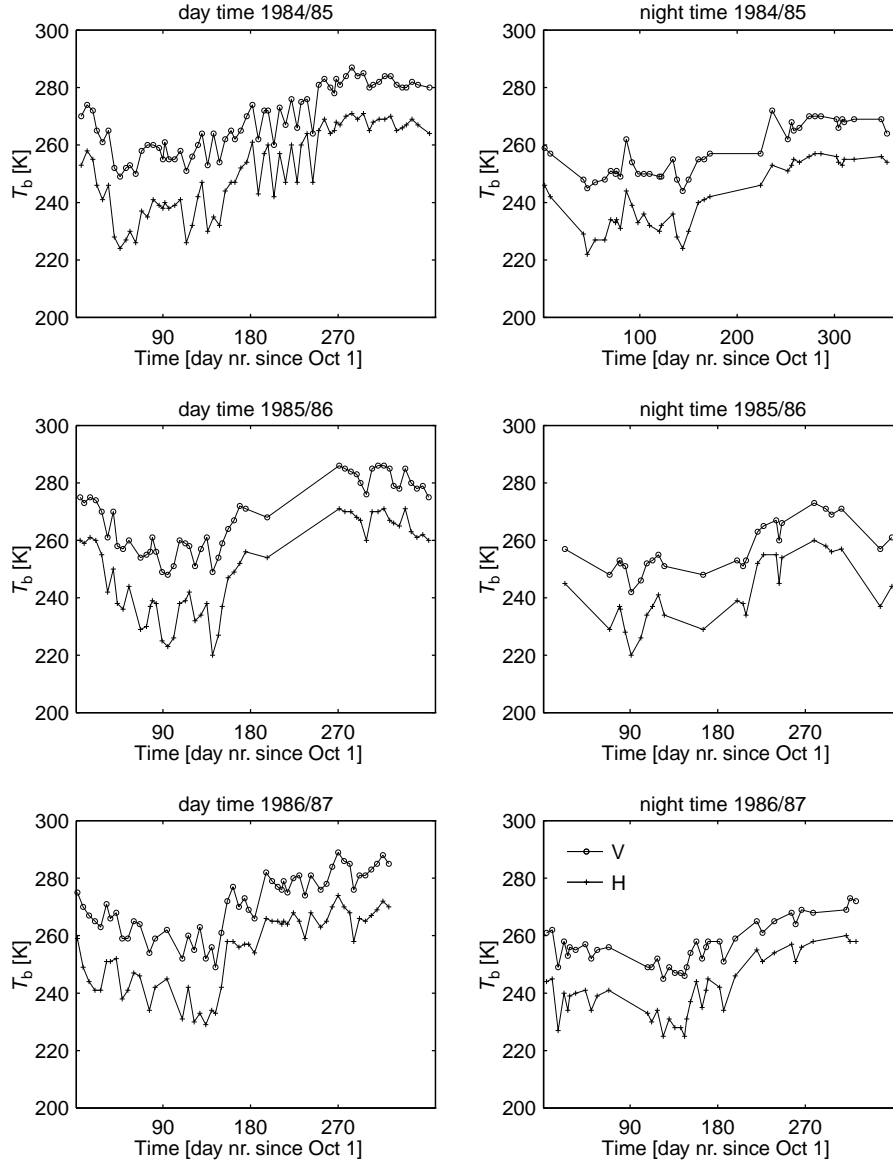
Figure 3.3: *Nimbus–7/SMMR 6.6 GHz passive microwave footprint T_b, collected over the West La Mancha area; period 1984/85 to 1986/87.*

Table 3.1: *Statistics of the first level orbit Nimbus–7/SMMR satellite passive microwave data used for analysis.*

Period	n	d_{tot}	d_{cntr}	$d_{S_{ftpr}}$	T_{bH} $\bar{X}$	S	$\bar{x}_{S_{ftpr}}$	$s_{S_{ftpr}}$	T_{bV} $\bar{X}$	S	$\bar{x}_{S_{ftpr}}$	$s_{S_{ftpr}}$
Day time												
1978/79	64	11	10	1	248	15.6	1.9	0.9	266	11.9	1.4	0.6
1979/80	62	8	8	–	253	13.3	1.7	0.8	270	10.4	1.3	0.6
1980/81	66	6	6	–	252	12.3	1.7	0.9	269	10.1	1.4	0.7
1981/82	60	6	6	–	251	15.3	1.7	0.8	269	11.0	1.5	0.7
1982/83	65	6	6	–	253	14.2	1.7	0.8	270	11.0	1.6	0.8
1983/84	65	7	6	1	249	15.5	1.8	0.9	267	11.5	1.4	0.7
1984/85	65	7	7	–	251	14.3	2.0	1.0	269	11.2	1.6	0.9
1985/86	49	7	7	–	250	15.5	2.0	0.9	268	12.0	1.7	0.8
1986/87	52	6	6	–	254	13.0	1.9	0.8	271	10.5	1.7	0.9
Total/	548	64	62	2								
Mean					251	14.5	1.8	0.9	269	11.2	1.5	0.8
Night time												
1978/79	21	5	3	2	240	9.5	1.3	0.5	256	7.5	0.9	0.4
1979/80	19	5	4	1	244	9.1	1.7	0.6	258	7.6	1.1	0.3
1980/81	39	7	6	1	241	10.1	1.7	0.8	257	9.6	1.2	0.4
1981/82	31	5	5	–	239	14.0	1.9	0.6	256	9.6	1.2	0.4
1982/83	41	6	6	–	242	10.6	1.9	0.8	258	7.9	1.4	0.6
1983/84	36	10	10	–	235	12.1	1.8	0.7	253	8.3	1.2	0.5
1984/85	40	4	3	1	242	11.2	2.0	1.2	258	8.8	1.4	0.7
1985/86	26	9	6	3	242	11.1	2.1	1.2	257	8.4	1.5	0.4
1986/87	38	7	7	–	241	10.3	2.3	0.7	257	7.6	2.0	0.8
Total/	291	58	50	8								
Mean					241	11.3	1.9	0.9	257	8.4	1.4	0.7

n	Number of data used for analysis
d_{tot}	Total number of data excluded from analysis
d_{cntr}	Number of data excluded from analysis on the basis of not containing an observation in the 6 central grids
$d_{S_{ftpr}}$	Number of data excluded from analysis because of excessively large standard deviation within the matrix footprint
T_{bH}	Horizontally polarized brightness temperature [K]
T_{bV}	Vertically polarized brightness temperature [K]
$\bar{X}$	Arithmetic mean of the weighted matrix footprint arithmetic mean
S	Standard deviation of the weighted matrix footprint arithmetic mean
$\bar{x}_{S_{ftpr}}$	Arithmetic mean of the standard deviation within the matrix footprint
$s_{S_{ftpr}}$	Standard deviation of the arithmetic mean of the standard deviation within the matrix footprint

3.3   Nimbus–7/SMMR 6.6 GHz data

3.3.1   Data collection

The Nimbus–7/SMMR lifetime extends from October 25 1978 to August 20 1987. Table 3.1 presents the Nimbus–7 Scanning Multichannel Microwave Radiometer (SMMR) 6.6 GHz data used in the present analysis ($\lambda = 4.5$cm). The data are also shown in Fig. 3.1 to Fig. 3.3. In perspective of the research objective outlined in Section 1.2 the data are grouped in hydrological years. The start of the hydrological year coincides with the start of the wet season, October 1, when moisture storage in the soil profile is lowest. The hydrological aspect of the study will be discussed in more detail in Chapter 4.

The Nimbus–7/SMMR data are made available by NASA/GSFC as maps of the Iberian Peninsula gridded to a one quarter degree scale, North Latitude $36^{\circ}00' - 44^{\circ}00'$, East Longitude $350^{\circ}30' - 3^{\circ}30'$. A grid square contains a brightness temperature value if the centre point of a pixel falls within it. The 6.6 GHz Nimbus–7/SMMR pixel is an oval of an approximate 150 km square size. For Spain, one degree of longitude is about 85 km and one degree of latitude is 110 km. Consequently, a matrix footprint of 7X5 quarter degree grid square dimension that covers the West La Mancha area, is cut from the maps (North Latitude $38^{\circ}45' - 40^{\circ}00'$, East Longitude $355^{\circ}45' - 357^{\circ}30'$).

Table 3.2: *Example of a first and second level orbit 6.6 GHz Nimbus–7/SMMR 7X5 quarter degree grid square matrix footprint, collected over the West La Mancha area.*

Period : 1982/83
Day nr. since Oct 1 : 181

Day time
First level orbit
Horizontal polarization

(N.Lat.40°00′, E.Long.355°45′)

258	257	257	255	255	254	255
258	256	255	254	254	254	255
258	256	254	255	254	253	254
257	257	256	254	254	252	253
257	256	255	255	254	253	252

(N.Lat.40°00′, E.Long.357°30′)

(N.Lat.38°45′, E.Long.355°45′)   (N.Lat.38°45′, E.Long.357°30′)

Vertical polarization

270	270	270	270	270	271	271
268	269	269	270	270	270	270
268	269	268	268	269	269	269
269	269	268	269	269	268	268
269	269	269	268	267	267	266

Second level orbit
Horizontal polarization

(N.Lat.40°00′, E.Long.355°45′)

—	257	—	—	255	—	—
—	—	256	—	254	—	—
259	—	255	—	—	254	—
258	—	257	—	—	253	—
258	—	—	255	—	—	253

(N.Lat.40°00′, E.Long.357°30′)

(N.Lat.38°45′, E.Long.355°45′)   (N.Lat.38°45′, E.Long.357°30′)

Vertical polarization

—	269	—	—	270	—	—
—	269	—	—	271	—	—
265	—	268	—	269	269	—
268	—	267	—	—	267	—
269	268	—	—	—	—	265

In total four maps are available: for the horizontal and vertical polarization direction and for the day- and night time. Nimbus–7 is a sun synchronous, near–polar, low earth orbit satellite. It crosses the equator in ascending orbit at local solar noon, while in descending orbit it crosses at midnight. The satellite orbit time is approximately 104 minutes. Therefore, the central Spain cross–over times are 12:12 hrs and 23:48 hrs local time (LT) for day- and night time, respectively.

A data gap in the day time series is present from March 24 to June 28 1986, due to a system breakdown. The malfunction is less prevalent in the night time data, although it appears to affect the number of data in the 1985/86 period (see Table 3.1).

3.3.2 First and second level orbit data

Some technical specifications of SMMR that are of interest to the present study are summarized below. A more detailed description of instrument specifications can be found in e.g. *Gloersen and Barath* [1977]; *NASA/GSFC* [1978]; *Maul* [1985].

The Nimbus–7/SMMR data have been made available by NASA/GSFC, processed in two different ways. The result is a first level and a second level orbit data set. First level orbit data are the original data as they were transmitted and received, although they have been calibrated. In this format, there are 96 measurements in one scan width. A complete scan width consists of a forward and a backward scan. The first pixel in each direction is a calibration, so in

Table 3.3: *Deviation between first and second level orbit data of the West La Mancha footprint T_b value for several years.*

Period	n_c	n_{nc1}	n_{nc2}	$\bar{X}_{T_{bH1}}$	$\bar{X}_{T_{bH2}}$	$\bar{X}_{T_{bV1}}$	$\bar{X}_{T_{bV2}}$	RMSD T_{bH} Total	Mean	RMSD T_{bV} Total	Mean
Day time											
1978/79	54	10	1	248	249	266	266	46	0.9 (2+)	29	0.5 (2+)
1979/80	62	—	5	253	253	270	269	41	0.7 (2+)	27	0.4 (1+)
1980/81	66	—	2	252	253	269	269	43	0.7 (2+)	34	0.5 (1+)
1981/82	60	—	3	251	252	269	269	42	0.7 (2+)	28	0.5 (1+)
Night time											
1978/79	12	9	–	240	240	256	256	10	0.8 (2+)	10	0.8 (2+)
1979/80	15	4	3	244	244	258	259	11	0.7 (2+)	19	1.3 (2+)
1980/81	37	2	4	241	243	257	259	40	1.1 (2+)	49	1.3 (2+)
1981/82	26	5	4	239	240	256	258	20	0.8 (2+)	32	1.2 (2+)

n_c	Number of first and second level data on corresponding days
n_{nc1}	Number of not corresponding days, present in 1st level data, not present in 2nd level data
n_{nc2}	Number of not corresponding days, not present in 1st level data, present in 2nd level data
$\bar{X}_{T_{bH,V,1,2}}$	Mean horizontally/vertically polarized footprint brightness temperature for 1st and 2nd level data
RMSD$_{T_{bH,V}}$	Root mean square difference in horizontally/vertically polarized brightness temperature,
	(2+)/(1+): 2nd level data higher/1st level data higher

reality there are only 94 data points, 47 in each direction (forward and backward). Since an orbit track is approximately 822 km wide, the distance between pixel centres is about 18 km. Also, since the spacecraft is moving, the distance between the forward and the reverse scans is about 28 km. This means, that there is a tremendous amount of overlap between separate observations.

Second level orbit data are generated by establishing 8 evenly spaced pixel centers across an orbit track, and averaging the 6 observations that fall across each of these 'synthetic' pixels. When creating a latitude–longitude map, there are only 8 pixel centres across an orbit track to fill the quarter degree grids. Consequently, there are a substantial number of unfilled grids in a map. For the first level data 47 pixel centres are available for each orbit track width to fill a grid map with. Consequently, there are no unfilled grids. If more than one observation falls within a given grid, they are averaged. Table 3.2 shows an example of a quarter degree gridded map of study area matrix footprint dimension. It clearly shows the effect of the level of data processing. In the present study initially second level orbit data are used. September 1996 first level orbit data became available, which are subsequently used.

3.3.3   Footprint brightness temperature

A weighted arithmetic mean footprint brightness temperature value is computed by assigning a weighting factor to the quarter degree grid squares in the 7X5 matrix footprint that contain data. The weight is assigned according to the fractional pixel surface cover over the 7X5 quarter degree grid square matrix footprint. This means the central grid square (provided it contains an observation) is assigned a relatively high weight. The pixel, of which the centre falls within the central grid, then covers the 7X5 matrix footprint almost completely. Conversely, relatively low weights are assigned to the bordering (data containing) grid squares. In case the six central grid squares do not contain data, the computed footprint T_b value is not considered representative and excluded from further analysis (d_{cntr} in Table 3.1). In addition, the standard deviation within

the 7X5 matrix footprint is computed. A total of 10 footprints of excessively large standard deviation within the matrix footprint, i.e. exceeding the mean S_{sftpr} by 10 times or more, see Table 3.1) is excluded. Most of the excluded footprints (7 out of 10) are located at the border of the satellite orbit track width.

The respective procedures of first and second level orbit data processing result in a slightly deviating footprint T_{b} value. This is explained by the creation of an average 'synthetic' pixel over 6 observations in the second level orbit data processing procedure. The averaged data in the second level orbit bordering grid squares therefore include observations from outside the 7X5 matrix footprint. Table 3.3 presents the difference between the first and second level orbit data sets of the West La Mancha footprint for several years. Overall, the rounded root mean square difference in footprint T_{b} value between the first and second level orbit data does not exceed one. The root mean square difference, RMSD, is here defined as:

$$\text{RMSD} = \sqrt{\frac{\sum_1^n (T_{\text{b1}} - T_{\text{b2}})^2}{n_c}} \tag{3.7}$$

where T_{b1} and T_{b2} are the respective first and second level orbit data footprint brightness temperature and n_c is the number of corresponding observation days. Surprisingly, not all days of observation appear to correspond in the two data sets. It is not clear why. This possibly due to errors at some stage in the data processing line. The mean footprint T_{b} value is virtually identical for the two data sets. Analysis of the RMSD shows that the 2nd level data generally exceed the 1st level data. The 2nd level orbit mean standard deviation within the matrix footprint, not presented in Table 3.3, systematically exceeds that of the 1st level data by several tenths of K.

The effect of the variation of footprint location on the footprint T_{b} value is evaluated for the 1978/79 period (first level orbit) data set. The West La Mancha 7X5 matrix footprint is shifted east (x+1,y), south (x,y–1) and east–south (x+1,y–1), where 1 stands for one quarter degree grid square. Table 3.4 shows that neither the mean footprint T_{b} value, nor the standard deviation within the matrix footprint is much affected. The RMSD is derived similarly as in Eq. 3.7 and remains below 1 degree. The number of corresponding days is 64 for the day time and 21 for the night time (see also Table 3.1) for all analysed matrix footprint locations: a one quarter degree shift does not enter additional observations in the 6 central matrix footprint grid squares. A shift in latitude south results in a decrease in footprint T_{b} value, while a shift in longitude east increases the footprint T_{b}.

The Nimbus–7/SMMR data here presented show that T_{bV} systematically exceeds T_{bH}. From Eq. 3.2 and Eq. 3.3 it follows that the horizontally polarized soil reflectance, $r_{s\text{H}}$, exceeds $r_{s\text{V}}$, provided the incidence angle is not equal to 0° or 90° (then $r_{s\text{H}} = r_{s\text{V}}$). From Eq. 3.1 it then follows that T_{bV} exceeds T_{bH}. This also applies to the soil emissivity, e_{s}. The Nimbus–7/SMMR incidence angle is 50.2°.

Table 3.4: *The effect of the variation of footprint location on footprint T_b for the period of 78/79.*

Location	$\bar{X}_{T_{bH}}$	$S_{T_{bH}}$	$\bar{X}_{S_{ftpr,H}}$	RMSD	$\bar{X}_{T_{bV}}$	$S_{T_{bV}}$	$\bar{X}_{S_{ftpr,V}}$	RMSD
								Day time
(x,y)	248	15.6	1.9	–	266	11.9	1.4	–
(x+1,y)	249	15.3	2.0	0.7 (+)	266	11.7	1.4	0.3 (+)
(x,y−1)	248	15.4	1.9	0.5 (−)	266	11.7	1.5	0.3 (−)
(x+1,y−1)	248	14.9	2.0	0.8 (+)	266	11.4	1.4	0.6 (+)
								Night time
(x,y)	240	9.5	1.3	–	256	7.5	0.9	–
(x+1,y)	240	9.3	1.4	0.4 (+)	256	7.3	0.9	0.2 (+)
(x,y−1)	240	9.3	1.2	0.2 (−)	256	7.2	0.9	0.3 (−)
(x+1,y−1)	240	9.5	1.3	0.4 (+)	256	7.5	0.9	0.4 (−)

$S_{T_{bH,V}}$	Standard deviation of mean footprint brightness temperature
$\bar{X}_{T_{bH,V}}$	Mean footprint brightness temperature
$\bar{X}_{S_{ftpr,H,V}}$	Mean standard deviation within the matrix footprint
RMSD	Root mean square difference, (+/−): higher/lower than (x,y)

The matrix footprint of second level orbit data in Table 3.2 demonstrates that the corresponding T_{bV} and T_{bH} pixel centres do not all have identical position. This is explained by the use of only one antenna for both polarization directions at 6.6 GHz frequency. First it measures a swath at horizontal polarization, then it measures the return swath at vertical polarization. Since the satellite is continuously moving, the pixel centres are not located at identical position for both polarization directions. This of course also affects the first level orbit data. The absence of unfilled grids, however, camouflages the shift of observations.

Table 3.1 shows that the number of night time data is slightly over half the number of day time data. The total number of excluded matrix footprints is about equal. Night time data, however, appear to have a larger number of quarter degree grid square matrix footprints of excessively large standard deviation within the matrix footprint. The difference between the mean day time and night time footprint T_b value is 10 K and 12 K for horizontal and vertical polarization, respectively. The higher day time footprint T_b value results from the higher day time surface temperature of the emitting plant and soil surface (see Eq. 3.1 and Eq. 3.6).

Table 3.5 shows only 30 days in total have both a day time and a night time observation in the central grids of the study area footprint. The mean difference in footprint T_b value between day time and night time observation for these days is 8.4 K and 10.3 K for horizontal and vertical polarization, respectively. The variation in the difference between the day and night time observation is seasonal: large in summer and small in winter.

Table 3.5: *Footprints of corresponding night- and day time observations, collected over the West La Mancha area.*

Period	r	d_{nr}	Day time		Night time			
			T_{bH}	T_{bV}	T_{bH}	T_{bV}	ΔT_{bH}	ΔT_{bV}
1978/79	1	26	256	272	244	260	12	12
	2	32	254	269	244	259	10	10
	3	38	248	265	243	259	5	6
	4	44	236	260	233	251	3	9
	5	278	261	277	249	265	12	12
1979/80	6	249	271	284	253	266	18	18
	7	349	264	280	253	267	11	13
1980/81	8	49	242	262	234	252	8	10
	9	105	236	256	235	251	1	5
1981/82	10	108	214	244	210	237	4	7
1982/83	11	199	257	272	235	255	22	17
	12	239	264	279	251	265	13	14
	13	267	257	276	246	264	11	12
1983/84	14	248	249	264	237	253	12	11
1984/85	15	46	224	249	222	245	2	4
	16	80	241	260	231	249	10	11
	17	86	239	259	244	262	5	3
	18	92	240	261	239	254	1	7
	19	120	232	256	230	249	2	13
	20	160	247	265	240	255	7	10
	21	256	269	283	253	268	16	15
	22	302	265	280	253	269	12	11
1985/86	23	79	239	261	237	253	2	8
	24	101	226	251	226	246	–	5
	25	107	238	260	234	252	4	8
	26	113	239	259	237	253	2	6
1986/87	27	26	241	263	234	253	7	10
	28	168	256	270	241	256	15	14
	29	316	272	288	258	273	14	15
	30	322	270	285	258	272	12	13
Mean			248	267	240	257	8.4	10.3

r	Rank number
d_{nr}	Day nr. since Oct 1
$\Delta T_{bH,V}$	Result of the extraction
	day time $T_{bH,V}$ - night time $T_{bH,V}$

3.4   Ground–based passive microwave experiment

3.4.1   Introduction

Application of satellite surface moisture monitoring over vegetation covered surfaces requires information on the influence of the vegetation cover on the microwave signal. Knowledge of this behaviour enables one to account for the vegetation effects on the signal observed by the satellite.

Previously mentioned studies of satellite microwave monitoring over a grass–shrub savanna area in Botswana, reported a strong seasonal variation of optical depth or vegetation transmissivity and showed a relationship with seasonal NDVI development [*Owe et al.*, 1992] (see also Section 3.5.4) or the seasonal vegetation cycle [*Van de Griend and Owe*, 1994b, a]. Single scattering albedo however, was shown to be seasonally invariant. Based on this latter finding, *Van de Griend and Owe* [1994b] found

$$A = \frac{\Gamma_H}{\Gamma_V} \tag{3.8}$$

and

$$B = \frac{\omega_H}{\omega_V} \tag{3.9}$$

to be seasonally independent for a 3–year modelling period, where subscripts H and V refer to horizontal and vertical polarization, respectively.

The difference between Γ_H and Γ_V is reported to depend largely on systematic differences in cultivation such as plant row direction and uniform canopy orientations [*Brunfeldt and Ulaby*, 1984; *Allen and Ulaby*, 1984]. The difference will be minimal for completely random canopies, such as those encountered under natural conditions. ω is previously described to vary inter alia with vegetation type (see Section 3.2.3). Little information is available on B however. Therefore, knowledge of the seasonal behaviour of the radiative transfer properties for the predominant vegetation type is essential to the present study. To obtain information on these properties at both horizontal and vertical polarizations, a field experiment was carried out according to a procedure described earlier by *Van de Griend et al.* [1996].

The measuring procedure is based on solving the radiative transfer function for vegetation covered areas (Eq. 3.6). Brightness temperature, T_{b_H} and T_{b_V}, surface temperature, T_s and T_c, and bare soil emissivity, e_{rs}, are measured for two surfaces with (near–)identical vegetation canopy, but different bare soil emissivity. ω and Γ are subsequently derived by simultaneously solving two equations, corresponding to the two different bare soil emissivities. The requirement of two (significantly) different bare soil emissivities is achieved by selecting two plots, of which one remains natural, while the other is flooded. The two plots of near–identical vegetation canopy are required to enable comparison of brightness temperature measurements before and after harvesting of both the dry (natural) and flooded plot.
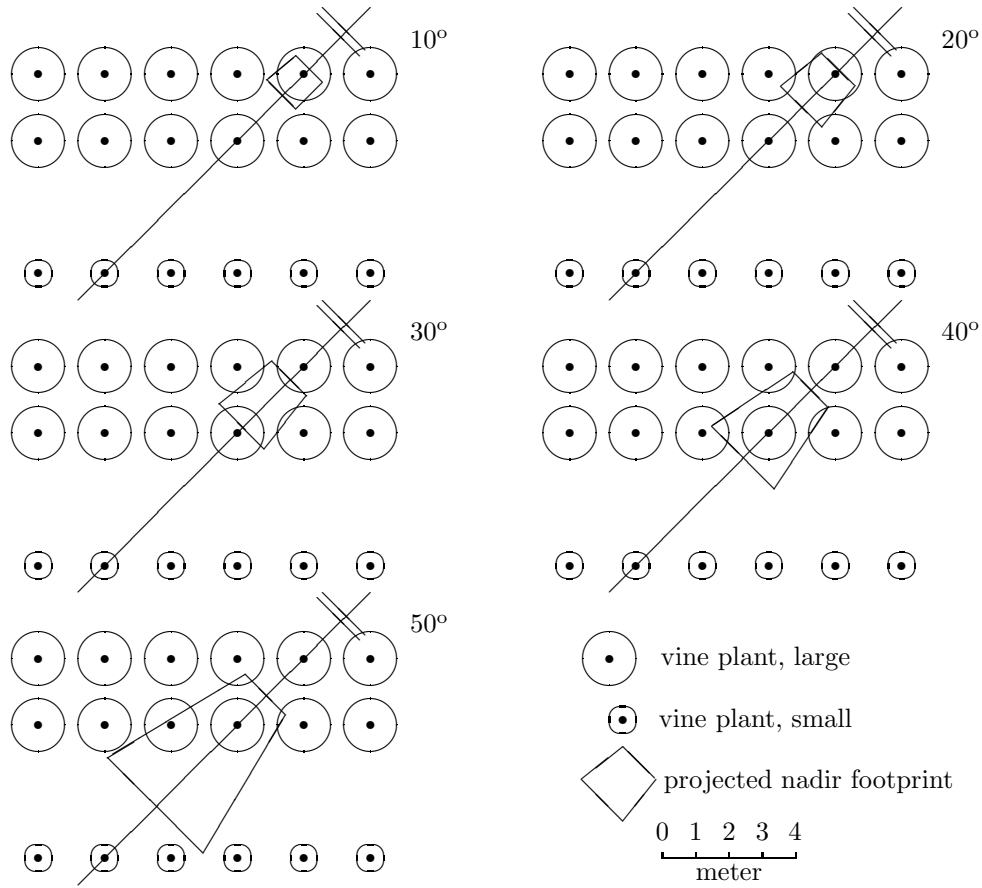
Figure 3.4: *Schematic top view of the projected nadir footprint in relation to vine plant cover and view angle.*

3.4.2   Experimental set–up and microwave measurements

The microwave brightness temperature measurements were carried out with 1.4 GHz and 5 GHz frequency radiometer systems. The instrument specifications have been reported by *Reutov and Shutko* [1992]. A portable, light–weight aluminum platform was developed to hold the radiometers and accompanying antennae. The antennae were attached to connecting turntables which could be rotated to enable simultaneous change of the polarization angle. The incidence angle was varied by raising the cross–bars which held the antennae. Regular instrument calibration was carried out by measurements of a blackbody surface and measurements of clear sky brightness temperature (see also: *Van de Griend et al.* [1996]).

The measurements were made over two plots in a vineyard test site. The test site was located at the compound of the Centro y Escuela de Capacitacion y Experimentacion Vitivinícola, Tomelloso. The compound is located at the NE Tomelloso city border, about 8 km NW of the EFEDA campaign experimental fields (see Fig 2.1). The vine plants are free standing bushes of a type known locally as Airen, the common type of vine grown in the West La Mancha area. The vines are planted in a grid pattern at a spacing of 2.5 m. One surface of the test site was flooded, while the other was maintained in its natural state. Figure 3.4 illustrates a schematic top–view of the projected footprint as it changes both in size and position with changing view angle. The approximate locations and sizes of the individual plants are also drawn. Although the plant spacing and coverage was quite uniform throughout the vineyard on a large scale, the size of the sensor footprint relative to the individual plant size and spacing resulted in both highly variable vegetation coverage and subsequent biomass density for each viewing angle. Furthermore, the vine plant canopy is characterized by a random orientation and distribution of stems and leaves. The individual vine plant geometry may therefore hinder the measurement procedure requirement that the two plots possess near–identical biomass density and plant structure. The implications of these effects on measurement results are discussed below. A second set of measurements was conducted after thinning approximately one half of the canopy. Finally, all vegetation was removed, and a complete set of measurements was made over the bare surface. The second plot was flooded to a uniform depth of approximately 8 cm, and a second sequence of measurements was made for both a full and partial canopy, with the final series of measurements made over water only. For each cover condition, a full series of measurements was made that consisted of both horizonal and vertical polarization at incidence angles of 0, 10, 20, 30, 40, and 50º for both frequencies. The vegetation was weighed wet, and then dried to determine both the wet and dry biomass for each cutting stage. The dry plot measurements were carried out during one day, while the flooded plot measurements were carried out during the following day.

The three measurement sets, i.e. full vegetation, partial vegetation and bare soil or surface water, took approximately 7 hours. This included the time for cutting, weighting, and packaging the plant material. The canopy and soil tem-

Table 3.6: *Biophysical measurements of the dry and flooded plot.*

Measurement set	Vegetation cover	Dry plot		Wet plot	
		Wet biomass	Dry biomass	Wet biomass	Dry biomass
1	Full	9.90	3.15	8.28	2.37
2	Partial	5.06	1.45	4.07	1.03
3	Bare/Water	–	–	–	–

Biomass in [kg]

perature were measured after each brightness temperature measurement with small digital probe–type thermometers at several locations within the plot.

The radiance measurements of soil and vine plant surface were made with a portable hand–held radiometer in the red and near infrared wavebands. The radiometer has a field of view of 12° and was maintained approximately 80 cm above the target surface, thus covering about 0.022 m^2. Two replications for each measurement were made from nadir. A reference plate measurement was made before and after each set of target measurements and used to calculate the hemispherical–conical reflectance as defined by *Kimes et al.* [1984]. Red and near infrared reflectance was used to calculate the NDVI (see Section 3.5.4). The average moisture content was 0.02 m^{3}m^{-3} in the surface 0–1 cm layer, and 0.07 m^{3}m^{-3} in the 0–5 cm layer.

3.4.3   Results

Biomass and brightness temperature measurements

The measurements were carried out for full vegetation conditions, partial vegetation conditions and bare soil or surface water during grape harvest time when the vines were fully grown. The plant height was approximately 1 m. Table 3.6 summarizes the biophysical measurements. The dry plot biomass turned out to be 25–30% of the wet plot biomass.

As detailed in the previous section, the incomplete vine plant soil surface cover combined with the changing nadir–footprint projection with view angle, causes the biomass density to differ for each view angle. The biomass density view angle dependency is evaluated by estimating the vegetation and bare soil/water fractional surface cover of the projected nadir–footprint (Fig. 3.4). Subsequently, a linear approach is used to determine the footprint–average NDVI from the estimated surface cover percentage. Table 3.7 summarizes the result.

In general, the projected footprint vegetation spatial coverage decreases with increasing view angle. It increases however from 30° to 40° view angle. The tabled NDVI target surface values for vines, bare soil and water are averaged from two replicate radiance measurements. The partial removal of vine plant vegetation causes a relatively large decrease in the dry plot NDVI. This seems to be in agreement with the larger amount of biomass cleared from the dry plot (Table 3.6). Overall however, the NDVI appears not to relate to vine plant

Table 3.7: *Estimated projected footprint–average fractional surface cover and the NDVI in relation to view angle.*

View angle	Surface cover fraction Vine	Bare/Water	NDVI Vine Dry	Wet	Bare	Water	Footprint Dry	Wet
Full vegetation cover								
10°	0.88	0.12	0.74	0.77	0.22	0.14	0.68	0.69
20°	0.46	0.54					0.46	0.43
30°	0.22	0.78					0.33	0.28
40°	0.35	0.65					0.40	0.36
50°	0.23	0.77					0.34	0.28
Partial vegetation cover								
10°	0.88	0.12	0.69	0.75	0.23	0.18	0.63	0.68
20°	0.46	0.54					0.44	0.44
30°	0.22	0.78					0.33	0.31
40°	0.35	0.65					0.39	0.38
50°	0.23	0.77					0.34	0.31

biomass very well. The relatively high vine plant biomass of the dry plot corresponds to a relatively low NDVI. Next, clearing of the wet plot vegetation hardly affects the NDVI. It appears therefore that vine plant NDVI is not very sensitive to variation in canopy thickness when the spatial coverage remains unchanged. Bare soil NDVI does not vary between the two measurement sets. Variation in the NDVI for water may result from wet plot drainage.

A linear approach is applied to determine the footprint–average NDVI from spatial coverage. The resulting differences in NDVI are expected to relate to differences in the vegetation transmissivity, which is discussed in the following sections.

The brightness temperature measurements at the (near–)nadir view angles (0° and 10°) appeared to be affected by antenna self–emission. This resulted in an increased horizontally polarized brightness temperature at nadir, where in theory it should equal vertically polarized brightness temperature. Consequently, measurements at nadir view angle are not included in the analysis. The (near–)nadir measurements are corrected for this effect.

Assessment of vegetation radiative transfer properties

The biomass totals in Table 3.6 indicate dry and flooded plot vegetation conditions are not identical, neither for full vegetation nor for partial vegetation. The difference in biomass is corrected for, following *Van de Griend et al.* [1996]:

$$\tau_{\text{cor}} = \frac{\tau_{\text{dryplot}}}{\tau_{\text{wetplot}}} = \frac{\text{Biomass}_{\text{dryplot}}}{\text{Biomass}_{\text{wetplot}}} \tag{3.10}$$

where τ is a linear function of biomass. Computation of τ_{cor} from Table 3.6 results in a slightly deviating τ_{cor} for wet biomass and dry biomass. Since τ_{cor}

Figure 3.5: *Derived vegetation transmissivity for horizontal and vertical polarization at 1.4 GHz and 5 GHz frequency as a function of view angle.*

excludes the vegetation water content, it seems a more true reflection of the vegetation biomass ratio. The vegetation water content however, is reported to be linearly related to the vegetation optical depth [*Owe et al.*, 1992]. The analysis results however, turned out to be comparable using the two correction ratios. Substitution of Eq. 3.10 in $\Gamma = e^{-\tau}$ gives wet plot vegetation transmissivity expressed by:

$$\Gamma_{\text{wetplot}} = \Gamma_{\text{dryplot}}^{\frac{1}{\tau_{\text{cor}}}} \tag{3.11}$$

Subsequently, radiative transfer properties ω, Γ_{wetplot} and Γ_{dryplot} are determined from simultaneously solving Eq. 3.11 and Eq. 3.6 for both the dry (natural) plot and the wet plot. A non–linear iterative optimization technique [*Marquardt*, 1963] is used to solve the equations.

Vegetation transmissivity

Fig. 3.5 shows the respective results for vegetation transmissivity at 1.4 GHz and 5 GHz frequency for full and partial vegetation conditions as a function of view angle. Γ increases with view angle for all measurements, the high view angle measurements for partial vegetation conditions at both frequencies excluded. For both 1.4 GHz and 5 GHz measurements, canopy thinning results in a slight decrease of Γ_H and Γ_V, the near–nadir view angle measurements of both vegetation conditions and frequencies excluded. In the here presented experimental set–up and in case of a complete vegetation cover, one would expect Γ to increase with decreasing biomass and, consequently, to decrease with increasing view angle. As detailed above, the presently investigated vegetation type does not completely cover the soil surface. As a result, the vegetation fractional surface cover of the projected nadir footprint generally decreases with increasing view angle. The footprint–average NDVI is estimated linearly from the fractional surface cover and used as a measure of the footprint–average biomass density.

In Fig. 3.6, Γ_H and Γ_V are again presented at 1.4 GHz and 5 GHz frequency for full and partial vegetation conditions, now as a function of the dry (natural) plot footprint–average NDVI. The depicted inverse linear relationship seems theoretically correct; high biomass density (NDVI) corresponding with low vegetation transmissivity and vice versa. The relatively lower values of Γ_H and Γ_V for partial vegetation cover seem a contradiction however. The decrease may be caused by insensitivity of Γ to vegetation canopy thinning for this vegetation type provided vegetation fractional cover remains unchanged, similar to NDVI. At near–nadir view angle (10º), the clearing of vegetation increases Γ_H and Γ_V. At this view angle the footprint–average NDVI is relatively high and the difference between the partial and the full vegetation NDVI is also relatively large. This may indicate a relative insensitivity of Γ to the variation in biomass density (and NDVI) below a certain threshold. For both the 1.4 and 5 GHz measurements Γ_H and Γ_V decrease at 50º view angle. This may be due to inclusion of non–flooded area or impervious material damming the water at the far edge of the flooded projected nadir–footprint. It is also possible that at 50º the measured microwave brightness temperature is contaminated by the sky. This causes T_b to be cooler than it should be.

Single scattering albedo

Fig. 3.7 shows the respective results for the single scattering albedo at 1.4 GHz and 5 GHz frequency for full and partial vegetation conditions as a function of view angle. The 1.4 GHz measurements demonstrate a greater dependence on view angle than the 5 GHz measurements. At both frequencies the measurement results are consistent. The vertical polarization measurements deviate, however, for partial vegetation conditions at 1.4 GHz frequency and for full vegetation conditions at 5 GHz frequency.
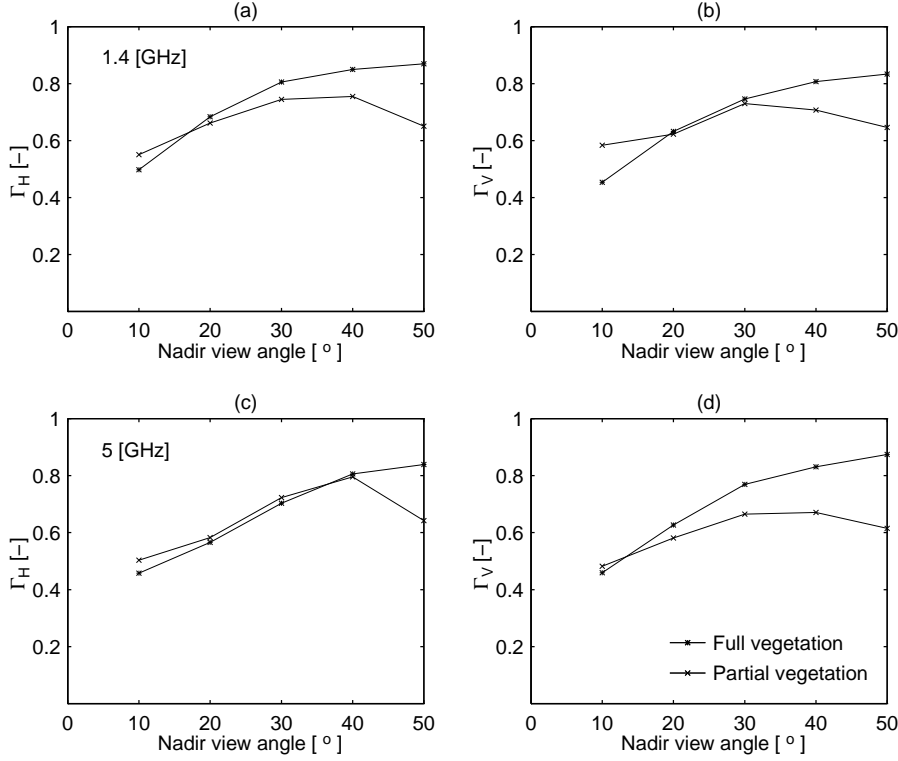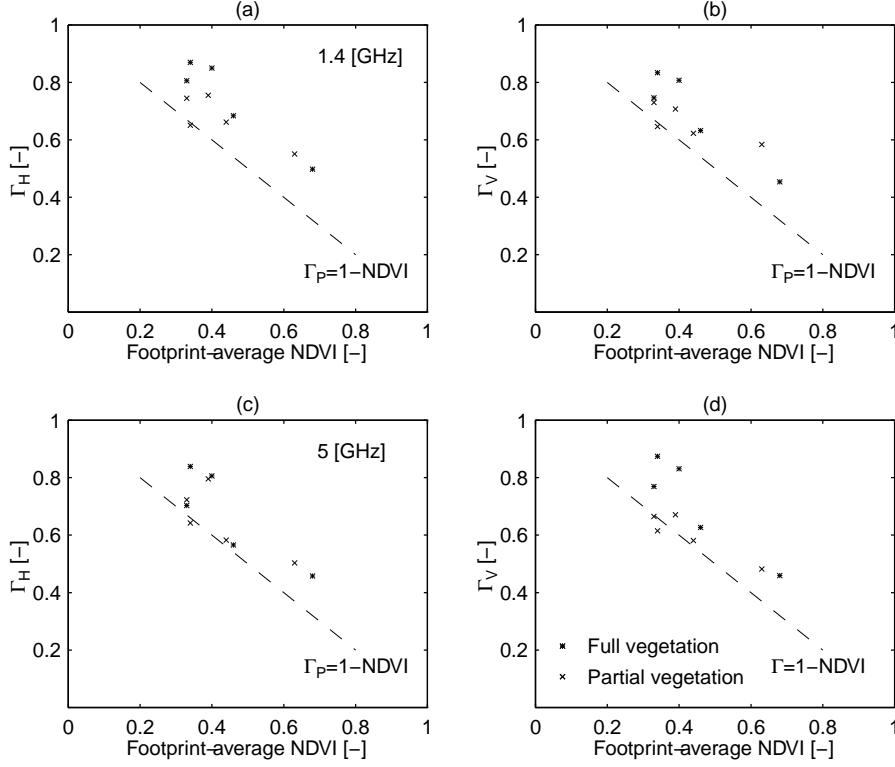
Figure 3.6: *Derived vegetation transmissivity for horizontal and vertical polarization at 1.4 GHz and 5 GHz frequency as a function of footprint–average NDVI.*

The values of ω appear to be independent of the polarization angle and the different biomass density resulting from vegetation clearing. As discussed earlier, biomass density also changes with view angle. The dependence on view angle may therefore also imply dependence on the biomass density. The consistency of the ω values for full and partial vegetation conditions may, however, indicate a dependency on view angle alone. Biomass density independence agrees with the concept of ω parameterizing the leaf surface albedo properties.

At both polarization angles, ω at 1.4 GHz frequency exceeds ω at 5 GHz frequency. Overall, the values of ω appear to fall within the range of values reported in the literature (see Section 3.2.3). The high view angle measurements at 1.4 GHz for both vegetation conditions are slightly in excess of that range. Conversely, ω_V at 5 GHz frequency remains below the lower boundary of that range for full vegetation conditions at all view angles.
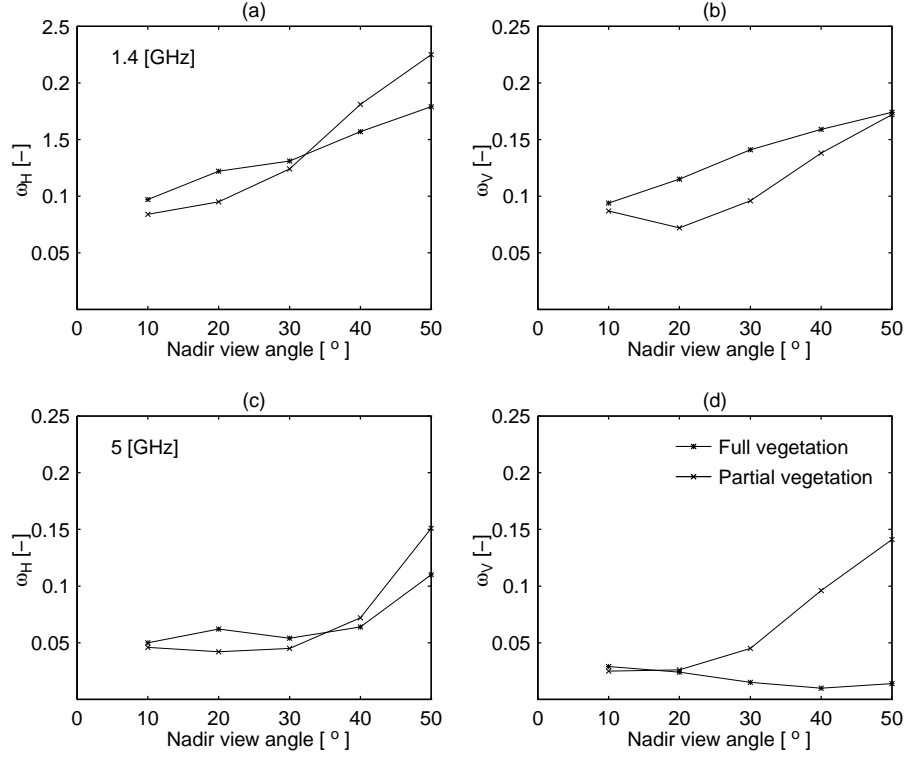
Figure 3.7: *Derived single scattering albedo for horizontal and vertical polarization at 1.4 GHz and 5 GHz frequency as a function of view angle.*

A, A" and B

Fig 3.8a,b shows the respective results for A at 1.4 GHz and 5 GHz frequency for full and partial vegetation conditions as a function of view angle. For all 1.4 GHz measurements A is just above 1, the 10° view angle for partial vegetation condition excluded. For partial vegetation conditions the 5 GHz measurements are just above 1 and for full vegetation conditions, A is just below 1. Overall, A is approximately unity, independent of biomass density and view angle. A" is defined as τ_H/τ_V. Due to the inverse exponential relationship of τ with Γ, deviation of A" from one is mirrored and larger (Fig. 3.8c,d). Independence of view angle and biomass density remains however.

Fig. 3.8e,f show the respective results for B at 1.4 GHz and 5 GHz frequency for full and partial vegetation conditions as a function of view angle. The 1.4 GHz measurements vary only slightly with view angle and vegetation condition. Overall, B remains rather constant. The 5 GHz measurements show large differences between partial and full vegetation conditions. The values of B for full vegetation conditions are not depicted, as they are too large to fit into Fig. 3.8e.
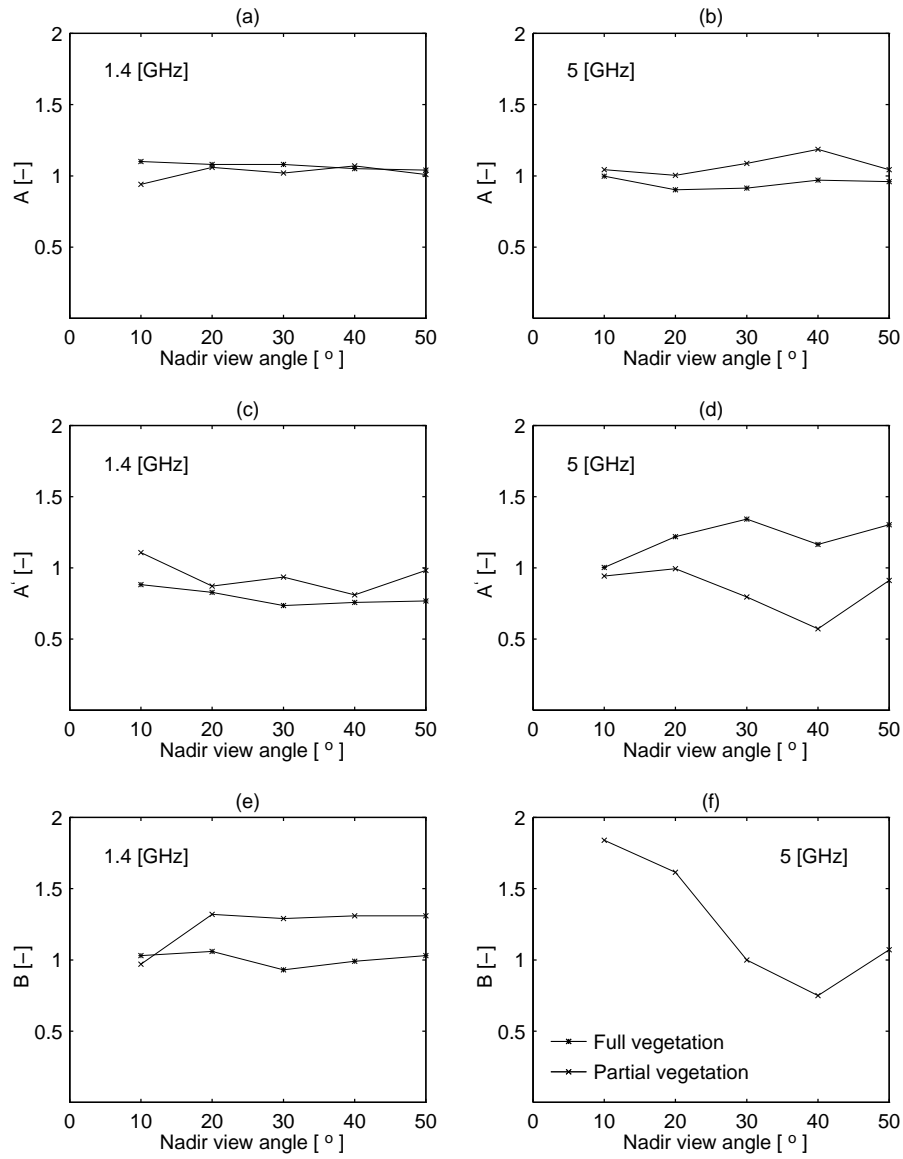
Figure 3.8: *Derived A, A" and B at 1.4 GHz and 5 GHz frequency as a function of view angle.*

This is mainly caused by deviating values of ω_V. The values of B for partial vegetation conditions appear to decrease at the higher view angle, where they are more in range with the 1.4 GHz measurements. The greater consistence of the 1.4 GHz measurements may be related to the larger penetration depth.

3.4.4   Conclusions

The described measurement procedure to determine vegetation radiative transfer properties requires two plots with a near–identical vegetation structure and vegetation density. Furthermore, it requires two different bare soil emissivities for both plots. The validity of the application of the measurement procedure to the investigated vegetation type seems uncertain. The incomplete vegetation cover and the non–uniform distribution and orientation of the leaves and stems of the vine plants seem to obstruct a proper application. Nevertheless, the derived vegetation radiative transfer properties are consistent. They also fall within the range of values reported in the literature. Application of the experimentally derived values for the vegetation radiative transfer properties in the satellite data analysis is described in the following sections.

3.5   Satellite derived surface moisture

3.5.1   Introduction

The present section describes the derivation of surface moisture from the Nimbus-7/SMMR data. In the analyses the first level orbit horizontal and vertical polarization day time and night time data are used. The first level orbit data are preferred over second level data, because they are the (calibrated) original data as transmitted and received by the SMMR antenna.

Surface moisture is inversely derived from the SMMR data by means of the radiative transfer equation (Eq. 3.6) using an iterative procedure [*Marquardt*, 1963]. Section 3.5.2 describes the derivation of parameter values for surface temperature, T_s and T_c. Section 3.5.3 presents derivation of the bare soil emissivity curve. The derived parameter values are subsequently implemented in the radiative transfer equation together with the experimentally derived vegetation radiative transfer property parameter values. Section 3.5.4 describes the derivation of surface moisture making use of the NDVI–based vegetation effect correction approach. Surface moisture is derived in Section 3.5.5 using the dual polarization vegetation correction approach.

3.5.2   Surface temperature

As described in Section 3.2.1 the surface emissivity may be derived from Eq. 3.1. The normalization of the satellite brightness temperature however, requires an estimate of the surface temperature. In the absence of surface temperature data for the Nimbus–7/SMMR lifetime, it is estimated alternatively. The daily air temperature data of the three major meteorological stations in the region are

Table 3.8: *Mean and standard deviation of the minimum and maximum air temperature data for the three major meteorological stations in the West La Mancha area.*

Period	Albacete			Cuenca			Ciudad Real			Average	
	$\bar{X}$	S	n_{na}	$\bar{X}$	S	n_{na}	$\bar{X}$	S	n_{na}	$\bar{X}$	S
										$T_{a_{min}}$	
1975/76	279.4	6.8	–	278.8	6.4	–	279.0	6.4	–	279.1	6.4
1976/77	279.6	5.4	–	278.8	5.0	–	279.5	4.8	–	279.3	5.0
1977/78	280.2	5.8	–	279.4	5.5	–	279.7	5.1	–	279.8	5.3
1978/79	280.3	6.2	–	279.5	5.7	–	280.5	5.8	–	280.1	5.8
1979/80	279.8	6.8	–	279.1	6.2	–	281.5	6.6	–	280.1	6.4
1980/81	279.3	7.2	–	278.7	6.7	–	281.3	7.4	–	279.8	7.0
1981/82	280.9	6.2	–	–	–	2	282.6	6.5	–	281.1	6.1
1982/83	279.9	7.5	–	–	–	1	281.4	7.3	–	280.0	7.1
1983/84	279.9	6.6	–	–	–	1	280.6	6.4	–	280.2	6.3
1984/85	280.8	6.8	–	279.6	6.6	–	281.8	6.9	–	280.7	6.7
1985/86	–	–	88	–	–	87	282.0	7.0	–	280.7	6.7
1986/87	–	–	211	–	–	222	282.1	7.0	–	281.3	6.5
1987/88	–	–	153	–	–	153	282.3	6.3	–	281.4	5.9
1988/89	281.0	7.2	–	282.0	7.4	–	279.6	6.9	–	280.9	7.1
1989/90	282.0	6.2	–	283.4	6.3	–	280.9	6.1	–	282.1	6.1
1990/91	–	–	1	–	–	1	282.1	7.3	–	280.9	7.1
Mean							281.1	6.5		280.5	6.3
										$T_{a_{max}}$	
1975/76	292.6	8.4	–	291.7	8.0	–	293.9	8.6	–	292.8	8.2
1976/77	292.3	7.9	–	290.3	8.0	–	293.0	8.0	–	291.9	7.9
1977/78	293.1	8.7	–	291.4	8.9	–	293.9	9.0	–	292.8	8.8
1978/79	293.4	8.6	–	291.8	8.7	–	294.3	8.8	–	293.2	8.6
1979/80	293.3	8.8	–	292.1	8.9	–	294.4	8.6	–	293.2	8.7
1980/81	293.4	8.8	–	292.4	8.8	–	294.4	9.0	–	293.4	8.8
1981/82	294.3	8.3	–	292.5	7.9	–	295.3	8.0	–	294.1	8.0
1982/83	293.5	9.1	–	292.0	8.5	–	294.1	8.8	–	293.2	8.7
1983/84	292.7	8.8	–	291.4	8.6	–	293.8	9.0	–	292.6	8.7
1984/85	293.5	9.0	–	292.0	9.3	–	294.7	9.3	–	293.4	9.1
1985/86	–	–	88	–	–	88	294.5	9.4	–	293.1	9.1
1986/87	–	–	122	–	–	334	295.2	8.7	–	294.2	8.5
1987/88	–	–	153	–	–	153	294.2	8.8	–	293.0	8.3
1988/89	–	–	1	292.6	8.1	–	295.2	9.3	–	293.8	8.6
1989/90	–	–	2	292.9	8.2	–	296.0	8.6	–	294.5	8.3
1990/91	–	–	1	–	–	1	294.9	9.7	–	293.2	9.7
Mean							293.9	8.9		293.3	8.6

$T_{a_{min}}$	Minimum air temperature [K]
$T_{a_{max}}$	Maximum air temperature [K]
n_{na}	Number of days not available
$\bar{X}$	Arithmetic mean
S	Standard deviation
Average	Arithmetic mean of the three stations

Table 3.9: *Mean and standard deviation of the minimum and maximum air temperature data for the three major meteorological stations in the West La Mancha area on days of satellite overpass.*

Period	Albacete			Cuenca			Ciudad Real			Average	
	$\bar{X}$	S	n_{na}	$\bar{X}$	S	n_{na}	$\bar{X}$	S	n_{na}	$\bar{X}$	S
										$T_{a_{min}}$	
1978/79	279.4	6.1	–	278.4	5.0	–	279.5	5.3	–	279.1	5.4
1979/80	282.1	6.8	–	281.7	6.6	–	283.8	7.0	–	282.5	6.7
1980/81	278.1	8.0	–	277.8	7.0	–	280.5	8.4	–	278.8	7.7
1981/82	281.7	5.7	–	280.5	5.6	–	283.2	6.3	–	281.8	5.8
1982/83	280.7	7.3	–	280.3	6.7	–	282.6	7.2	–	281.2	6.9
1983/84	278.9	6.5	–	277.8	6.6	–	279.6	6.5	–	278.8	6.5
1984/85	280.7	8.0	–	279.0	7.2	–	281.3	7.6	–	280.3	7.5
1985/86	–	–	5	–	–	5	280.5	7.0	–	279.4	6.7
1986/87	–	–	25	–	–	25	280.5	6.0	–	280.0	5.7
Mean							281.3	6.8		280.2	6.5
										$T_{a_{max}}$	
1978/79	292.5	8.6	–	291.0	8.6	–	293.5	8.9	–	292.3	8.6
1979/80	294.4	8.8	–	293.1	9.2	–	295.6	8.7	–	294.4	8.8
1980/81	293.1	9.0	–	291.6	9.4	–	294.1	9.1	–	292.9	9.1
1981/82	293.8	8.3	–	292.0	7.9	–	294.7	8.0	–	293.5	8.0
1982/83	293.4	9.4	–	291.8	8.5	–	293.6	9.0	–	292.9	8.9
1983/84	291.9	8.8	–	290.5	8.6	–	292.8	9.0	–	291.7	8.7
1984/85	293.3	8.8	–	291.6	9.3	–	294.4	9.3	–	293.1	9.1
1985/86	–	–	12	–	–	12	293.8	9.8	–	292.4	9.3
1986/87	–	–	14	–	–	14	294.8	8.4	–	293.8	8.2
Mean							294.1	8.9		293.0	8.7

$T_{a_{min}}$	Minimum air temperature [K]
$T_{a_{max}}$	Maximum air temperature [K]
n_{na}	Number of days not available
$\bar{X}$	Arithmetic mean
S	Standard deviation
Average	Arithmetic mean of the three stations

used to derive an area–averaged air temperature. These stations are Albacete (N. Lat. 38º56′, E. Long. 358º09′, elevation: 698.5 m above Mean Sea Level (MSL)), Ciudad Real (N. Lat. 38º59′, E. Long. 356º05′, elevation: 628 m MSL) and Cuenca (N. Lat. 40º03′, E. Long. 357º47′, elevation: 955 m MSL) (see also Fig. 1.1). Ciudad Real is the only station actually located in the earlier defined West La Mancha satellite footprint. The two remaining stations are located just outside the footprint. Data from the three stations are averaged to obtain a regional minimum and maximum air temperature. Table 3.8 summarizes the statistics of the available air temperature data. It demonstrates that not all data are available. The Ciudad Real station however, presents a continuous record. Gaps in the data records of the two remaining stations are filled using a linear regression equation with the Ciudad Real station. Linear regression
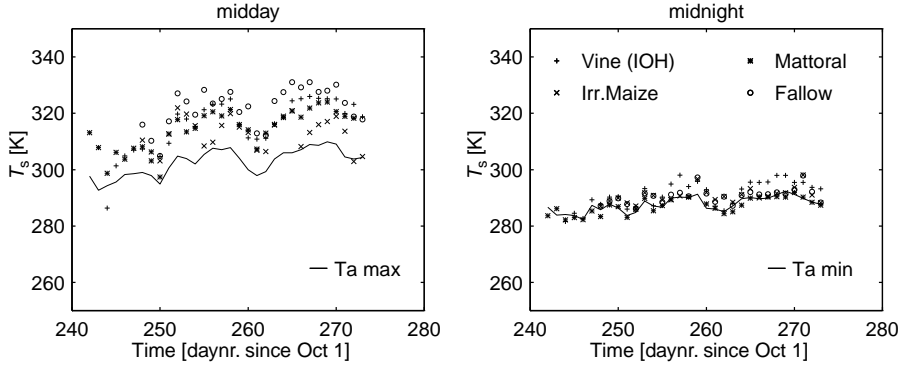
Figure 3.9: *Hourly averages of surface temperature at midday and midnight for several individual fields of various types of surface cover together with the area–averaged minimum and maximum air temperature.*

analysis shows that r^2 varies between 0.86–0.95 from period to period for the daily minimum air temperature data. Similarly, an r^2 range of 0.91–0.96 is observed for the daily maximum air temperature data. For both the minimum and maximum air temperature data the lower range of r^2 values is observed for the station of relatively high elevation, Cuenca.

From the data presented in Table 3.8 the days coinciding with days of satellite overpass are selected. The maximum air temperature data refer to the day time overpass, the minimum air temperature data to the night time overpass. The maximum air temperature is typically recorded in the (late) afternoon after the sun has reached its zenith. The minimum air temperature occurs in the early morning before sunrise. This implies the night time satellite overpass of just before midnight (23:48 hrs LT, see Section 3.3.1) acquires the minimum air temperature of the following day. Table 3.9 summarizes the statistics of the sampled air temperature data.

Comparison of Table 3.8 and Table 3.9 indicates that the difference between the arithmetic mean of the sampled and original population of $T_{a_{min}}$ is relatively large, probably due to the small sample size of the night time data. This implies that the night time data are relatively less representative of a full seasonal cycle.

An analysis of the adjustment of air temperature to surface temperature is carried out by making use of surface temperature measurements of the EFEDA campaign (see Section 1.1.2 and Section 4.3.1) at satellite overpass time for a range of surface cover types. The data are taken from a CD–ROM collection of EFEDA field measurement results. A more detailed description of the measurements by various research groups can be found in *Bolle and Streckenbach* [1992] and *Bolle and Streckenbach* [1993]. Fig. 3.9 presents the measurement results for several fields of various surface cover types together with the area–averaged

Table 3.10: *Adjustment of area–averaged air temperature to surface temperature measurements for surface cover types in the West La Mancha area.*

Surface cover type	Research group	Location	ΔT_a	RMSD	n
					$T_{a_{min}}$
Mean	All	All	0.7	1.8	32
Fallow/Bare soil	CNRM, KARL, WAU	Tom, Bar	0.6	1.7	26
Vegetated surface	BERL, COP, IH, KARL, WAU	Bar, Bel, Tom	0.8	1.7	32
Fallow/Bare soil	CNRM, KARL	Bar	1.4	1.7	26
Bare soil in vineyard	WAU	Tom	−0.5	3.8	20
Irrigated vegetation	COP, KARL	Bar, Bel, Tom	1.0	1.1	29
Non–irrigated vegetation	BERL, IH, WAU	Bar, Bel, Tom	0.9	2.1	32
Fallow	KARL	Bar	1.2	2.0	26
Irrigated maize	KARL	Bar	1.2	2.1	26
Mattoral	BERL	Bel	−0.2	1.3	30
Vine	BERL, IH, WAU	Bel, Tom	1.0	2.2	32
Vine	BERL	Bel	2.3	2.8	11
Vine	IH	Tom	1.8	2.3	30
Vine	WAU	Tom	0.2	2.4	22
					$T_{a_{max}}$
Mean	All	All	6.0	2.4	32
Fallow/Bare soil	CNRM, KARL, WAU	Tom, Bar	2.8	3.2	27
Vegetated surface	BERL, COP, IH, KARL, WAU	Bar, Bel, Tom	6.9	2.7	32
Fallow/Bare soil	CNRM, KARL	Bar	8.7	3.4	26
Bare soil in vineyard	WAU	Tom	−1.0	3.5	24
Irrigated vegetation	COP, KARL	Bar,Bel, Tom	6.8	2.2	29
Non–irrigated vegetation	BERL, IH, WAU	Bar, Bel, Tom	7.1	3.0	32
Fallow	KARL	Bar	9.4	3.6	26
Irrigated maize	KARL	Bar	4.5	4.8	26
Mattoral	BERL	Bel	6.0	3.2	31
Vine	BERL, IH, WAU	Bel, Tom	7.5	2.6	32
Vine	BERL	Bel	10.9	4.3	11
Vine	IH	Tom	6.5	5.0	30
Vine	WAU	Tom	7.3	2.5	26

ΔT_a	Air temperature adjustment [K]
RMSD	Root Mean Square Difference [K]
n	Number of data
BERL	University of Berlin
COP	University of Copenhagen
CNRM	Centre National de Recherches Meteorologique Toulouse
IH	Institute of Hydrology Wallingford
KARL	University of Karlsruhe
WAU	Wageningen Agricultural University
Bar	Barrax
Bel	Belmonte
Tom	Tomelloso

air temperature.

An adjustment of the area–averaged air temperature to surface temperature is carried out using the following expression:

$$T_{se} = T_a + (\Delta T_a + \sin((DOY/n_{DOY})2\pi - (0.5\pi))\Delta T_a) \qquad (3.12)$$

where T_{se} is the estimated surface temperature [K], T_a is the area–averaged air temperature [K], DOY is Day Of Year and n_{DOY} is the number of days in the year. ΔT_a is the air temperature adjustment [K], which is determined by minimizing the Root Mean Square Difference (RMSD) between the surface temperature measurement at the (projected) satellite overpass time, T_{sm} [K], and the estimated surface temperature, T_{se}:

$$RMSD = \sqrt{\frac{\sum_1^n (T_{sm} - T_{se})^2}{n}} \qquad (3.13)$$

where n refers to the number of surface temperature measurements. The surface temperature measurements were carried out in June 1991. Assuming the difference between daily (maximum) air temperature and surface temperature

decreases towards winter, air temperature is adjusted to surface temperature
over the full seasonal cycle by means of Eq. 3.12.

Table 3.10 summarizes the result of air temperature adjustment analysis for the
night and day satellite overpass time. It shows ΔT_a is relatively large for the
midday satellite overpass, while it does not exceed the RMSD for the midnight
satellite overpass. It further shows that differences in ΔT_a occur between differ-
ent fields of corresponding surface cover type. Parts of bare soil between vines
are cool compared to fields of bare soil, both for midday and midnight. ΔT_a is
relatively high for vines in Belmonte, while vineyards in Tomelloso also differ in
ΔT_a. Some of the variation in the surface temperature measurements may be
explained by the different ways it was measured by the different research groups
(e.g. resistance thermometers, infrared thermometers). Overall, it appears the
surface of fallow/bare land is warm compared to vegetated surface at midday.
From Table 3.10 it appears an air temperature adjustment of several K at the
midday satellite overpass time seems justified. An air temperature adjustment
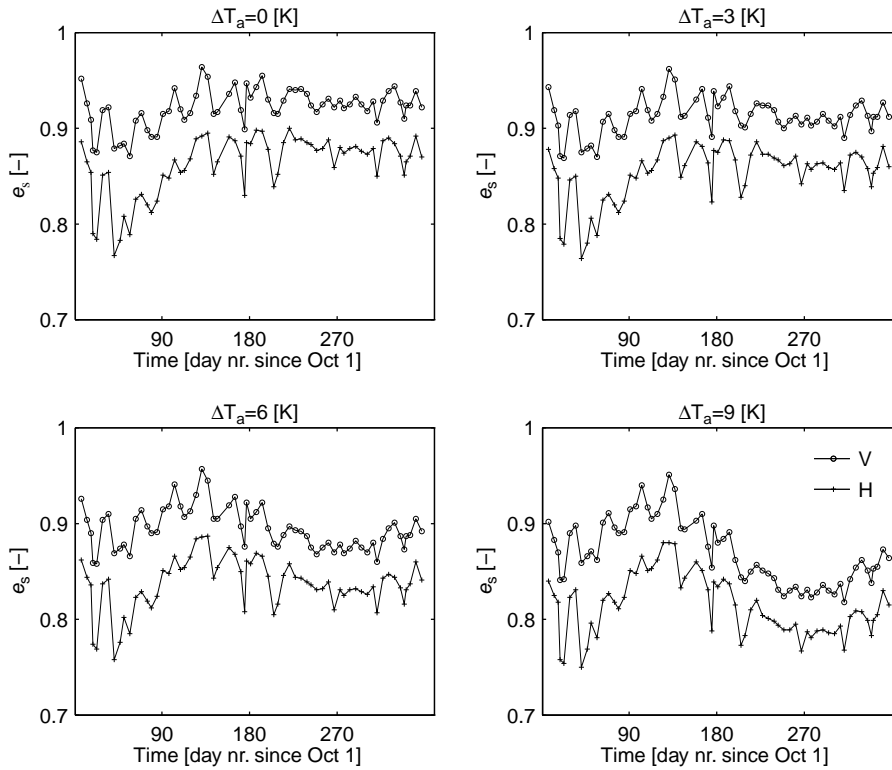for the midnight satellite overpass seems less appropriate.

Figure 3.10: *The effect of an increase in ΔT_a on the day time satellite e_s for
the period 1982/83.*

3.5.3   Bare soil emissivity

As discussed in Section 3.2.1 the soil dielectric constant may be derived in two ways. It may be modeled using a dielectric mixing model [e.g. *Dobson et al.*, 1985] or it may be measured in the field or laboratory. In the present study the dielectric constant of a soil sample is measured for a range of moisture content levels in the laboratory at 1.4 GHz [*IROE*, 1995]. A polynomial function is fitted through the measured data. The real and imaginary part of the dielectric constant at 6 GHz is estimated from the polynomial fit at 1.4 GHz following *Dobson et al.* [1985]. The real part of the dielectric constant at 6 GHz is estimated to be 96% of that at 1.4 GHz at a soil moisture level of 0.3 m^3m^{-3}. At a soil moisture content of 0.1 m^3m^{-3} this is $\pm$ 93%. The imaginary part of the dielectric constant is estimated to be 117% of that at 1.4 GHz at a soil moisture level of 0.3 m^3m^{-3}. At a soil moisture content of 0.1 m^3m^{-3} the imaginary parts are approximately equal. The soil sample was taken from the vineyard test site described earlier in Section 3.4. Fig. 3.11a shows the laboratory–determined real and imaginary parts of the complex dielectric constant at 1.4 GHz together with the polynomial fit. It further shows the estimated relation between the dielectric constant and moisture content at 6 GHz. The displayed curve is relatively steep compared to modelled curves of K (see e.g. *Owe et al.* [1992]). This may be related to the relatively high $CaCO_3$ content of 55% for the soil sample. Fig. 3.11b shows the relationship between moisture content and soil sample emissivity at 6 GHz for horizontal and vertical polarization. Computed e_s for the measured K is also depicted. The soil emissivity is derived by computing the soil sample reflectivity, r_s, using Eq. 3.2 and Eq. 3.3 and $e_s=1-r_s$.

Fig. 3.11b illustrates the range of e_s is larger at horizontal polarization than at vertical polarization. It implies horizontally polarized bare soil surface emissivity is more sensitive to moisture variation than vertically polarized e_s for the 50.2º SMMR antenna view angle over the complete range of moisture conditions. For the drier range of moisture conditions, i. e. 0–0.2 m^3m^{-3}, the slope of the emissivity curve is steeper at horizontal polarization than at vertical polarization. In the case where the range of e_s is identical at both polarization angles, the range of moisture conditions is larger at vertical polarization than at horizontal polarization.

3.5.4   NDVI–based vegetation correction approach

Introduction

As outlined in Section 3.1, the optical thickness of the vegetation canopy may be parameterized using the Normalized Difference Vegetation Index, i.e. NDVI. *Owe et al.* [1992] found a two–part linear relation between the vegetation transmissivity, Γ, and the NDVI for data collected over a shrub/grass savanna area in Botswana, Africa. In the present analysis the vegetation radiative transfer property parameter values, derived in the earlier described ground–based passive microwave measurement experiment (Section 3.4), are applied. The parameter values for surface temperature, T_s and T_c, and the polynomial fit e_s relation
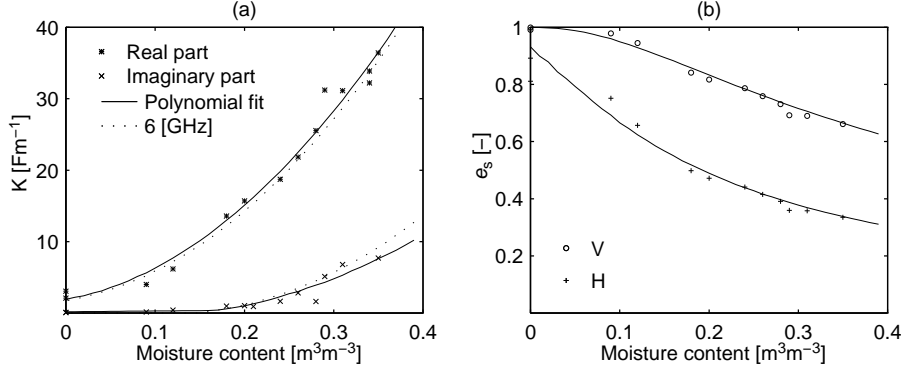
Figure 3.11: *(a) Laboratory–determined real and imaginary parts of the dielectric constant at 1.4 GHz for a range of moisture content levels for a soil sample. K at 6 GHz is estimated from the polynomial fit through the measured data. (b) The derived relation between e_{sV}, e_{sH} and moisture content at 6 GHz together with the computed emissivity for measured K.*

with surface moisture are implemented as well. To analyse the sensitivity of the derived surface moisture estimates to parameter variation, the parameter values in the radiative transfer equation (Eq. 3.6) are varied $-/+$ 10%. The effect of the air temperature adjustment to surface temperature is further analysed by setting $\Delta T_a = 0$ K. The sensitivity of the surface moisture estimates to vegetation correction is additionally analysed by setting $\Gamma = 1$. Furthermore, the effect of a smoothed NDVI–series is analysed (see Fig. 3.12). Sensitivity analysis is carried out for the 1981/82 period.

The ω_H and Γ_H parameter values are taken from the 5 GHz measurement results, being the frequency closest to the satellite frequency. Fig. 3.7 illustrates the ω_H parameter value estimate of 0.05. The determination of an ω_V value is more difficult, as it deviates between full and partial vegetation cover and ranges between 0.01–0.15. Consequently, in the first instance the ω_P estimate is set equal for both polarization directions. The Γ_P–NDVI relation may be approximated by a linear relation at both polarization angles, as is shown in Fig. 3.6. In the case where the vegetation canopy transmits all soil emitted radiation, the Γ_P parameter value is maximum and equal to 1. The linear relation is expressed by:

$$\Gamma_P = 1 - C_{NDVI,P}(NDVI) \qquad (3.14)$$

where $_P$ is the polarization angle ($_{H,V}$). $C_{NDVI,P}$ is a constant of value 1. In perspective of the sensitivity analysis it is varied over 10% between 0.9–1.1 to change the slope of the line. In the case where $C_{NDVI} = 1.1$, the NDVI may not exceed 0.91.

The parameter value of the air temperature adjustment to surface temperature, ΔT_{a}, is determined from Table 3.10. For the bare soil surface and the vegetated surface an average ΔT_{a} parameter value and individual parameter values, ΔT_{ab} and ΔT_{ac}, are evaluated (see Table 3.13 and Table 3.14). The regional surface cover development of the predominant cover types in the West La Mancha area over the period of 1975–1990 is reported by *Thornes et al.* [1996]. Table 4.3 shows that bare soil covers only a few per cent of the total area surface. The largest surface cover fractions consist of permanent agriculture, semi–natural vegetation and spring cropping agriculture. It appears therefore, that the regional surface cover is predominantly vegetated. As described in Section 3.4 for a vine surface cover, the vegetation density may vary, leaving parts of the bare soil exposed. The size of bare soil parts between vegetation varies with both vegetation type and seasonal vegetation development. Although it proves difficult to determine a bare soil surface total, it is obviously larger than only a few per cent of the total surface area. Furthermore, the surface temperature for parts of the bare soil between vegetation and fields of completely bare soil appears to be very different, especially during day time (see Section 3.5.2). In any case, an analysis of the effect of a differentiation between the surface temperature of bare soil and vegetation seems appropriate.

The bare soil emissivity curve, computed from laboratory–determined dielectric properties of a soil sample (Section 3.5.3) is applied and varied in value $-/+$ 10%. As no parameter value of the soil surface roughness, h, is available from field measurements, it is varied in two steps over the range of values reported in Section 3.2.2).

The sensitivity of surface moisture estimates to parameter variation in the radiative transfer equation is analysed by comparison with a fixed parameter matrix. In summary, the fixed matrix features the following characteristics:

- $\omega_{\mathrm{H}} = \omega_{\mathrm{V}} = 0.05$.

- $\Gamma_{\mathrm{H}} = \Gamma_{\mathrm{V}} = 1 - \mathrm{NDVI}$, where NDVI is a smoothed NDVI–series, as illustrated in Fig. 3.12.

- $\Delta T_{\mathrm{a}} = 0$ K, for both day and night time observations.

- $h = 0$.

- e_{s} is related to moisture content for both polarization directions by the polynomial fit curve to laboratory–determined data, as illustrated in Fig. 3.11.

The following section describes the general characteristics, derivation and processing of the NDVI data. Analysis results and discussion of the derivation of surface moisture using the NDVI–based vegetation correction approach are then presented.
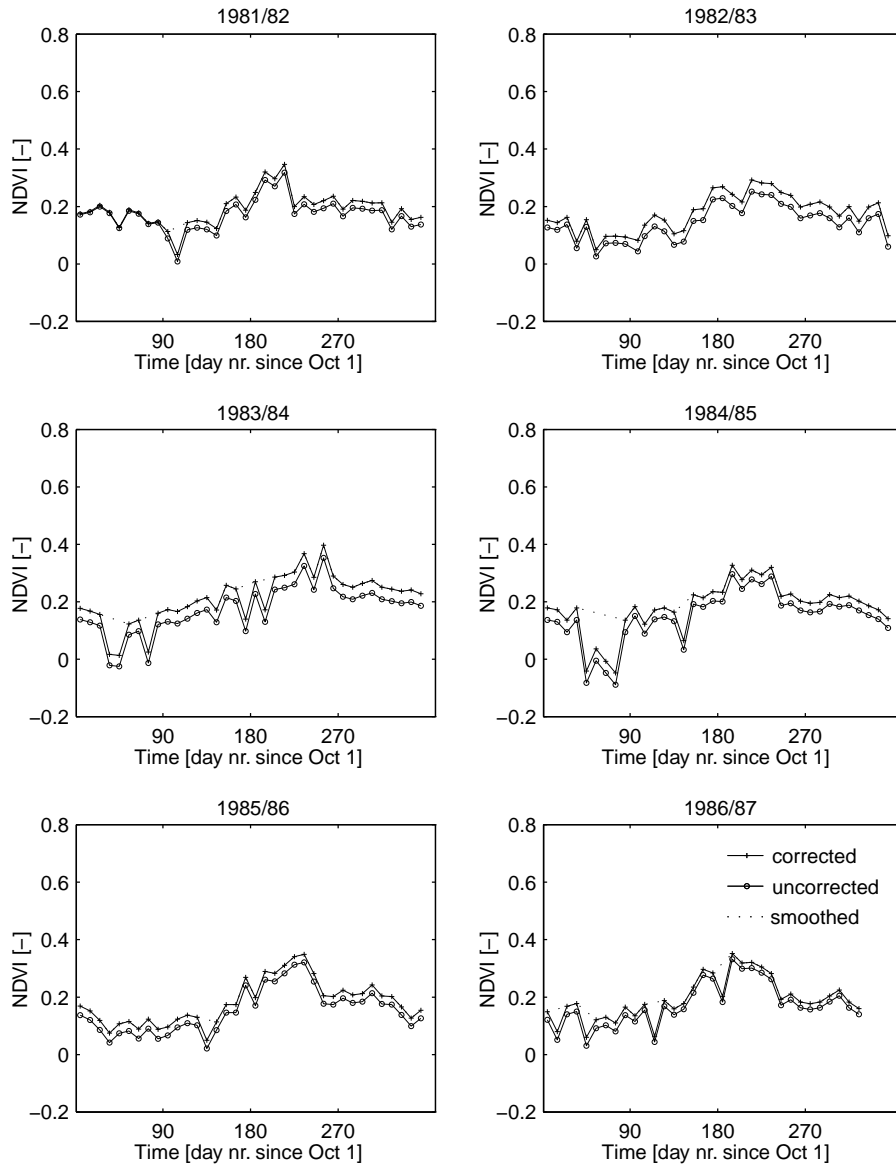
Figure 3.12: *Time series of 10–day composite footprint NDVI, collected over the West La Mancha area for the period 1981/82 to 1986/87.*

NDVI time series

Theoretical overview and data specifications   The NDVI data form part
of the Pathfinder Advanced Very High Resolution Radiometer (AVHRR) Land
Composite Data Set and are downloaded from the Goddard Distributed Active
Archive Center (DAAC) anonymous ftp site. A more detailed description of the
theoretical background and data specifications can be found at the Global Land
Biosphere Data and Information Web Site at http://daac.gsfc.nasa.gov.
On the NOAA–7, NOAA–9 and NOAA–11 satellites, the AVHRR sensor mea-
sures emitted and reflected radiation in five channels (bands) of the electromag-
netic spectrum. The first channel is a visible band $(0.58 - 0.68 \mu m)$ in a part
of the spectrum where chlorophyll causes considerable absorption of incoming
radiation. The second channel is a near–infrared band $(0.725 - 1.1 \mu m)$ where
spongy mesophyll leaf structure leads to considerable reflectance. The contrast
between responses of the two bands can be shown by a ratio transform, i.e. di-
viding one band by the other. Several ratio transforms have been proposed for
different land surfaces [*Tucker*, 1979]. The Normalized Difference Vegetation
Index (NDVI) is one such ratio, which has been shown to be highly correlated
with vegetation parameters such as green–leaf biomass and green–leaf area and,
hence, is of considerable value for vegetation discrimination [*Justice et al.*, 1985].
A ratio between bands is of considerable use in reducing variations caused by
surface topography [*Holben and Justice*, 1981]. It compensates for variations in
radiance as a function of sun elevation for different parts of an image. The ratios
do not eliminate additive effects caused by atmospheric attenuation, but the ba-
sis for the NDVI and vegetation holds generally. However, the soil background
contributes a reflected signal apart from the vegetation, and interacts with the
overlying vegetation through multiple scattering of radiant energy. *Huete* [1988]
found the NDVI to be as sensitive to soil darkening (moisture and soil type) as
to plant density over partially vegetated area. The NDVI ranges between –1
and + 1 and is derived by:

$$\text{NDVI} = \frac{(\text{channel2}_\text{reflectance} - \text{channel1}_\text{reflectance})}{(\text{channel2}_\text{reflectance} + \text{channel1}_\text{reflectance})} \tag{3.15}$$

Data processing   In the present study, 10–day NDVI composites are used.
The composites are created from daily data by choosing values for each bin
(pixel) based on the day that has the highest NDVI value during the interval.
Compositing of the NDVI data is a useful tool to filter out cloud contamination.
In compositing, all data is quality controlled. Prior to 10–day compositing the
data is resampled to 8 km X 8 km spatial resolution.

Time series   NDVI data are available from June 23 1981 onwards. Temporal
overlap with Nimbus–7/SMMR extends from the launch date of NOAA–7 (June
23 1981) via the launch date of NOAA–9 (December 12 1984) to the termination
date of SMMR (August 20 1987). Identical to the Nimbus–7, the NOAA–series
is a sun synchronous, near polar, low earth orbiting satellite. The orbit time

Table 3.11: *The effect of variation of footprint location on the average 10–day composite footprint NDVI for the period 1981/82.*

Location	Matrix size	$\bar{X}$	S	$\bar{X}_{S_{ftpr}}$
(x,y)	21X19	0.17	0.062	0.071
(x+5,y)		0.16	0.059	0.061
(x–5,y)		0.20	0.068	0.087
(x,y+6)		0.17	0.062	0.070
(x,y–6)		0.21	0.064	0.086
(x+1,y+1)	19X17	0.17	0.061	0.068
(x+6,y+1)		0.15	0.059	0.056
(x–4,y+1)		0.20	0.067	0.086
(x+1,y+7)		0.16	0.062	0.069
(x+1,y–5)		0.21	0.064	0.084

S	Standard deviation of mean footprint NDVI
$\bar{X}$	Arithmetic mean footprint NDVI
$\bar{X}_{S_{ftpr}}$	Mean standard deviation within the footprint

is 102 minutes. Equatorial crossing times are 14:30 hrs LT and 14:20 hrs LT for the NOAA–7 and NOAA–9 satellite, respectively. Therefore, the central Spain cross–over times are 14:41 hrs LT and 14:31 hrs LT for the NOAA–7 and NOAA–9 satellite, respectively.

The NDVI data are made available as maps of Europe with an 8 km X 8 km spatial resolution, North Latitude $76^{o}42' - 23^{o}24'$, East Longitude $347^{o}00' - 60^{o}30'$. A 185X133 matrix, that covers the Iberian Peninsula, is cut from the maps (North Latitude $35^{o}00' - 44^{o}30'$, East Longitude $350^{o}38' - 6^{o}36'$). Next, the matrices are resampled for geometrical correction, using a linear fit with nearest neighbour interpolation. The correction introduces a RMS error of 0.44, expressed in input image units, i.e degrees. In the geometrically corrected matrix therefore, a mean error in coordinate location of 5 columns in the longitude and/or 6 rows in the latitude is introduced. A 21X19 matrix of latitude–longitude coordinates identical to the earlier defined Nimbus–7/SMMR matrix footprint is cut from the resampled Iberian Peninsula maps. The 21X19 matrix results in a 168 km X 152 km footprint size, i.e. larger than the Nimbus–7/SMMR 7X5 quarter degree grid matrix footprint of 149 km x 138 km. Resampling may, however, have changed the 8 km X 8 km spatial resolution. The effect on the 10–day composite average footprint NDVI of a 19X17 matrix size, i.e. a 152 km X 136 km footprint, is evaluated for the 1981/82 period. The effect of a 5 column shift east (x+5,y) and west (x–5,y) and a 6 row shift north (x,y+6) and south (x,y–6) is also analysed. Table 3.11 presents the results. A shift of footprint to the north and to the west increases the average 10–day composite footprint NDVI, while a shift to the south and to the east results in a

decrease. An increase in average footprint NDVI is accompanied by an increase in the standard deviation within the matrix footprint and vice versa. This may indicate the footprint is bounded to the north and to the west by areas of a comparatively higher vegetation density. To the east, and in a lesser degree to the south, the footprint appears to extend to a relatively homogeneous area of low vegetation density. For all footprints a reduction in matrix size results in a small decrease in the average footprint NDVI. Processing of the NDVI data is carried out with the IDRISI software program.

The Global Land Biosphere Data and Information Web Site reports that coding errors in the Pathfinder AVHRR Land (PAL) software have introduced errors in the NDVI data. The channel 1 and channel 2 reflectances have not been normalized for variations in solar zenith angle. The difference in NDVI before and after normalization for solar illumination is very small however (less than 0.008), and is caused by rounding errors beyond the third decimal during the processing of NDVI. A second error concerns the correction for Rayleigh scattering and ozone absorption in the atmosphere. The correction, carried out for channel 1 and channel 2, has been underestimated. The RMS difference between the Pathfinder NDVI and the more accurately corrected NDVI was found to be 0.05. The data used in the present analysis have been extracted and processed prior to the re–issue of a corrected 10–day composite data set on the Goddard DAAC ftp site.

Fig. 3.12 shows the series for the 10 day–composite West La Mancha footprint NDVI. The data are corrected for sensor degradation using an algorithm reported by *Loss* [1993]. Fig. 3.12 shows the effect of the sensor degradation correction which has been executed on the NDVI footprint averages. The NDVI series do not demonstrate a smooth curve, but alternate strongly from 10–day period to 10–day period. Low NDVI values occur in the period October–January, when some values remain below zero. These outlying 10–day composite values are deleted, because they are considered to be related to measuring or processing errors (e.g. look angle variation, atmospheric absorption, cloud contamination) rather than to vegetation biomass development.

Maximum NDVI is recorded in May. This seems to indicate the NDVI is mainly controlled by (irrigated) spring cropping agriculture, and to a lesser degree by permanent agriculture (vine, olive) and semi–natural vegetation. The NDVI maintains a comparatively intermediate level from June to September, the period of vine plant growth, before dropping to a low in mid–October. The footprint NDVI appears to be quite insensitive to vine plant development, as only a slight response seems visible in the relatively constant NDVI level from June to September. A similar insensitivity of the NDVI to changing vine vegetation biomass density on the plot–scale is described earlier in Section 3.4.3.

Table 3.12 presents the statistics of the 10–day composite footprint NDVI. The mean standard deviation within the NDVI footprint for all periods is large, i.e. about a third of the mean footprint NDVI. No footprints of excessively large standard deviation within the NDVI footprint occur: all remain within three times the mean standard deviation within the footprint. Linear interpolation between the 10–day composite NDVI values is used to determine the NDVI on

Table 3.12: *Statistics of the 10–day composite NDVI footprints, collected over the West La Mancha area.*

Period	n	$\bar{\mathrm{X}}_{\mathrm{uncor}}$	$\mathrm{S}_{\mathrm{uncor}}$	$\bar{\mathrm{X}}_{\mathrm{S_{ftpr}}}$	$\bar{\mathrm{X}}_{\mathrm{cor}}$	$\mathrm{S}_{\mathrm{cor}}$
1981/82	36	0.17	0.056	0.071	0.19	0.058
1982/83	36	0.14	0.060	0.065	0.18	0.064
1983/84	36	0.17	0.083	0.071	0.21	0.085
1984/85	36	0.15	0.091	0.066	0.18	0.088
1985/86	36	0.15	0.077	0.073	0.18	0.076
1986/87	33	0.17	0.075	0.078	0.19	0.073

n	Number of data
$\bar{\mathrm{X}}_{\mathrm{(un)cor}}$	Arithmetic mean footprint NDVI, (not) corrected for sensor degradation
$S_{\mathrm{(un)cor}}$	Standard deviation of mean footprint NDVI, (not) corrected for sensor degradation
$\bar{\mathrm{X}}_{\mathrm{S_{ftpr}}}$	Mean footprint standard deviation within footprint

days of Nimbus–7/SMMR satellite overpass. In the case of a decreasing trend, the 10–day composite NDVI value is shifted to the first day of the 10–day period and vice versa. As mentioned above, a smoothing of the NDVI series is carried out by deleting outlying (negative) 10–day composite values, as illustrated in Fig. 3.12.

Results and discussion

Sensitivity analysis Table 3.13 and Table 3.14 list the results of sensitivity analysis of surface moisture estimates to parameter variation for the 1981/82 period at horizontal and vertical polarization, respectively. Fig. 3.13 and Fig. 3.14 present a selection of the parameter variations listed in Table 3.13.
A striking feature in the analysis results is the difference in moisture conditions of the time series of satellite derived surface moisture at horizontal and vertical polarization. The difference in the range of moisture conditions corresponds with the difference in the range of day and night time satellite observed emissivities, i.e. e_{H}=0.75–0.91 and e_{V}=0.85–0.95 (with $\Delta T_{\mathrm{a}} = 0$ K), respectively. This is illustrated in the right–hand graph of Fig. 3.13a. With $\Gamma_{\mathrm{P}} = 1$, the difference in the range of moisture conditions at the two polarization angles directly relates to the bare soil emissivity curve and the range of the satellite observed emissivity. For the two polarization angles to have an identical range of moisture conditions, the observed range of satellite e_{H} should decrease to 0.5–0.67 (see Fig. 3.11b). Conversely, e_{V} should increase to 0.98–1. Apart from the bare soil emissivity curve, the parameters in the radiative transfer equation have all been assumed equal at the two polarization angles (see Introduction, this section). For h or T_{s} there is no reason to assume a different value at the

Table 3.13: *Results of sensitivity analysis of surface moisture estimates to parameter variation for the period 1981/82 at horizontal polarization. θ_{sat} is derived using the NDVI–based vegetation correction approach.*

Parameter variation	θ_{sat}			Γ_H		
	$\bar{X}$	$\Delta\bar{X}$	S	$\bar{X}$	$\Delta\bar{X}$	S
Horizontal polarization, day time						
Fixed input matrix	0.051	–	0.016	0.80	–	0.052
ΔT_a=6	0.061	20	0.015	0.80	0	0.052
ΔT_{ab}=9, ΔT_{ac}=7	0.065	27	0.015	0.80	0	0.052
Γ_H=1	0.027	47	0.013	1	25	–
Γ_H=0.9–NDVI	0.071	39	0.022	0.70	13	0.052
Γ_H=1–0.9(NDVI)	0.048	6	0.016	0.81	1	0.048
Γ_H=1–1.1(NDVI)	0.054	6	0.017	0.77	4	0.058
non–smoothed NDVI–series	0.048	6	0.015	0.81	1	0.055
ω_H=0.045	0.051	0	0.016	0.80	0	0.052
ω_H=0.055	0.050	2	0.016	0.80	0	0.052
h=0.25	0.059	16	0.018	0.80	0	0.052
h=0.50	0.068	33	0.021	0.80	0	0.052
e_{sH} + 10%	0.079	55	0.016	0.80	0	0.052
e_{sH} − 10%	0.018	65	0.017	0.80	0	0.052
Horizontal polarization, night time						
Fixed input matrix	0.055	–	0.021	0.80	–	0.049
ΔT_a=1	0.057	4	0.022	0.80	0	0.049
Γ_H=1	0.030	45	0.015	1	25	–
Γ_H=0.9–NDVI	0.077	29	0.029	0.70	13	0.049
Γ_H=1–0.9(NDVI)	0.051	7	0.020	0.82	3	0.044
Γ_H=1–1.1(NDVI)	0.059	7	0.022	0.78	3	0.053
non–smoothed NDVI–series	0.052	5	0.017	0.82	3	0.060
ω_H=0.045	0.056	2	0.021	0.80	0	0.049
ω_H=0.055	0.054	2	0.021	0.80	0	0.049
h=0.25	0.064	16	0.023	0.80	0	0.049
h=0.50	0.073	33	0.027	0.80	0	0.049
e_{sH} + 10%	0.083	51	0.021	0.80	0	0.049
e_{sH} − 10%	0.023	58	0.022	0.80	0	0.049

θ_{sat}	Satellite derived surface moisture [m^{3}m^{-3}]
Γ_H	Vegetation transmissivity at hor. pol. [–]
S	Standard deviation
$\bar{X}$	Arithmetic mean
$\Delta\bar{X}$	Proportional change of $\bar{X}$ by parameter variation [%]

Table 3.14: *Results of sensitivity analysis of surface moisture estimates to parameter variation for the period 1981/82 at vertical polarization. θ_{sat} is derived using the NDVI–based vegetation correction approach.*

Parameter variation	θ_{sat}			Γ_V		
	$\bar{X}$	$\Delta\bar{X}$	S	$\bar{X}$	$\Delta\bar{X}$	S
Vertical polarization, day time						
Fixed input matrix	0.156	–	0.020	0.80	–	0.052
ΔT_a=6	0.180	15	0.021	0.80	0	0.051
ΔT_{ab}=9, ΔT_{ac}=7	0.189	21	0.025	0.80	0	0.052
Γ_V=1	0.131	16	0.016	1	25	–
Γ_V=0.9–NDVI	0.175	15	0.025	0.70	13	0.052
Γ_V=1–0.9(NDVI)	0.153	2	0.019	0.82	3	0.048
Γ_V=1–1.1(NDVI)	0.159	2	0.020	0.77	4	0.058
non–smoothed NDVI–series	0.153	2	0.018	0.81	1	0.055
ω_V=0.045	0.157	1	0.020	0.80	0	0.052
ω_V=0.055	0.154	1	0.020	0.80	0	0.052
h=0.25	0.165	6	0.022	0.80	0	0.052
h=0.50	0.175	12	0.024	0.80	0	0.052
e_{sV} + 1%	0.163	4	0.019	0.80	0	0.052
e_{sV} − 10%	0.019	88	0.084	0.80	0	0.052
Vertical polarization, night time						
Fixed input matrix	0.166	–	0.028	0.80	–	0.049
ΔT_a=1	0.170	2	0.029	0.80	0	0.049
Γ_V=1	0.137	17	0.021	1	25	–
Γ_V=0.9–NDVI	0.188	13	0.036	0.70	13	0.049
Γ_V=1–0.9(NDVI)	0.162	2	0.027	0.82	3	0.044
Γ_V=1–1.1(NDVI)	0.170	2	0.029	0.78	3	0.053
non–smoothed NDVI–series	0.162	2	0.024	0.82	3	0.060
ω_V=0.045	0.167	1	0.028	0.80	0	0.049
ω_V=0.055	0.164	1	0.028	0.80	0	0.049
h=0.25	0.176	6	0.030	0.80	0	0.049
h=0.50	0.187	13	0.033	0.80	0	0.049
e_{sV} + 1 %	0.173	4	0.027	0.80	0	0.049
e_{sV} − 10%	0.034	80	0.102	0.80	0	0.049

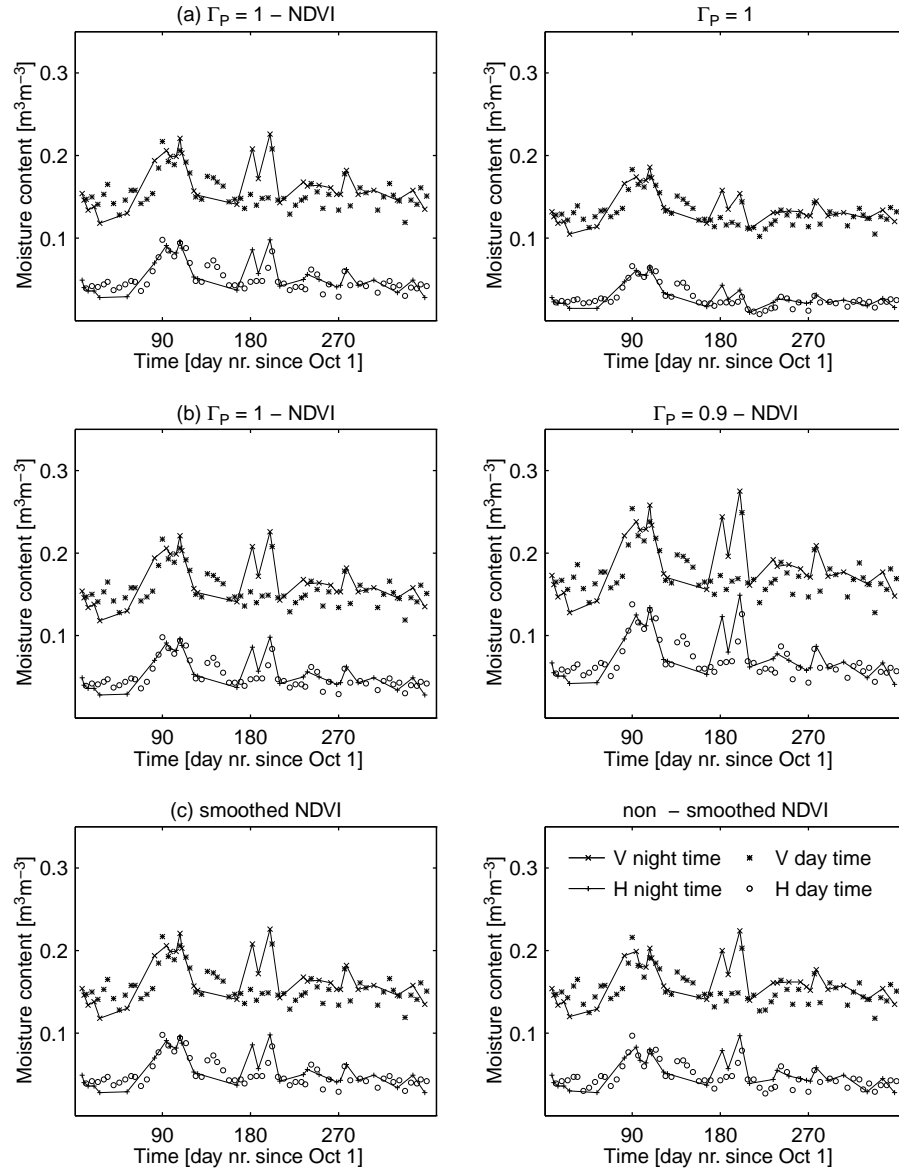|	
θ_{sat}	Satellite derived surface moisture [m^{3}m^{-3}]
Γ_V	Vegetation transmissivity at ver. pol. [–]
S	Standard deviation
$\bar{X}$	Arithmetic mean
$\Delta\bar{X}$	Proportional change of $\bar{X}$ by parameter variation [%]

Figure 3.13: *Sensitivity of the satellite derived moisture content estimate at horizontal polarization for the 1981/82 period using using the NDVI–based vegetation correction approach to a) the vegetation effect correction b)* Γ_P *c) smoothing of the NDVI–series.*
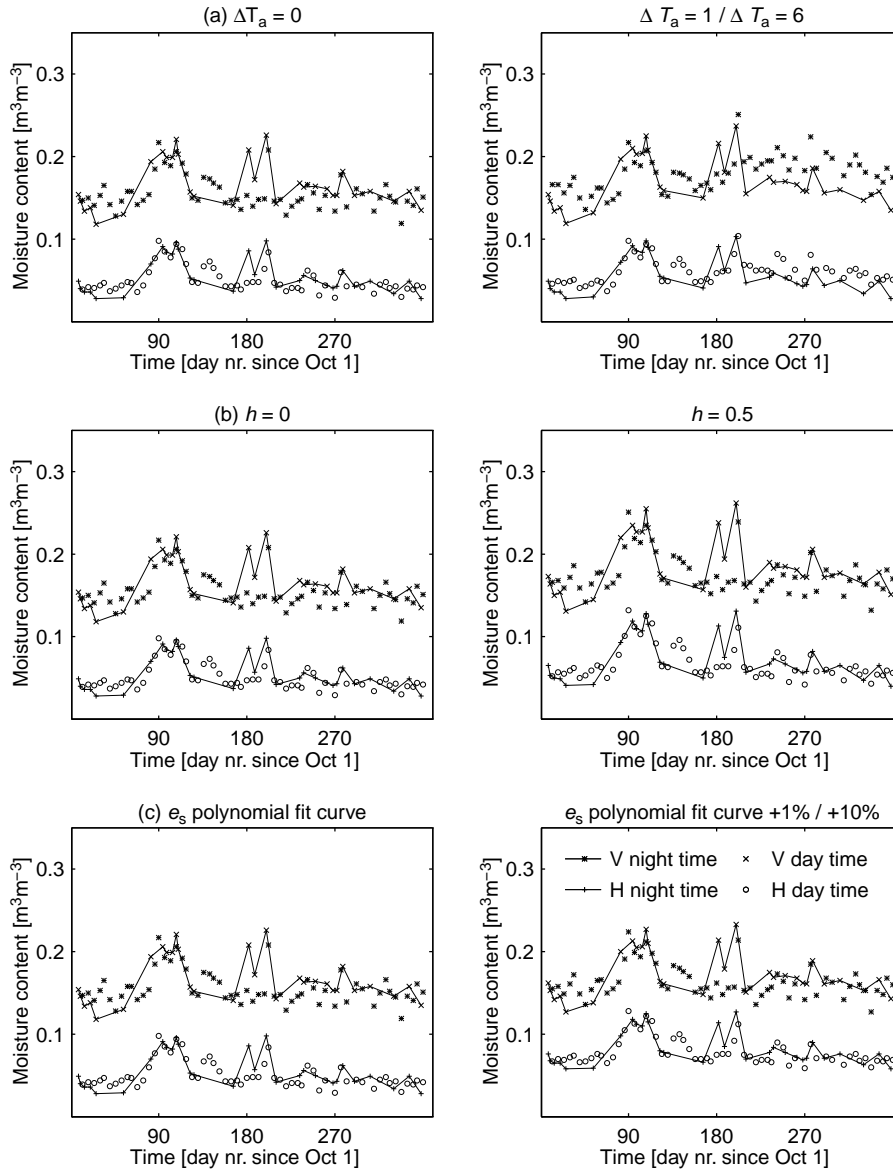
Figure 3.14: *Sensitivity of the satellite derived moisture content estimate at horizontal polarization for the 1981/82 period using the NDVI–based vegetation correction approach to a) the air temperature adjustment to surface temperature b) the soil surface roughness c) the level of the bare soil emissivity curve.*

two polarization angles. Although the difference for a true random canopy will be minimal, the vegetation radiative transfer property parameter values, Γ_P and ω_P, may well be different. In fact, adjustment of the vegetation transfer property parameter values to fit the time series of satellite derived moisture at horizontal and vertical polarization may provide an indication of their relative proportion, i.e. A and B (see Section 3.4).

Adjustment of the earlier defined vegetation radiative transfer property parameter values in the fixed parameter matrix, implies that the experimentally derived parameter values are partly abandoned. The adjustment should, however, preferably be carried out within the range of the experimental results. The Γ_P–NDVI linear relation may have a different slope and/or intercept or it may be non–linear, but Γ_P is expected to remain > 0.5. Furthermore, the experimentally derived ω_H value of 0.05 seems consistent. Conversely, ω_V may have any value in the experimentally derived range of 0.01–0.15 (see Fig. 3.7). The sensitivity of the time series of derived surface soil moisture to variation in the vegetation radiative transfer property parameters for the 1981/82 period is listed in Table 3.13 and Table 3.14. A decrease of Γ_P and ω_P leads to an upward shift of the time series for derived surface moisture. This is explained by the decrease in bare soil emissivity, e_{sP}. With $e_{cP} = (1 - \omega_P)(1 - \Gamma_P)$, the decrease in e_{sP} compensates for an increase in the vegetation emissivity, e_{cP} (see Eq. 3.6). A decrease in Γ_P further increases the range of moisture conditions. A decrease in ω_P decreases the range. The derived surface moisture content is more sensitive to variation in Γ_P than in ω_P. So, in order to match the time series of satellite derived surface moisture at vertical and horizontal polarization, $\Gamma_H < \Gamma_V$ and $\omega_H < \omega_V$.

From Eq. 3.14 it follows that Γ_V may only increase by decreasing $C_{NDVI,V}$. Since we assume Γ_V is dependent on NDVI, $C_{NDVI,V} > 0$. A decrease in Γ_H leads to an upward shift of the time series for derived surface moisture and increases the range of moisture conditions. An increase in Γ_V leads to a downward shift of the time series of satellite derived surface moisture and decreases the range of moisture conditions. In order to minimize the difference in the range of moisture conditions at the two polarization angles, $C_{NDVI,V}$ is chosen as 1. For the same reason ω_V is set to 0.12, the maximum value of ω_P reported in the literature, at least for cultivated vegetation (see Section 3.2.3).

The match of the time series of satellite derived surface moisture at the two polarization angles is thus carried out by shifting the time series of satellite derived surface at horizontal polarization upwards. In order to minimize the difference in the range of moisture conditions at the two polarization angles, the time series of satellite derived surface moisture at vertical polarization remains approximately level, i.e.:

- $\Gamma_V = 1$–NDVI

- $\omega_V = 0.12$

The Root Mean Square Difference (RMSD) between the time series of satellite derived surface moisture content at the respective vertical and horizontal

polarization angle, $\theta_{\text{sat,V}}$ and $\theta_{\text{sat,H}}$ [m^{3}m^{-3}], is defined as:

$$\text{RMSD} = \sqrt{\frac{\sum_1^n (\theta_{\text{sat,V}} - \theta_{\text{sat,H}})^2}{n}} \qquad (3.16)$$

where n is the number of observations. It appears that the match of the time series of satellite derived surface moisture at horizontal polarization to the time series of satellite derived surface moisture at vertical polarization is best by applying:

- Γ_{H}=0.7-0.6(NDVI)

- ω_{H}=0

Application of the optimum fit of the Γ_{H}–NDVI relation results in values of Γ_{H} corresponding with the (lower) range of the experimentally derived values of Γ_{H} (see Table 3.15). The optimum value of ω_{H}=0 does not correspond with the experimentally derived value of ω_{H}=0.05. Furthermore, the range of moisture conditions on the time series of satellite derived surface moisture at horizontal polarization and vertical polarization do not correspond very well. The range is much larger at horizontal polarization, as is shown in the upper–left graph in Fig. 3.15 and Fig. 3.16.

The matching of the time series of satellite derived surface moisture at vertical and horizontal polarization provides for an indication of A(= $\Gamma_{\text{H}}/\Gamma_{\text{V}}$) and B(= $\omega_{\text{H}}/\omega_{\text{V}}$). For the 1981/82 period, the best fit results in a value of A $\approx$ 0.8 and B=0. The optimum value of A falls outside the range of experimentally derived values of A, i.e. 0.9–1.2 (see Fig. 3.8). The optimum value of B and the experimentally derived value of B do not correspond. The derived ratios are, however, merely an indication. The rigid parameterization of Γ_{P} using the NDVI does not allow an accurate fit of the range of moisture conditions at horizontal and vertical polarization. The optimum value of ω_{H}=0 may therefore be an artifact of the NDVI parameterization of Γ_{H}. A decrease in Γ_{H} leads to an upward shift of the time series of satellite derived surface moisture and an increase in the range of moisture conditions. The increase in the range of moisture conditions is compensated for by a value of $\omega_{\text{H}} = 0$.

In summary, the matching of the time series of derived moisture provides an indication of the value of A $\approx$ 0.8. It furthermore indicates $\omega_{\text{V}} \approx 0.12$. With a value of ω_{H} in the range 0–0.05, B $\leq$ 0.5. The derived ratios are used to derive a time series of surface moisture using the dual polarization vegetation correction approach. This is described in the following section.

Fig. 3.14a illustrates the result of air temperature adjustment to surface temperature using ΔT_{a}. As described in Section 3.5.2, a day time air temperature adjustment of several degrees seems justified. Conversely, at night time an adjustment of the air temperature may be neglected. Since the adjustment of air temperature to surface temperature is largest in summer (see Eq. 3.12), the decrease in satellite emissivity is largest in summer. This leads to an upward shift

on the time series of satellite derived surface moisture content in the (dry) summer period. The average footprint air temperature adjustment seems, therefore, not to lead to an improved estimate of the day time surface moisture content. This may partly be explained by the high degree of spatial variation in the day time surface temperature (see Table 3.10). A partitioning of ΔT_a between bare soil and vegetated surface leads, however, to a similar result, i.e. an increased surface moisture content in the dry summer period (see Table 3.13 and Table 3.14). So, although $\Delta T_a > 0$ in day time, an increase in $T_{a_{max}}$ does not lead to satisfactory results. Since ΔT_a may be disregarded at night time, the use of these data seems preferable. The number of night time data is, however, about half the number of day time data (see Table 3.1).

Setting $\Delta T_a = 0$ K, the range of moisture conditions is comparable at day and night time. This may indicate that the day time temperature of the emitting soil layer is (much) cooler than the estimated day time T_s and that the $T_{a_{max}}$ is a reasonable estimate of the day time temperature of the emitting layer. An alternative explanation of the decrease in surface emissivity may be contamination by the sky of the satellite observed T_b. As mentioned in Section 3.4.3, this may cause the observed microwave brightness temperature to be cooler than it should be at the larger antenna view angle. At the 50.2° satellite antenna view angle, a cooler T_b results in a decrease of the satellite emissivity, i.e. an increase of the derived surface moisture content. So, while a normalization of the day time satellite observed T_b with $T_{a_{max}}$ ($\Delta T_a = 0$ K) leads to better results, it possibly only masks the contamination of T_b by the sky. The effect of sky contamination may be expected to be largest at day time in summer, when the difference between T_s and T_a is largest. At night time, the sky contamination may be expected to be relatively small, since $T_s \approx T_a$. Overall, the time series of derived surface moisture at night time are regarded more reliable.

Fig. 3.14b shows the effect of variation in h. Since an increase in h increases the bare soil emissivity, it leads to an upward shift of the time series of the inversely derived surface moisture. The range of moisture conditions increases as well. Fig. 3.13c shows that the time series of derived moisture are only slightly affected by smoothing of the NDVI time series. Furthermore, the time series of satellite derived surface moisture content appear to be very sensitive to variation in the bare soil emissivity. The time series of satellite derived surface moisture are more sensitive to parameter variation at horizontal polarization than at vertical polarization.

Time series   Table 3.15 present results of the satellite derived surface moisture content estimates for the period 1981/82 to 1986/87 using the NDVI–based vegetation correction approach. Fig. 3.15 and Fig. 3.16 present the time series of satellite derived surface moisture at the horizontal and vertical polarization angle, respectively. The time series of surface moisture content are derived using the Γ_P–NDVI relations and the ω_P values derived in the previous section. The values of the remaining parameters are set identical to the values in the parameter matrix defined in Section 3.5.4. The parameter values are set identical for

Table 3.15: *Satellite derived moisture content estimates for the period 1981/82 to 1986/87 using the NDVI–based vegetation correction approach.*

Period	θ_{sat}		Γ_{P}	
	$\bar{\mathrm{X}}$	S	$\bar{\mathrm{X}}$	S
Horizontal polarization, day time				
1981/82	0.125	0.041	0.62	0.030
1982/83	0.112	0.035	0.63	0.032
1983/84	0.140	0.045	0.60	0.041
1984/85	0.124	0.036	0.62	0.026
1985/86	0.110	0.030	0.65	0.025
1986/87	0.116	0.030	0.61	0.037
Mean	0.122	0.037	0.62	0.032
Horizontal polarization, night time				
1981/82	0.139	0.055	0.62	0.031
1982/83	0.117	0.035	0.62	0.032
1983/84	0.162	0.066	0.60	0.040
1984/85	0.115	0.032	0.62	0.021
1985/86	0.115	0.034	0.62	0.049
1986/87	0.110	0.027	0.63	0.041
Mean	0.126	0.041	0.62	0.035
Vertical polarization, day time				
1981/82	0.134	0.025	0.80	0.052
1982/83	0.128	0.026	0.81	0.054
1983/84	0.138	0.027	0.77	0.068
1984/85	0.135	0.023	0.79	0.043
1985/86	0.134	0.020	0.84	0.042
1986/87	0.124	0.032	0.78	0.062
Mean	0.132	0.026	0.80	0.054
Vertical polarization, night time				
1981/82	0.145	0.029	0.80	0.049
1982/83	0.134	0.018	0.81	0.052
1983/84	0.150	0.028	0.78	0.064
1984/85	0.131	0.028	0.80	0.035
1985/86	0.129	0.022	0.80	0.080
1986/87	0.132	0.020	0.82	0.065
Mean	0.137	0.024	0.80	0.066

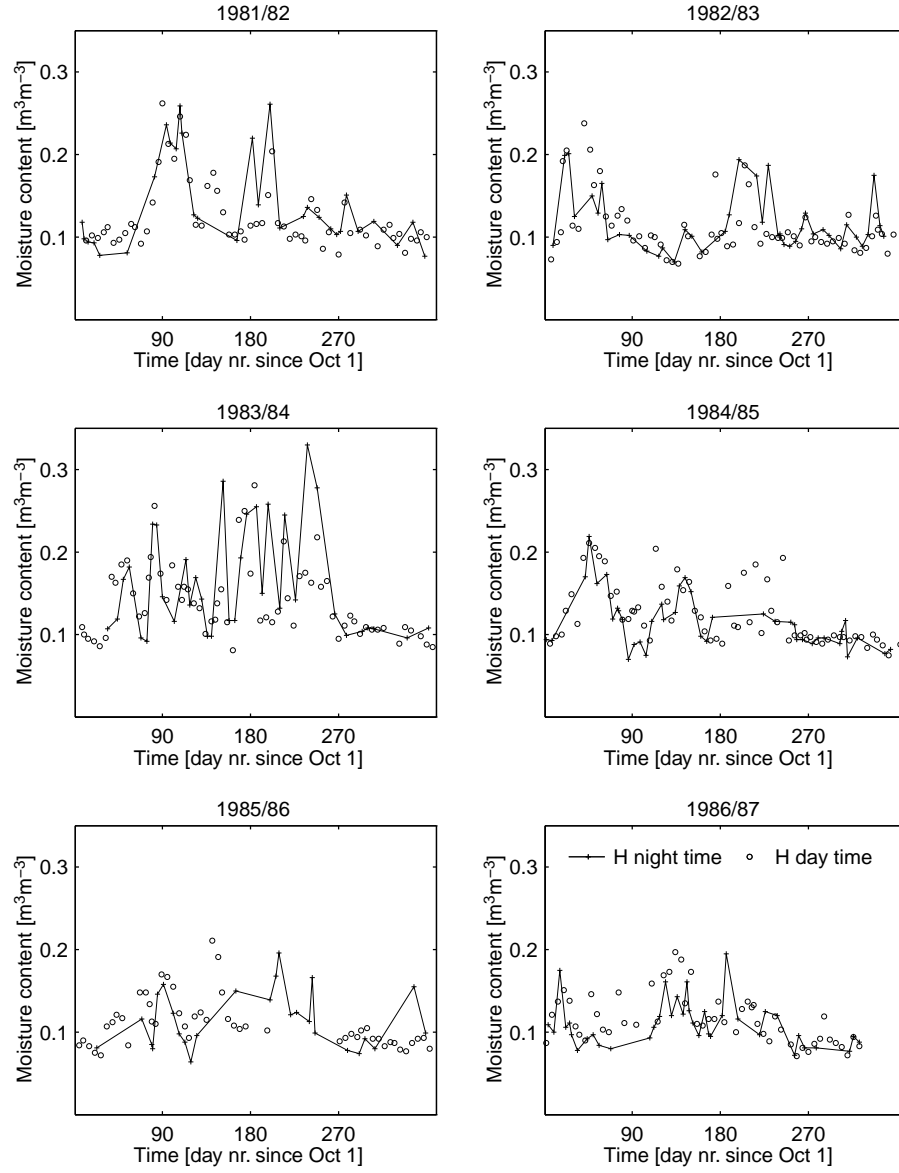|	
θ_{sat}	Satellite derived surface moisture $[\mathrm{m}^3\mathrm{m}^{-3}]$
Γ_{P}	Transmissivity $(\mathrm{P=H,V})$ $[-]$
S	Standard deviation
$\bar{\mathrm{X}}$	Arithmetic mean

Figure 3.15: *Satellite derived moisture content estimates for the period 1981/82 to 1986/87 at horizontal polarization using the NDVI–based vegetation correction approach.*
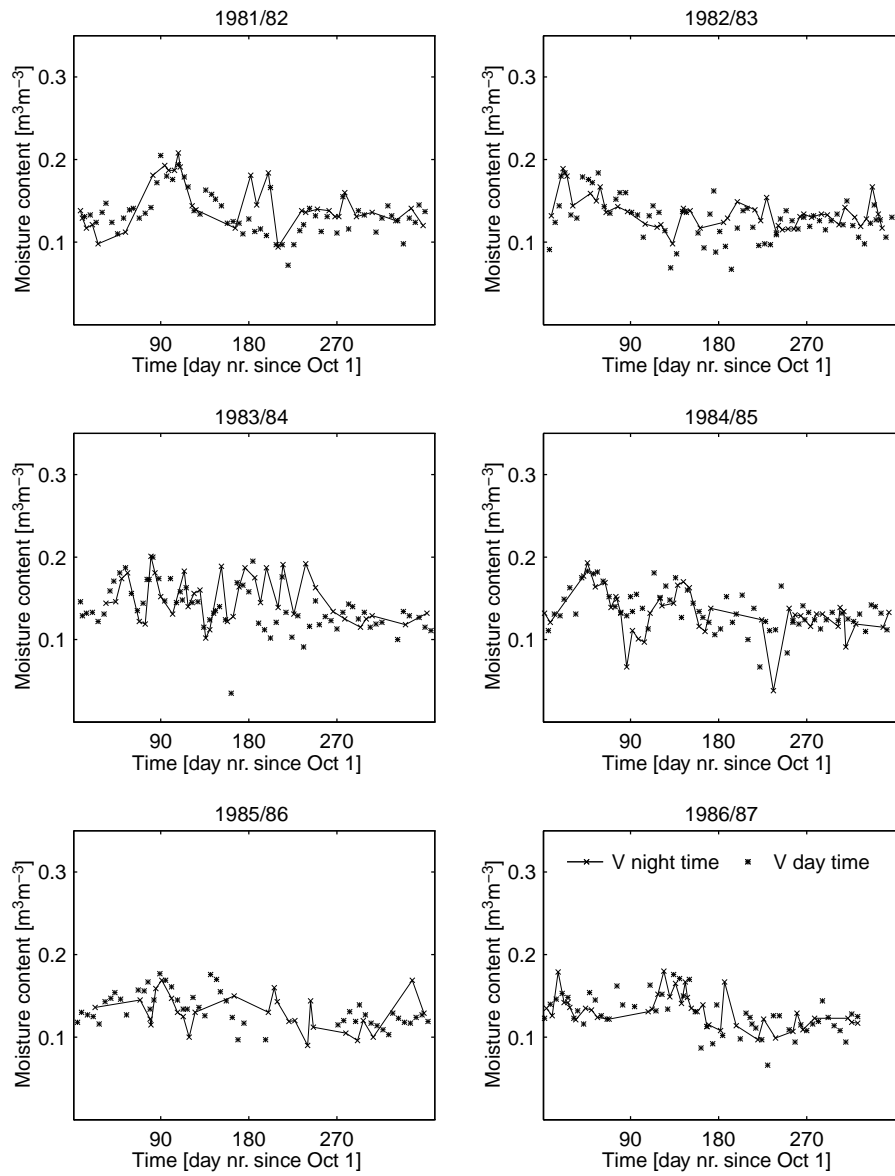
Figure 3.16: *Satellite derived moisture content estimates for the period 1981/82 to 1986/87 at vertical polarization using the NDVI–based vegetation correction approach.*

all periods to enable comparison of the derived surface moisture estimates over time.

As discussed in the previous section, the time series of satellite derived moisture content at night time are regarded the most reliable. The time series of satellite derived surface moisture at horizontal polarization indicate that the 1981/82 and the 1983/84 periods are relatively wet. The time series at day time horizontal polarization also reflect this pattern, although the 1984/85 period is also relatively wet. The difference appears to result from the data gap in the range of day nrs. 180–270 since October 1 1984 at night time (see Fig. 3.15). The time series of satellite derived surface moisture for the period 1983/84 indicates an exceptionally wet period with strongly alternating surface moisture conditions. The time series of satellite derived surface moisture for the 1983/84 period at vertical polarization is also relatively wet, although the range of moisture conditions is comparable to those of other periods. The time series of satellite derived surface moisture at vertical polarization appear to reflect a less clear pattern altogether. Apart from the 1981/82 period, which was studied in detail in the previous section, no seasonal cycle of the moisture conditions is recognized in the remaining periods. Furthermore, the range of moisture conditions is comparatively small. The deviating points of low moisture content, for example in the 1983/84 and the 86/87 periods, may indicate that the applied value of $\omega_V = 0.12$ is too high. The earlier described gap in the day time SMMR data (see Section 3.3.1) is visible in the 1985/86 period at horizontal polarization, but not at vertical polarization. Overall, the difference between wet and dry periods is smaller in day time.

Although only six periods are available and the term trend should preferably not be used in the present context, it should be noted that the last three periods at night time horizontal polarization are relatively dry.

3.5.5   Dual polarization vegetation correction approach

Introduction

As briefly introduced in Section 3.1, a second method may be used to correct for the contribution of vegetation to the microwave signal. This method is known as the dual polarization approach (see Section 3.4). By assuming a constant and seasonally independent ratio of the radiative transfer properties, A and B, the radiative transfer equation at horizontal and vertical polarization may be solved for surface moisture content and Γ_H. Similar to the previous vegetation correction approach, a fixed parameter matrix is defined for the 1981/82 period to analyse the sensitivity of the derived surface moisture content to parameter variation. The parameter values are set identical to those in the earlier defined parameter matrix (Section 3.5.4), except for the vegetation radiative transfer property parameter values. In the present analysis, the experimentally derived vegetation radiative transfer property parameter values are not directly applied, but adjusted to the findings in the previous section. The experimentally derived values of Γ range between 0.9–1.2, while an analysis of A using the NDVI–based

Table 3.16: *Results of sensitivity analysis for surface moisture estimates to parameter variation for the period 1981/82. Surface moisture is derived using the dual polarization vegetation correction approach.*

Parameter variation	θ_{sat}			Γ_H		
	$\bar{X}$	$\Delta\bar{X}$	S	$\bar{X}$	$\Delta\bar{X}$	S
						Day time
Set input matrix	0.148	–	0.028	0.51	–	0.053
$\Delta T_a=6$	0.183	24	0.024	0.52	2	0.052
$\Delta T_{ab}=9$, $\Delta T_{ac}=7$	0.195	32	0.028	0.52	2	0.052
$\Gamma_P=1$	0.027	82	0.013	1	92	–
A=0.72	0.143	3	0.022	0.52	2	0.059
A=0.88	0.152	3	0.036	0.51	0	0.047
$\omega_H=0.045$	0.156	5	0.026	0.51	0	0.055
$\omega_H=0.055$	0.140	5	0.030	0.52	2	0.051
B=0.45	0.139	6	0.029	0.53	4	0.049
B=0.55	0.156	5	0.027	0.50	2	0.056
$h=0.25$	0.155	5	0.028	0.53	4	0.056
$h=0.50$	0.162	9	0.028	0.56	10	0.060
$e_s + 10\%$	0.214	45	0.029	0.45	12	0.159
$e_s - 10\%$	0.051	66	0.016	0.64	25	0.069
						Night time
Set input matrix	0.160	–	0.034	0.52	–	0.056
$\Delta T_a=1$	0.166	4	0.034	0.52	0	0.057
$\Gamma_P=1$	0.030	81	0.015	1	92	–
A=0.72	0.153	4	0.026	0.52	0	0.064
A=0.88	0.168	5	0.043	0.51	2	0.049
$\omega_H=0.045$	0.168	5	0.031	0.52	0	0.059
$\omega_H=0.055$	0.153	4	0.036	0.52	0	0.054
B=0.45	0.152	5	0.035	0.53	2	0.052
B=0.55	0.168	5	0.032	0.51	2	0.060
$h=0.25$	0.167	4	0.034	0.54	4	0.060
$h=0.50$	0.175	9	0.033	0.56	8	0.064
$e_s + 10\%$	0.219	37	0.038	0.40	23	0.287
$e_s - 10\%$	0.062	61	0.029	0.64	23	0.050

θ_{sat}	Satellite derived surface moisture [m^{3}m^{-3}]
Γ_H	Vegetation transmissivity at hor. pol. [–]
S	Standard deviation
$\bar{X}$	Arithmetic mean
$\Delta\bar{X}$	Proportional change of $\bar{X}$ by parameter variation [%]

vegetation correction approach indicates a value of ~ 0.8. A B value of approximately 1 is derived for the 1.4 GHz measurements, while no consistent value could be determined from the 5 GHz observations. Analysis of the time series of derived moisture for the 1981/82 period in the previous section indicates B ≤ 0.5. In summary, the fixed parameter matrix features the following characteristics:

- $\omega_{\mathrm{H}} = 0.05$.

- A = 0.8.

- B = 0.5.

- ΔT_{a}=0 K, for both day and night time observations.

- $h = 0$.

- e_{s} is related to moisture content for both polarization directions by the polynomial fit curve to laboratory–determined data, as illustrated in Fig. 3.11.

To analyse the sensitivity of the surface moisture estimates to parameter variation, they are varied $+/-$ 10%. The results of the sensitivity analysis are presented in the following section.

Sensitivity analysis

Table 3.16 summarizes results of the sensitivity analysis of surface moisture estimates to parameter variation for the 1981/82 period. Fig. 3.18 and Fig. 3.19 present a selection of the parameter variations listed in Table 3.16. The radiative transfer equation at horizontal and vertical polarization angle is simultaneously solved for surface moisture content and Γ_{H}. The arithmetic mean of the derived values of $\Gamma_{\mathrm{H}}(\approx 0.5)$ corresponds with the lower range of the experimentally derived Γ_{H} values (see Fig. 3.6). The lower range of Γ_{H} values is, however, derived at a footprint average NDVI of 0.6 on the plot scale. The satellite footprint average NDVI does not exceed 0.4, as is shown in Fig. 3.12. Furthermore, the value of Γ_{H} remains below the values of Γ_{H} using the NDVI–based vegetation correction approach (see Table 3.15). Fig. 3.17 shows the Γ_{P}–NDVI relation for different values of A and B for the 1981/82 period. A decrease in B results in an increase of the minimum value of $\Gamma_{\mathrm{P}} > 0.45$. The linear dependency decreases however, making Γ_{P} almost independent of NDVI. A decrease in A increases Γ_{V}, while Γ_{H} is also slightly increased. Overall, a decrease in A and B results in values of Γ_{P} being more in accordance with the experimentally derived values. A linear dependency on NDVI is, however, not very evident.
Simultaneously, a decrease in A and B results in a downward shift of the time series of derived surface moisture. With $e_{\mathrm{cP}} = (1 - \omega_{\mathrm{P}})(1 - \Gamma_{\mathrm{P}})$, the increase in Γ_{V} leads to a decrease in the vegetation emissivity at vertical polarization, e_{cP} (see Eq. 3.6). Balanced by an increase in the bare soil emissivity, e_{sV}, this
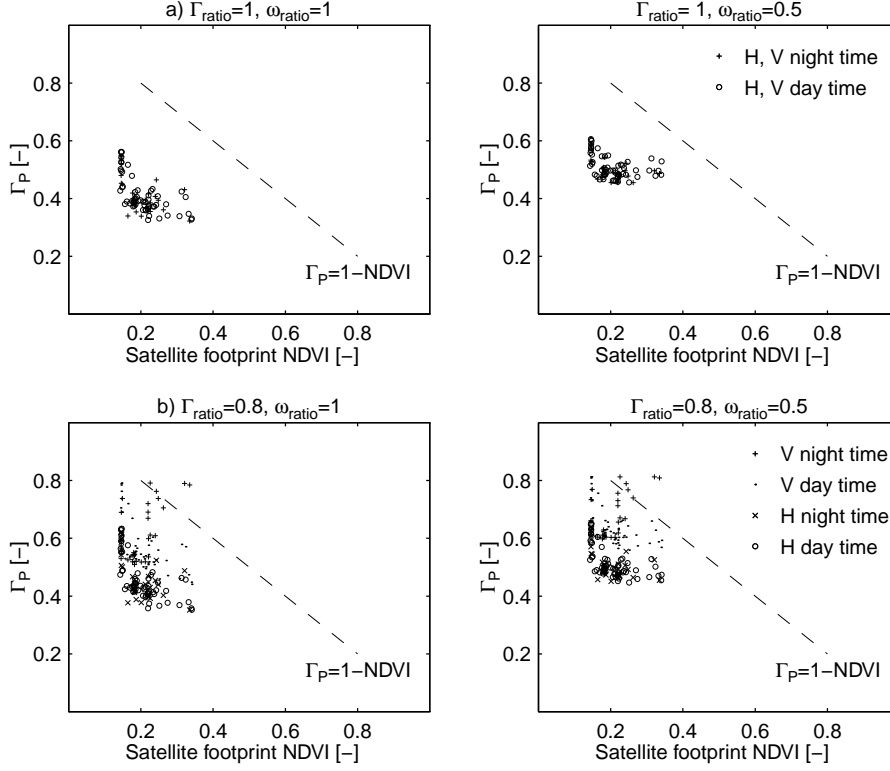
Figure 3.17: *The Γ_P–NDVI relation for different values of A and B for the period 1981/82. Γ_H is derived using the dual polarization vegetation correction approach.*

leads to a downward shift of the time series of satellite derived surface moisture at vertical polarization. Conversely, Γ_H does not change much by the decrease in A. The time series of satellite derived surface moisture at dual polarization therefore experiences a downward shift, mainly because of the increase in Γ_V.

Similarly, a decrease in B results in a decrease in e_{cV}. Balanced by an increase in the bare soil emissivity, e_{sV}, the time series of derived surface moisture shifts downward. Contrary to Γ_H however, ω_H is fixed. The time series of satellite derived surface moisture at dual polarization therefore experiences a downward shift because of the increase in ω_V alone.

With a constant B, a decrease in ω_H leads to a simultaneous decrease in ω_V. This leads to a decrease in e_c at both polarization angles. Balanced by a decrease in bare soil emissivity, e_{sP}, the time series of satellite derived surface moisture at dual polarization shifts upward.

Using the NDVI–vegetation correction approach, Γ_P is forced by NDVI. In turn, derivation of the surface moisture content is forced by Γ_P. Using the dual po-
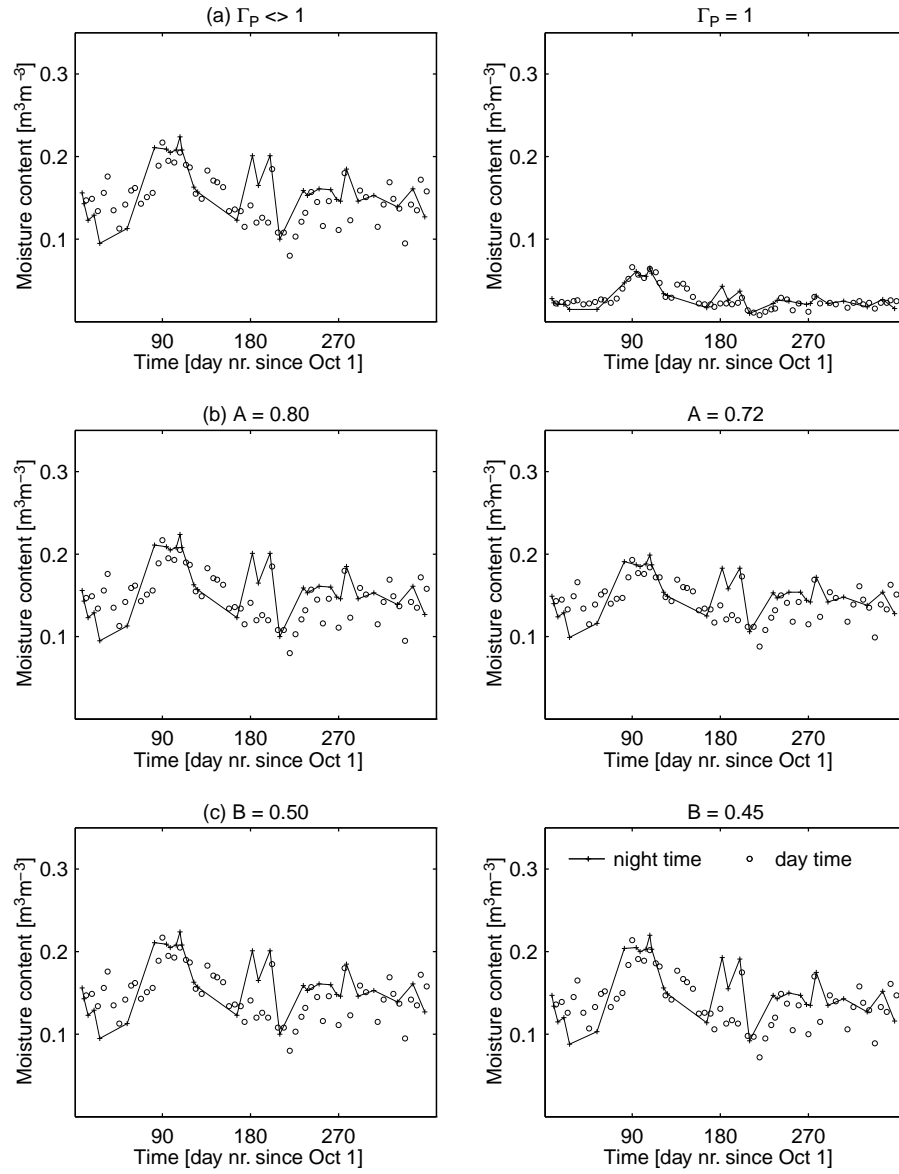
Figure 3.18: *Sensitivity of the satellite derived surface moisture content estimate for the 1981/82 period using the dual polarization vegetation correction approach to a) the vegetation effect correction b) A c) B.*
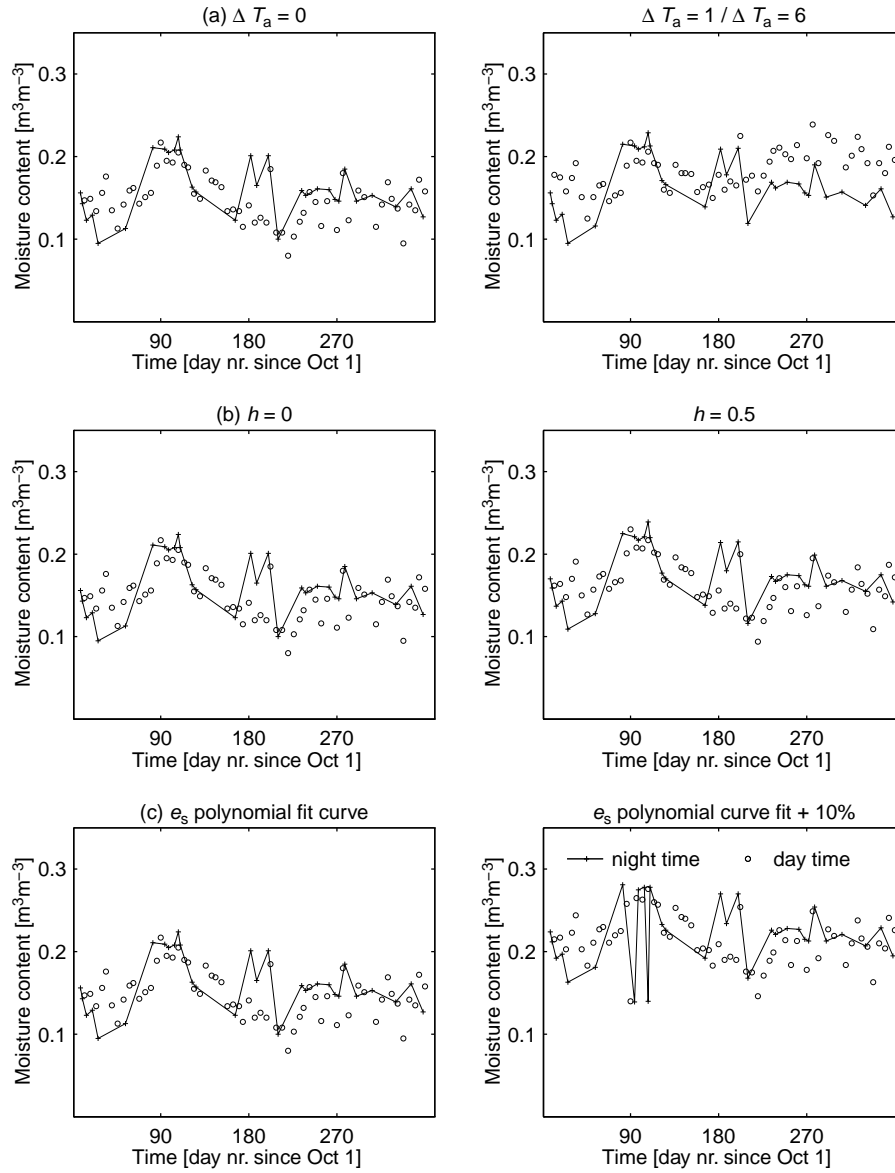
Figure 3.19: *Sensitivity of the satellite derived surface moisture content estimate for the 1981/82 period using the dual polarization vegetation correction approach to a) the air temperature adjustment to surface temperature b) the soil surface roughness c) the level of the bare soil emissivity curve.*

larization approach, Γ_H and moisture content are solved for simultaneously. As a result, they experience an increased interdependence, which is balanced by the ratio of the horizontal and vertical polarization radiative transfer equation. Variation in the ratioing parameters, A and B, changes the solution of the equation at one polarization angle, thus changing the solution of the equation at dual polarization. The ratio of vegetation radiative transfer properties therefore determines which polarization angle is dominant in the solution of the radiative transfer equation at dual polarization.

Fig. 3.19a shows that the air temperature adjustment to surface temperature results in an increase of derived surface moisture content in summer. With $\Delta T_a > 0$ K, the increase in derived surface moisture content corresponds with a decrease in vegetation emissivity, e_c, resulting in an increase in Γ_H. As discussed in Section 3.5.4, the time series of satellite derived surface moisture at night time are regarded the most reliable.

Fig. 3.19c illustrates that the derived surface moisture content is very sensitive to variation in the level of the bare soil emissivity curve. An increase in h increases bare soil emissivity. Consequently, the time series of inversely derived surface moisture experiences an upward shift, as illustrated in Fig. 3.19b. For all variations in bare soil emissivity, an increase in the derived moisture content is compensated for by a decrease in Γ_H.

Time series

Table 3.17 presents the results of satellite derived moisture content estimates for the period 1978/79 to 1986/87 using the dual polarization vegetation correction approach. Fig. 3.20 and Fig. 3.21 present the time series of derived surface moisture. The time series are derived using the earlier defined fixed parameter matrix input (see Section. 3.5.5). The parameter values are set identical for all periods to enable comparison of the moisture estimates over time.

As outlined earlier, the surface moisture content derived from night time data is considered the more reliable estimate. Table 3.17 indicates that the 1979/80, 1981/82 and 1983/84 periods are relatively wet. Corresponding wet periods are present in the time series of derived moisture in day time, although the 1978/79 period is also relatively wet. This may be explained by the relatively small number of night time data in the 1978/79 period. Table 3.17 further shows that the difference between wet and dry periods is smaller at day time than at night time. The here distinguished wet and dry periods correspond to those discerned using the NDVI–based vegetation correction approach. Although the number of periods has increased from six to nine compared to the previous satellite time series analysis (see Section 3.5.4), the detection of a trend still seems difficult. In analogy to the previous time series analysis, the relatively dry periods appear to represent an average. The number of relatively wet periods in the first half of the Nimbus–7/SMMR lifetime exceeds that in the second half.

Comparison of Fig. 3.21 to Fig. 3.16 reveals a close similarity. This indicates that the radiative transfer equation at vertical polarization dominates the solution of the radiative transfer equation at dual polarization. As discussed in

Table 3.17: *Satellite derived moisture content estimates for the period 1978/79 to 1986/87 using the dual polarization approach.*

Period	θ_{sat}		Γ_{H}	
	$\bar{\text{X}}$	S	$\bar{\text{X}}$	S
				Day time
1978/79	0.163	0.030	0.52	0.052
1979/80	0.153	0.025	0.50	0.042
1980/81	0.148	0.024	0.51	0.035
1981/82	0.148	0.028	0.51	0.053
1982/83	0.139	0.034	0.51	0 046
1983/84	0.153	0.030	0.52	0.052
1984/85	0.150	0.029	0.51	0.044
1985/86	0.148	0.027	0.52	0.046
1986/87	0.137	0.031	0.51	0.041
Mean	0.149	0.029	0.51	0.046
				Night time
1978/79	0.148	0.025	0.50	0.033
1979/80	0.160	0.024	0.48	0.029
1980/81	0.140	0.032	0.50	0.033
1981/82	0.160	0.034	0.52	0.056
1982/83	0.149	0.024	0.50	0.041
1983/84	0.165	0.031	0.52	0.050
1984/85	0.146	0.035	0.50	0.042
1985/86	0.142	0.031	0.50	0.038
1986/87	0.147	0.028	0.50	0.038
Mean	0.150	0.030	0.50	0.041

θ_{sat}	Satellite derived surface moisture $[\text{m}^3\text{m}^{-3}]$
Γ_{H}	Transmissivity, hor. pol. $[-]$
S	Standard deviation
$\bar{\text{X}}$	Arithmetic mean

the previous section, the ratio of vegetation radiative transfer parameters determines which polarization angle is dominant in the solution of the radiative transfer equation at dual polarization. The value of both A < 1 and B < 1 therefore determines that the radiative transfer equation at vertical polarization is dominant in the time series of derived moisture at dual polarization. As outlined in Section 3.5.4, the seasonal course in the time series of derived moisture at vertical polarization is less pronounced than at horizontal polarization (see Fig. 3.15 and Fig. 3.16). Furthermore, the time series of derived surface moisture at vertical polarization show some deviating points of low moisture content and a comparatively small range of moisture conditions. An increase in A and/or B increases the weight of the radiative transfer equation at horizontal polarization in the time series of derived surface moisture at dual polarization. As a result, the seasonality and the range of moisture conditions for the time series of derived surface moisture increases. An increase of B leads, however, to a decrease in Γ_P to values < 0.45 (see Fig. 3.17), which contradicts the experimentally derived values of Γ_P. An increase of A offers a compromise between the experimentally derived values of Γ_P and the range of moisture conditions of the time series of derived surface moisture at dual polarization. However, this contradicts the dual polarization vegetation correction approach and the NDVI–based vegetation correction approach. With A > 0.8 and/or B > 0.5, non–corresponding time series of surface moisture are derived at horizontal and vertical polarization using the NDVI–based vegetation correction approach.

3.6   Conclusions

Surface moisture content may be inversely derived from passive microwave satellite data by solving the radiative transfer equation. The equation is solved in two ways. The methods differ in the way the contribution of the vegetation to the satellite microwave signal is corrected for. One method uses NDVI to parameterize the vegetation transmissivity and is called the NDVI–based vegetation correction approach. The other uses constant ratios of the vegetation radiative transfer properties at two polarization angles and is called the dual polarization approach. In the present chapter both approaches are used to derive time series of surface moisture content for the West La Mancha area over a period of several years. The NDVI–based vegetation correction approach is applied for the period 1981/82 to 1986/87. The dual polarization vegetation correction approach is applied for the period 1978/79 to 1986/87.

To solve the radiative transfer equation for surface moisture content using the Nimbus/SMMR passive microwave data, values are assigned to the model parameters. The experimentally derived parameter values of the vegetation radiative transfer properties are applied. Air temperature data are adjusted to obtain bare soil surface and vegetation surface temperature. Bare soil emissivity is determined from dielectric constant laboratory measurements of a soil sample. The NDVI data form part of the AVHRR Land Composite Date set and are provided by the Goddard DAAC.
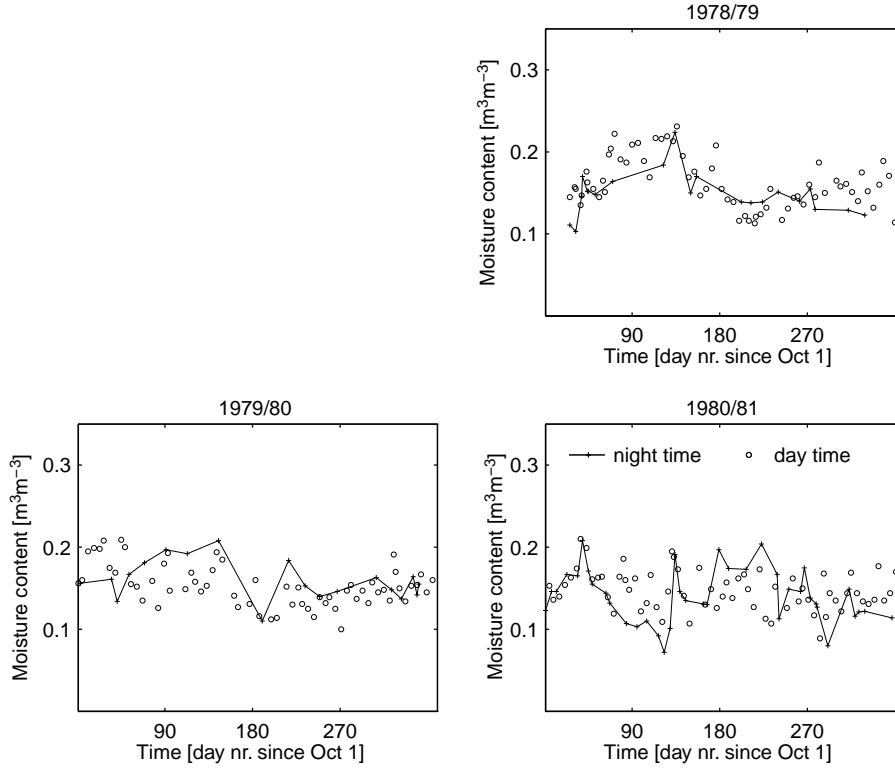
Figure 3.20: *Satellite derived surface moisture content estimates for the period 1978/79 to 1980/81 using the dual polarization approach.*

The derivation of surface moisture content using the NDVI–based vegetation correction approach under the assumption of identical parameter values at both polarization angles, results in non–corresponding levels for the time series of derived surface moisture content at horizontal and vertical polarization. It indicates that the vegetation radiative transfer properties at the horizontal and vertical polarization angle are not identical. Fitting of the time series of derived surface moisture at the two polarization angles indicates A $\approx$ 0.8 and B $\leq$ 0.5. These values do not correspond with the experimentally derived values of A and B of $\sim$ 1. Derivation of surface moisture content for the period 1981/82 to 1986/87 using the adjusted Γ_P–NDVI relation, distinguishes relatively wet and dry periods. At horizontal polarization, the time series of derived surface moisture presents a relatively large range of moisture conditions and a pronounced seasonal course, as opposed to that for derived surface moisture at vertical polarization. A time series analysis over a relatively short time prevents the detection of a (long–term) trend. The first half of the studied period contains two relatively wet periods however, while the second half contains none.
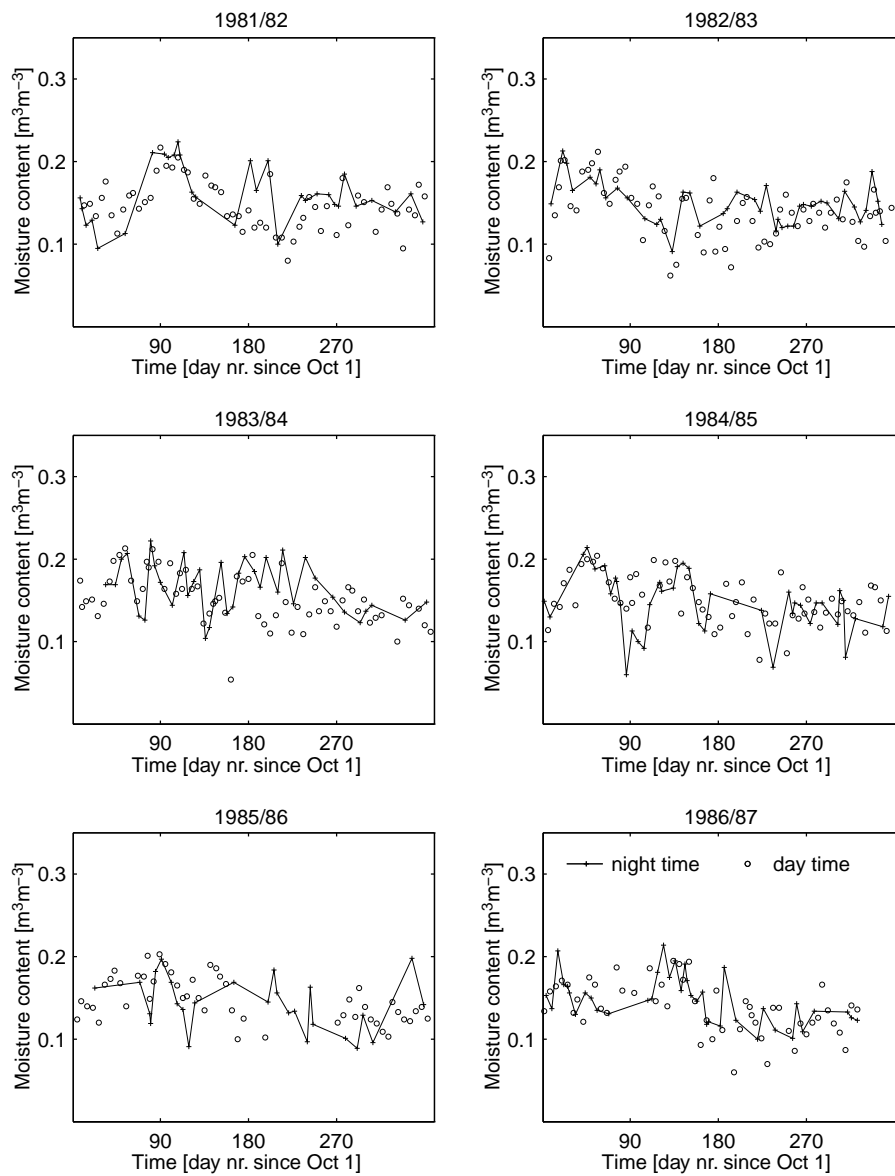
Figure 3.21: *Satellite derived surface moisture content estimates for the period 1981/82 to 1986/87 using the dual polarization approach.*

Application of A=0.8 and B=0.5 in the derivation of surface moisture content using the dual polarization vegetation correction approach, results in time series of moisture dominated by the radiative transfer equation at vertical polarization. This indicates that the ratio of vegetation radiative transfer properties determines which polarization angle is dominant in solution of the radiative transfer equation at dual polarization. The derivation of surface moisture content over the period 1978/79 to 1986/87 distinguishes relatively wet and dry periods. These correspond with those discerned using the NDVI–based vegetation correction approach. By analogy, the relatively wet periods appear to occur more frequently in the first half of the analysed time period. A pronounced seasonal course within the periods is absent however, because of vertical polarization transfer equation dominance at dual polarization. An increase of A and/or B increases the weight of the radiative transfer equation at horizontal polarization in the time series of derived surface moisture at dual polarization. As a result, the seasonal course and the range of moisture conditions for the time series of derived surface moisture increases. A > 0.8 and/or B > 0.5 results, however, in two non–corresponding levels of the time series of derived surface moisture content at horizontal and vertical polarization using the NDVI–based vegetation correction approach. An increase of A and/or B therefore contradicts the two vegetation correction approaches.

The application of adjusted air temperature to surface temperature, ΔT_{a}, results in a decrease of satellite emissivity. The effect is largest for the summer day time observations, resulting in an increase of the derived surface moisture content. The estimation of T_{s} by an increase of T_{a} seems, therefore, not to lead to an improved estimate of surface emissivity. Neglecting ΔT_{a}, the night time observations are considered to provide a more reliable surface moisture content estimate. The number of night time data is, however, only about half that of day time data. To neglect ΔT_{a} in day time leads to time series of derived moisture comparable to those at night time. This may indicate that the temperature of the emitting soil layer is cooler than the estimated T_{s}, and that $T_{\mathrm{a_{max}}}$ is a reasonable estimate of that temperature. Alternatively, it may indicate that the (day time) satellite observed T_{b} is contaminated by the cooler sky.

Apart from the correction for the vegetation effect, the time series of derived surface moisture content appears to be very sensitive to variation in the bare soil emissivity. The correctness of the use of the bare soil emissivity curve, derived from the laboratory determined dielectric properties of a single soil sample, is therefore uncertain. A dielectric mixing model could be used to evaluate the area representativeness of the derived emissivity curve. These models would, however, need an area representative input of soil textural composition. Uncertainty would therefore remain to some degree. Furthermore, the use of a single bare soil emissivity curve does not obstruct monitoring of the change in surface moisture conditions over time.

In the following chapter a soil moisture balance model is used to compute time series of topsoil moisture content on a regional scale. These time series of modeled topsoil moisture are compared to the time series of satellite derived surface moisture in Chapter 5. The comparison may provide more clarity on the value of

the time–invariant parameter in the radiative transfer equation. Furthermore, it may indicate which of the vegetation correction approaches is the more valid.

Chapter 4

Soil moisture model

4.1 Introduction

To reflect the research objectives and approach outlined earlier, it becomes necessary to develop a methodology to evaluate the relationship between the available remote sensing data sets on the one hand and the meteorological and hydrological data sets on the other. Such a methodology is necessary to properly assess the related parameters and processes, especially moisture content and downward moisture percolation, at an appropriate spatial and temporal scale.

The spatial scale is defined primarily by instrument resolution. The Nimbus–7/SMMR has a spatial resolution of approximately 150 km square, which makes it useful for regional application. Since daily meteorological data are available and satellite passive microwave observations over the study area are collected approximately once every four days (see Section 3.3), a daily time resolution is considered appropriate. Integration of modeled daily moisture percolation estimates over time enables comparison with independently derived regional groundwater recharge estimates.

This chapter presents the description and application of a soil moisture balance approach. Section 4.2 provides a description of the soil moisture balance model and Section 4.3 describes its implementation to the study area. Section 4.4 presents a sensitivity analysis of model results with parameter variation. Section 4.5 describes the model results.

4.2 Model description

The model structure for moisture transport in the subsoil, as illustrated in Fig. 4.1, is described by *Gouweleeuw et al.* [1996]. Vertical moisture flow is modeled according to the *Richards* [1931] equation for one–dimensional flow:
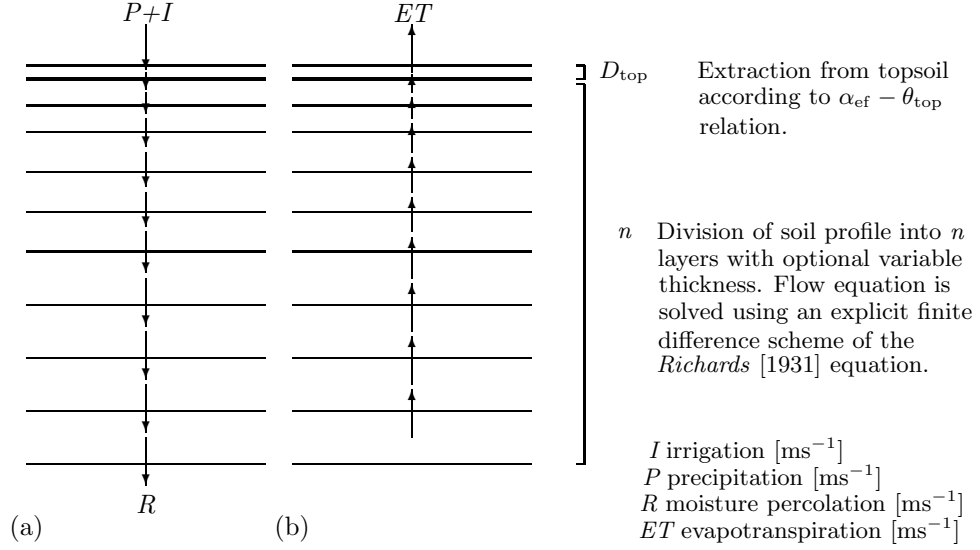
Figure 4.1: *Schematic representation of the soil moisture balance model a) wetting up b) drying down.*

$$\frac{\partial \theta}{\partial t} = \frac{\partial}{\partial z}\left[K_{\mathrm{h}}(\frac{\partial \psi}{\partial z} - 1)\right] \tag{4.1}$$

where θ is the volumetric water content [$\mathrm{m^3 m^{-3}}$], t is time [s], z is depth below the surface [m], K_{h} is the hydraulic conductivity [$\mathrm{ms^{-1}}$], and ψ is matric potential [m].

Matric potential and hydraulic conductivity are estimated as functions of soil moisture using the *Clapp and Hornberger* [1978] parameterization:

$$K = K_{\mathrm{s}}(\frac{\theta}{\theta_{\mathrm{s}}})^{2\bar{b}+3} \tag{4.2}$$

$$\psi = \psi_{\mathrm{s}}(\frac{\theta}{\theta_{\mathrm{s}}})^{-\bar{b}} \tag{4.3}$$

where θ_{s} is the saturation wetness [$\mathrm{m^3 m^{-3}}$], K_{s} is the conductivity at saturation [$\mathrm{ms^{-1}}$], and ψ_{s} is the matric potential at saturation [m]. $\bar{b}$ is a fitting parameter determined by soil texture. By changing the parameters the model is able to simulate a wide range of soil conditions. Table 4.1 summarizes the main characteristics of the *Clapp and Hornberger* soil types. θ_{fc} is the moisture content at field capacity [$\mathrm{m^3 m^{-3}}$], where field capacity is defined as the moisture content at $\psi \approx 316$ m (pF=2.5). θ_{wp} is the moisture content at wilting point (pF=4.2). An explicit finite difference method [*Camillo et al.*, 1983] is used to solve the

Table 4.1: *Soil types of the* Clapp and Hornberger *classification and their main characteristics.*

Soil type	θ_{s}	θ_{fc}	θ_{wp}	ψ_{s}	K_{s}	b
Sand	0.385	0.172	0.065	-0.121	176.0	4.05
Loamy sand	0.410	0.182	0.074	-0.090	156.3	4.38
Sandy loam	0.435	0.252	0.113	-0.218	34.1	4.90
Silt loam	0.485	0.373	0.178	-0.786	7.2	5.3
Loam	0.451	0.318	0.154	-0.478	7.0	5.39
Sandy clay loam	0.420	0.301	0.174	-0.299	6.3	7.1
Silty clay loam	0.477	0.360	0.217	-0.356	1.7	7.75
Clay loam	0.476	0.394	0.249	-0.630	2.5	8.52
Sandy clay	0.426	0.318	0.218	-0.153	2.2	10.4
Silty clay	0.482	0.403	0.277	-0.490	1.0	10.4
Clay	0.482	0.402	0.286	-0.405	1.3	11.4

θ_{s}	Saturation wetness [$\mathrm{m}^3\mathrm{m}^{-3}$]
θ_{fc}	Moisture content at field capacity [$\mathrm{m}^3\mathrm{m}^{-3}$]
θ_{wp}	Moisture content at wilting point [$\mathrm{m}^3\mathrm{m}^{-3}$]
ψ_{s}	Matric potential at saturation [m]
K_{s}	Conductivity at saturation [$10^{-6}\mathrm{ms}^{-1}$]
b	Fitting parameter [-]

moisture flow equation. Integration with depth is performed by dividing the soil into n layers with optional variable thickness, small enough to enable θ between two adjacent layers to be adequately represented. The time integration satisfies stability and convergence criteria and is realized by automatically adapting the time step to changing conditions of moisture diffusion.

The solution to the flow equation requires that the soil moisture balance model is initialized with either a moisture flux or moisture content at the upper and lower boundary of the soil profile. For the bottom layer four options are available: a constant moisture content, a downward moisture flux equal to the hydraulic conductivity of the bottom layer (i.e. free drainage), a zero flux, or a constant downward flux. In the present analysis the downward moisture flux is set equal to the hydraulic conductivity.

The moisture flux at the air/soil interface is described by:

$$D_{\mathrm{top}}\frac{\mathrm{d}\theta_{\mathrm{top}}}{\mathrm{d}t} + R = -ET + P + I \qquad (4.4)$$

where θ_{top} is the moisture content in the topsoil [$\mathrm{m}^3\mathrm{m}^{-3}$], D_{top} is the thickness of the topsoil [m], R is the downward vertical moisture percolation [ms^{-1}], ET is evapotranspiration [ms^{-1}], P is precipitation [ms^{-1}], I is irrigation [ms^{-1}].

The basis for the calculation of evaporative losses is the *Priestley–Taylor* potential evapotranspiration (*PET*) model [*Priestley and Taylor*, 1972]. The *PET* model relates evapotranspiration to topsoil moisture. The choice for the *Priestley–Taylor* model is motivated by the key role of topsoil moisture in the

followed research approach. Furthermore, the model is very useful for semi–arid land application at the spatial and temporal resolution of the satellite sensor with limited climate data. The evaporative loss from the topsoil is described by:

$$ET = \alpha_{\text{ef}} \frac{(R_{\text{n}} - G)}{\lambda_{\text{v}}} \left(\frac{\Delta}{\Delta + \gamma} \right) \tag{4.5}$$

where R_{n} is the net radiation $[\text{Wm}^{-2}]$, G is the soil heat flux $[\text{Wm}^{-2}]$, Δ the slope of the saturated vapour pressure curve, λ_{v} is latent heat of vaporization $[\text{Jm}^{-3}]$, and γ is the psychrometer constant $(0.66 \text{ mbarK}^{-1}])$. The term α_{ef} is an empirical constant, which is determined by fitting the equation to known data. It was found to equal 1.26 for a well–watered grass covered surface transpiring at potential level [*Priestley and Taylor*, 1972]. *Owe and Van de Griend* [1990] modified this concept, where α_{ef} referred to as the evaporative fraction (ef), is dynamic and defined as a function of available topsoil moisture. They also demonstrated that α_{ef} is dependent on surface cover conditions and the thickness of the topsoil layer (D_{top}), which can be defined in accordance with experimental conditions. θ_{top} is the normalized soil moisture [–] and is defined as a ratio of the field capacity. It was found that the relationship between α_{ef} and θ_{top} may be described for a bare soil surface by:

$$\alpha_{\text{ef}} = a + b \exp(c\theta_{\text{top}}) \tag{4.6}$$

where a, b and c are fitting parameters [–] which are optimized by fitting the model to experimental data. A similar relationship for vegetated surfaces is reported by *Davies and Allen* [1973]:

$$\alpha_{\text{ef}} = d \left[1 - \exp(-e\theta_{\text{top}}) \right] \tag{4.7}$$

where d and e are again fitting parameters [–].
In the case of a bare soil surface, α_{ef} reacts immediately to changes in topsoil moisture. In the case of a vegetation–covered soil, α_{ef} remains more or less constant for an extended range of surface moisture conditions. One must realize however, that while the soil moisture for both of the above examples was measured in the topsoil profile, most of the moisture loss in the vegetated case occurs from the root zone and not exclusively from the topsoil profile. Fig. 4.2 depicts both examples, i.e. a bare soil surface and a vegetation–covered surface. The example curves correspond to the above described relations respectively reported by *Owe and Van de Griend* [1990] and *Davies and Allen* [1973] as a best fit to experimental data.

Table 4.2: *Model input and output parameters.*

Time–invariant input parameters	
Evaporation fraction curve	α_{ef} [–]
Soil hydraulic properties	θ_{s} [m^{3}m^{-3}], θ_{fc} [m^{3}m^{-3}], ψ_{s} [m]
	θ_{wp} [m^{3}m^{-3}], K_{s} [ms^{-1}], $\bar{b}$ [-]
Topsoil depth	D_{top} [m]
Soil profile depth	– [m]
Daily input parameters	
Net radiation	R_{n} [Wm^{-2}]
Soil heat flux	G [Wm^{-2}]
Air temperature	T_{a} [K]
Precipitation	P [ms^{-1}]
Irrigation	I [ms^{-1}]
Daily output parameters	
Topsoil moisture content	θ_{5cm} [m^{3}m^{-3}]
Evapotranspiration	ET [ms^{-1}]
Recharge/downward moisture percolation	R [ms^{-1}]

4.3 Model implementation

4.3.1 Introduction

The implementation of the above described model to the West La Mancha region first requires the assessment of the model input parameters listed in Table 4.2. This is described in the present section. Most of the parameter values assigned here are the result of point measurements conducted during the EFEDA campaign of May–June 1991 (see Section 1.1.2). Subsequent regional implementation of these parameters requires some assumption as to their representativeness. A sensitivity and error analysis of model results comparing the values of these parameters is therefore considered appropriate. This is described in Section 4.4.

4.3.2 Calibration of modified *Priestley-Taylor PET* concept

Derivation of the evaporative fraction curve

Regional implementation of an adapted *Priestley–Taylor PET* concept to the West La Mancha study area warrants an assessment of the individual $\alpha_{\text{ef}} - \theta_{\text{top}}$ curve for each surface cover type analysed. Bare soil surfaces and surfaces fully covered by deep rooted agricultural or semi–natural vegetation, e.g. vines, trees and shrubs, may be regarded as end–members of this family of curves (see Fig. 4.2). Surfaces fully or partly covered by shallow rooted agricultural crops, e.g. maize, barley and vetch, and semi–natural grassland, may represent intermediate curves.

As outlined earlier in Section 3.2.4, the penetration depth of passive microwave radiation is considered not to exceed a few tenths of a wavelength under even
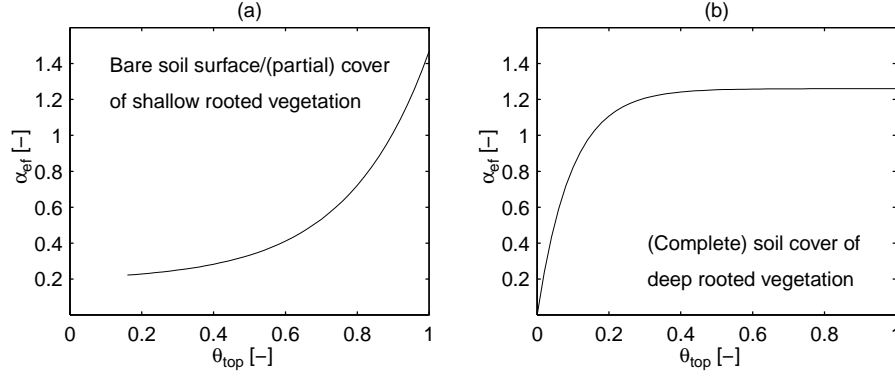
Figure 4.2: *Relation between α_{ef} and θ_{top} for a a) bare soil surface/(partial) cover of shallow rooted vegetation and b) complete soil cover of deep rooted vegetation.*

the most optimum conditions. The analyses carried out in the previous chapter relate to 6.6 GHz satellite passive microwave data, i.e. $\lambda \approx 4.5$ cm. This implies that a minimum topsoil thickness, D_{top}, is considered to enable comparison of modeled topsoil moisture content with satellite derived surface moisture content.

Data from two sites which are representative of the predominant agriculture types in the la Mancha area are used. These are a partly irrigated area in the East la Mancha region near the village of Barrax and a dry cultivation area in the West La Mancha region near the town of Tomelloso (see Fig. 2.1). Four test fields with corresponding moisture content monitoring observations at 5 cm soil depth and surface energy flux measurements are selected. These are data from two test fields with surface covers of vetch and vines at the Tomolloso site and two fields with surface covers of irrigated maize and bare soil at the Barrax site. Daily mean and total net radiation, latent heat flux, soil heat flux, air temperature and precipitation/irrigation are analysed for the behaviour of α_{ef}, which is subsequently plotted against field–average 5 cm soil depth θ_{top}. Due to the sampling method, the moisture data from the Tomelloso and the Barrax sites do not entirely relate to the same soil depth. Moisture content at the Tomelloso test field was determined gravimetrically, while at the Barrax site it was measured using a TDR probe. The moisture content at the Tomelloso fields therefore represents a more averaged value over the sampling depth. The ground measurements at the test fields were conducted by the Institute of Hydrology (vines and vetch, Tomelloso), CNRM Toulouse (bare soil, Barrax) and the University of Karlsruhe (irrigated maize, Barrax). Further specifications of measuring procedures and equipment can be found in *Bolle and Streckenbach* [1992] and *Bolle and Streckenbach* [1993].

Due to irrigation at the Barrax site, the range of surface moisture conditions (and the associated surface energy fluxes) encountered there do not correspond
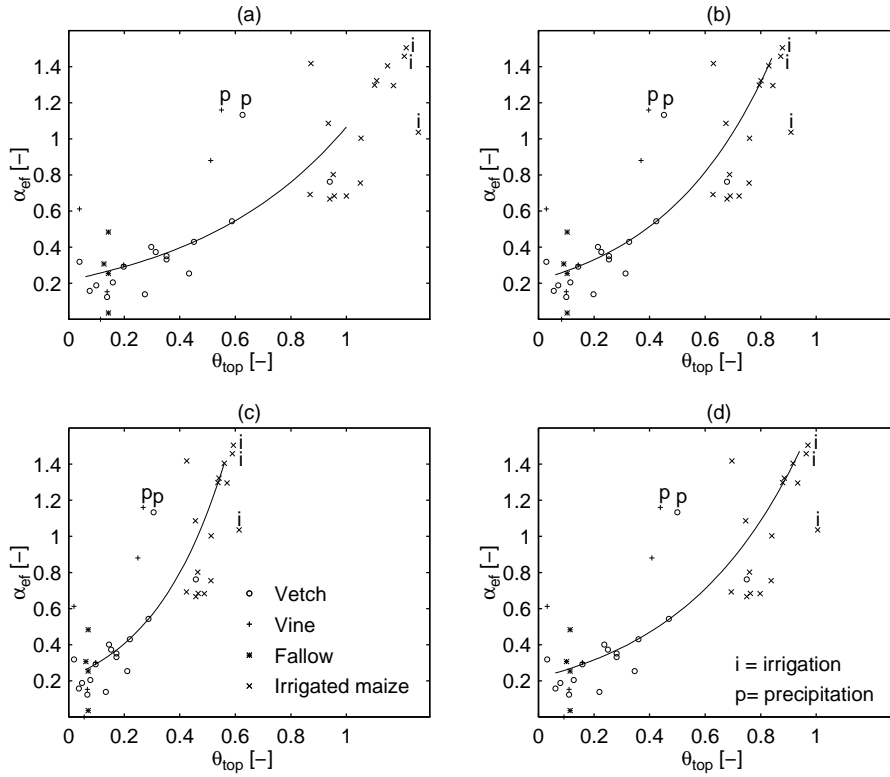
Figure 4.3: *Derived area–average 5 cm depth $\alpha_{ef} - \theta_{top}$ curve with θ_{top} normalized for a) the loamy sand soil type b) the sandy loam soil type c) the silt loam soil type d) the soil type characterized by the median of the experimentally derived Mualem–Van Genuchten (MVG) parameters. Data points marked with i or p relate to days of observation coinciding with irrigation and rainfall, respectively.*

with the range of moisture conditions encountered at the dry farmed site near Tomelloso. At the former site, moisture conditions are constantly maintained at near field capacity, whereas at the latter site surface moisture conditions are always at near–wilting point conditions. Consequently, none of the measured moisture series represent a full dry–down cycle from near–saturation to wilting point by themselves. As a result, defining an evaporative fraction curve for an individual surface cover is difficult. An areal averaging of the data sets provides a full range of surface moisture conditions however and permits assessment of an area–averaged evaporative fraction curve.

Fig. 4.3 illustrates the area–averaged evaporative fraction curve for 5 cm soil depth derived as a best fit of Eq. 4.6 to experimental field data (n=36). As discussed earlier, soil moisture content is normalized as a fraction of field capacity, where θ_{fc} is determined from Table 4.1. A particle size distribution analysis of 86 samples over a 50 cm soil profile depth reported by *Droogers et al.* [1993] is used to determine the predominant soil type at the Barrax and Tomelloso test sites, according to the *Clapp and Hornberger* (CH) classification. Further analysis indicates that the sandy loam and silt loam soil types are predominant in the reported soil sample population. Additionally, an area–averaged estimate of θ_{fc} is derived from an analysis of soil hydraulic parameters reported by *Droogers et al.* [1993]. The *Mualem–Van Genuchten* [*Van Genuchten*, 1980] parameters for 142 soil samples were determined using laboratory multi-step outflow measurements. From these parameters the median is determined in order to obtain area–averaged moisture retention and conductivity curves (see Section 4.3.3). θ_{fc} for the retention curve characterized by the median of the experimentally derived *Mualem–Van Genuchten* (MVG) parameters is 0.228 m^3m^{-3}.

Fig. 4.3 shows that the soil sample moisture content of the maize field is relatively high, due to irrigation. Some of the corresponding α_{ef} values exceed the 1.26 value *Priestley and Taylor* found for a grass–covered surface with freely available soil water. Reported values of α_{ef} indicate its maximum value does not equal 1.26 for all surfaces [*Owe and Van de Griend*, 1990]. The moisture content in the maize field does not appear to exceed a maximum threshold value. As mentioned earlier, this may indicate the maize field is irrigated to the extent that a moisture surplus is gravitationally drained to deeper soil layers. Thus the maximum threshold moisture content value provides an indication of θ_{fc}. Fig. 4.3b,d show that this value corresponds to the θ_{fc} for the sandy loam soil type and the soil type characterized by the median of the experimentally determined MVG parameters.

The concave shape of the derived $\alpha_{\text{ef}} - \theta_{\text{top}}$ curve indicates that loss of moisture at the analysed fields primarily occurs from the topsoil. Some outlying data points plot above the derived evaporative fraction curve however. As these points relate to vegetation–covered surfaces, a best fit curve of convex shape through these points may be considered as well. Closer analysis reveals, however, that the outlying points relate to a single storm. While there is a time lag of soil moisture following precipitation, the latent heat flux and therefore α_{ef}, is increased directly. In the observed case evaporation probably occurs primarily from water ponded on the soil surface. This implies that the derived evaporative

fraction curve appears to represent a 'drying' curve. Application of the curve in the case of rainfall seems to lead to an underestimation of *ET*. An adjustment for the estimation of *ET* on days of rainfall therefore seems appropriate. This will be further discussed in Section 4.4.

The vine field data point plotted directly under the precipitation data points relates to one day after the rain storm. While the latent heat flux has dropped off, moisture content is still level. The corresponding vetch field data point (of the next day) has dropped back on the evaporation fraction curve with a decreased moisture content. This may indicate that the deep rooted vines provide the surplus of latent heat without depleting the topsoil. This data point may then relate to an $\alpha_{\text{ef}} - \theta_{\text{top}}$ curve of convex shape. The number of data to construct such a curve is small however (n=3). Furthermore, it may be argued that the effect of transpiration by deep rooting vegetation on the θ_{top} of shallow soil depth is relatively small, as moisture loss then primarily occurs from the root profile. For the purpose of comparing θ_{top} with satellite derived surface moisture estimates, the derivation of a separate $\alpha_{\text{ef}} - \theta_{\text{top}}$ curve for deep rooted vegetation is therefore not required. However, transpiration by deep rooted vegetation forms a component of the regional water balance (see Eq. 5.1). As outlined in Section 1.2, closure of the regional water balance is of primary importance to the present study, as it is used as a control on the soil moisture balance results. An alternative estimation of transpiration by deep rooting vegetation is therefore necessary. This will be discussed in the following section.

Contrary to rainfall on the dry farmed fields, in one case α_{ef} is not immediately increased by irrigation on the maize field. Although the latent heat flux is immediately raised, the evaporative fraction value remains low because of the relatively high extra energy released from the soil ($-G$). This is also shown in Fig. 4.5, which depicts the G/R_{n} ratio for all the data analysed here. In the observed cases the ratio of the amount of precipitation to irrigated water is $\sim$ 1:10.

Table 4.3: *Regional surface cover fraction distribution in the West La Mancha area (after Thornes et al. [1996]).*

Surface cover type	1975/76	1986/87	1987	1987/88	1988	1990
Bare soil	0.05	0.03	0.04	0.03	0.04	0.06
Semi–natural vegetation	0.26	0.23	0.20	0.18	0.21	0.21
Summer cropping	0.02	0.03	0.03	0.04	0.03	0.03
Spring cropping	0.43	0.43	0.39	0.44	0.51	0.36
Permanent agriculture	0.24	0.27	0.33	0.28	0.19	0.32
Unclassified	0.00	0.01	0.01	0.03	0.02	0.02

Transpiration by deep rooted vegetation

In the present study, field data to evaluate the evaporative fraction curve are available almost exclusively for agricultural crops. Table 4.3 presents regional surface cover estimates from Landsat Multi–Spectral Scanner (MSS) image clas-

sification for the period of 1975–1990, reported by *Thornes et al.* [1996]. Images
have been extracted for specific target days and have a 200 m resampled spatial
resolution. The table shows that the average regional surface cover fraction of
agricultural crops is over 70%. Fields of permanent agriculture, such as vine-
yards and olive groves, constitute about one third of this fraction. The remain-
der of the agricultural fraction consists of shallow rooted crops, which relate to
the above derived evaporation fraction curve. Transpiration rate estimates for
deep rooted permanent agriculture, particularly vines, is reported by various
authors for the Tomelloso site. These estimates vary from about 1 mmday^{-1}
[*Oliver and Sene*, 1992; *Sene*, 1994] to 0.33 mmday^{-1} [*Ogink-Hendriks et al.*,
1995] and 0.44 mmday^{-1} [*Bromley et al.*, 1996]. The estimates vary in mea-
suring period, local conditions and method of investigation. The extension of
an intermediate transpiration rate of 0.5 mmday^{-1} over the entire vine growing
season (June–October) would imply a moisture loss of about 75 mm.

The deep rooted traditional agricultural crops (see Section 2.2) are considered to
have adjusted to the prevailing natural conditions by adapting to an economic
water consumption. In this way they relate to the semi–natural vegetation. The
EFEDA campaign does not provide data on the transpiration rate of deep rooted
semi–natural vegetation. For practical convenience therefore, it is assumed equal
to the vine transpiration rate. The extension of the assumed transpiration rate
over the growing season of semi–natural vegetation (March–October) implies a
water consumption of around 120 mm. In 1990 permanent agriculture (32%)
and semi–natural vegetation (21%) comprised about half of the regional surface
total (see Table 4.3). An estimate of the regional transpiration rate by deep–
rooted vegetation over the growing season would then be in the order of 50 mm,
i.e. slightly over 10% of the area–average annual precipitation over the period
of 1975–1991 (see Table 4.7). Although the relative proportion of the regional
surface cover fraction of permanent agriculture and semi–natural vegetation has
changed between 1975–1991, the sum of the fractions has remained at an ap-
proximately constant level of 50%. The estimated area–averaged transpiration
total also remains at an approximately constant level as well. In 1988, however,
a temporarily drop is noted in the sum of the deep rooted vegetation fractions
to 0.4, resulting in a area–averaged transpiration estimate of 40 mm. Overall,
the transpiration estimate may be regarded as an indication of the magnitude
of error in the regional water balance closure.

4.3.3   Soil hydraulic properties

As outlined in Section 4.2, the soil hydraulic properties are modeled using the
Clapp and Hornberger (CH) parameterization. Since this is able to simulate a
wide range of soil conditions (see Table 4.1), its straight–forward parameter-
ization makes it a practical tool for numerical computer modelling purposes.
Alternatively, the *Mualem–Van Genuchten* (MVG) parameterization accurately
describes soil hydraulic properties in a closed–form curve. The latter parameter-
ization may be used to fit retention and conductivity curves to measured sample
data. Matric potential and hydraulic conductivity [*Van Genuchten*, 1980] are

described by:

$$\Theta = [1+ \mid \alpha_{\mathrm{mvg}}\psi_{\mathrm{mvg}} \mid^{\mathrm{n_{mvg}}}]^{-\mathrm{m_{mvg}}} \tag{4.8}$$

$$K_{\mathrm{mvg}} = K_{\mathrm{s-mvg}}\Theta^{\mathrm{L}} \left[1 - (1 - \Theta^{1/\mathrm{m_{mvg}}})^{\mathrm{m_{mvg}}}\right]^2 \tag{4.9}$$

where

$$\Theta = \frac{\theta - \theta_{\mathrm{r}}}{\theta_{\mathrm{s}} - \theta_{\mathrm{r}}} \tag{4.10}$$

and

$$\mathrm{m_{mvg}} = 1 - \frac{1}{\mathrm{n_{mvg}}} \tag{4.11}$$

where $\alpha_{\mathrm{mvg}}[\mathrm{cm}^{-1}]$, $\mathrm{n_{mvg}}$ [–] and L [–] are empirical parameters, θ_{r} is residual moisture content [$\mathrm{m^3m^{-3}}$], θ_{s} is saturated moisture content [$\mathrm{m^3m^{-3}}$] and $K_{\mathrm{s-mvg}}$ is saturated hydraulic conductivity [$\mathrm{cmhr^{-1}}$].

As mentioned earlier, *Droogers et al.* [1993] determined the MVG parameters of 142 soil samples at the Tomelloso and Barrax site using laboratory multi–step outflow measurements. Table 4.4 lists the statistical characteristics of the population of determined MVG parameters. The most shallow soil sample is taken at 5–10 cm depth ($\bar{\mathrm{d}}_{\mathrm{s}}$=7.5 cm), while the deepest sample is taken at 55–60 cm soil depth ($\bar{\mathrm{d}}_{\mathrm{s}}$=57.5 cm). All populations of the MVG parameters are skewed to some degree. The largest variation (S> $\bar{\mathrm{X}}$) occurs in the population of parameters related to hydraulic conductivity, $K_{\mathrm{s-mvg}}$ and L. Since all populations are skewed, the median value is regarded as the best measure of central tendency. The median MVG values are used to derive area–averaged moisture retention and hydraulic conductivity curves. Fig. 4.4 presents the respective curves together with several soil types of the CH classification. The laboratory multi–step outflow measurements were conducted for the ψ range 0–1000 cm. As a result, the moisture retention and soil hydraulic conductivity curves characterized by the median of the determined MVG parameters do not extend outside this range. The applicability of the curves for the purpose of modelling is hereby restricted. Fig. 4.4 demonstrates that the median MVG curves are on average most closely related to the sandy loam curves in the CH classification. In the dry moisture range however, the median MVG moisture retention curve relates to the silt loam CH curve, while in the wet moisture range it relates to the sand and loamy sand CH curves. These similarities are mirrored for the median MVG hydraulic conductivity curve.

4.3.4 Rooting depth and soil profile

As described in Section 2.3.2 the presence of a calcareous crust, i.e *caliche*, just below the surface is widespread in the central plain of the region. The depth

Table 4.4: *Statistical properties of the population of determined* Mualem–Van Genuchten *parameters by Droogers et al. [1993].*

Parameter	X̄	Mode	Median	S	Skewness
$\bar{z}_s$	21.1	12.0–12.5	21.8	10.1	0.876
α_{mvg}	0.0520	0.0200–0.0300	0.0333	0.0560	0.482
n_{mvg}	1.71	1.40–1.50	1.60	0.509	0.519
$K_{s-\mathrm{mvg}}$	2.62	0–0.200	0.628	3.63	0.694
θ_{r}	0.164	0.140–0.150	0.173	0.0705	0.0507
		0.170–0.180			
θ_{s}	0.403	0.400–0.410	0.398	0.0292	−0.0714
L	−0.508	−2.00–1.95	−0.714	1.26	1.16

$\bar{z}_s$	Mean of sampling depth interval [cm]
α_{mvg}	Empirical parameter [–]
n_{mvg}	Empirical parameter [–]
$K_{s-\mathrm{mvg}}$	Saturated hydraulic conductivity [cmhr^{-1}]
θ_{r}	Residual moisture content [m^{3}m^{-3}]
θ_{s}	Saturated moisture content [m^{3}m^{-3}]
L	Empirical parameter [–]
X̄	Arithmetic mean
S	Standard deviation

of the crust is generally between 0.1–1 m below the surface. Infiltrating water may penetrate or pass the calcareous horizon through fractures to reach the underlying lithology. Shallow rooted crops cannot take water from the *calciche* crust and water drained to this layer may be considered as recharge. Vine roots are, however, able to penetrate the caliche layer and to take water from it. Thus the vine is well adapted to survive the dry environmental conditions. In the perspective of recharge, knowledge of vine rooting depth is important. *Ogink-Hendriks et al.* [1995] observed a maximum root density between 0.2–0.4 m below the surface in a dug pit near Tomelloso, decreasing regularly to a depth of 0.8 m. *Bromley et al.* [1996] found an influence of moisture loss by vine root extraction up to 1–2 m below the surface in neutron probe observations, also near Tomelloso. Rooting depth of semi–natural vegetation in the basin boundary hills near Belmonte may be up to several metres [*Imeson and Bergkamp*, 1996]. Soil depths in these parts are reported to range from 0.1 to over 1.5 m, dependent on the position of the soil on the hillslope (top/valley). While most soils contain stones, no calcareous crust is present in these parts; the soils are directly on top of the underlying lithology.

As described in Section 4.3.2, no relation could be established between observed rates of transpiration by deep rooted vegetation and topsoil moisture. In the present study therefore, transpiration by deep rooted vegetation is estimated and not modeled. Consequently, for modelling purposes the soil profile is not extended to include the root zone, but restricted to the soil depth on top of the *caliche* layer or underlying lithology. The modeled downward moisture percolation at the bottom of the shallow soil profile integrated over the hydrological
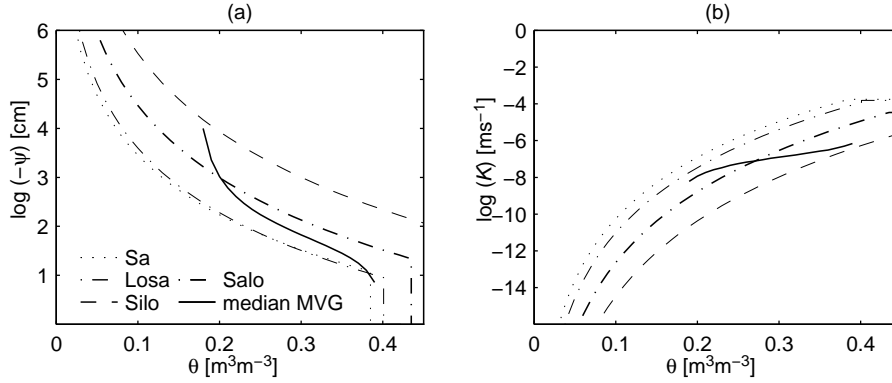
Figure 4.4: *Moisture retention curve (a) and soil hydraulic conductivity curve (b) for several soil types of the* Clapp and Hornberger *(CH) classification, together with the soil type characterized by the median of the experimentally determined* Mualen–Van Genuchten *(MVG) parameters.*

year is adjusted for deep rooted vegetation transpiration by simple subtraction. An average soil depth of 0.5 m is assumed.

4.3.5 Soil heat flux

Generally, the soil heat flux is difficult to estimate. It may be modeled or measured using a number of techniques, usually based on soil profile temperature gradient. The regional application of such methods is hampered by the unavailability of input parameters, partly due to the high spatial variation on this scale. Consequently, in modelling daily *ET* the soil heat flux is often assumed 0. *Owe et al.* [1992] pointed out the neglect of G may lead to a substantial overestimation of *ET*, as G is predominantly unidirectional during daytime, when most of the *ET* may occur. The soil heat flux was proposed to be estimated as a fraction of R_n, dependent on moisture content. Fig. 4.5 depicts the G/R_n ratio as a function of moisture content for data from the test fields, previously analysed for α_{ef} (n=36) (see Section 4.3.2). The figure shows the data with θ_{top} normalized for field capacity of the sandy loam and the silt loam CH soil types. On days coinciding with or directly after rainfall/irrigation, energy is released from the soil resulting in low or negative ratios. On one occasion G is not decreased by irrigation, but it is not clear why. Although some relation between the observed G/R_n ratio and moisture content appears to be present, the curve of best fit coincides with a constant ratio equal to the arithmetic mean for almost the complete range of moisture conditions. Near the maximum observed θ_{top} the fitted curve is forced through 0. The root mean square error of the fitted curve is about equal to the standard deviation of the G/R_n values (=0.10). The sensitivity of moisture modelling results to the estimation of G is analysed for both the fitted curve and the constant ratio equal to the arithmetic mean.
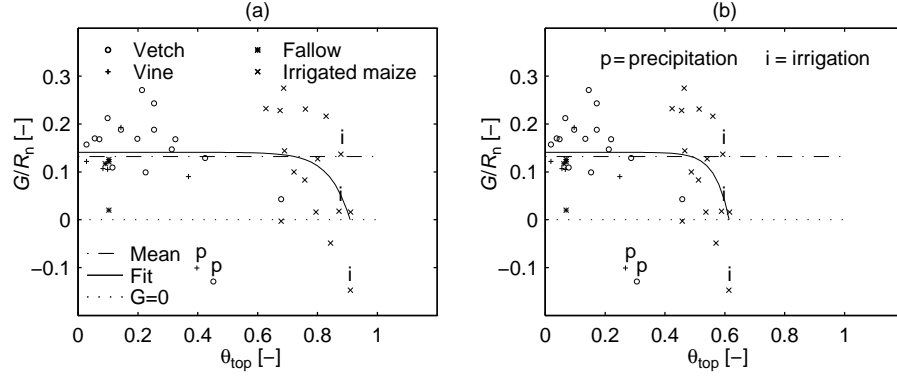
Figure 4.5: *Ratio G/R_n as a function of 5 cm soil depth θ_{top}, normalized as a fraction of field capacity for a) the sandy loam CH soil type b) the silt loam CH soil type. Data points marked with* i *or* p *relate to days of observation coinciding with irrigation and rainfall, respectively.*

The effect on modelling results of setting $G=0$ is also analysed (see Section 4.4).

4.3.6   Net radiation

Net radiation data is available for a large number of EFEDA test fields. The estimation of regional R_n for the Nimbus–7/SMMR satellite lifetime period requires, however, a method of net radiation parameterization based on routinely available data. As outlined in Section 3.5.2, the air temperature data are provided by the three major meteorological stations in the region. These stations also provide insolation data as a fraction of sunshine hours. The fraction is defined as the number of bright sunshine hours and the number of daylight hours. Table 4.5 summarizes the statistics of the available data for the sunshine hour fraction. Not all data are available. The Ciudad Real station presents a continuous record however. Gaps in the data records of the two remaining stations are filled using a linear regression equation with the Ciudad Real station; r^2 varies between 0.54–0.75 over the period 1975–1991. The range of r^2 values for the Cuenca station exceeds that for the Albacete station. This indicates a larger variability in the sunshine hour fraction from period to period, relative to the Ciudad Real station.

Similar to a preliminary study by *Gouweleeuw et al.* [1992], in the present study net radiation is estimated from its constituting components using air temperature and the fraction of sunshine hours. This is carried out by applying theoretical methods and empirical formulae described by *Brutsaert* [1982], i.e.:

$$R_n = R_s(1 - \alpha_s) + \epsilon_s R_{ld} - R_{lu} \qquad (4.12)$$

where R_s is the (global) shortwave radiation [Wm^{-2}], α_s is the albedo of the

surface [–], R_{ld} is the downward longwave radiation [Wm^{-2}], ϵ_{s} is the emissivity of the surface [–], and R_{lu} is the upward longwave radiation [Wm^{-2}].

Global shortwave radiation   Average estimates of R_{s} may be derived from a simple equation proposed by *Prescott* [1940]:

$$R_{\mathrm{s}} = R_{\mathrm{se}}[k + l(\mathrm{n_s}/\mathrm{N_s})] \qquad\qquad (4.13)$$

where $(\mathrm{n_s}/\mathrm{N_s})$ is the fraction of sunshine hours, in which $\mathrm{n_s}$ is the number of bright sunshine hours [–] and $\mathrm{N_s}$ is the number of daylight hours [–]. The value of the constants k and l [–] depend on location, season and state of the atmosphere. R_{se} [Wm^{-2}] may be computed for a given latitude and time of year when the solar constant is known. In the present study daily totals based on calculations by Milankovitch [*List*, 1971] applied to a solar constant of 1370 Wm^{-2} are used. Values of k and l are reported for many locations. Here, average values of k=0.25 and l=0.50 are used [*Brutsaert*, 1982].

Albedo   The surface albedo, α_{s}, is an important parameter in the radiation balance, controlling the amount of reflected shortwave radiation. Although mean albedo values are usually used for calculations of daily radiation totals, α_{s} exhibits a seasonal and diurnal variation. The diurnal variation of most surfaces depends on sun altitude. On a regional scale the seasonal variation of α_{s} is related to inter alia topsoil moisture content and the fraction of vegetation cover.

Surface albedo estimates for 20 m resolution NS001 data from the Barrax and Tomelloso EFEDA test sites are reported by *Ogink-Hendriks et al.* [1995]. The spatial variation of the test fields on June 29 1991 10^{00} UTC at the irrigated Barrax site ($\alpha_{\mathrm{s}} \approx$ 0.15–0.31) is relatively large compared to the test fields at the Tomelloso site ($\alpha_{\mathrm{s}} \approx$ 0.18–0.24). A mean surface albedo estimate of 0.285 for a test field with a sparse vineyard canopy in June near Tomelloso is reported by *Van den Hurk* [1996]. *Oliver and Sene* [1992] report mean α_{s} values of 0.27 for a vine test field and 0.23 for a vetch test field in June, also near Tomelloso.

The spatial and seasonal variation of α_{s} appear to make an estimation of daily shortwave radiation at the regional scale on the basis of a mean surface albedo very approximate. Nevertheless, in the present study a mean α_s is determined by comparing estimated net radiation to the arithmetic mean for the net radiation data of the EFEDA test fields (see Conclusion, this Section). While the spatial variability is thus taken into account to some degree, the seasonal variation is not.

In spring/summer α_{s} is expected to decrease because of the increase in vegetation cover fraction. Conversely, drying of the topsoil in summer causes α_{s} to increase. In autumn/winter these effects are directed vice versa. Overall, α_{s} may be expected to be at a low in spring, while higher values occur in the remainder of the season. Apart from spring, the simultaneous and opposite directed effects may cancel out seasonally. In fact, the spatial variation (e.g.

irrigated maize vs. dry bare soil) may well exceed the seasonal variation. In the
first instance therefore, α_s is chosen to be seasonally invariant.

Table 4.5: *Mean and standard deviation of the fraction of sunshine hours for the three major meteorological stations in the West La Mancha area.*

Period	Albacete			Cuenca			Ciudad Real			Average	
	$\bar{X}$	S	n_{na}	$\bar{X}$	S	n_{na}	$\bar{X}$	S	n_{na}	$\bar{X}$	S
									fraction of sunshine hours		
1975/76	0.61	0.27	–	0.52	0.28	–	0.61	0.28	–	0.58	0.28
1976/77	0.59	0.30	–	0.46	0.30	–	0.57	0.30	–	0.55	0.30
1977/78	0.57	0.30	–	0.46	0.30	–	0.56	0.30	–	0.53	0.30
1978/79	0.59	0.29	–	0.48	0.31	–	0.60	0.29	–	0.57	0.30
1979/80	0.58	0.28	–	0.50	0.30	–	0.60	0.28	–	0.56	0.29
1980/81	0.59	0.28	–	0.56	0.28	–	0.63	0.26	–	0.60	0.27
1981/82	0.59	0.28	–	0.64	0.31	–	0.60	0.27	–	0.60	0.29
1982/83	–	–	1	0.66	0.28	–	0.61	0.25	–	0.62	0.26
1983/84	–	–	1	0.62	0.34	–	0.56	0.29	–	0.58	0.31
1984/85	0.54	0.33	–	0.64	0.32	–	0.56	0.27	–	0.59	0.30
1985/86	–	–	86	–	–	62	0.58	0.29	–	0.59	0.30
1986/87	–	–	294	–	–	212	0.58	0.30	–	0.59	0.29
1987/88	–	–	164	–	–	169	0.54	0.30	–	0.56	0.31
1988/89	–	–	27	0.64	0.30	–	0.58	0.27	–	0.60	0.28
1989/90	–	–	36	0.56	0.33	–	0.57	0.29	–	0.57	0.30
1990/91	–	–	85	–	–	63	0.54	0.30	–	0.56	0.30
Mean							0.58	0.28		0.58	0.29

$\bar{X}$	Arithmetic mean
S	Standard deviation
Average	Arithmetic mean of the three stations
n_{na}	Number of days not available

Upward longwave radiation R_{lu} may be obtained from:

$$R_{lu} = \epsilon_s \sigma T_s^4 \qquad (4.14)$$

where $\sigma(5.67\text{X}10^{-8}\text{Wm}^{-2}\text{K}^{-4} = 4.90\text{X}10^{-3}\text{Jm}^{-2}\text{day}^{-1}\text{K}^{-4})$ is the Stefan–Boltzmann constant, T_s is the surface temperature [K], and ϵ_s is the surface emissivity [–]. Although ϵ_s is not well known for surfaces other than water, it is usually close to unity. In the present study an average value of ϵ_s=0.98 is chosen. Surface temperature measurements from EFEDA are available for a range of surface cover types (see Table 3.10). To obtain a regional mean daily estimate of the surface temperature, T_{se}, for the Nimbus–7/SMMR lifetime period, surface temperature is related to air temperature similar to the analysis in Section 3.5.2. An estimate of the mean daily air temperature, $T_{a_{mean}}$ [K], is derived by:

$$T_a = \frac{T_{a_{min}} + T_{a_{max}}}{2} \qquad (4.15)$$

Table 4.6: *Vegetation cover classes after Thornes et al. [1996] together with test field specifications of radiation measurements.*

	Test field	Site	Research group
Bare soil	Bare soil	Bar	CNRM
	Fallow	Bar	KARL
Semi–natural vegetation	Mattoral	Bel	BERL
	Mattoral	Bel	BERL
Summer cropping	Barley (Irr.)	Bar	INRA
	Maize (Irr.)	Bar	KARL
Spring cropping	Sunflower	Bel	COP
	Vetch	Tom	REA
	Vetch	Tom	IH
	Vetch	Tom	CNRM
Permanent agriculture	Vine	Bel	BERL
	Vine	Tom	CNRM
	Vine	Tom	COP
	Vine	Tom	IH
	Vine	Tom	REA
	Vine	Tom	WSC
	Vine	Tom	WAU
	Vine	Tom	WAU

BERL	University of Berlin
COP	University of Copenhagen
CNRM	Centre Nationale de Recherches Meteorologique Toulouse
INRA	Institute National de la Recherche Agronomique Bordeaux
IH	Institute of Hydrology Wallingford
KARL	University of Karlsruhe
REA	University of Reading
WAU	Wageningen Agricultural University
WSC	Winand Staring Centre Wageningen
Bar	Barrax
Bel	Belmonte
Tom	Tomelloso

where $T_{a_{min}}$ and $T_{a_{max}}$ are the respective daily minimum and maximum temperature, computed as the arithmetic mean of the three major meteorological stations in the region (see Section 3.5.2). Both a weighted and an unweighted mean of the measured daily surface temperature at the test fields is computed. The weighted mean is calculated on the basis of the regional surface cover fraction reported by *Thornes et al.* [1996] (see Table 4.3). The various surface cover types are grouped as indicated in Table 4.6. The difference between the weighted and unweighted mean turned out to be relatively small (RMSE=0.6 K, n=32). Therefore, T_{sm} is obtained by simply computing the unweighted arithmetic mean of the measured daily surface temperature for the test fields. T_a is subsequently related to T_{sm} using Eq. 3.12 and Eq. 3.13. The air temperature

adjustment, ΔT_a, to obtain a mean daily surface temperature estimate, T_{se}, from the mean daily air temperature, T_a, is 2.4 K (n=32, RMSE=1.0 K , see Eq. 3.13).

Downward longwave radiation R_{ld} is affected by cloudiness. An empirical equation to take this effect into account based on adaption of the calculated net radiation under clear skies, R_{nlc} [Wm^{-2}], is [*Penman*, 1948]:

$$R_{nl} = R_{nlc}[j + (1-j)(n_s/N_s)] \qquad (4.16)$$

where R_{nl} is the longwave radiation [Wm^{-2}], R_{nlc} is the net longwave radiation under clear skies [Wm^{-2}] and j is a constant [–]. Analogous to Eq. 4.13 the fraction of sunshine hours (n_s/N_s) is used here as an approximation of cloud cover. For practical calculations an average value of j=0.2 may be used. R_{nlc} may be computed as:

$$R_{nlc} = \epsilon_s R_{ldc} - R_{lu} \qquad (4.17)$$

where R_{ldc} is the downward longwave radiation under clear skies [Wm^{-2}]. In turn, an estimate of R_{ldc} may be derived using:

$$R_{ldc} = \epsilon_{ac}\sigma T_a^4 \qquad (4.18)$$

where T_a is the air temperature [K] at standard screen height and ϵ_{ac} is the atmospheric emissivity under clear skies [–]. ϵ_{ac} is estimated by an empirical equation based on temperature alone, following *Idso and Jackson* [1969]:

$$\epsilon_{ac} = 1 - 0.261 \exp[-7.77\text{x}10^{-4}(273 - T_a)^2] \qquad (4.19)$$

The equation appeared to be valid over a wide temperature range, although it was concluded that it is less accurate at temperatures below freezing [*Aase and Idso*, 1978].

Conclusion It is obvious that the daily mean R_n estimate derived as described above is approximate, if not incorrect. To examine wheher the derived R_n estimate is anywhere near observed values of R_n, it is compared with daily values of measured R_n at the EFEDA test fields. Both a weighted and an unweighted mean of the R_n data is computed. As indicated above, the weighting factor is determined on the basis of the regional surface cover fraction of the cover classes in Table 4.3. It appears that the difference between the weighted and unweighted mean is relatively small (RMSE=4.7 Wm^{-2}, n=28). Therefore, the unweighted mean of daily R_n is chosen for comparison with the EFEDA test field measurements. In Fig. 4.6 the daily mean R_n of the surface cover classes
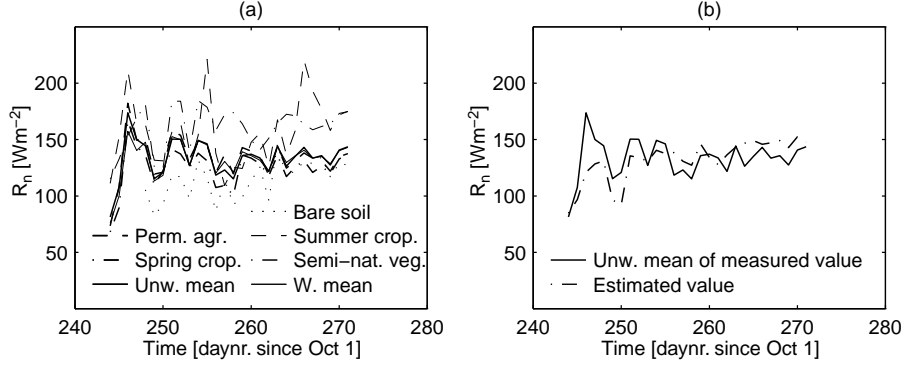
Figure 4.6: *(a) Measured daily R_n of surface cover classes, together with the (un)weighted mean (b) Measured daily R_n and estimated daily R_n.*

is depicted together with the (un)weighted mean R_n. The figure shows that daily R_n of summer cropping agriculture and semi–natural bush vegetation is relatively high, while daily R_n of the bare soil is low. The difference is explained by the high α_s (low R_s) and high T_s (high R_{lu}) of bare soil. Conversely, T_s and α_s of the semi–natural bush vegetation and the summer crops (after irrigation) are low. The surface cover classes of permanent agriculture and spring cropping agriculture show intermediate curves. Table 4.6 lists specifications of the radiation measurement test fields [after *Bolle and Streckenbach*, 1993] grouped according to vegetation cover class (Table 4.3).

Comparison of measured daily R_n and estimated daily R_n shows that the RMSE is minimum (16.6 Wm^{-2}, n=28) when α_s=0.28, as shown in Fig. 4.6. While the RMSE in estimated daily R_n is $\sim 10\%$ of measured daily R_n, the R_n estimate is able to follow alternations in measured daily R_n reasonably well, due to the sunshine hour fraction parameterization. The peak in measured daily R_n at the start of the measuring period does not however, coincide with a peak in the fraction of sunshine hours and/or air temperature. The observed increase of estimated R_n over the measuring period is caused by the increase of T_a.

Net radiation is an important control on evaporation, which in turn is an important component in the water balance. The sensitivity of moisture modelling results to variation in the mean daily R_n estimate is discussed in Section 4.4.

4.3.7 Precipitation and irrigation

The spatial and temporal variability of rainfall is reflected in the number of rainfall stations in the region. While the major meteorological stations monitor insolation and air temperature, precipitation is measured at over 50 stations.

The spatial variability of rainfall implies that moisture content and therefore recharge are also spatially variable. As described in the previous chapter, in the present study moisture content estimates are derived from satellite data on

a regional scale. Comparison of these moisture content estimates with modeled moisture content implicitly assumes that model input parameters may be represented by large–scale averages. With respect to rainfall, being the spatially most variable (meteorological) input parameter, it is assumed that area–averaged precipitation may be obtained by computing the (weighted) arithmetic mean of rainfall point measurements.

Many rainfall stations appear to have missing data. In fact, not a single continuous record for the satellite lifetime period of 1978–1987 is available, while only 10 stations have a continuous record of half the period or longer.

Where possible, gaps in the record are filled using a regression equation of the daily record against the daily record of a nearby station, i.e. within a radius of ∼ 25 km. The decision criteria to select one of the nearby stations are the degree of correlation, the distance between the stations, the similarity of the cumulative precipitation curve and the availability of data at the one station missing in the other. Although neighbouring stations are generally related to some degree, large variations in the correlation coefficient occur from period to period due to local storms.

As it turned out to be impossible to reconstruct a complete data record for the entire satellite lifetime period, it is split up into 5–year periods. For these 5–year periods complete records of a set of stations are constructed. To obtain area–averaged precipitation estimates, a Thiessen polygon network [*Thiessen*, 1911] is constructed for each 5–year period using the IDRISI software program. Area–averaged precipitation is determined by summing area weights of precipitation records for the individual measuring stations. As a result, extremes in local precipitation are averaged to some degree. Furthermore, local storms of a single day are clustered to form regional storms of several days duration.

Table 4.7 summarizes the computed area–averaged precipitation depth totals for the period 1975–1991. Precipitation depth total is here defined as the volume of precipitation per unit area summed over the hydrological year (see below). Although some consistency may be lost from 5–year period to 5–year period due to the different number of rainfall stations used, a pattern of relatively wet and dry periods may be discerned. The period 1976–1979 is relatively wet, while that of 1980–1987, coinciding with the Nimbus–7/SMMR lifetime, is relatively dry. The period 1987/88 is again relatively wet, while the period 1990/91 is relatively dry. Area–averaged precipitation depth totals in the period 1988/89 and 1989/90 have intermediate values. An analysis of temporal variability of rainfall in the region over the period of 1956–1991 is reported by *Thornes et al.* [1996]. Apart from a general decline in rainfall since 1956, a corresponding pattern of relatively wet and dry periods is found for the presently analysed period. Table 4.7 further shows that the weighted area–averaged precipitation total is typically a few per cent below the unweighted area–averaged precipitation total. Fig. 4.7 shows the cumulative weighted area–averaged daily precipitation curve for the satellite lifetime period. Most of the rainfall is recorded between October and April, while the summer months are generally dry. For this reason the hydrological year is chosen from October 1 to September 30.

To account for the amount of irrigated water in surplus of rainfall some adjust-

ment to the area–averaged precipitation estimate is required. The irrigation events included in Fig. 4.3 for irrigated maize in Barrax range between 22–40 mm day^{-1} [*Bolle and Streckenbach*, 1992]. *Llamas et al.* [1996b] report a total amount of water of 493 mm and 582 mm for two respective irrigation seasons between June–August 1994 and 1995 for a plot in Barrax. Irrigation is applied by day, every one or two days with a maximum of 16 mm day^{-1}. The area–averaged amount of irrigated water added to precipitation is computed as the daily average amount of irrigated water ($\sim$ 6mm day^{-1}) times the regional surface cover fraction (Table 4.3). Thus, irrigation of summer cropping agriculture adds 0.18 mm day^{-1} to the area–averaged precipitation between June–August, i.e. 4% of the mean annual area–averaged precipitation over the period 1975–1991.

Between 1974–1987 spring cropping agriculture (i.e. cereal) has experienced the largest increase in area under irrigation [*Llamas*, 1989]. An approximated increase of the spring cropping area under irrigation from 0 in 1975/76 to 10% in 1988, results in an increase of the estimated area–averaged amount of irrigated water applied to this crop type from 0 to 0.31 mm day^{-1}. Integrated over the period of April–May the total amount of irrigated water is about 4% of the mean annual area–averaged precipitation. Here, as above, an average irrigation rate of 6 mm day^{-1} is assumed. The sensitivity of moisture modelling results to various irrigation scenarios is discussed in Section 4.4.

4.4 Sensitivity analysis

4.4.1 Introduction

Ideally, the implementation of the soil moisture balance model to the West La Mancha region is validated by comparison with time series of measured soil moisture. While this is feasible on the plot scale [*Gouweleeuw et al.*, 1996], areal averaging of moisture measurements proves rather difficult and may introduce large errors at a regional scale. Furthermore, measured time series of soil moisture are available for a restricted period of time in summer only. Instead, the performance of the soil moisture balance model is validated by comparison of the computed annual downward moisture percolation at the bottom layer of the soil profile with the long–term annual recharge estimate from river flow. This is described in Chapter 5. Furthermore, a sensitivity and error analysis of model results to parameter variation is carried out, which is presented in this section. Similar to Section 3.5.4 and Section 3.5.5, the sensitivity analysis relates to the period 1981/82, i.e. October 1 1981 to September 30 1982. The sensitivity of model results to parameter variation is carried out by comparison with a fixed model parameter matrix. In summary of the sections above, the fixed model parameter matrix features the following characteristics:

- Soil hydraulic properties relate to the sandy loam soil type according to the *Clapp and Hornberger* classification.
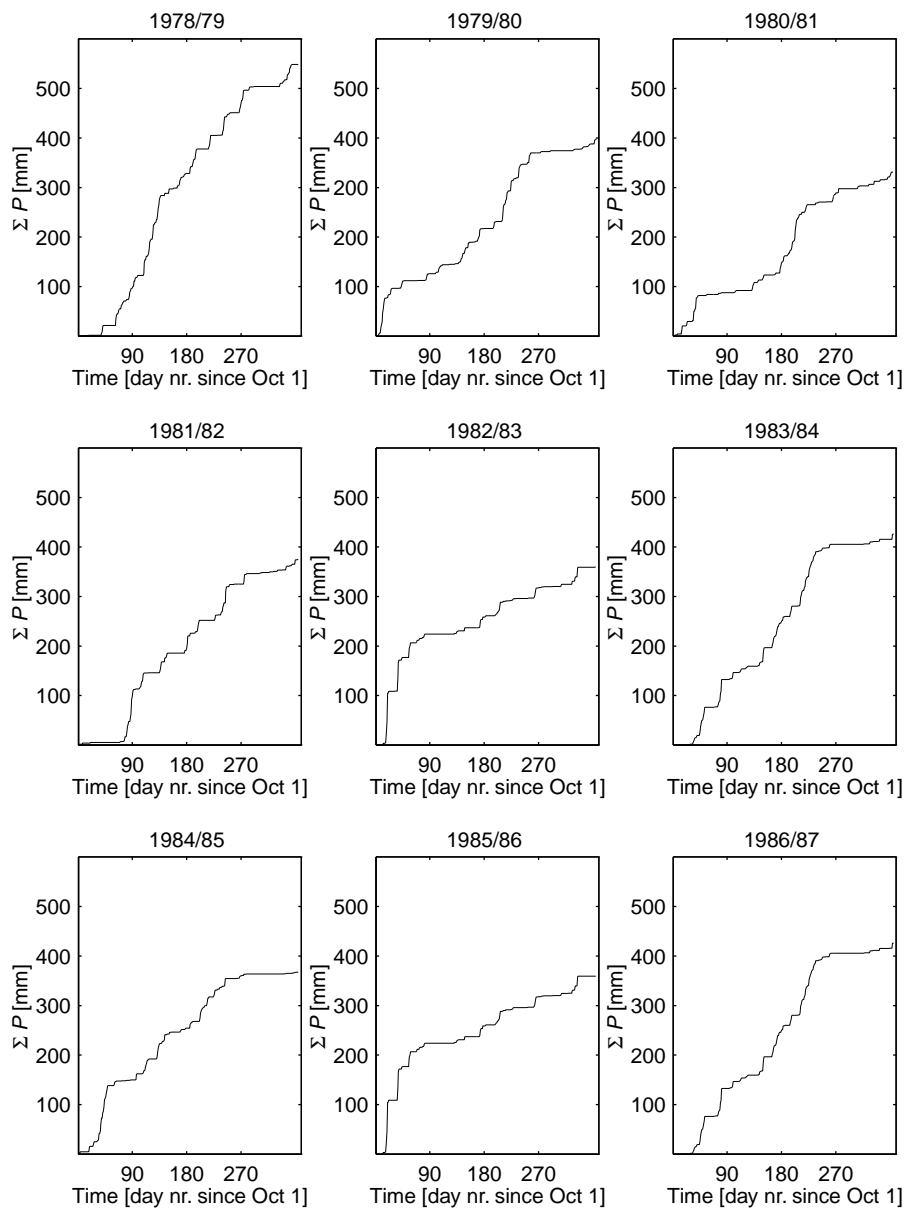
Figure 4.7: *Cumulative area–averaged daily precipitation curves for the West La Mancha area over the satellite lifetime period 1978–1987.*

Table 4.7: *Characteristics of regional estimates of precipitation totals for the West La Mancha area.*

Period	ΣP		n
	$\bar{X}$	$\bar{X}_w$	
1975/76	381.4	370.5	30
1976/77	574.5	556.4	
1977/78	599.4	578.5	
1978/79	563.6	548.6	
1979/80	413.5	396.6	
1980/81	338.0	331.3	24
1981/82	392.9	375.2	
1982/83	372.5	359.5	
1983/84	443.3	426.0	
1984/85	380.5	367.2	
1985/86	431.4	409.7	27
1986/87	358.7	332.4	
1987/88	553.9	527.3	
1988/89	500.5	483.0	
1989/90	442.3	422.0	
1990/91	376.2	361.5	
Mean	445.2	427.9	

ΣP	Yearly cumulative precipitation [mm]
$\bar{X}$	Arithmetic mean
$\bar{X}_w$	Weighted arithmetic mean
n	Number of rainfall stations

- Evapotranspiration is computed according to the derived area–averaged 5 cm depth evaporative fraction curve (see Fig. 4.3b).

- The depth of the soil profile is 0.5 m with a 5 cm nodal spacing, i.e. 10 layers of 5 cm thickness.

- Net radiation is modeled using a seasonally invariant surface albedo, α_s, of 0.28.

- Soil heat flux is modeled according to the derived relation between G/R_n and θ_{top} (see Fig. 4.5a).

- No adjustment is made for α_{ef} on days of rainfall (see Section 4.3.2).

- Irrigation is not taken into account.

- The daily values for R_n, T_a and P are distributed evenly over the day. Diurnal variation is neglected.

The model parameters and assumptions listed above are all varied in order to determine the sensitivity of the model. This is carried out by analysing the output values for 5 cm topsoil moisture content ($\theta_{5\mathrm{cm}}$), cumulative evapotranspiration (ΣET) and cumulative downward vertical moisture percolation (ΣR). ET is defined such, it includes bare soil evaporation and transpiration by shallow rooting vegetation. R is computed by setting the downward moisture flux equal to the hydraulic conductivity of the bottom layer at 50 cm depth. The initial moisture profile is chosen such that the change of moisture storage in the soil profile over the hydrological year/period is zero. To achieve this condition the moisture model is run twice. The initial soil moisture profile in the second run is set equal to the final soil moisture profile after the first run. The minimum topsoil moisture content is set at 0.03 $\mathrm{m}^3\mathrm{m}^{-3}$. In the case $\theta_{5\mathrm{cm}}$ is equal to or below the minimum moisture content, ET is set 0. The following section presents results from the sensitivity analysis.

4.4.2   Results and discussion

Table 4.8 and Table 4.9 summarize results of the sensitivity analysis of the moisture model results to parameter variation for the 1981/82 period. Fig. 4.8, Fig. 4.9 and Fig. 4.10 present a selection of the listed parameter variations. The area–averaged precipitation depth total summed over the 1981/82 period, ΣP, is 375.2 mm. ΣET and ΣR of the fixed model parameter matrix are 69% and 31% of ΣP, respectively (see Table 4.8).

Soil type and soil hydraulic properties   Variation of the soil type implies a variation of the soil hydraulic properties, i.e. the moisture retention curve and the hydraulic conductivity curve (see Table 4.1). From sand to silt loam the soil hydraulic conductivity decreases, while the moisture retention capacity increases. As a result, ΣR decreases and the moisture content over the soil profile increases. The rise in $\theta_{5\mathrm{cm}}$ causes ΣET to increase.
Maximum ΣET is computed for the silt loam soil type, i.e. 76% of ΣP. The combined moisture retention capacity and hydraulic conductivity of this soil type optimizes the volume of moisture available for evapotranspiration. Maximum ΣR (45% of ΣP) is calculated for the soil type with the highest soil hydraulic conductivity and lowest moisture retention capacity, i.e. sand.

Soil profile depth   A decrease in soil profile depth reduces both the volume of moisture in the soil profile and the moisture retention capacity of the soil. While the decrease of $\theta_{5\mathrm{cm}}$ reduces ΣET, the decreased retention capacity increases ΣR. The soil profile depth is varied by changing the number of layers, i.e. the 5 cm nodal spacing remains unchanged.

Surface albedo   Seasonal variation of α_s affects the incoming shortwave radiation, which in turn affects net radiation (see Eq. 4.12). The derived average α_s value of 0.28 for the EFEDA test field data of June 1991 (see Section 4.3.6)

Table 4.8: *Results of the sensitivity analysis of moisture model results to varia-tion of (daily) input parameters averages for the period 1981/82.*

Parameter variation	θ_{5cm}			ET		R	
	$\bar{X}$	$\Delta\bar{X}$	S	ΣX	$\Delta\Sigma X$	ΣX	$\Delta\Sigma X$
Fixed input matrix	0.124	–	0.081	257.9	–	117.3	–
Sand	0.107	14	0.048	205.9	20	169.3	44
Loamy sand	0.116	6	0.056	219.8	15	155.4	32
Silt loam	0.145	17	0.108	285.7	11	89.4	24
Loam	0.139	12	0.102	274.0	6	101.8	13
Soil profile depth = 0.25 m	0.117	6	0.082	232.7	10	142.5	21
Soil profile depth = 0.75 m	0.140	13	0.074	273.2	6	102.0	13
$\alpha_s = 0.23 - 0.28$	0.122	2	0.081	262.9	2	112.3	4
$G/R_n = 0.13$	0.125	1	0.082	253.8	2	121.4	3
$G = 0$ (1)	0.118	5	0.083	259.4	6	115.8	1
$G = 0$ (2)	0.142	15	0.072	257.0	0	118.2	1
$\alpha_{ef} = \alpha_{ef_{max}} if P > 0\text{mm}$ (3)	0.117	6	0.083	260.0	1	115.2	2
$\alpha_{ef} = \alpha_{ef_{max}} if P > 0\text{mm}$ (4)	0.113	9	0.085	257.8	0	117.4	0
$\alpha_{ef} = \alpha_{ef_{max}} if P > 5\text{mm}$ (3)	0.123	1	0.082	259.0	0	116.2	1
$\alpha_{ef} = \alpha_{ef_{max}} if P > 10\text{mm}$ (3)	0.124	0	0.081	257.2	0	118.0	1
$\alpha_{ef} + 10\%$	0.121	2	0.083	257.9	0	117.3	0
$\alpha_{ef} - 10\%$	0.139	12	0.073	257.4	0	117.8	0
P + summer irrigation	0.125	1	0.081	273.1	6	118.4	1
P + spring irrigation	0.125	1	0.081	264.9	2	118.8	1
P + summer/spring irrigation	0.126	2	0.081	281.1	8	119.0	1
$ET + 10\%$	0.120	3	0.082	260.5	1	114.7	2
$ET + 20\%$	0.117	6	0.082	265.0	3	110.2	6
$R_n + 10\%$	0.120	3	0.082	260.5	1	114.7	2
$R_n -10\%$	0.139	12	0.073	254.9	1	120.3	3
$T_a + 10\%$	0.123	1	0.082	257.7	0	117.4	0
$T_a -10\%$	0.128	3	0.079	257.5	0	117.7	0
$P + 10\%$	0.138	11	0.075	276.2	7	136.5	16
$P - 10\%$	0.120	3	0.081	239.3	7	98.2	16

θ_{5cm}	5 cm topsoil moisture content [$m^3 m^{-3}$]
$\bar{X}$	Arithmetic mean
$\Delta\bar{X}$	Proportional change of $\bar{X}$ by parameter variation [%]
S	Standard deviation
ET	Evapotranspiration
R	Downward moisture percolation
	at the bottom layer of the soil profile
ΣX	Cumulative X over the hydrological year/period [mm]
$\Delta\Sigma X$	Proportional change of ΣX [%]

is seasonally varied over 0.05 to reach a minimum of 0.23 in spring. The seasonal decrease of α_s results in an increase of R_n, which increases ET. A raised ET, decreases θ_{5cm}, which in turn reduces ET. The increase in ET therefore, is partly discounted in the topsoil moisture content. Table 4.8 shows that the overall effect of a seasonal variation in α_s is limited.

Soil heat flux   The effect of setting the G/R_n ratio equal to the arithmetic mean of the EFEDA test field data is small. Fig. 4.5 demonstrates that the difference between the constant G/R_n fraction and the θ_{top} dependent fraction is a maximum when θ_{5cm} exceeds the maximum observed moisture content of the EFEDA test field data ($\sim 0.25 \text{m}^3 \text{m}^{-3}$). For the fixed model parameter matrix this occurs during a restricted period of time only (spring), as illustrated in Fig. 4.8. The effect is expected to increase with increasing θ_{5cm}, i.e. generally from sand to clay (see Fig. 4.8).
The sensitivity of model results to the assumption of $G=0$ integrated over 24 hours may be considered in two ways. According to Eq. 4.5, setting $G=0$ increases ET. The increase of ET is partly discounted in θ_{5cm} and partly in ΣET. ((1) in Table 4.8). The assumption of $G = 0$ over 24 hours however, actually requires a recalibration of the evaporative fraction curve. Application of the recalibrated evaporative fraction curve results in a decreased evaporative demand, i.e. a reduced α_{ef} value for each θ_{5cm}. A reduced ET increases θ_{5cm}, which in turn increases ET. Therefore, ΣET remains about equal. The increase in θ_{5cm} is relatively large. This may indicate that the moisture depletion rate of the topsoil is at a near–maximum. Furthermore, an increase in θ_{5cm} increases the hydraulic conductivity of the topsoil, which in turn facilitates upward capillary flow towards the topsoil ((2) in Table 4.8).

The evaporative fraction   As described in Section 4.3.2, the evaporative fraction curve may be considered to represent a 'drying' curve. The delayed reaction of θ_{5cm} on P causes α_{ef} to be underestimated on days of precipitation (see Fig. 4.3). The effect is analysed by setting α_{ef} equal to the value of $\alpha_{ef_{max}}$ (i.e. when $\theta_{top}=1$) in case of rainfall. The analysis is carried out for $P > 0$ mm (all rainstorms), $P > 5$ mm and $P > 10$ mm. The difference between α_{ef} and $\alpha_{ef_{max}}$ is largest in summer, when θ_{5cm} is at a minimum. Table 4.8 shows the effect on model results for the condition of $\alpha_{ef} = \alpha_{ef_{max}}$ if $P > 0$ mm is largest. There is no effect for the condition of $\alpha_{ef} = \alpha_{ef_{max}}$ if $P > 10$ mm. This is because the latter condition only affects a restricted number of rain storms. Overall, setting $\alpha_{ef} = \alpha_{ef_{max}}$ in case of rainfall does not affect ΣET and slightly decreases the mean θ_{5cm}. In summer the effect is small, because θ_{5cm} is at a minimum and the depleted topsoil is not able to provide for an increased ET demand. In winter the effect is small because α_{ef} is already at a high level from the relatively high θ_{5cm} ((3) in Table 4.8). Assuming ET in case of rainfall is provided by ponded water on the soil surface when θ_{5cm} is below the minimum topsoil moisture content, ET is subsequently subtracted from P. ((4) in Table 4.8). The increase of ET by its subtraction from P on days of
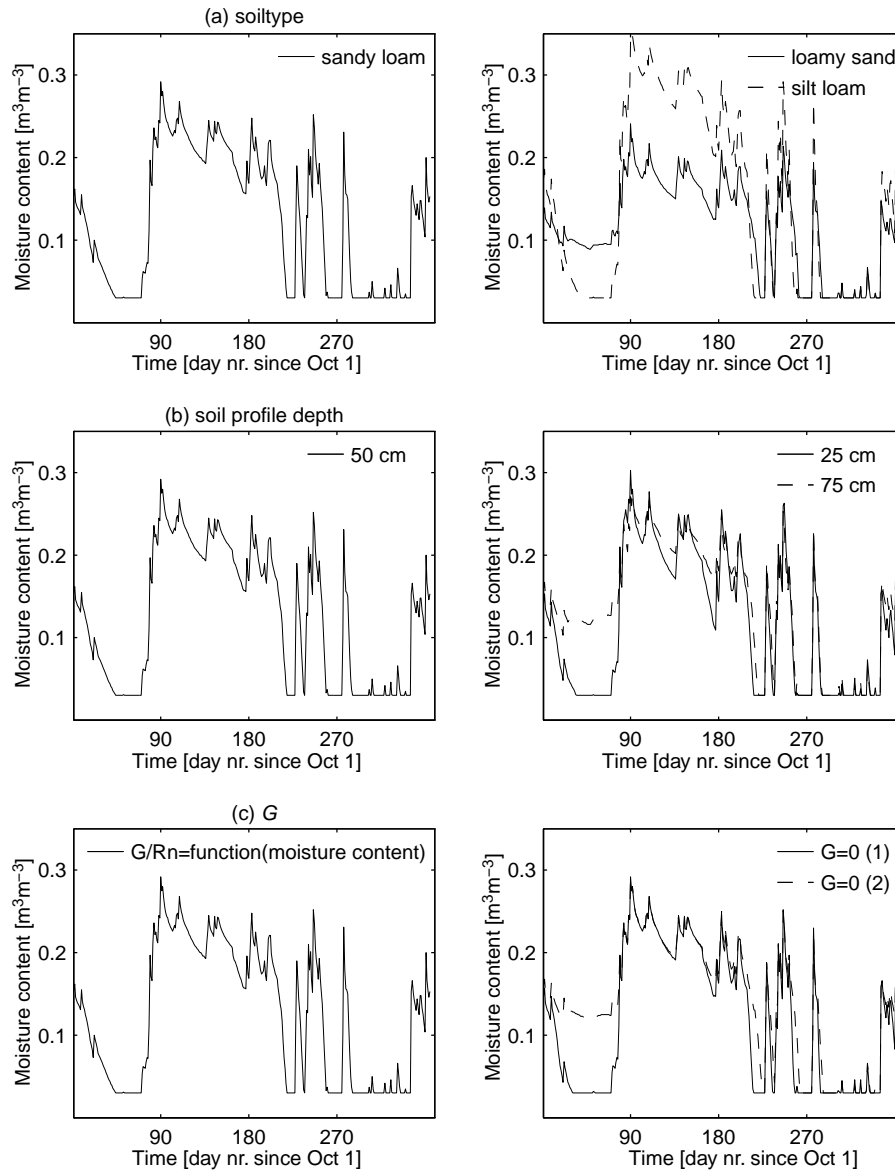
Figure 4.8: *Sensitivity of modeled topsoil moisture content for the 1981/82 period to a) soil type b) soil profile depth c) soil heat flux parameterization .*
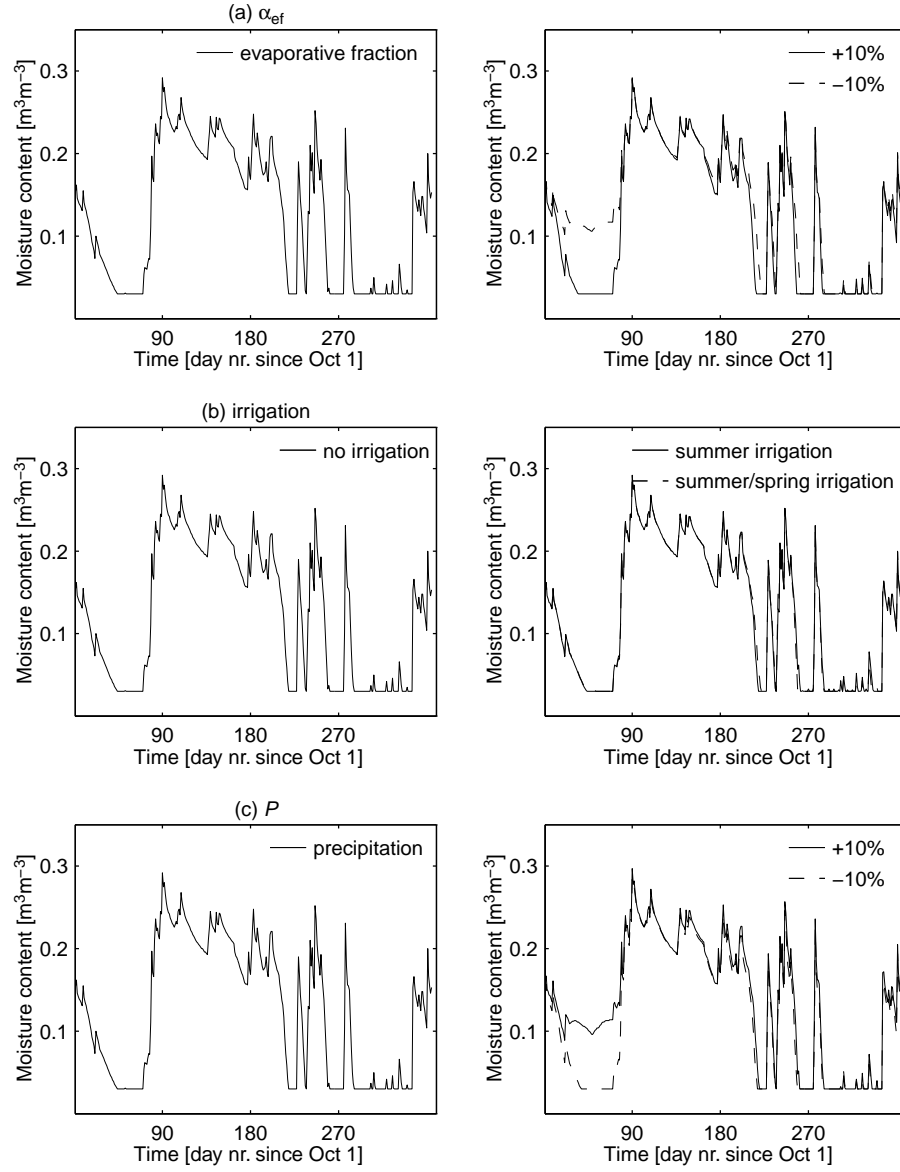
Figure 4.9: *Sensitivity of modeled topsoil moisture content for the 1981/82 period to a) α_{ef} b) irrigation c) precipitation.*

minimum θ_{5cm} is overruled by the reduction of P. The decrease of θ_{5cm} by the reduction of rainfall causes ΣET to decrease.

A 10% increase in the value of α_{ef} results in a 2% decrease in the mean θ_{5cm}, while a 10% decrease in α_{ef} results in a 12% increase of θ_{5cm}. The variation of ET causes θ_{5cm} to change and ΣET to remain about equal. The increase in ET has a restricted effect on mean θ_{5cm}. As mentioned above, this appears to indicate that depletion of the topsoil is at a near–maximum level. In this perspective, the relatively large increase in mean θ_{5cm} with a decrease of ET may be explained. Furthermore, an increase of θ_{5cm} increases the hydraulic conductivity of the topsoil, which enhances the upward capillary flow towards the topsoil.

Irrigation   As described in section 4.3.7, irrigation is applied both in spring (April–May) and in summer (June–August). For the 1981/82 period the area–averaged depth of irrigated water added to the area–averaged precipitation depth is estimated to be 8.5 mm and 16.3 mm for spring- and summer cropping agriculture, respectively. Table 4.8 demonstrates that almost all irrigated water evapotranspires. Here, daily average irrigation is considered, i.e. the irrigated depth of water is evenly distributed over 24 hours and spatially averaged. The effect of the application of the identical depth of water over a shorter period of time is described below. Reduction of the irrigated water depth by spatial averaging probably also affects the model result. The spatial resolution is, however, defined by the satellite antenna resolution and therefore inherent to the research approach.

Evapotranspiration at night   Since $R_n - G$ (see Eq. 4.5) generally becomes negative after sunset, the use of 24–hour averages of R_n results in an underestimation of the ET daily total. The sensitivity of model results to evapotranspiration during night time is analysed by setting night time ET equal to 10% and 20% of the daily ET total. The 10% and 20% increase in daily ET raises the evapotranspiration summed over the year, ΣET, by 1% and 3%, respectively. The mean θ_{5cm} is decreased by 3% and 6%, respectively. As described earlier, the effect of an increase in ET is restricted. It seems to indicate that the depletion rate of moisture in the topsoil is at a near–maximum level. The effect of the application of a diurnal course of R_n on model results is described below.

Variation of R_n, T_a and P   The 10% increase in R_n results in a partial increase of ET and a partial decrease of θ_{5cm}, identical to a 10% increase of ET (see Eq. 4.5). The decrease of R_n results in a relatively large increase in θ_{5cm}. This may be explained by the reduction of the near–maximum moisture depletion rate. Furthermore, a rise in θ_{5cm} facilitates upward capillary flow by the increase in hydraulic conductivity of the topsoil. Variation of T_a affects the model results in a similar way. The sensitivity of the model results to T_a is limited however. A variation in P has a large effect on the model results, especially on θ_{5cm} and ΣR.

Table 4.9: *Results of the sensitivity analysis of moisture model results to diurnal variation of input parameters for the period 1981/82.*

Diurnal variation	θ_{5cm}			ET		R	
	$\bar{X}$	$\Delta\bar{X}$	S	ΣX	$\Delta\Sigma X$	ΣX	$\Delta\Sigma X$
Fixed input matrix	0.124	–	0.081	257.9	–	117.3	–
R_n	0.116	6	0.083	264.0	2	111.2	5
R_n, 10% night time ET	0.113	9	0.082	268.0	4	107.2	9
R_n, 20% night time ET	0.109	12	0.082	268.7	4	106.5	9
R_n, skewed to afternoon (50%)	0.109	12	0.082	268.6	4	106.6	9
R_n, skewed to afternoon (75%)	0.109	12	0.082	268.6	4	106.6	9
R_n, skewed to afternoon (100%)	0.107	14	0.082	267.5	4	107.7	8
R_n, skewed to morning (50%)	0.109	12	0.082	268.5	4	106.7	9
R_n, skewed to morning (75%)	0.109	12	0.082	268.0	4	107.2	9
R_n, skewed to morning (100%)	0.109	12	0.082	266.5	3	108.7	7
T_a	0.125	1	0.081	257.7	0	117.5	0
P 12 hour duration [6–18]	0.124	0	0.080	254.5	1	120.7	3
P 12 hour duration [24–6,18–24]	0.125	1	0.082	255.7	1	119.5	2
P 6 hour duration [12–18]	0.125	1	0.081	253.0	2	122.2	4
P 6 hour duration [18–24]	0.128	3	0.085	256.0	1	119.2	2
P 6 hour duration [24–6]	0.128	3	0.076	251.2	3	124.0	6
P 6 hour duration [6–12]	0.125	1	0.080	251.6	2	123.6	5
P 3 hour duration [12–15]	0.125	1	0.080	252.0	2	123.2	5
P 3 hour duration [21–24]	0.129	4	0.089	253.3	2	121.9	4
P 3 hour duration [24–3]	0.134	8	0.072	257.8	0	117.4	0
P 3 hour duration [3–6]	0.124	0	0.078	248.6	4	126.6	8
P 1 hour duration [12–1]	0.134	8	0.075	237.1	8	138.1	18
P 1 hour duration [21–22]	0.131	6	0.086	228.0	6	147.2	25
P 1 hour duration [24–1]	0.136	10	0.073	235.7	9	139.5	19
P 1 hour duration [3–4]	0.135	9	0.073	240.3	7	134.9	15
P depth/duration distribution	0.123	1	0.081	252.1	2	123.1	5
1 hour irrigation duration [12–13]	0.126	2	0.081	281.2	8	118.9	1
1 hour irrigation duration [15–16]	0.126	2	0.081	281.2	8	118.9	1
1 hour irrigation duration [9–10]	0.126	2	0.081	281.1	8	119.0	1
R_n, P depth/duration distribution	0.114	8	0.082	263.2	2	112.0	5
Diurnal course, all	0.115	7	0.082	288.6	12	109.8	6

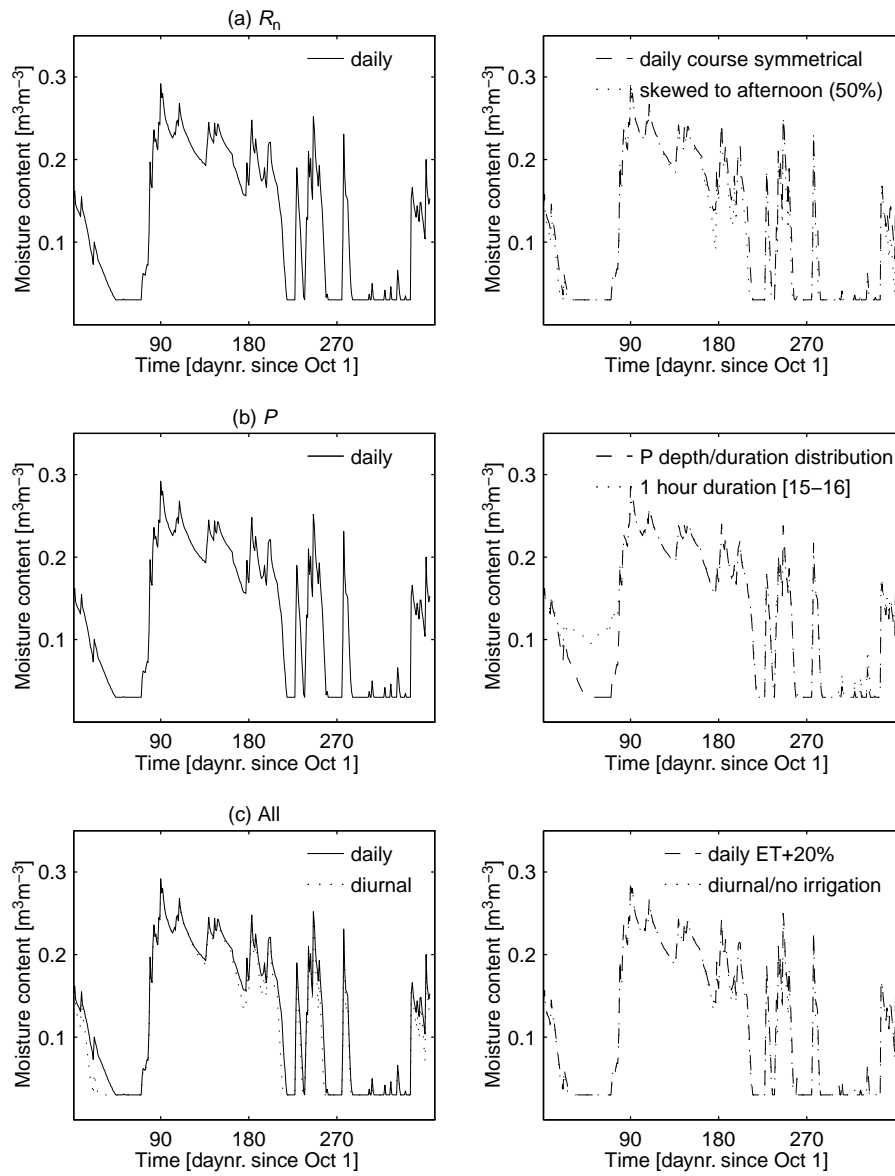|	
θ_{5cm}	5 cm topsoil moisture content [m^3m^{-3}]
$\bar{X}$	Arithmetic mean
$\Delta\bar{X}$	Proportional change of $\bar{X}$ by parameter variation [%]
S	Standard deviation
ET	Cumulative evapotranspiration
R	Cumulative downward moisture percolation
	at the bottom layer of the soil profile
ΣX	Cumulative X over the hydrological year/period [mm]
$\Delta\Sigma X$	Proportional change of ΣX [%]

Figure 4.10: *Sensitivity of modeled topsoil moisture content for the 81/82 period to a) diurnal course of R_n b) rainfall intensity c) diurnal variation of R_n, T_a, P and irrigation.*

Diurnal variation   As described in Section 4.1, in a perspective of the available meteorological and satellite data, a daily time resolution of the soil moisture model is considered appropriate. Consequently, a modified *Priestley–Taylor PET* model is applied, using daily averages of R_n, T_a, P and irrigation. For application on a diurnal basis the *Priestley–Taylor* concept is less suitable, as α_{ef} is more sensitive to the evaporative demand over the course of the day than to the available amount of moisture in the topsoil [*Owe and Van de Griend*, 1990]. The use of 24–hour averages of R_n results, however, in an underestimation of *ET*. Furthermore, temporal averaging of precipitation and irrigation over 24 hours results in a loss of the structure of the data, i.e. the rainfall/irrigation intensity. Rainfall intensity may be expected to affect the relative proportion of components in the hydrological balance equation at least to some degree (Eq. 5.1). The present paragraph describes analysis of the sensitivity of model results to the diurnal variation of R_n, T_a, P and I. The results are listed in Table 4.9.

Hourly data for the EFEDA test fields of several cloud free days in June 1991 indicates that R_n typically varied between 600 $\mathrm{Wm^{-2}}$ at midday and –75 $\mathrm{Wm^{-2}}$ before sunrise (5:00 hrs UTC) and after sunset(19:00 hrs UTC) [*Bolle and Streckenbach*, 1993]. The maximum number of bright sunshine hours is provided by the meteorological stations in the region (see Section 4.3.6). These appear to vary between 9 in winter and 15 in summer for the 1981/82 period. Multiplication of daily R_n for June 1991 by –0.4 results in R_n values in the order of –75 $\mathrm{Wm^{-2}}$, which is subsequently applied over the season to compute hourly R_n before sunrise and after sunset. Hourly R_n values during daytime are computed using:

$$R_{n_{hour}} = R_n + (MR_n + \sin((t_h/N_s)2\pi - (0.5\pi))MR_n) \qquad (4.20)$$

where $R_{n_{hour}}$ is hourly net radiation [$\mathrm{Wm^{-2}}$], M is a multiplication factor [–], t_h is time (UTC) [hr] and N_s is the number of bright sunshine hours [–]. M varies with N_s and is chosen such that the 24–hour average of $R_{n_{hour}}$ equals daily R_n. Table 4.9 summarizes the underestimation of daily *ET* using 24–hour averages of R_n. The introduction of a diurnal course of R_n results in a 6% decrease in the mean θ_{5cm} and a 2% increase of ΣET. The model result is comparable to an increase of daily *ET* by 20% (see Table 4.8). Setting night time *ET* equal to a fraction of the *ET* daily total, i.e. 10% and 20%, further decreases the mean θ_{5cm} and increases ΣET.

The sensitivity of model results to the distribution of R_n over the day is analysed by creating a skewed diurnal distribution of R_n. This is carried out by respectively adding/subtracting 50%, 75% and 100% of hourly R_n in the morning/afternoon, and vice versa. This is carried out such that the 24–hour R_n remains equal. Table 4.9 shows that a skewed distribution of R_n over the day further decreases the mean θ_{5cm}. It is, however, not much affected by the degree of skewness. This may indicate that the maximum depletion rate of the topsoil moisture content is achieved by a 50% increase of hourly R_n in the

morning/afternoon. A further increase in evaporative demand by an increase of hourly R_n for one day half is not able to deplete θ_{5cm} any further. The effect of a diurnal distribution of R_n skewed to the morning or to the afternoon is comparable. Further variation in the diurnal R_n distribution, i.e. alternating skewed distributions to the morning/afternoon from day to day, also give similar model results.

Diurnal variation of T_a is carried out by varying the daily average over the range $T_{a_{max}} - T_{a_{min}}$. $T_{a_{min}}$ occurs in the early morning before sunrise and T_a reaches a maximum in the late afternoon before sunset. Table 4.9 shows that a diurnal variation of T_a using daily averages of R_n does not very much affect the model result.

The sensitivity of model results to rainfall intensity is analysed by restricting the rainfall duration for all rainstorms from 24 hours to 12, 6, 3 and 1 hour, respectively. Table 4.9 shows that ΣR increases with decreasing rainfall duration, i.e. increasing rainfall intensity. The moment of rainfall in the day also affects the model results. This is explained by the diurnal course of θ_{5cm}, causing variation of ΣET and ΣR. If rain falls early in the day, i.e shortly after midnight, the increase of θ_{5cm} causes the largest fraction of the precipitation to be evapotranspired during the remainder of the day. ΣR is maximum when the balance between the time for moisture to drain to depth and the evaporative loss is optimal. The moisture drainage time is related to the rainfall intensity. Since not all rain storms are expected to have equal intensity, the rainfall duration is subsequently assumed to be inversely related to rainfall depth. Table 4.10 presents the distribution of rain storms by precipitation depth for the 1981/82 period, together with the assumed rainfall duration. Based on field experience, it is furthermore assumed that high intensity/low duration rainfall occurs in the (late) afternoon. Table 4.9 shows that the assumed precipitation depth/duration distribution results in a 5% ΣR increase. A subsequent decrease of the P threshold value for 1 hour rainfall duration from 25 mm to 0 mm changes model results towards the results for the 1 hour rainfall duration for all storms (see above).

The sensitivity of model results to irrigation intensity is analysed by restricting the irrigation duration to 1 hour. By analogy to irrigation applied evenly over the day, Table 4.9 shows almost all irrigated water evapotranspires. It seems therefore that temporal averaging of irrigation water depth over the day does not significantly affect the model result. As mentioned earlier, a decrease in the (local) irrigation intensity by spatial data averaging may well be an important factor, causing the larger part of the irrigated water to be evapotranspired. It seems, therefore, that the moisture model is not able to adequately account for the effect of irrigation on the scale of the satellite antenna resolution. Variation of the moment of irrigation in the day does not much affect the model result, probably due to the small area–averaged irrigation depth.

The model result combining the diurnal course of R_n and T_a and the restricted duration of P is similar to that for a diurnal course of R_n alone. Here, night time ET is assumed 0 and precipitation occurs according to the earlier described depth/duration distribution (Table 4.10). It appears therefore, that the diurnal course of R_n affects the model results to a larger degree than the rainfall inten-

Table 4.10: *Distribution of rainstorms by daily precipitation depth for the 81/82 period, together with the assumed rainstorm duration.*

ΣP	n	P_d
> 25	1	1
20–25	1	3
15–19	2	6
10–14	6	9
5–9	16	12
< 5	77	24

ΣP	Daily cumulative precipitation [mm]
n	Number of rainstorms
P_d	Rainfall duration [hr]

sity and the diurnal course of T_a. The inclusion of irrigation during one hour at midday further increases ΣET.

Conclusion   From the analyses it appears the model results are most sensitive to variation in the soil hydraulic properties, i.e the soil type, the thickness of the soil profile and precipitation/irrigation. While θ_{5cm}, ΣET and ΣR are sensitive to variation in precipitation, irrigation only affects ΣET because of its shallow area–averaged depth. The model results appear to be rather insensitive to an increase of ET, directly or indirectly e.g. by an increase of R_n. The effect of a decrease in ET is, however, comparatively large. This seems to indicate that the moisture depletion rate of the topsoil is at a near–maximum level. A variation in ET is partly discounted in θ_{5cm} and partly in ET. This implies that a decrease in ET primarily affects the mean θ_{5cm}, while ΣET remains about equal.
Analyses further indicate that the model results are sensitive to the use of 24–hour averages for R_n. The use of a diurnal course in R_n decreases the mean θ_{5cm} and increases ΣET. Application of a diurnal course of R_n compares with a 20% increase in daily ET, as illustrated in the right–hand graph of Fig. 4.10c. The model results also appear to be sensitive to rainfall intensity. ΣR may increase by 25% when restricting all rainstorms to a 1 hour duration. Application of an assumed precipitation depth/duration distribution increases ΣR by 5%. Diurnal variation of T_a and restriction of irrigation duration have, however, a limited effect on the model results. Combination of the diurnal course of R_n and T_a and the duration of P indicates that model results are most sensitive to the diurnal course of R_n. The increased downward percolation induced by a restricted rainfall duration is overruled by the increased ET caused by the diurnal course of R_n.

Table 4.11: *Modeled 5 cm topsoil moisture content for the period 1975/76 to 1990/91.*

Period	θ_{5cm}		R_n	T_a	P	ET	F	R	F
	$\bar{X}$	S	$\bar{X}$	$\bar{X}$	ΣX	ΣX		ΣX	
1975/76	0.135	0.070	67.2	285.9	370.5	320	86	50.5	14
1976/77	0.155	0.085	68.0	285.6	556.4	320	58	236	42
1977/78	0.158	0.086	67.2	286.3	578.5	322	56	257	44
1978/79	0.144	0.086	69.2	286.6	548.6	327	60	222	40
1979/80	0.147	0.080	68.4	286.7	396.6	309	78	87.4	22
1980/81	0.140	0.074	68.5	286.6	331.3	277	84	54.3	16
1981/82	0.117	0.082	70.0	287.5	375.2	264	70	111	30
1982/83	0.125	0.084	70.0	286.6	359.5	197	55	163	45
1983/84	0.142	0.086	68.0	286.4	426.0	289	68	137	32
1984/85	0.134	0.085	70.5	287.0	367.2	225	61	143	39
1985/86	0.136	0.087	71.2	286.9	409.7	256	63	153	37
1986/87	0.132	0.083	71.4	287.7	332.4	238	71	94.8	29
1987/88	0.155	0.081	69.2	287.2	527.3	361	68	166	32
1988/89	0.157	0.076	69.0	287.3	483.0	373	77	111	23
1989/90	0.136	0.080	70.8	288.2	422.0	262	62	160	38
1990/91	0.143	0.083	69.3	287.0	361.5	259	72	103	28
Mean	0.141	0.082	69.2	286.8	427.9	288	68	141	32

θ_{5cm}	5 cm topsoil moisture content $[\text{m}^3\text{m}^{-3}]$
$\bar{X}$	Arithmetic mean
ΣX	Cumulative X over hydrological year/period [mm]
S	Standard deviation
R_n	Daily average net radiation $[\text{Wm}^{-2}]$
T_a	Daily average air temperature [K]
P	Precipitation
ET	Evapotranspiration
R	Downward moisture percolation
	at the bottom layer of the soil profile
F	Fraction of P [%]

4.5   Time series

Although the model results are affected by the diurnal course of R_n and by rainfall intensity, daily values are used to model θ_{5cm} over the period 1975/76 to 1990/91. As described earlier, the modified *Priestley–Taylor* model is less suitable for application on a diurnal basis. To compensate for the use of 24–hour averages of R_n, the daily *ET* estimate is increased by 20%. Irrigation is also disregarded. While any estimate of applied irrigation depth remains very approximate, its effect on modeled topsoil moisture content is limited (see Fig. 4.9b). At the scale of the satellite antenna resolution irrigation seems not well represented. The analyses in the previous section indicate almost all spatially averaged irrigated water evapotranspires. Therefore, apart from the increase of the daily *ET* estimate by 20%, the input parameter matrix is set identical to that defined in Section 4.4.

Fig. 4.11 to Fig. 4.13 demonstrate that the seasonal course of modeled topsoil moisture time series consists of two parts. In the period from (late) autumn to (late) spring the mean θ_{5cm} exceeds 0.20 m^{3}m^{-3}. In this period the topsoil moisture content usually reaches a maximum, while θ_{5cm} only occasionally falls to a minimum of 0.03 m^{3}m^{-3}. In the period from late spring to the end of summer, θ_{5cm} is at a minimum almost constantly. Rain storms cause isolated peaks in the topsoil moisture content of several days duration. Overall, the seasonal course of moisture conditions appears to be quite large. On a regional scale, one would expect the extremes in (high) moisture content to be averaged out to some degree. On the other hand, the large range of moisture conditions may be explained by the shallow topsoil depth. Apart from precipitation, the seasonal variation of θ_{5cm} appears to be strongly related to the amount of energy available for evapotranspiration.

Table 4.11 shows that the model results, on the longer term, generally follow the earlier described pattern in the precipitation record of a relatively wet period (1976–1979) and dry period (1980–1987) (see Section 4.3.7). The year–to–year variation of P dominates over the slight increase of R_n and T_a. ΣR is generally relatively large in wet years, while ΣET is comparatively large in dry years. Seasonality, however, also affects the model results. This is related to the distribution of rainfall over the year, the (antecedent) soil moisture conditions and the evaporative demand. While rainfall evapotranspires for the larger part in spring/summer, it is recharged in autumn/winter. The relatively high ΣR fraction of ΣP in the relatively dry period of 1982/83, for example, is caused by a concentration of large rainfall storms in the (wet) autumn. For the fixed parameter matrix, the annual downward moisture percolation averages 32% of annual P.
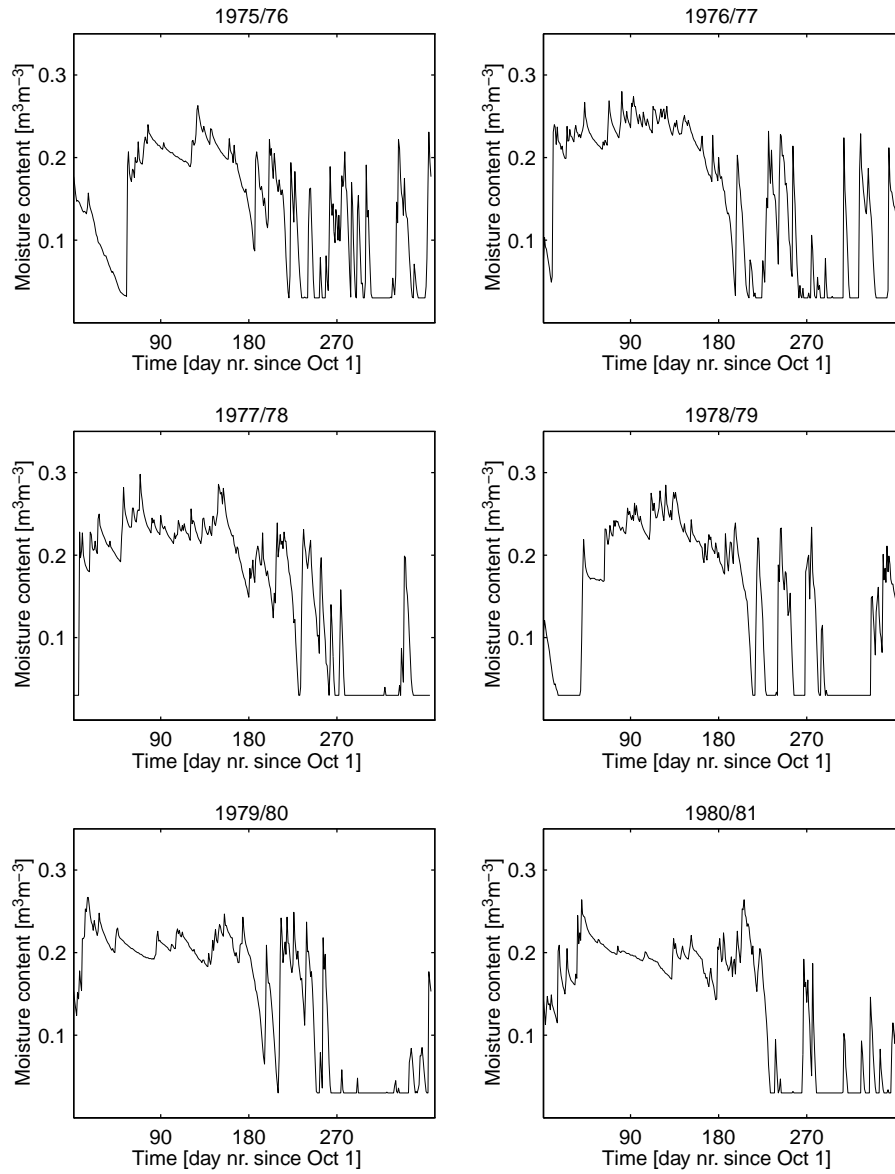
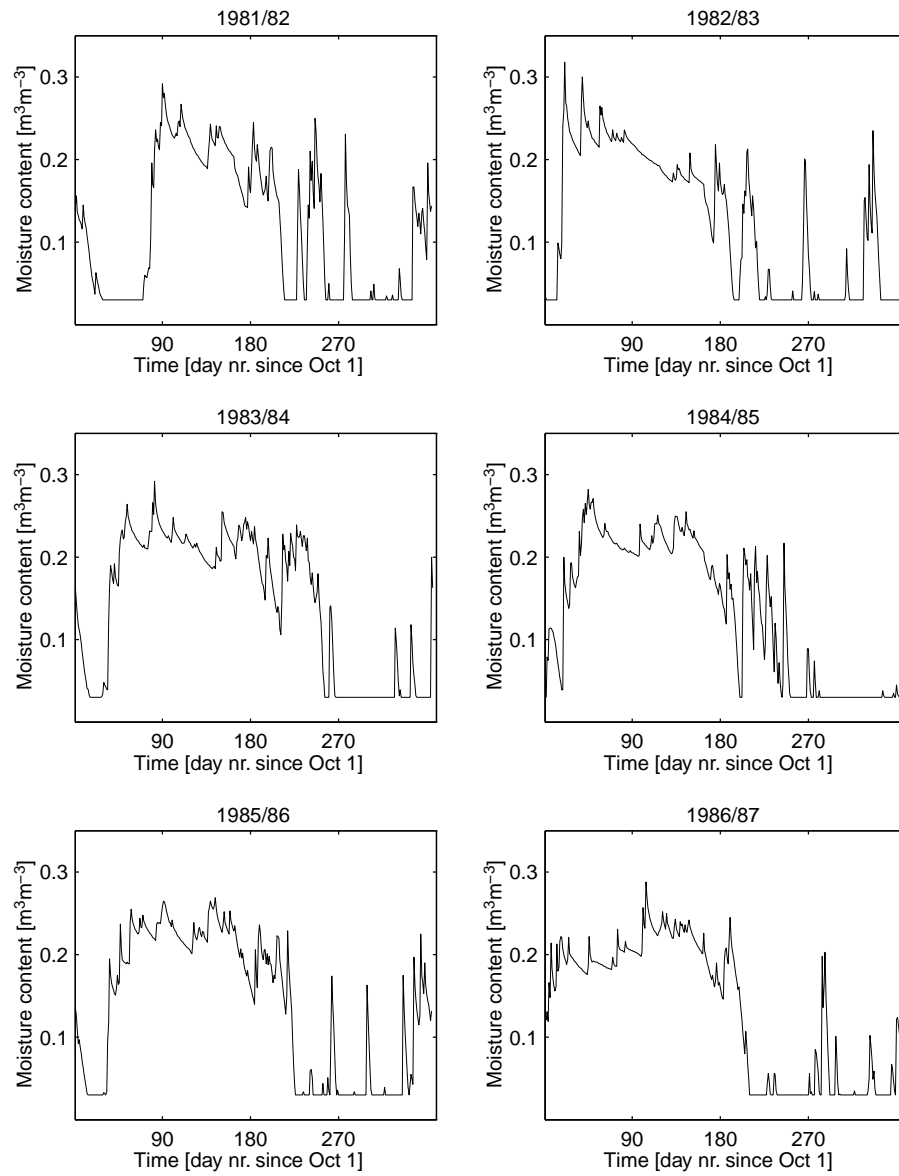Figure 4.11: *Modeled topsoil moisture content for the period 1975/76 to 1980/81.*

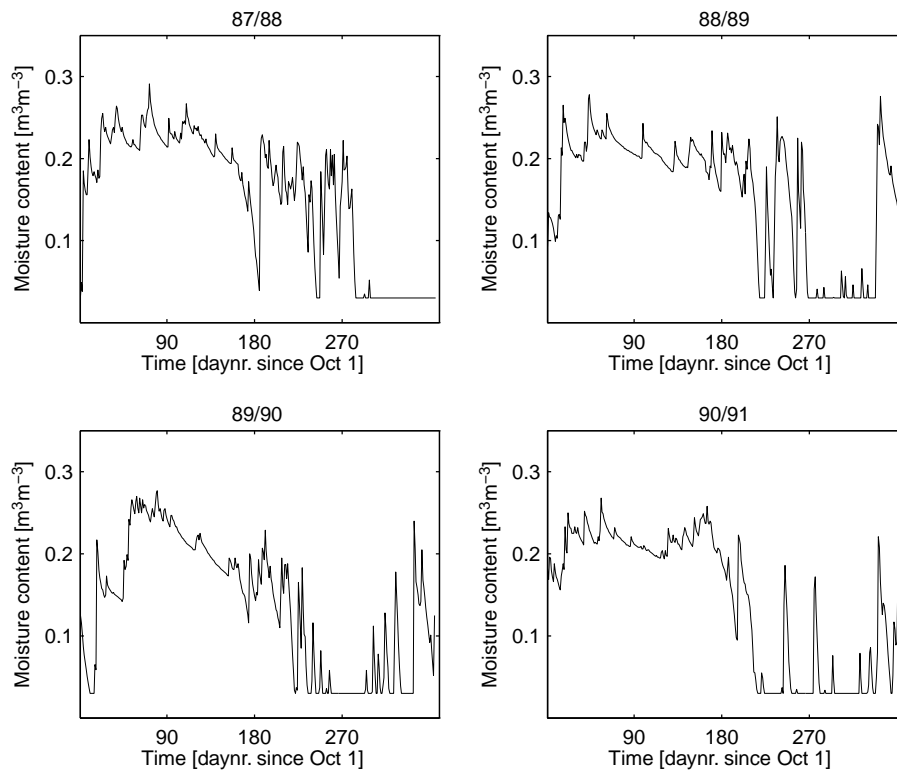Figure 4.12: *Modeled topsoil moisture content for the period 1981/82 to 1986/87.*

Figure 4.13: *Modeled topsoil moisture content for the period 1987/88 to 1990/91.*

4.6   Conclusions

Time series of 5 cm topsoil moisture content are modeled using a regional scale soil moisture balance approach. Implementation of the soil moisture balance model to the West La Mancha area requires some assumption as to the representativeness of a number of model parameters.

A modified *Priestley–Taylor PET* concept is used to compute evaporative losses. Experimental data are used to derive an area–averaged evaporative fraction curve for bare soil surfaces and surfaces with shallow rooted vegetation. The derivation of a separate evaporative fraction curve for deep rooted vegetation is hampered by the absence of ample experimental data. Consequently, the moisture balance model does not consider transpiration by deep rooted vegetation. Since moisture loss by transpiration primarily occurs from the soil profile, its effect on topsoil moisture content may be considered to be relatively small. A transpiration rate estimate is required, however, for closure of the regional waterbalance. On the basis of estimated rates of vine transpiration and the regional surface cover fraction of (semi–)natural vegetation and permanent agriculture, transpiration by deep rooted vegetation is estimated to equal 10% of the annual long–term area–averaged precipitation depth.

The moisture model is most sensitive to the soil hydraulic properties, the soil profile depth and precipitation. The model is relatively insensitive to a direct or indirect increase of ET, e.g. by an increase in the daily R_n. A decrease in ET, however, results in a comparatively large increase in topsoil moisture content. This seems to indicate that the evapotranspiration rate is at a near–maximum topsoil moisture depletion rate. Therefore, while the daily R_n estimate is rather approximate, it does not appear to be underestimated.

Regional scale application of the soil moisture balance model complicates a proper representation of irrigation. While the area under irrigation increased from about 3% to 10% of the surface area total between 1974–1987, model simulations tend to evapotranspire all spatially averaged irrigated water. However, neutron probe observations at irrigated sites indicate a large fraction of the applied water actually drains to depth [*Bromley et al.*, 1996]. The precipitation depth appears to be less affected by spatial averaging. This is because the precipitation depth is generally larger and rainfall usually covers a relatively extended area.

The use of 24–hour averages of net radiation results in an underestimation of daily evapotranspiration. Neglecting rainfall intensity results in an underestimation of downward moisture percolation. The combination of a diurnal course of R_n and a rainfall depth/duration distribution indicates that the model results are comparatively more sensitive to the diurnal course of R_n. The use of a 24–hour average R_n may be compensated for by a 20% increase in the daily ET estimate.

The time series of modeled topsoil moisture over the period 1975–1991 shows that the range of moisture conditions is relatively large. Although on a regional scale one would expect the (high) extremes in moisture content to be averaged to some degree, this may be explained by the shallow topsoil depth. With

regard to moisture fluxes, the model results generally follow the year–to–year variation in precipitation. Seasonality, i.e. the distribution of precipitation over the year, the amount of energy available for evapotranspiration and the (antecedent) moisture conditions also affect the model results.

The performance of the soil moisture balance model is evaluated in the following chapter. Annual modeled downward moisture flux at the 50 cm depth bottom layer of the soil profile is compared with regional estimates of natural recharge obtained from surface river flow. Additionally, time series of satellite derived surface moisture content are compared with those of the modeled topsoil moisture content.

Chapter 5

Recharge and soil moisture

5.1 Introduction

The performance on a regional scale of the soil moisture balance model described in the previous chapter may be evaluated by considering the computed moisture fluxes in the perspective of a regional water balance. Water balance equations can provide for an estimate of recharge, though the accumulated error may be as large as 100% [*Lerner et al.*, 1990]. Assuming no leakage is present, the general form of the water balance equation may be given as [e.g. *Ward*, 1974]:

$$\Sigma P = \Sigma ET + \Sigma Q + \Delta S_{\text{sm}} + \Delta S_{\text{gw}} \tag{5.1}$$

where ΣP is the cumulative precipitation [mm], ΣET is the cumulative actual evapotranspiration [mm], ΣQ is the cumulative discharge [mm], ΔS_{sm} is the change in soil moisture storage [mm] and ΔS_{gw} is the change in groundwater storage [mm]. Over a full hydrological year, i.e. from October to September, ΔS_{sm} and ΔS_{gw} may be disregarded, since the change in storage tends to be minimal over the seasonal cycle.

This chapter presents a comparison of the time series of modeled topsoil moisture and satellite derived surface moisture, using the annual recharge estimate from river flow as a criterion. Section 5.2 presents a comparison of the annual modeled downward moisture percolation at the bottom layer of the soil profile with the annual recharge estimate from river flow. Section 5.3 comparises the time series of modeled topsoil moisture with the time series of satellite derived surface moisture.

5.2   Estimation of recharge from surface flow

5.2.1   Introduction

Surface water flow records at the Upper Guadiana Catchment outlet have been used to determine regional annual recharge for the period 1943–1974 [*Young*, 1996]. During this period the natural conditions in the catchment were undisturbed, i.e. relatively little groundwater abstraction occurred. The discharged base flow therefore directly equates to an estimate of recharge. The moisture balance model described in the previous chapter does not, however, consider a separate component for (subsurface) lateral runoff. That is, at the surface–atmosphere boundary precipitation either evapotranspires or increases the soil moisture content (see Eq. 4.4) and subsequently infiltrates the soil vertically. In the present analysis therefore, all surface flow is assumed to originate from groundwater storage. Consequently, computed downward moisture percolation at the bottom layer of the soil profile is compared to an annual recharge estimate equal to the total surface flow and not to the base flow component of the surface flow. This implies that the estimated annual recharge is overestimated. Over the entire period the annual river flow averages 25 mm, while the estimated base flow is 18 mm [*Young*, 1996]. Over a drier sequence of years (1943–1959) the annual river flow falls to 16 mm (base flow: 9 mm), while from 1959–1974 the annual river flow averages 35 mm (base flow: 28 mm). Under these natural conditions an additional estimated annual amount of water of 9 mm was lost by direct evaporation from wetland areas. After 1974 the groundwater system was no longer in equilibrium and recharge analysis using this technique ceases to be valid.

The computed annual estimate of downward moisture percolation at the 50 cm depth bottom layer of the soil profile over the period 1975–1991 for the set parameter matrix averages 141 mm (see Table 4.11). For the dry sequence of years 1979–1987 an average of 118 mm is computed, while the downward moisture percolation for the wet period 1976–1979 averages 238 mm. The modeled percolation rate needs to be corrected for estimated annual transpiration by deep rooted vegetation. In the case of an average transpiration rate of 0.5 mm day^{-1}, the annual rate is about 50 mm (see Section 4.3.2). After subtraction, the modeled percolation rate still exceeds the estimate from surface river flow by several times. When the transpiration rate by deep rooted vegetation is doubled to 1 mm day^{-1}, the percolation rate averages about 40 mm year^{-1}. This estimate is relatively close to the 35 mm year^{-1} recharge estimate from river flow. However, since the semi–natural vegetation and permanent agriculture are considered to have adjusted to the prevailing dry conditions by adapting an economic water consumption, a doubling of the transpiration rate may be regarded as rather extreme.

The annual recharge estimate derived from river flow relates to the period 1943–1974, whereas the time series of downward moisture percolation is computed over the period 1975–1991. Although different periods are considered, the annual precipitation for the two periods of over 400 mm is comparable [*SGDGOH*,

1988]. The annual rainfall of 370 mm of the two drought sequences , i.e. 1943–1959 and 1979–1987, is also similar. The annual rainfall of 560 mm over the very wet period 1976–1979 does not compare with the annual rainfall of 458 mm over the relatively wet period 1959–1974.

As described in Section 2.4, the onset of large–scale water abstraction in the early 1970s has changed the hydrogeological functioning of the groundwater system. The correctness of comparing recharge estimates from riverflow and downward percolation at the bottom layer of the 50 cm soil profile prior to and after the start of water abstractions may therefore be questioned. The abstraction of groundwater has caused a lowering of the groundwatertable. As a result, the time for moisture to percolate from the bottom of the soil profile to the groundwater table has increased considerably. In places, the unsaturated zone and the groundwater table has been disconnected completely. In the present analysis all moisture that has percolated below the 50 cm soil profile after subtraction of evapotranspiration by deep rooted vegetation is considered as recharge, i.e. it is assumed to be discharged at the basin outlet. This assumption is valid only when the system is stationary, i.e. prior to the groundwater abstractions. Therefore, the recharge estimate derived from riverflow may be considered merely an indication for the modeled downward moisture percolation.

The moisture model considers percolation of moisture through the upper 50 cm of the profile. The percolation through this part is inter alia determined by the antecedent moisture conditions. While the lowering of the groundwater table has an effect on the wetness of the soil, this may in part be compensated for by the increase of irrigation in spring/summer. Rainfall seems, however, to be a more important factor for determining the (antecedent) soil conditions, and therefore the downward moisture percolation through the upper 50 cm of the profile. Since rainfall may be considered independent of the hydrogeological functioning of the groundwater system, to some degree the downward moisture percolation may be as well.

The contribution of preferential flow to recharge is not considered in the soil moisture model. In fact, little is known about the contribution of preferential flow to recharge. *Gouweleeuw* [1994] found indications of preferential drainage in the Miocene deposits of the central Llanura Manchega plain using tritium profiles. From the analysis of chloride profiles *Fienig and Gouweleeuw* [1996] concluded that preferental recharge in dry branches of a drainage network located on Pleistocene sediments in the southern Llanura Manchega plain (see Fig.2.5) may be masked by migration of these branches in time. *Imeson and Bergkamp* [1996] concluded that preferential drainage through fissures and cracks may be considered small in the northern undulating relief of the Sierra de Altomira, since the fraction of fractured area may be assumed small.

Table 5.1: *Modeled 5 cm topsoil moisture content for the period 1975/76 to 1990/91, adjusted to the annual recharge estimate from river flow.*

Period	$\theta_{5\mathrm{cm}}$		P	ET	F	R	F
	$\bar{\mathrm{X}}$	S	ΣX	ΣX		ΣX	
1975/76	0.148	0.094	370.5	354	95	17.0	5
1976/77	0.188	0.113	556.4	364	65	193	35
1977/78	0.192	0.116	578.5	370	64	208	36
1978/79	0.172	0.116	548.6	368	67	180	33
1979/80	0.179	0.104	396.6	356	90	40.4	10
1980/81	0.160	0.091	331.3	321	97	10.1	3
1981/82	0.140	0.109	375.2	309	82	66.4	18
1982/83	0.156	0.116	359.5	234	65	126	35
1983/84	0.174	0.113	426.0	339	79	87.4	21
1984/85	0.164	0.116	367.2	267	73	100	27
1985/86	0.164	0.115	409.7	302	74	107	26
1986/87	0.155	0.107	332.4	281	84	51.6	16
1987/88	0.186	0.108	527.3	405	77	122	23
1988/89	0.188	0.103	483.0	421	87	61.7	13
1989/90	0.163	0.108	422.0	305	72	117	28
1990/91	0.174	0.108	361.5	310	85	54.9	15
Mean	0.169	0.109	427.9	332	79	96	21

$\theta_{5\mathrm{cm}}$	5 cm topsoil moisture content [$\mathrm{m^3 m^{-3}}$]
$\bar{\mathrm{X}}$	Arithmetic mean
ΣX	Cumulative X over hydrological year/ period [mm]
S	Standard deviation
P	Precipitation
ET	Evapotranspiration
R	Downward moisture percolation at the bottom layer of the soil profile
F	Fraction of P [%]

5.2.2 Modeled downward vertical moisture percolation

Assuming an annual transpiration rate by deep–rooted vegetation of 50 mm, the modeled annual downward moisture percolation at the bottom layer of the soil profile exceeds the long–term annual recharge estimate from river flow. A doubling of the transpiration rate by deep rooted vegetation leads to a modeled downward percolation relatively close to the recharge estimate. Alternatively, the soil moisture balance model parameters may be adjusted to arrive at an estimate closer to the recharge estimate from surface flow. As described in Section 4.4.2, model results appear to be most sensitive to the soil hydraulic properties, the soil profile depth and precipitation/irrigation.

As described in Section 4.3.2, on the basis of particle size distribution analyses and laboratory multi–step outflow measurements the sandy loam soil type is considered the most widespread soil type in the West La Mancha area. The analysis in Section 4.4.2, however, indicates that the downward moisture percolation rate at the bottom layer of the soil profile computed for the silt loam soil type is lower and therefore closer to the recharge estimate derived from river flow.

An increase of the soil profile depth reduces the modeled downward vertical moisture percolation. Apart from local valleys in the basin boundary hills of the area, soils in the area are generally relatively thin. Although the average soil depth of 50 cm is considered an appropriate estimate, it is increased to 75 cm to reduce the modeled downward moisture percolation.

A decrease in precipitation reduces the relative proportion of downward moisture percolation to precipitation. The area–averaged precipitation is, however, considered to be computed correctly. It is therefore left unchanged. The modeled downward moisture percolation is not affected by irrigation, since all spatially averaged irrigated water tends to evapotranspire.

In summary, it appears that downward moisture percolation may be adjusted towards the recharge estimates from river flow by a change in the soil hydraulic properties by varying the soil type to silt loam and an increase of the soil profile depth to 75 cm. Table 5.1 presents the model results; Fig. 5.1 to Fig. 5.3 demonstrate the computed time series of evapotranpiration and downward moisture percolation for the period 1975–1991.

The figures show that recharge mainly occurs in winter. In some dry years hardly any recharge takes place at all, e.g. in 1975/76 and in 1980/81. The modeled recharge demonstrates a peak in the wet sequence of years 1976–1979. As described in Section 4.5, the modeled recharge in the dry year 1982/83 is relatively high. This is explained by the concentration of a number of large rainstorms in autumn. The bulk of the soil moisture evapotranspires in spring, when both ample energy and soil moisture are available. For the remainder of the year the evapotranspiration rate is relatively low. This is because in summer the topsoil moisture is (already) depleted, while in autumn/winter relatively little energy is available for evapotranpiration.

The annual downward moisture percolation for the adjusted input matrix averages 97 mm over the period 1975–1991. Corrected for transpiration by deep

rooted vegetation, about 50 mm of recharge remain. For the dry period 1979–1987 the annual net recharge, i.e. after correction for transpiration by deep rooted vegetation, is 25 mm. For the wet period 1976–1979 the annual net recharge is 140 mm. Since in the present study the contribution of transpiration to the evapotranspiration total is estimated and not modeled, it is considered to be static. That is, it is assumed to remain constant independent of dry and wet sequences of years. In reality, a wet period will trigger vegetation growth, which subsequently will increase transpiration. Conversely, a dry period reduces vegetation growth and transpiration. In reality therefore, the differences in net recharge between a succession of wet and dry years are expected to level to some degree.

5.2.3   Conclusions

The annual river flow during the period of 1943–1974 averages 25 mm. Together with direct evaporation from wetland areas, the long–term recharge averages 35 mm. When the average transpiration rate by deep rooted vegetation is assumed to be 0.5 mm day^{-1}, the modeled annual downward moisture percolation exceeds the annual recharge estimate from river flow by several times. If the average transpiration rate is assumed to be 1 mm day^{-1}, the modeled annual percolation is closer to the estimated annual recharge, i.e. 40 mm. Alternatively, the modeled annual downward moisture percolation corrected for transpiration by deep rooted vegetation using an adjusted input matrix is 50 mm. For both adjustments the modeled downward moisture percolation and the recharge estimate for the dry periods 1943–1959 and 1979–1987 are also comparable. The annual recharge estimates over the very wet period 1976–1979 and the relatively wet period 1960–1974 do not correspond. It is not clear which of the two adjustments to the modeled downward moisture percolation rate is preferable. A comparison of the time series of modeled topsoil moisture and satellite derived surface moisture may provide more clarity. This is discussed in detail in Section 5.3.

As mentioned earlier, the soil moisture model does not consider a (subsurface) lateral flow component. Therefore, all surface flow is assumed to be derived from groundwater storage. Precipitation generated river flow, i.e. storm flow, does occur during wet years, mainly in the winter months [*Young*, 1996]. Therefore, both modeled downward moisture percolation and recharge estimates from river flow are overestimated.

Thornes et al. [1996] conclude that recharge in the Upper Guadiana Catchment may vary considerably, both in time and space. The variation is mostly related to the timing, intensity and spacing of rainfall. Timing of rainfall on a daily basis is represented in the model and the effect of rainfall intensity is evaluated in Section 4.4.2. Due to the spatial resolution of the SMMR satellite antenna the spatial variation of rainfall is not considered however. Spatial variation of recharge caused by the spatial variation of rainfall is therefore also not considered.

Apart from the spatial variation of rainfall, recharge is affected by the spatial variation of the (sub)soil. In the moisture model, downward moisture percolation in the soil profile is assumed to represent the predominant recharge process. This may be true for a major part of the Upper Guadiana Catchment, i.e. the central Llanura Manchega plain, which constitutes about one third of the total catchment area. It is probably less valid for the basin boundary hills. In these areas preferential infiltration of rainwater in cracks and/or fissures is likely to occur by the exposure of bare rock, e.g. karstic limestone. Furthermore, the relief may induce surface runoff, thus reducing direct infiltration. Indirect recharge from infiltrating surface water may then occur. Little is known, however, about the contribution of preferential drainage to regional scale recharge. *Imeson and Bergkamp* [1996] conclude that it may be assumed small when the fraction of fractured/fissured area is small.

Modeled recharge estimates are computed using spatially averaged input parameters. Spatially integrated recharge estimates from surface flow at the Upper Guadiana Catchment outlet may therefore provide an indication for the modeled recharge estimates. Although the annual modeled moisture percolation rate exceeds the annual long–term recharge estimate from surface flow, it may be adjusted to more corresponding estimates. However, the recharge mechanism of vertical downward moisture percolation assumed in the moisture model probably represents only part of the actual recharge process.
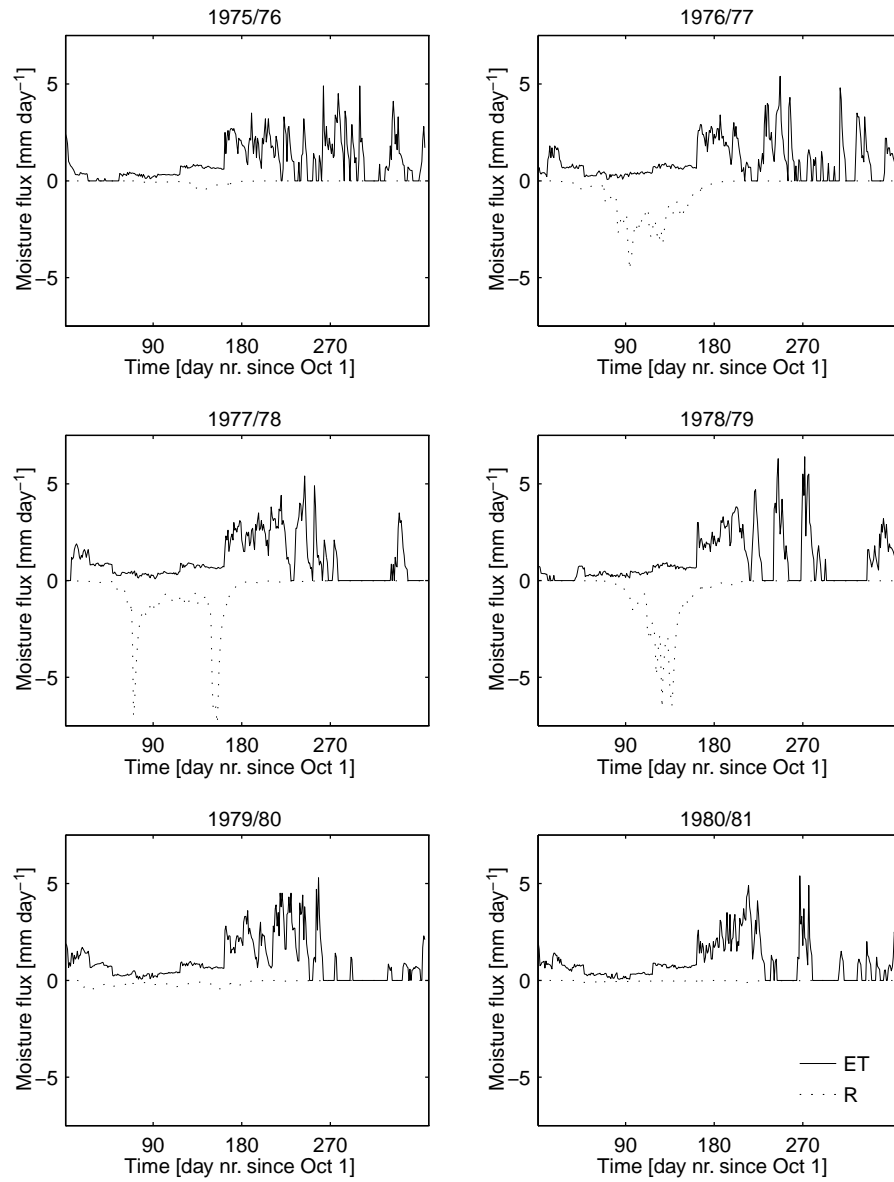
Figure 5.1: *Modeled downward vertical moisture percolation and evapotranspiration for the period 1975/76 to 1980/81 using the adjusted 'silt loam' input matrix.*
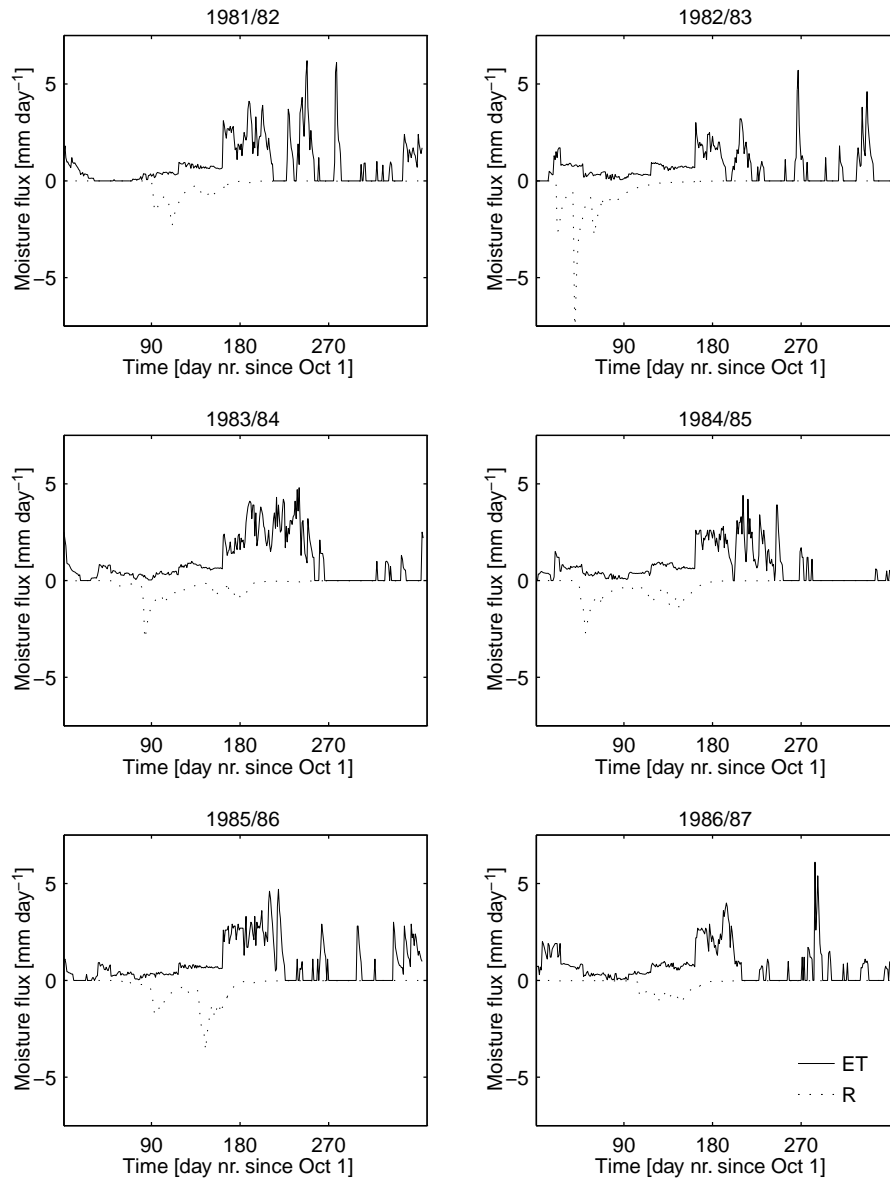
Figure 5.2: *Modeled downward vertical moisture percolation and evapotranspiration for the period 1981/82 to 1986/87 using the adjusted 'silt loam' input matrix.*
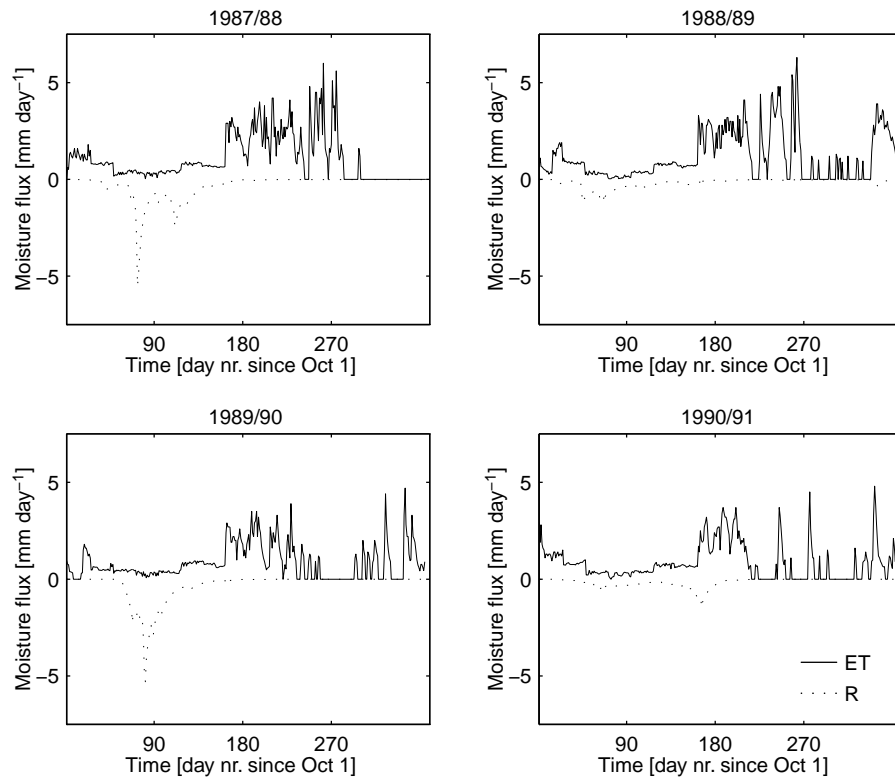
Figure 5.3: *Modeled downward vertical moisture percolation and evapotranspi-ration for the period 1987/88 to 1990/91 using the adjusted 'silt loam' input matrix.*

Table 5.2: *Modeled 5 cm topsoil moisture content for the period 1978/79 to 1986/87 on the days of satellite overpass.*

Period	n	Fixed input matrix 'sandy loam' θ_{5cm}		Adjusted input matrix 'silt loam' θ_{5cm}	
		$\bar{X}$	S	$\bar{X}$	S
				Day time	
1978/79	64	0.149	0.088	0.179	0.116
1979/80	62	0.141	0.082	0.171	0.107
1980/81	66	0.139	0.076	0.161	0.092
1981/82	60	0.117	0.081	0.141	0.109
1982/83	65	0.127	0.084	0.159	0.116
1983/84	65	0.152	0.084	0.186	0.110
1984/85	65	0.136	0.086	0.168	0.117
1985/86	49	0.142	0.087	0.174	0.116
1986/87	52	0.135	0.081	0.161	0.106
Total	548				
Mean		0.138	0.083	0.167	0.110
				Night time	
1978/79	21	0.137	0.081	0.162	0.107
1979/80	19	0.125	0.081	0.150	0.106
1980/81	39	0.139	0.075	0.161	0.091
1981/82	31	0.135	0.084	0.160	0.111
1982/83	41	0.119	0.084	0.148	0.116
1983/84	36	0.172	0.076	0.216	0.100
1984/85	40	0.142	0.091	0.177	0.125
1985/86	26	0.148	0.088	0.180	0.115
1986/87	38	0.157	0.077	0.193	0.102
Total	291				
Mean		0.142	0.082	0.173	0.108

n	Number of days/nights of satellite overpass
θ_{5cm}	5 cm topsoil moisture content $[\mathrm{m^3 m^{-3}}]$
$\bar{X}$	Arithmetic mean
S	Standard deviation

5.3 Surface soil moisture content

5.3.1 Comparison of time series

In the present section, the time series of satellite derived surface moisture content are compared with the time series of modeled topsoil moisture content. Table 5.2 summarizes the statistical properties of the time series of modeled topsoil moisture on days of satellite overpass at day and night time. Topsoil moisture is computed using both the fixed 'sandy loam' input parameter matrix, as defined in Section 4.4.1, and the 'silt loam' input matrix adjusted to the annual regional recharge estimate from river flow (see Section 5.2.2). The topsoil moisture content is computed on a daily basis, i.e. over 24 hours. The night time satellite observation at 23:48 hrs LT is therefore better synchronized with the modeled moisture content output than the daytime observation at 12:12 hrs LT.

Table 4.11, Table 5.1 and Table 5.2 show that the mean daily θ_{5cm} and the mean θ_{5cm} for days of satellite overpass is approximately equal at daytime. At night time the difference between mean daily θ_{5cm} and mean θ_{5cm} for nights of satellite overpass is relatively large, because of the small number of data. The mean θ_{5cm} is also affected by the distribution of the satellite observations over the year. At night time the sampling of satellite overpasses changes the relative proportion of dry and wet periods, e.g. for the 1981/82 and the 1982/83 periods. The effect of satellite overpass sampling on the time series of modeled topsoil moisture content is illustrated in Fig. 5.4 and Fig. 5.5.

The relatively wet period of 1983/84 distinguished in the time series of satellite derived moisture content (see Table 3.15 and Table 3.17), is also recognized in the time series of modeled topsoil moisture content on days/nights of satellite overpass. The relatively wet periods 1979/80 and 1981/82 are, however, not clearly present in the sampled time series of modeled topsoil moisture content. Further comparison indicates that the seasonal course is consistently larger for the time series of modeled topsoil moisture content, as illustrated in Fig. 5.6, Fig. 5.7 and Fig. 5.8.

Table 5.3 presents the Root Mean Square Difference (RMSD) between modeled topsoil moisture content and the satellite derived surface moisture content. Analogous to Eq. 3.7, RMSD is defined as:

$$\text{RMSD} = \sqrt{\frac{\sum_1^n (\theta_{\text{sat}} - \theta_{5cm})^2}{n}} \tag{5.2}$$

where θ_{sat} is the satellite derived surface moisture content $[\text{m}^3\text{m}^{-3}]$, θ_{5cm} is the modeled 5 cm topsoil moisture content $[\text{m}^3\text{m}^{-3}]$ and n is the number of days/nights of satellite overpass. The modeled topsoil moisture content is compared with satellite derived moisture content using both the NDVI–based vegetation correction approach and the dual polarization vegetation correction approach. It appears that the RMSD of the adjusted 'silt loam' input matrix consistently exceeds that for the fixed 'sandy loam' input matrix. While the

model results of the adjusted input matrix agree better with the recharge estimate derived from surface flow, the RMSD of modeled topsoil moisture content and the satellite derived moisture content are comparatively larger. This may indicate that an increase of the transpiration rate by deep rooted vegetation is a more proper adjustment to model results in order to decrease the annual downward moisture percolation. Mainly because of the difference in the seasonal course, the RMSD with the time series of satellite derived surface moisture is very large for both the time series of modeled topsoil moisture. In the following section therefore, the time series of satellite derived surface moisture content are fitted to the time series of modeled topsoil moisture content by optimization of the time–invariant parameter values in the radiative transfer equation (Eq. 3.6).

Adjustment of parameter values in the radiative transfer equation to match the time series of soil moisture indicates that the parameter values applied in Chapter 3 do not lead to satisfactory results. The significance of the difference between the optimum values of the parameters to match the time series of soil moisture and the parameter values applied in Chapter 3 is discussed in the following section.

Table 5.3 shows that the RMSD for the vertical polarization NDVI–based vegetation corrected approach and the dual polarization vegetation correction approach are comparable. This is explained by the similarity of the two time series for derived surface moisture (see Fig. 3.16 and Fig. 3.21).

Fig. 5.4 and Fig. 5.5 illustrate the difference in seasonal course between the time series of satellite derived surface moisture and the time series of modeled topsoil moisture. Peaks in the moisture content caused by precipitation, however, generally coincide.

Table 5.3: *RMSD between modeled 5 cm topsoil moisture content on days of satellite overpass and satellite derived surface moisture content for the period 1978/79 to 1986/87.*

Period	n	Fixed input matrix 'Sandy loam' RMSD			Adjusted input matrix 'Silt loam' RMSD		
		NDVI–based		Dual	NDVI–based		Dual
		Hor.	Ver.		Hor.	Ver.	
							Day time
1978/79	64			0.077			0.104
1979/80	62			0.077			0.101
1980/81	66			0.072			0.089
1981/82	60	0.059	0.072	0.077	0.087	0.097	0.098
1982/83	65	0.074	0.075	0.075	0.114	0.110	0.106
1983/84	65	0.066	0.078	0.076	0.103	0.113	0.108
1984/85	65	0.066	0.076	0.077	0.105	0.111	0.107
1985/86	49	0.076	0.077	0.075	0.116	0.114	0.107
1986/87	52	0.068	0.076	0.068	0.099	0.105	0.095
Total	548						
Mean		0.068	0.076	0.075	0.104	0.109	0.102
							Night time
1978/79	21			0.065			0.091
1979/80	19			0.078			0.096
1980/81	39			0.071			0.091
1981/82	31	0.053	0.065	0.068	0.080	0.092	0.089
1982/83	41	0.083	0.078	0.081	0.119	0.110	0.108
1983/84	36	0.074	0.070	0.067	0.108	0.112	0.104
1984/85	40	0.082	0.086	0.085	0.128	0.127	0.122
1985/86	26	0.090	0.080	0.076	0.128	0.116	0.110
1986/87	38	0.084	0.070	0.062	0.125	0.109	0.097
Total	291						
Mean		0.079	0.075	0.073	0.117	0.112	0.102

n	Number of days/nights of satellite overpass
RMSD	Root Mean Square Difference between modeled topsoil moisture content and satellite derived surface moisture content $[\text{m}^3\text{m}^{-3}]$

Figure 5.4: *Satellite derived surface moisture content and modeled topsoil moisture content at day time satellite overpass. Moisture content is derived from satellite data using the NDVI–based vegetation correction approach at horizontal polarization and the dual polarization vegetation correction approach. Topsoil moisture content is modeled using the adjusted 'silt loam' input parameter matrix.*
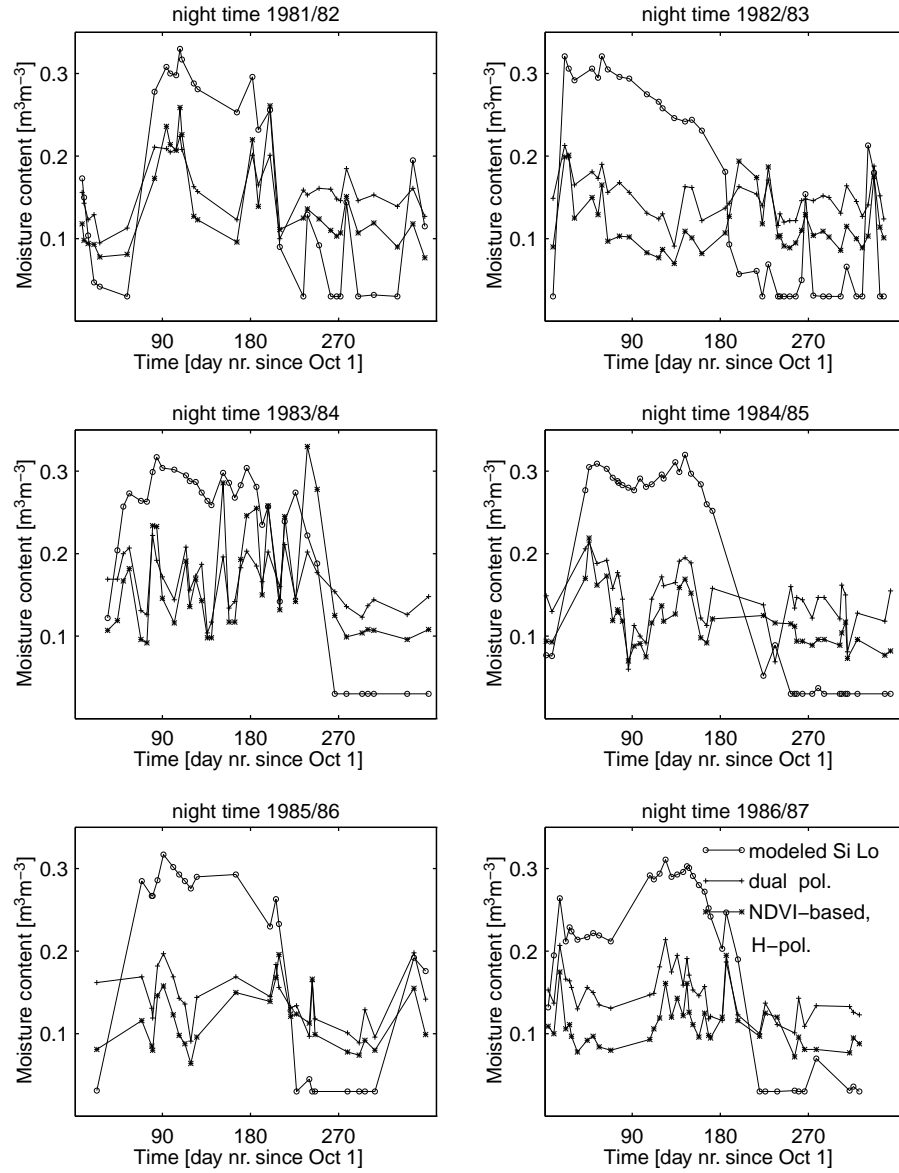
Figure 5.5: *Satellite derived surface moisture content and modeled topsoil mois-*
ture content at night time satellite overpass. Moisture content is derived from
satellite data using the NDVI–based vegetation correction approach at horizontal
polarization and the dual polarization vegetation correction approach. Topsoil
moisture content is modeled using the adjusted 'silt loam' input parameter ma-
trix.
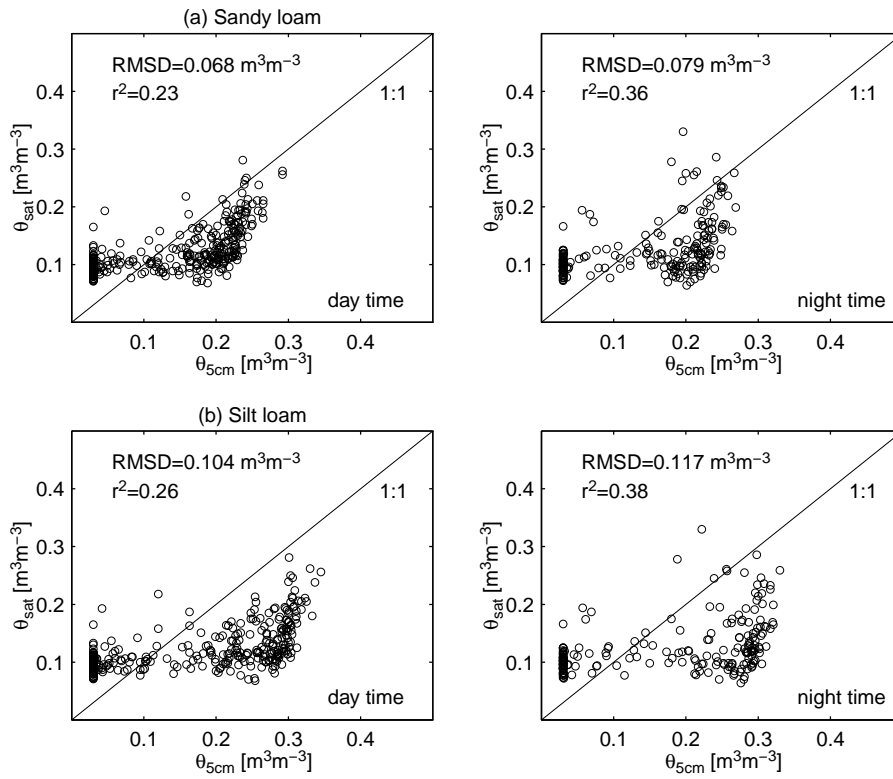
Figure 5.6: *Modeled topsoil moisture content and surface moisture content derived at horizontal polarization using the NDVI–based vegetation correction approach.*
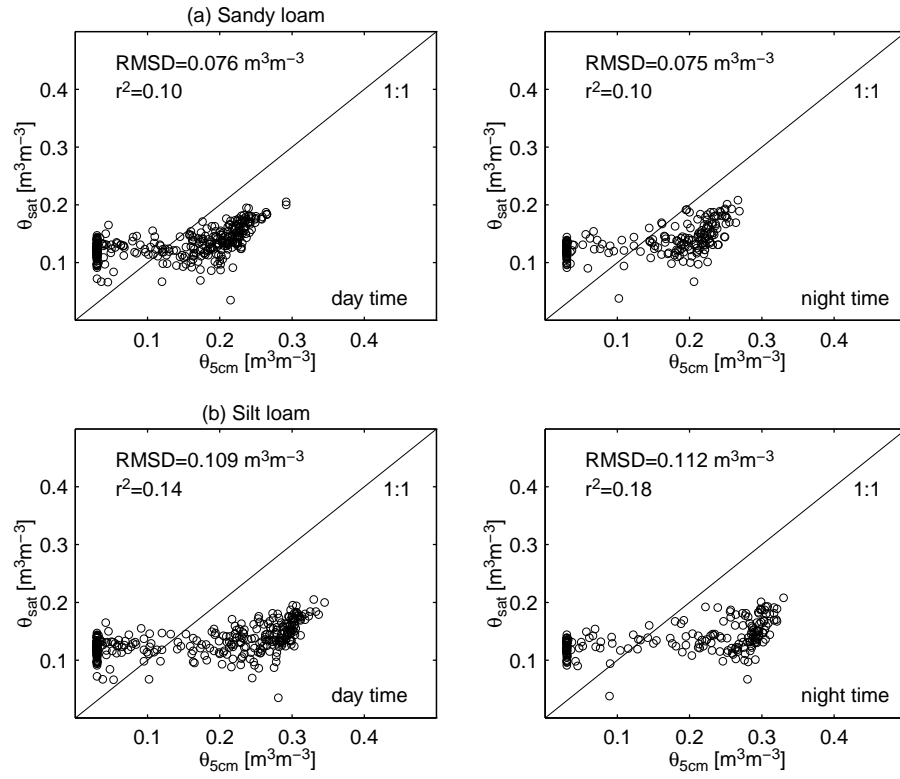
Figure 5.7: *Modeled topsoil moisture content and surface moisture content derived at vertical polarization using the NDVI–based vegetation correction approach.*
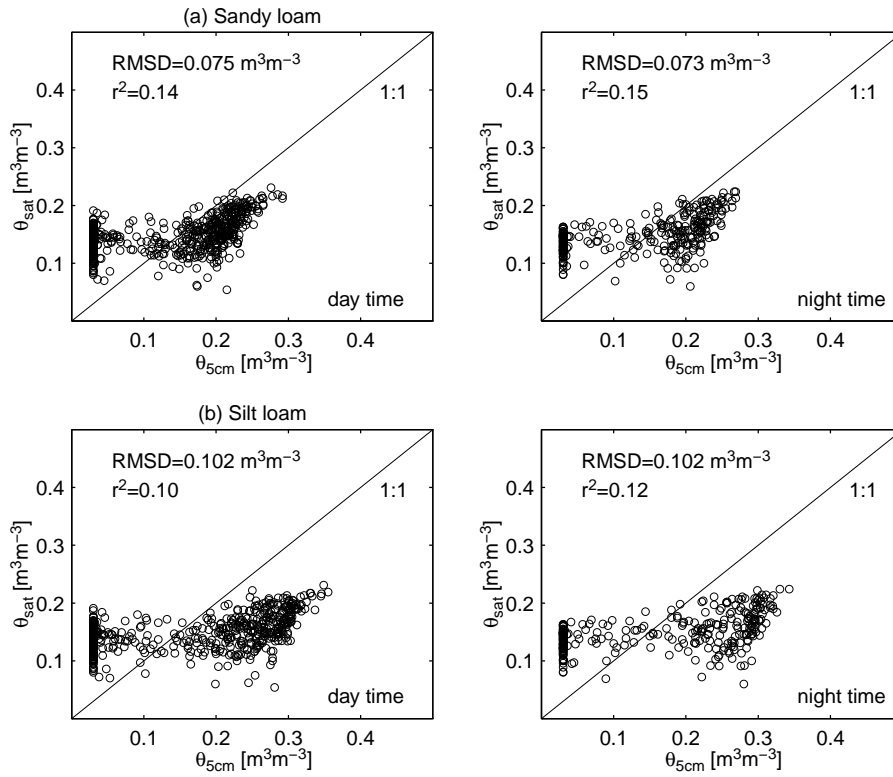
Figure 5.8: *Modeled topsoil moisture content and surface moisture content derived using the dual polarization vegetation correction approach.*

5.3.2   Optimum parameter values

The optimum values of the time–invariant parameters in the radiative transfer equation (Eq. 3.6) are derived by matching the time series of satellite derived surface moisture to the time series of modeled topsoil moisture. For the satellite derived moisture content using the NDVI–based vegetation correction approach, optimimum values of the following parameters are derived:

- h

- ω_{P}

- The linear coefficients of the Γ–NDVI relation

Optimization is carried out at both the horizontal and vertical polarization angle. For the satellite derived moisture content using the dual polarization vegetation correction approach, optimum values of the following parameters are derived:

- h

- ω_{H}

- $A(=\Gamma_{\mathrm{H}}/\Gamma_{\mathrm{V}})$

- $B(=\omega_{\mathrm{H}}/\omega_{\mathrm{V}})$

Matching of the time series of satellite derived surface moisture is carried out for modeled topsoil moisture using both the fixed 'sandy loam' input parameter matrix and the adjusted 'silt loam' input parameter matrix. Furthermore, matching of the time series of moisture content is carried out for both day and night time satellite observations. The time series of satellite derived moisture content using the NDVI–based vegetation correction approach are matched over the period 1981–1987. The time series of satellite derived moisture content using the dual polarization vegetation correction approach are matched over the period 1978–1987.

NDVI–based vegetation correction approach

Fig. 5.11 and Fig. 5.12 present the matched time series of modeled topsoil moisture and satellite derived surface moisture using the NDVI–based vegetation correction approach. Table 5.4 presents the derived optimum parameter values together with the RMSD. Although the matching increases correlation between the time series of soil moisture, the explained variance does not exceed 64%, i.e. $r^2 = 0.41$. The lowest RMSD and the highest correlation is with the time series of modeled topsoil moisture using the fixed 'sandy loam' input matrix. Furthermore, the match is comparatively better at horizontal polarization than at vertical polarization.

Table 5.4: *Optimum parameter values derived by matching the time series of satellite derived surface moisture and modeled 5 cm topsoil moisture.*

Vegetation correction	P	n	h	ω_P	B	Γ_P	A	RMSD
								Day time
					Fixed 'sandy loam' input matrix			
NDVI–based	H	356	2.6	0.17		1.1–0.8(NDVI)		0.062
NDVI–based	V	356	0.0	0.11		0.7–0.0(NDVI)		0.073
Dual polarization		548	1.6	0.15	0.6		0.6	0.060
					Adjusted 'silt loam' input matrix			
NDVI–based	H	356	3.0	0.17		1.1–0.5(NDVI)		0.086
NDVI–based	V	356	1.0	0.11		0.7–0.0(NDVI)		0.098
Dual polarization		548	2.2	0.16	0.6		0.6	0.079
								Night time
					Fixed 'sandy loam' input matrix			
NDVI–based	H	212	3.3	0.12		1.2–0.0(NDVI)		0.066
NDVI–based	V	212	0.8	0.16		0.9–0.5(NDVI)		0.072
Dual polarization		291	1.5	0.14	0.5		0.6	0.061
					Adjusted 'silt loam' input matrix			
NDVI–based	H	212	3.8	0.13		1.3–0.0(NDVI)		0.091
NDVI–based	V	212	1.7	0.17		0.9–0.5(NDVI)		0.098
Dual polarization		291	2.4	0.16	0.8		0.7	0.082

n	Number of days/nights of satellite overpass
P	Polarization angle
h	Soil surface roughness [–]
ω_P	Single scattering albedo at P–polarization angle [–]
B	ω_H/ω_V [–]
Γ_P	Transmissivity at P–polarization angle [–]
A	Γ_H/Γ_V [–]
RMSD	Root Mean Square Difference [m^3m^{-3}]
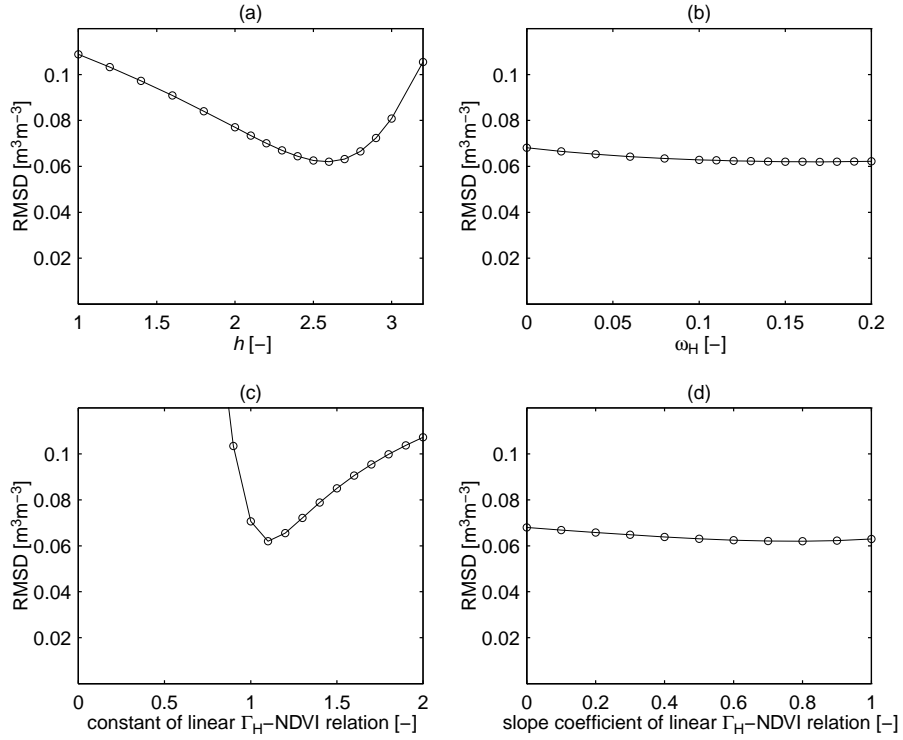
Figure 5.9: *Behaviour of RMSD by varying (a) h (b) ω_{H} (c) the constant of the linear Γ_{H}–NDVI relation (d) the slope coefficient of the linear Γ_{H}–NDVI relation. The time series of satellite derived surface moisture is derived using the NDVI–based vegetation correction approach at day time horizontal polarization. It is compared with the time series of modeled topsoil moisture using the fixed 'sandy loam' input matrix.*

Matching of the time series of surface soil moisture results in some deviating points of low surface moisture content at vertical polarization (Fig. 5.12). Furthermore, the optimization only slightly increases the correlation between the time series of soil moisture by a small increase of the seasonal course of satellite derived surface moisture. It remains smaller however, than the seasonal course of modeled topsoil moisture time series. The small increase in correlation by optimization agrees with the relative insensitivity of the satellite derived surface moisture content to parameter variation at vertical polarization, described in Section 3.5.4.

Optimization of the time—invariant parameters at horizontal polarization leads to a significant increase in correlation and a decrease of the RMSD. The seasonal course of the derived surface moisture is shifted upward however, and increased to a degree that it exceeds the seasonal course of the time series of modeled topsoil moisture. As a result, $\theta_{\mathrm{sat}} > \theta_{\mathrm{5cm}}$ in the dry summer. Apart from a number of outlying points of extremely high soil moisture content, $\theta_{\mathrm{5cm}} < \theta_{\mathrm{sat}}$ for the remainder of the year. Since the depth of the microwave emitting soil is $\sim 1[\mathrm{cm}]$, the relation between θ_{sat} and θ_{5cm} is reversed. The reversed relation may be explained by the matching of satellite derived surface moisture to the large seasonal course of the modeled topsoil moisture.

The significance of the derived optimum parameter values is analysed by studying the behaviour of the RMSD by varying the individual parameter values. The analysis is carried out for all matched time series of surface soil moisture. Fig. 5.9 and Fig. 5.10 present results for the time series of modeled topsoil moisture using the fixed 'sandy loam' input matrix for day time at horizontal and at vertical polarization, respectively. For reasons of brevity not all the analyses are presented, but the results are similar.

Fig. 5.9b shows that the optimum of ω_{H} is not very well defined. In fact, ω_{H} may have any value in the range 0–0.2 without a significant increase in the RMSD. The derived optimum value of ω_{H}=0.17 exceeds the range of values reported in the literature, i.e. $0.04 < \omega_{\mathrm{H}} < 0.12$ (for cultivated vegetation). From Fig. 5.9b it follows that the significance of the optimum value for ω_{H} is comparatively relative. This agrees with the relative insensitivity of the satellite derived surface moisture content to variation of ω_{P}, as described in Section 3.5.4 (see Table 3.13 and Table 3.14). For day time vertical polarization the optimum of ω_{V} is more clearly defined. It may, however, still vary between 0.08–0.14 without a significant increase in the RMSD, as illustrated in Fig. 5.10b.

The optimum value of the slope coefficient for the linear relation Γ_{H}–NDVI is not clearly defined, as illustrated in Fig. 5.9d. This may explain the variation in the optimum value for $C_{\mathrm{NDVI,P}}$ at horizontal and vertical polarization (see Table 5.4). The optimum of $C_{\mathrm{NDVI,H}} = 0$ at night time is relatively well defined, i.e. comparable to the optimum value of $C_{\mathrm{NDVI,V}} = 0$ at daytime (Fig. 5.10d). An optimum of $C_{\mathrm{NDVI,P}} = 0$ implies that Γ_{P} is a constant, independent of NDVI. Furthermore, when $C_{\mathrm{NDVI,P}} = 0$, the optimum of Γ_{H} is > 1 (see Table 5.4).

The optimum for h is well defined at horizontal and vertical polarization for different values. At vertical polarization, the optimum value of $h = 0$ is most clearly defined (see Fig. 5.10a). At horizontal polarization all optima are about

equally well defined for $h > 0$. The optimum value for h is determined by the match of the time series of satellite derived surface moisture to the seasonal course of the modeled topsoil moisture. Since at vertical polarization the seasonal course of the matched time se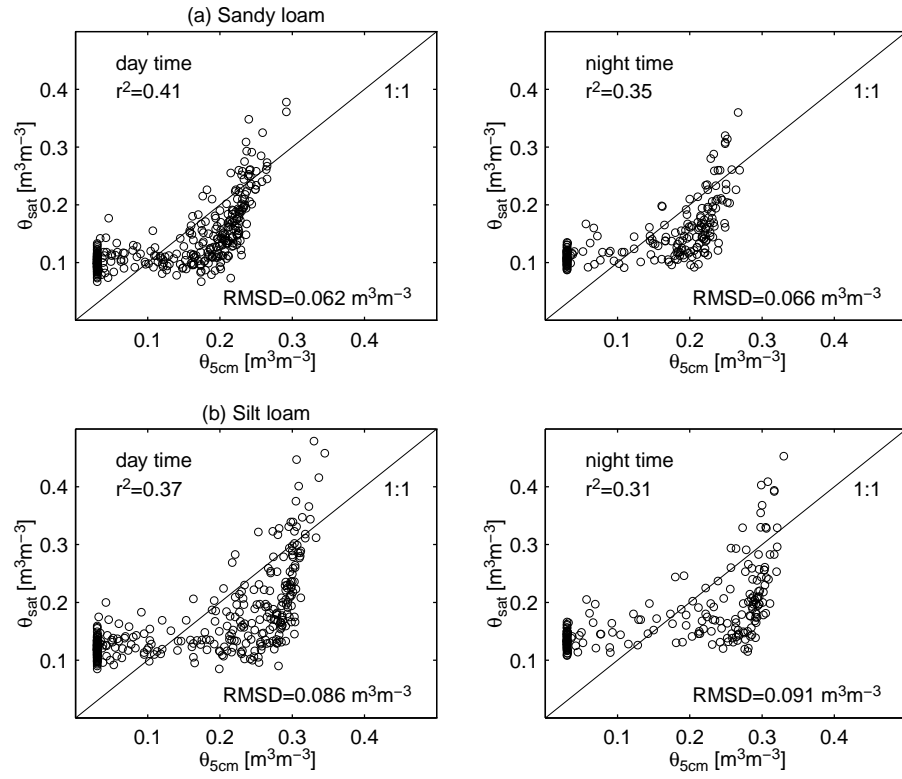ries of satellite derived surface moisture is relatively small, h is relatively small. Furthermore, since it is determined by the seasonal course of the matched time series of satellite derived surface moisture, it is difficult to relate the optimum value for h to an average footprint surface roughness. A value of $h > 0$ may, however, relate to the footprint relief, i.e. the central Llanura Manchega plain surrounded by the basin boundary hills.

In summary, it appears that the time series of satellite derived surface moisture using the NDVI–based vegetation correction approach and the modeled topsoil moisture do not match very well. Deviating points of low moisture content occur at vertical polarization and the seasonal course of derived surface moisture is small. At horizontal polarization, deviating points of high moisture content occur. Furthermore, $\theta_{\mathrm{sat}} > \theta_{\mathrm{5cm}}$ in summer, while in the remainder of the year $\theta_{\mathrm{sat}} < \theta_{\mathrm{5cm}}$. The match with the time series of modeled topsoil moisture using the fixed 'sandy loam' input matrix is best with an $r^2 = 0.41$, i.e. an explained variance of 64%. The RMSD is 0.062 $\mathrm{m}^3\mathrm{m}^{-3}$ however, i.e. over 40% of the average θ_{5cm}.

The optimum values for the time–invariant parameters are not well defined and/or rather inconsistent. While ω_{P} may have a broad range of values, the optimum value for Γ_{P} appears to be a constant close to 1, independent of NDVI. Since the optimum for h is determined by the seasonal course of the matched time series of satellite derived surface moisture, it is difficult to relate it to an average footprint soil surface roughness.
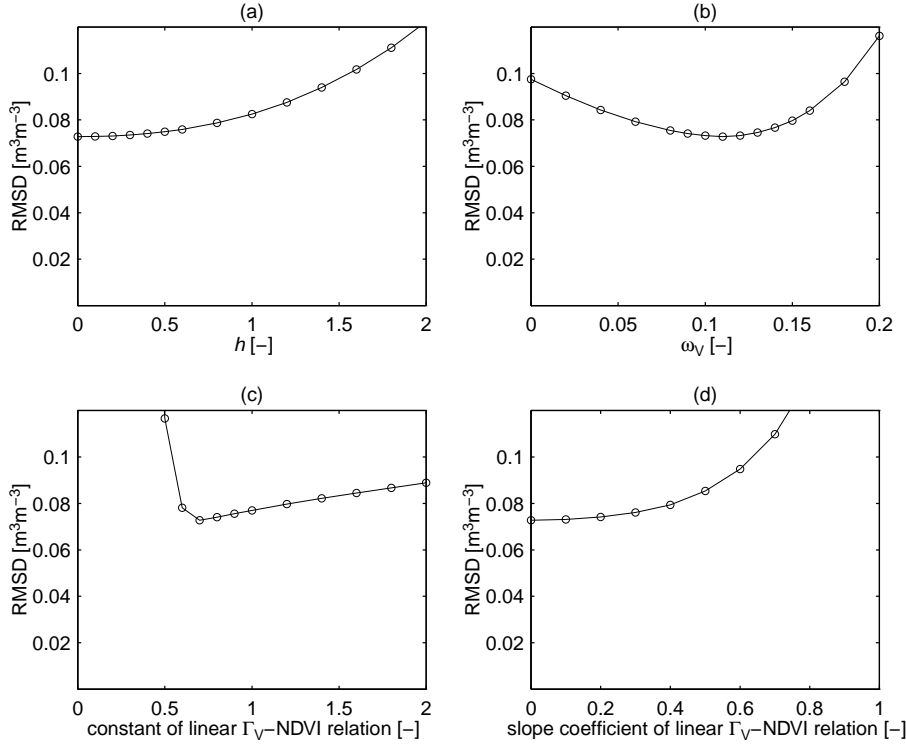
Figure 5.10: *Behaviour of RMSD by varying (a) h (b) ω_V (c) constant of the linear Γ_V–NDVI relation (d) slope coefficient of the linear Γ_V–NDVI relation. The time series of satellite derived surface moisture is derived using the NDVI—based vegetation correction approach at day time vertical polarization. It is compared with the time series of modeled topsoil moisture using the fixed 'sandy loam' input matrix.*

Figure 5.11: *Satellite derived surface moisture content matched to modeled top-soil moisture content. Moisture content is derived using the NDVI–based vegetation correction approach at horizontal polarization.*
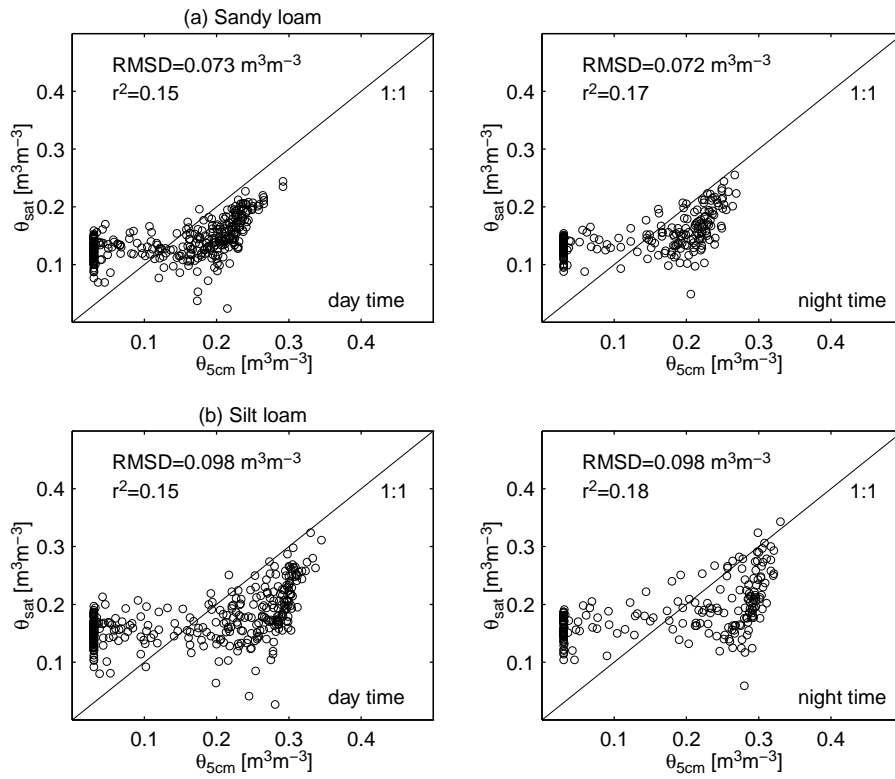
Figure 5.12: *Satellite derived surface moisture content matched to modeled top-soil moisture content. Moisture content is derived using the NDVI–based vegetation correction approach at vertical polarization.*

Dual polarization vegetation correction approach

Fig. 5.14 to Fig. 5.19 present the matched time series of modeled topsoil moisture content and satellite derived surface moisture content using the dual polarization vegetation correction approach. Table 5.4 presents the derived optimum parameter values together with the RMSD. Optimization of the time–invariant parameters results in a significant increase in correlation and a decrease of the RMSD. Similarly to the NDVI–based vegetation approach, the match of modeled topsoil moisture time series using the fixed 'sandy loam' input matrix is best. The seasonal course and the range of moisture conditions for the satellite derived surface moisture and modeled topsoil moisture compare relatively well. This is reflected by the relatively high correlation coefficient.

The significance of the derived optimum parameter values is studied by analysing the sensitivity of the RMSD to variation of the individual parameter values. The analysis is carried out for day and night time and for both the time series of modeled topsoil moisture. Fig. 5.13 presents the result for the time series of modeled topsoil moisture using the fixed 'sandy loam' input matrix at daytime. For reasons of brevity results from the remaining analyses are not presented, but are comparable.

Figure 5.13d shows that the optimum for B ($= \omega_H/\omega_V$) is least clearly defined. A value of $0.3 < B < 1.2$ has no significant effect on the RMSD. It appears therefore, that ω_V may be approximately equal to ω_H. The optimum value of $\omega_H = 0.16$ (Fig 5.13c) exceeds, however, the range of values reported in the literature (see previous section). Although a local minimum is present at low ω_H values, the optimum is relatively clearly defined.

Fig. 5.15 presents the interdependency of Γ_H and NDVI at dual polarization with parameter values in the range $0.4 < \Gamma_H < 1$. Although some linear dependency may be present, the two parameters appear independent at low Γ_H and at low NDVI. This agrees with the finding in the previous section with regard to the parameterization of Γ_P using NDVI. Γ_H appears, however, to be constant only at the minimum value. The optimum of A($= \Gamma_H/\Gamma_V$) < 1 is well defined (Fig. 5.13b), though RMSD increases comparatively slowly towards values of $A > 0.6$. When $A < 1$, the maximum values of Γ_V are close to and/or in excess of 1 (see Fig. 5.15).

While the optimum value of the time–invariant radiative transfer parameters is consistent, the optimum value for h is different for the match with the two time series of modeled topsoil moisture. Due to the larger seasonal course, the optimum value for h when matching the time series of modeled topsoil moisture using the 'silt loam' input matrix is larger. Since two optimum values for h are derived to fit the two time series of modeled topsoil moisture, it is difficult to relate h to a footprint average surface roughness. As mentioned in the previous section, a value of surface roughness > 0 may relate to the flat central Llanura Manchega plain surrounded by the basin boundary hills.

In summary, the time series of satellite derived surface moisture using the dual polarization vegetation correction approach and modeled topsoil moisture may be matched. The optima for ω and Γ are, however, close to or in excess of their

maxima. The maxima probably result from fitting the satellite derived surface moisture to the large seasonal course of the modeled topsoil moisture. Apart from soil surface roughness, the optimum for the time–invariant parameter values is consistent. The match is best with the time series of modeled topsoil moisture using the fixed 'sandy loam' input matrix with an explained variance of 76% ($r^2 = 0.59$). The RMSD is, however, 0.060 m^{3}m^{-3}, i.e. over 40% of the average θ_{5cm}.
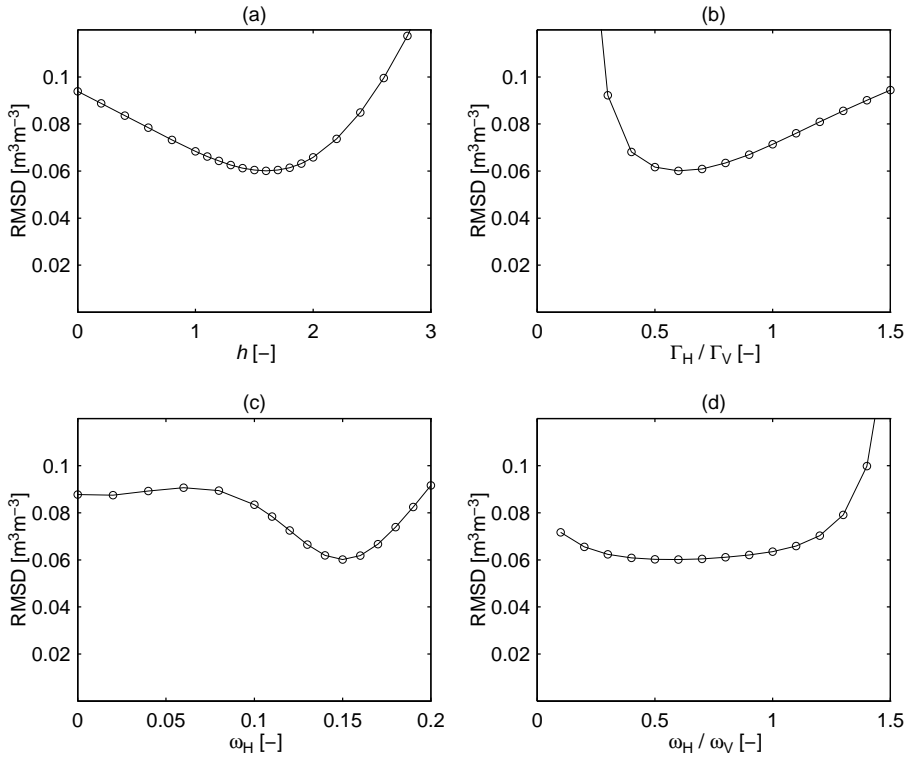

Figure 5.13: *Behaviour of RMSD by varying (a) h (b) A (=Γ_H/Γ_V) (c) ω_H (d) B (=ω_H/ω_V). The time series of surface moisture is derived by the dual polarization vegetation correction approach at day time. It is compared with the time series of modeled topsoil moisture using the fixed 'sandy loam' input matrix.*

Conclusions

While peaks in the moisture content caused by precipitation generally coincide, the difference between the time series of modeled topsoil moisture and satellite derived surface moisture lies mainly in the seasonal course. The range of satellite derived surface moisture using the radiative transfer parameter values applied in Chapter 3 is smaller than that for the modeled topsoil moisture, as shown in Fig. 5.4 and Fig. 5.5. Matching the range of moisture conditions by optimization of the time–invariant parameters in the radiative transfer function is comparatively more successful using the dual polarization vegetation correction approach than from the NDVI–based vegetation correction approach. Furthermore, the optima of the time–invariant parameters are more consistent and more clearly defined. The optima of the time–invariant radiative transfer parameters are, however, close to or slightly in excess of their maximum values. The optimum for Γ_P using the NDVI–based approach appears to be a constant close to 1, independent of NDVI.

The maxima for the time–invariant parameters are forced by matching the time series of satellite derived surface moisture to the seasonal course of the time series for modeled topsoil moisture. This may indicate that the seasonal course of the modeled topsoil moisture is in excess of the maximum seasonal course of the time series for satellite derived surface moisture. The seasonal course of modeled topsoil moisture time series may be diminished by adjusting the soil hydraulic properties in the soil moisture model by a change of soil type to loamy sand or sand (see Section 4.4.2). This, however, further increases the modeled downward moisture percolation in excess of the recharge estimate from river flow (see Section 5.2.2).

In summary, it is possible to match the time series for satellite derived surface moisture and modeled topsoil moisture using the dual polarization vegetation approach. The maximum explained variance is 77%, i.e. r^2=0.59. The minimum RMSD, however, is 0.060 m^{3}m^{-3}, i.e. over 40% of the average θ_{5cm}. The substantial difference between modeled soil moisture and satellite derived surface moisture may be explained by comparison of the soil moisture over different depths. While the microwave emitting layer is $\sim$ 1 cm, topsoil moisture is modeled over 5 cm depth. This may explain the relatively strong alternation in the satellite derived moisture content, as illustrated in Fig. 5.16 to Fig. 5.19. In summer, however, $\theta_{sat} > \theta_{5cm}$, while in the remainder of the year $\theta_{sat} < \theta_{5cm}$. Since the depth of the microwave emitting layer is relatively shallow, the relation between θ_{sat} and θ_{5cm} is reversed. The reversed relation may be explained by matching the time series for satellite derived surface moisture to the large seasonal course of the modeled topsoil moisture. A less pronounced seasonal course would improve the match for the soil moisture time series. It may furthermore re–invert the relation between θ_{sat} and θ_{5cm}.
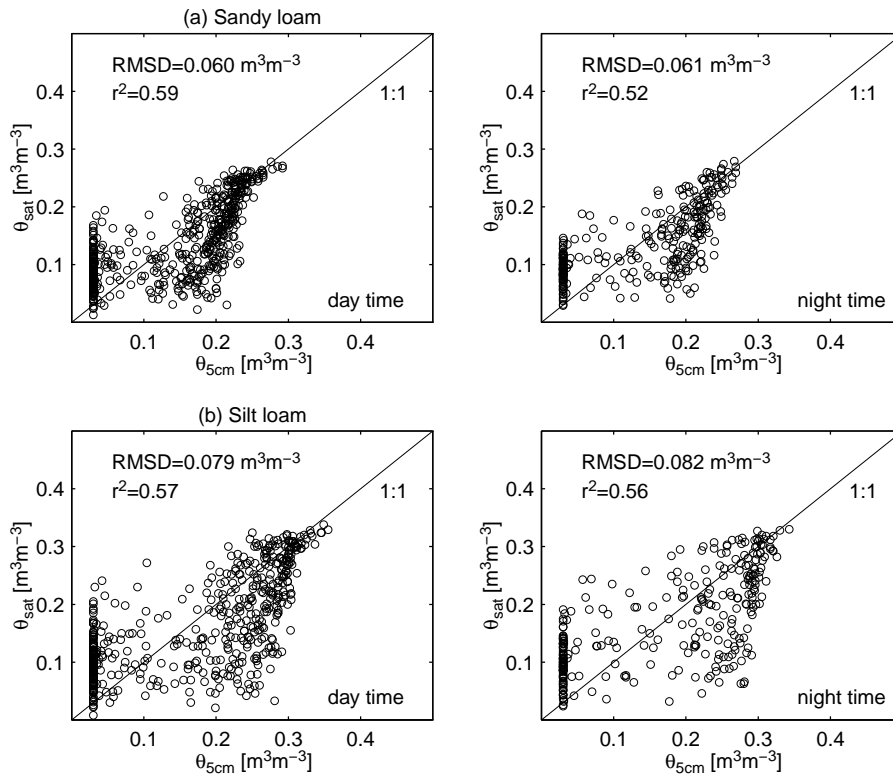
Figure 5.14: *Satellite derived surface moisture content matched to modeled top-soil moisture content. Moisture content is derived using the dual polarization approach.*
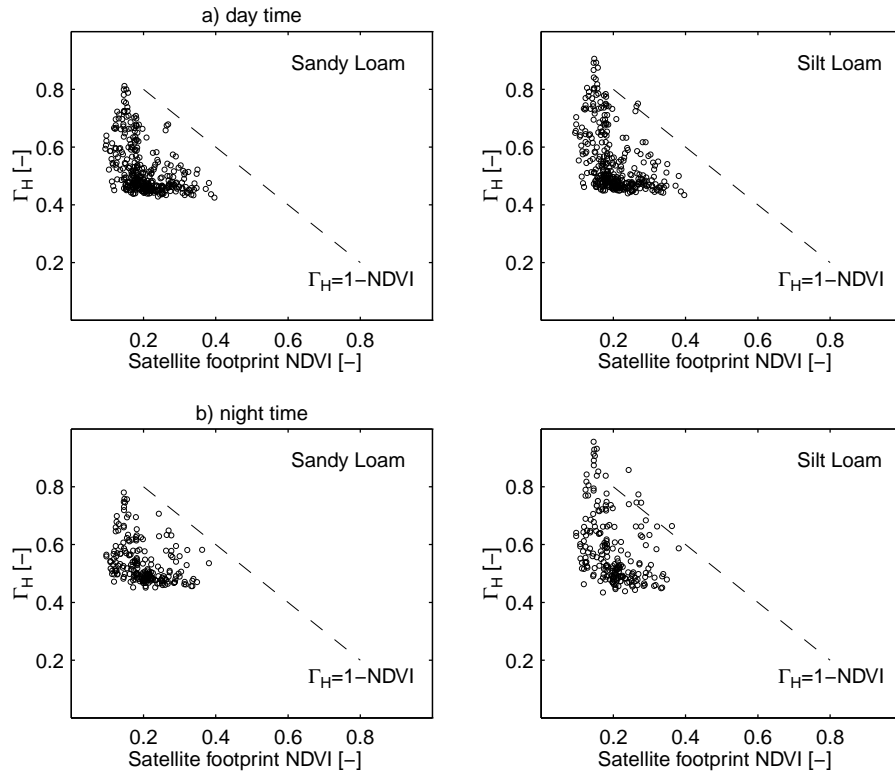
Figure 5.15: *Optimum values of* Γ_H *derived using the dual polarization vegetation correction approach plotted against NDVI. With* A <1, *the optimum values of* Γ_V *exceed 1.*
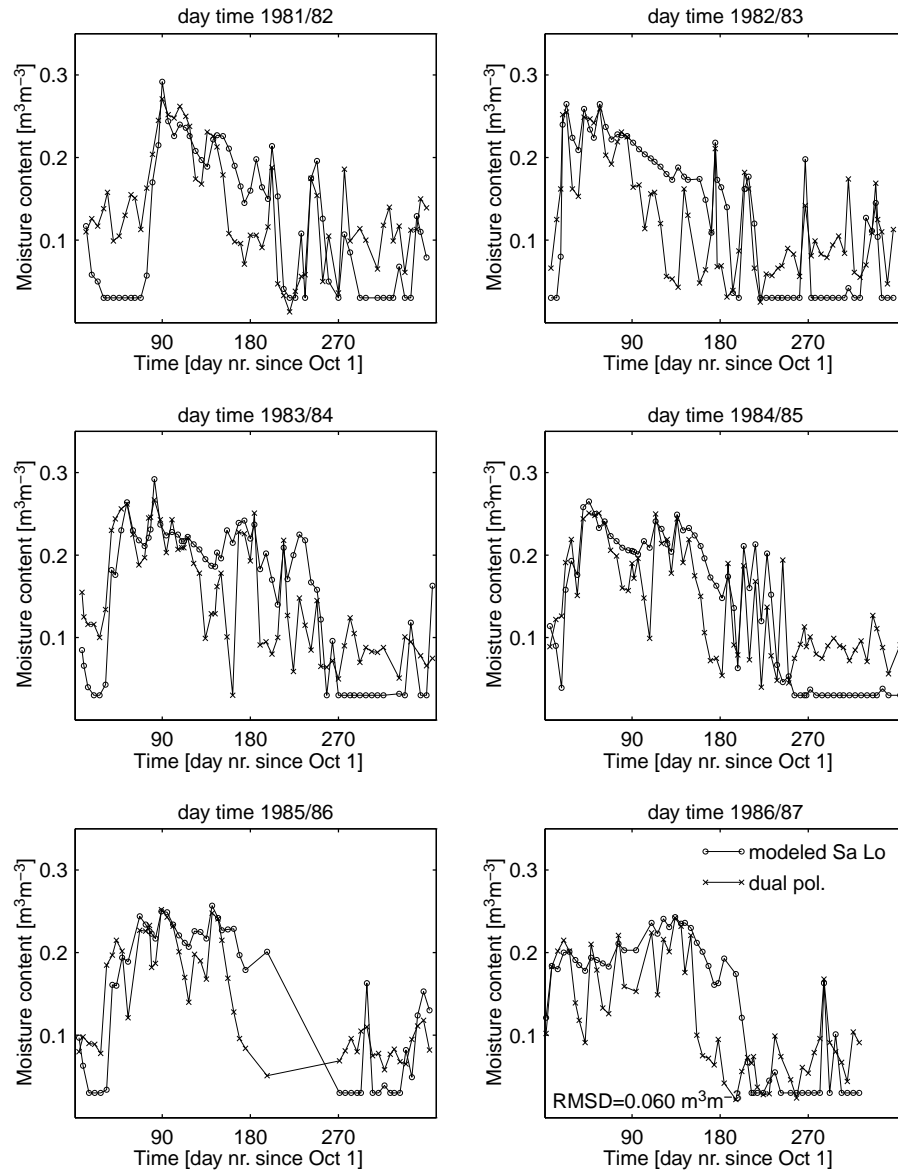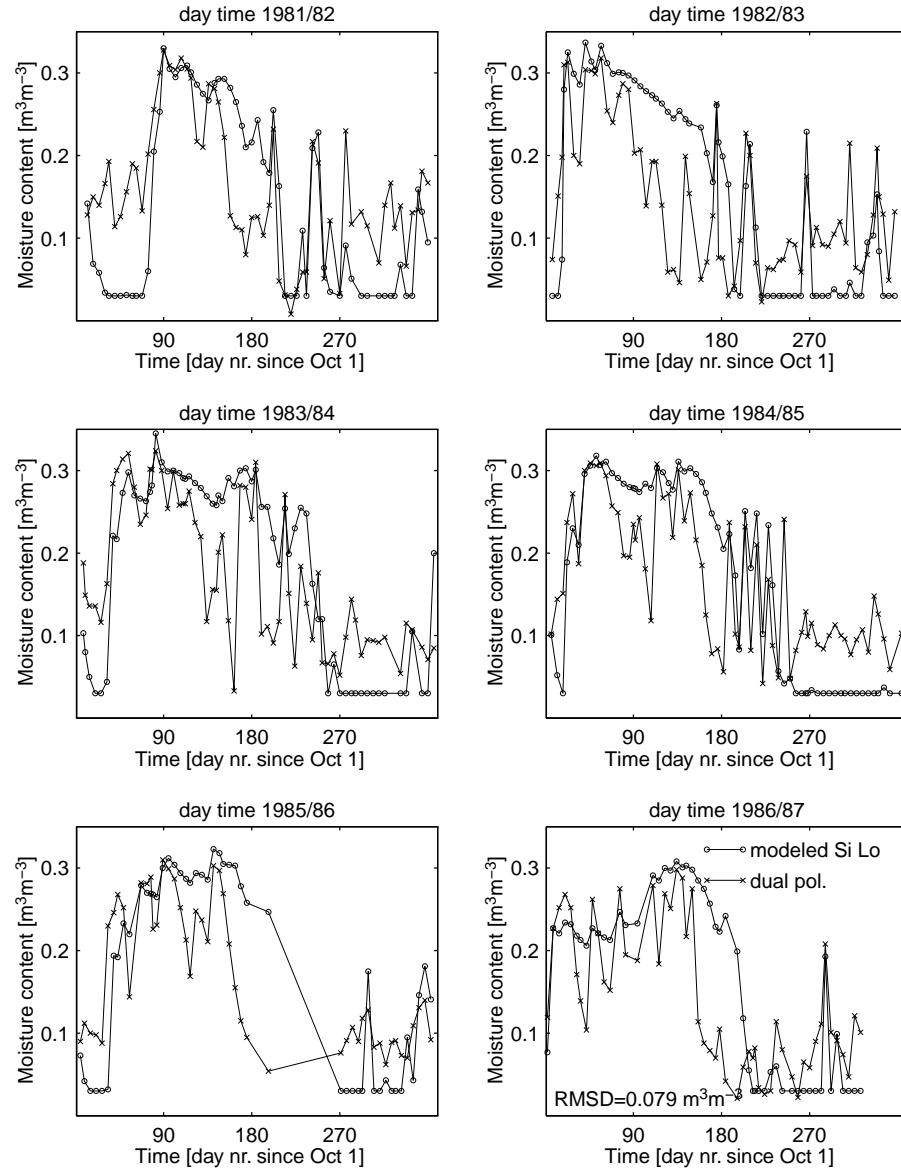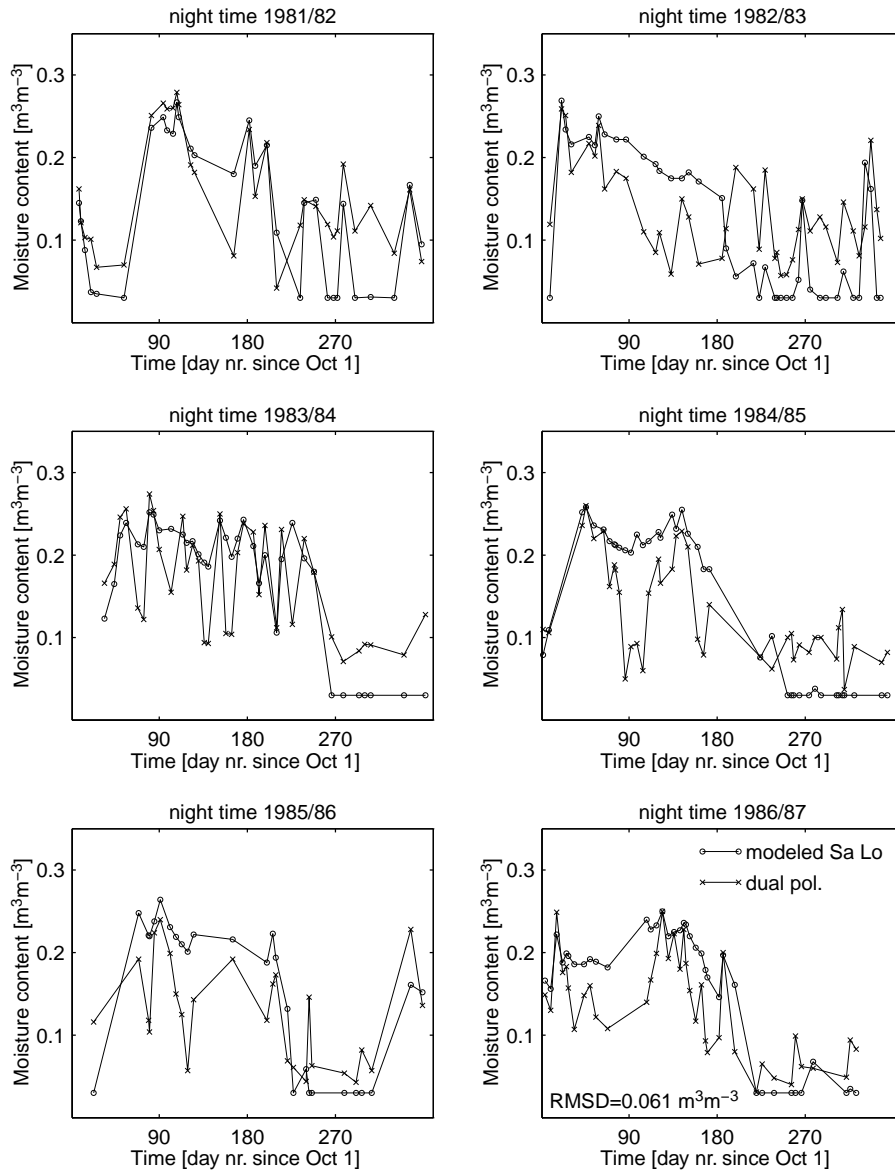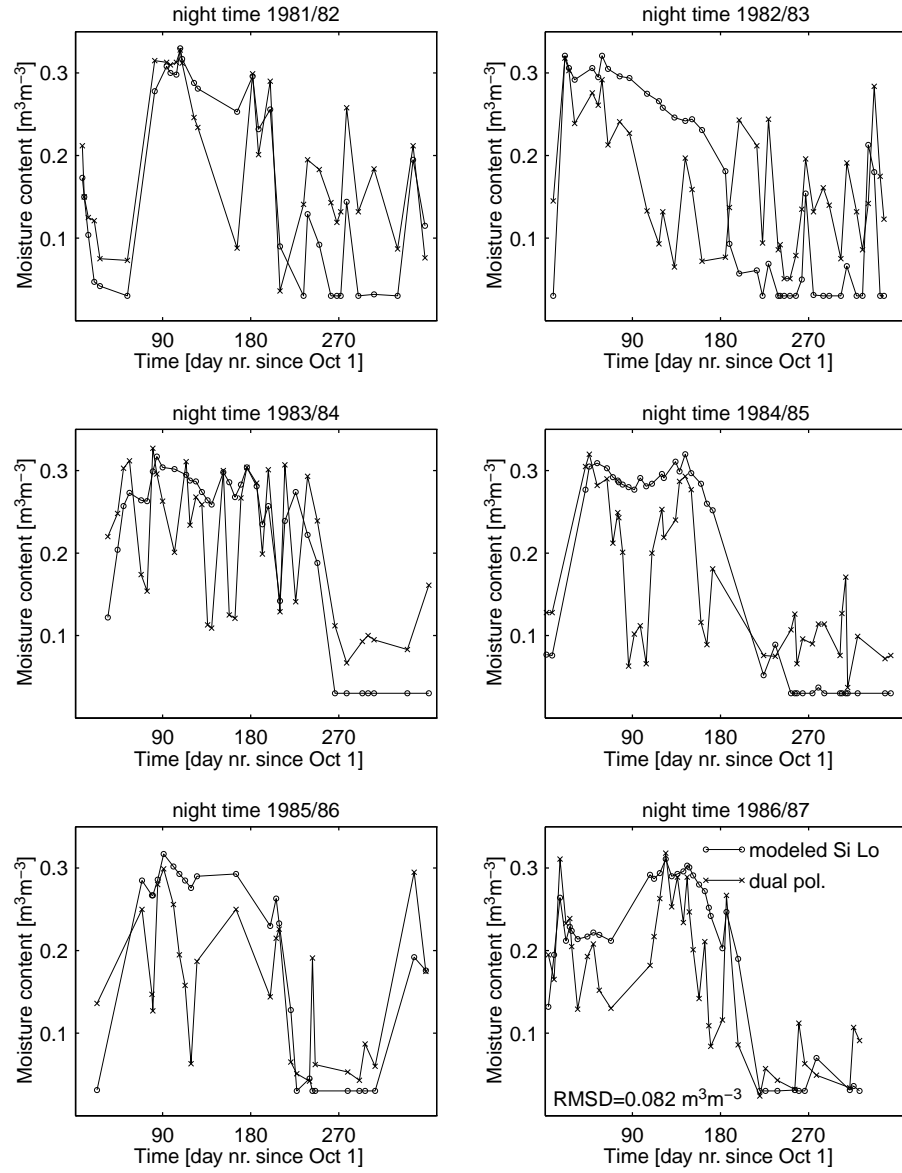
Figure 5.16: *Satellite derived surface moisture content matched to modeled top-soil moisture content at day time satellite overpass. Moisture content is derived using the dual polarization vegetation correction approach. Topsoil moisture content is modeled using the fixed 'sandy loam' input parameter matrix.*

Figure 5.17: *Satellite derived surface moisture content matched to modeled top-soil moisture content at daytime satellite overpass. Moisture content is derived using the dual polarization vegetation correction approach. Topsoil moisture content is modeled using the adjusted 'silt loam' input parameter matrix.*

Figure 5.18: *Satellite derived surface moisture content matched to modeled top-soil moisture content at night time satellite overpass. Moisture content is derived using the dual polarization vegetation correction approach. Topsoil moisture content is modeled using the fixed 'sandy loam' input parameter matrix.*

Figure 5.19: *Satellite derived surface moisture content matched to modeled top-soil moisture content at night time satellite overpass. Moisture content is derived using the dual polarization vegetation correction approach. Topsoil moisture content is modeled using the fixed 'silt loam' input parameter matrix.*

5.4 Conclusions

The annual modeled downward moisture percolation at the bottom layer of the soil profile using hydraulic properties of a sandy loam soil type and a 50 cm soil profile depth, exceeds the annual long–term recharge estimate from river flow by several times. A doubling of the transpiration rate by deep rooted vegetation leads to a more comparable moisture percolation rate. An adjustment of the hydraulic properties by a change of soil type to silt loam and an increase in the soil profile depth to 75 cm, also leads to an improved downward percolation estimate.

The seasonal course of the time series for satellite derived surface moisture is much smaller than that of the time series for modeled topsoil moisture. Peaks in the moisture content caused by precipitation, however, generally coincide.

Since the seasonal course for the time series of soil moisture is not comparable, the series are subsequently matched by optimization of the parameter values in the radiative transfer equation. Using the NDVI–based vegetation correction approach, the range of moisture conditions for the time series of satellite derived surface moisture and that for the modeled top soil moisture remains relatively incomparable. Furthermore, the optima of the time–invariant parameters in the radiative transfer function do not have consistent values and/or are not well defined. The optimum value for the radiative vegetation transmissivity appears to be a constant close to 1, independent of NDVI. In the present study the parameterization of Γ_P as a linear function of NDVI is therefore not very reliable. Using the dual polarization vegetation correction approach, the range of moisture conditions for the matched soil moisture time series compares relatively well. The optimum time–invariant parameter values are more consistent and more clearly defined, although they are close to the maximum value. This may indicate that the seasonal course of the time series for modeled topsoil moisture is close to or in excess of the maximum seasonal course of the time series for satellite derived surface moisture. An adjustment to the soil hydraulic properties in the soil moisture balance model by a change in soil type to loamy sand or sand would decrease the seasonal course. It would, however, further increase the modeled downward moisture percolation in excess of the recharge estimate from river flow.

In the research approach followed, the recharge estimate from river flow is used as an indication for model results. The best match of the time series for satellite derived surface moisture is with the time series for modeled topsoil moisture using a sandy loam soil type. An increase in the transpiration rate by deep rooted vegetation therefore seems the proper adjustment to the model results. The feasibility of validating the satellite derived surface moisture using recharge as a control would be improved by a reliable regional estimation of the transpiration rate. A sound estimation of the transpiration rate may also provide an indication for the soil hydraulic properties.

The time series of surface moisture may be derived from passive microwave data with a 43% relative difference with the mean θ_{5cm}. This substantial difference may be explained by comparising soil moisture over different depths. While

the microwave emitting soil layer is ~ 1 cm, the moisture modelling depth is 5 cm. This may account for the relatively large fluctuation in the satellite derived surface moisture content. In summer, however, $\theta_{sat} > \theta_{5cm}$, while in the remainder of the year $\theta_{sat} < \theta_{5cm}$. Since the depth of the microwave emitting layer is relatively shallow, the relation between θ_{sat} and θ_{5cm} is reversed. The reversed relation may be explained by the matching of satellite derived surface moisture to the large seasonal course for the modeled topsoil moisture. A decreased seasonal course would improve the time series match of soil moisture and may re–invert the relation between θ_{sat} and θ_{5cm}. A less pronounced seasonal course is obtained by adjustment of the soil hydraulic properties in the soil moisture balance model by a change in soil type to loamy sand or sand. Such an adjustment would, however, further increase the modeled downward moisture percolation in excess of the recharge estimate from river flow. As mentioned above, a sound estimation of the regional transpiration rate by deep rooted vegetation would help in evaluating the feasibility of such an adjustment.

When matching the time series for modeled topsoil moisture and satellite derived surface moisture using the dual polarization vegetation correction approach, the optima for the time–invariant parameters are consistent. The soil surface roughness, h, appears to be the only parameter that may be related to the modeled downward vertical moisture percolation. It should therefore be possible to estimate downward moisture percolation when h is known. However, since the difference between satellite derived surface moisture and modeled topsoil moisture is substantial, the value of the estimated downward moisture percolation is uncertain. Furthermore, a reliable estimate of the regional transpiration rate by deep rooted vegetation is required.

In summary, validation of the time series for satellite derived surface moisture proves to be laborious, potentially inaccurate and data demanding. Additionally, the difference between the time series of modeled topsoil moisture and satellite derived surafe moisture is substantial. The validation of the time series of satellite derived surface moisture using the regional (soil) water balance is therefore limited.

Chapter 6

Conclusions and recommendations

Objective and approach   The primary objective of the present study is to investigate the potential of passive microwave surface moisture monitoring as a tool for the detection of regional scale climate variability and land–use change. This is carried out by a retrospective analysis of long–term time series of meteorological, hydrological and remote sensing data for the West La Mancha region in semi–arid central Spain. The analysis is based on derivation of regional surface moisture from passive microwave data and the regional application of a soil moisture balance model. The time series of hydrological data are used as a control on the soil moisture balance results and, as such, on the satellite derived surface moisture. If the proposed method is succesful, then passive microwave observations may be used to assess regional surface moisture and subsequently to estimate individual components in the regional waterbalance, e.g. recharge. A reliable assessment of recharge from satellite observations may assist in efforts towards a more sustainable development of the West La Mancha region.

Satellite passive microwave observations   Since the onset of large–scale water abstraction for irrigated cultivation in the early 1970s, the West La Mancha area has experienced a considerable decline in the groundwater level of its main aquifer. Coinciding with a drought period in the 1980s, groundwater fell to a dangerously low level and rivers and wetlands dried up. The lifetime of Nimbus–7/SMMR from 1978–1987 corresponds with this drought period. Based on solving the radiative transfer function for vegetation covered areas, relatively dry and wet years are discerned. No drying trend, however, is found in the time series of derived surface moisture and the effects of irrigation and/or land–use change are also not detected.
Two methods are used to solve the radiative transfer equation, which differ in the way the contribution of vegetation to the microwave signal is corrected for. One method uses NDVI to parameterize vegetation transmissivity and is called the

NDVI–based vegetation correction approach. A second method uses constant ratios of the vegetation radiative transfer properties to solve the equation at two polarization angles and is called the dual polarization vegetation correction approach. Vegetation radiative transfer properties derived from a ground–based microwave experiment are implemented in the radiative transfer equation to assist with interpretating the satellite data. The application of experimentally derived vegetation radiative properties results in two non–corresponding time series of satellite derived surface moisture using the two vegetation correction approaches. An adjustment of the vegetation radiative transfer properties to match the time series of satellite derived surface moisture leads to a domination of the radiative transfer function at the vertical polarization angle. As a result, the time series of satellite derived surface moisture lack a clear seasonal cyclicity and the range of moisture conditions is relatively small. A change in the vegetation radiative transfer properties leads to a more pronounced seasonal course and an increase in the range of moisture conditions. This leads simultaneously to non–corresponding time series of derived surface moisture at horizontal and vertical polarization using the NDVI–based vegetation correction approach. Matching the time series for satellite derived surface moisture to those for regional surface moisture provides more clarity on the value of the (time–invariant) parameters in the radiative transfer function. Furthermore, it may indicate which of the two vegetation correction approaches is the more valid. Since no time series of regional surface moisture are available, the time series of satellite derived surface moisture are compared to those for modeled topsoil moisture.

An estimate of regional surface temperature is required in order to determine the satellite observed passive microwave emissivity. The use of daily air temperature data from regional meteorological stations leads to time series of satellite derived surface moisture that are consistent and comparable at day and night time. It appears therefore, that the air temperature data are a reasonable estimate of day and night time surface temperature . Due to the relatively large spatial variation of surface temperature in day time, the T_s estimate at night time is considered more reliable.

Soil moisture balance model   The time series of topsoil moisture are modeled using a regional scale soil moisture balance approach. Implementation of the soil moisture balance model to the West La Mancha area implies some assumptions as to the representativeness of a number of the model parameters. A parameter sensitivity study indicates that model results are most sensitive to soil hydraulic properties, the soil profile depth and precipitation. The moisture model results are relatively insensitive to a direct or indirect increase in evapotranspiration. A decrease in *ET* leads, however, to a relatively large increase in topsoil moisture content. This seems to indicate that evapotranspiration is at a near–maximum depletion rate for the topsoil.

In the soil moisture balance model evaporative loss from the topsoil is computed using a modified *Priestley–Taylor PET* concept. In this modified concept

an evaporative fraction curve relates evapotranspiration to topsoil moisture content. Construction of an area–averaged evaporative fraction curve for bare soil surfaces and surfaces with shallow rooted vegetation is feasible using experimental data from the EFEDA campaign. Derivation of a separate curve for deep rooted vegetation is hampered, however, by the absence of ample experimental data. Transpiration by deep rooted vegetation is therefore not considered in the soil moisture balance model. Alternatively, it is estimated on the basis of reported rates of vine transpiration in the literature and the regional surface cover fraction of deep rooted vegetation. Estimation of the transpiration rate by deep rooted vegetation is required for closure of the regional water balance. A proper representation of irrigation is complicated by the regional scale application of the soil moisture balance model. The area under irrigation has increased from 3% to 10% of the total surface area between 1974–1987, while the annual amount of irrigated water has increased from 10 mm to 40 mm. The time series of modeled topsoil moisture show no effect of irrigation, however, since all irrigated water evapotranspires. This is probably explained by the high evaporative demand during the months of irrigation. The spatial averaging of the depth of irrigated water further prevents it from draining to depth.

The use of 24–hour averages of net radiation results in an underestimation of daily evapotranspiration. This may be compensated by a 20% increase in the daily ET estimate. Neglect of rainfall intensity results in an underestimation of the downward moisture percolation. The combination of a rainfall depth/duration distribution and a diurnal course of R_n indicates that model results are relatively more sensitive to the diurnal course of R_n.

The time series of modeled topsoil moisture over the period 1975–1991 show that the seasonal course is relatively large. While on the regional scale one would expect the extremes in moisture content to be levelled out to some degree, the large seasonal course may be explained by the shallow 5 cm topsoil modelling depth. With regard to moisture fluxes, the model results generally follow the year–to–year variation in precipitation. The distribution of precipitation over the year, the energy available for evapotranspiration and the (antecedent) moisture condition, also seasonally affect the model results.

Recharge and soil moisture Long–term annual recharge of the West La Mancha region is estimated on the basis of river flow at the outlet of the Upper Guadiana Catchment. The annual modeled downward moisture percolation rate at the bottom layer of the soil profile exceeds this estimate by several times. A doubling of the transpiration rate by deep rooted vegetation leads to a more comparable annual percolation rate. Alternatively, an adjustment in the soil moisture balance model soil hydraulic properties by a change of soil type from sandy loam to silt loam and an increase in the soil profile depth, also lead to an improved percolation estimate.

The seasonal course of the time series for modeled topsoil moisture is considerably larger than that for the satellite derived surface moisture. Peaks in the moisture content do coincide, however. Since the seasonal courses of the time

series for satellite derived surface moisture and modeled topsoil moisture do not compare, a time series matched is attempted by optimizing the time–invariant parameter values in the radiative transfer function. Using the NDVI–based vegetation correction approach, the range of moisture conditions remains relatively incomparable. Furthermore, the optima for the time–invariant parameter values in the radiative transfer function do not have consistent values and/or are not well defined. The optimum value for vegetation transmissivity appears to be a constant close to 1, independent of NDVI. In the present study the parameterization of Γ_P as a linear function of NDVI appears, therefore, to be not very reliable. Although parameterization of Γ_P as a non–linear function of NDVI may lead to better results, the value for the NDVI–based vegetation correction approach seems uncertain.

Using the dual polarization approach, the range of moisture conditions for the matched time series of soil moisture compares relatively well. The optima of parameter values are consistent, though they are close to their maximum value. This may indicate that the seasonal course of the time series for modeled topsoil moisture is close to or in excess of the maximum seasonal course for the satellite derived surface moisture.

In the research approach followed the recharge estimate from river flow is used as a control on model results. The best match of the time series for satellite derived surface moisture is with that for modeled topsoil moisture using the sandy loam soil type. The root mean square error is 0.060 $\mathrm{m^3m^{-3}}$, i.e. 43% of the mean θ_{5cm}. An increase in the transpiration rate by deep rooted vegetation therefore seems the proper adjustment to the model results. The feasibility of validating the satellite derived surface moisture using regional recharge as a control would be improved by reliable estimation of the regional transpiration rate by deep rooted vegetation.

The time series of surface moisture may be derived from passive microwave data with a 43% deviation from the mean θ_{5cm}. This substantial difference may be explained by the comparison of soil moisture over different depths. The shallow microwave emitting layer of ~ 1 cm explains the larger alternation in satellite derived surface moisture content. In summer the satellite derived surface moisture content, however, generally exceeds the modeled topsoil moisture content, while in the remainder of the year the modeled topsoil moisture is higher. The reversed relation may be explained by matching the time series for satellite derived surface moisture with the large seasonal course of the time series for modeled topsoil moisture. A decreased seasonal course may improve the time series match and re–invert the relation between satellite derived surface moisture and modeled topsoil moisture. A less pronounced seasonal course may be obtained by adjustment in the soil moisture model to a soil type with a higher hydraulic conductivity and lower moisture retention capacity, e.g. loamy sand or sand. Such an adjustment would, however, further increase the modeled downward percolation to a value in excess of the recharge estimate from river flow. A sound estimation of the regional transpiration rate would therefore help in evaluating of the feasibility of such an adjustment.

When matching the time series of modeled topsoil moisture and satellite de-

rived surface moisture using the dual polarization approach, the optima for the time–invariant parameters in the radiative transfer function are consistent. Apart from soil surface roughness, h, they seem to be unrelated to the downward moisture percolation. With h known, it should be possible to estimate downward moisture percolation from satellite observations. However, since the difference between the surface moisture estimates is substantial, the value of the downward moisture percolation estimate is uncertain. The estimated downward moisture percolation is at best in the same order of magnitude as the regional recharge estimate from river flow. Furthermore, additional information on the regional transpiration rate by deep rooted vegetation is required.

Outlook The use of a soil moisture model to derive time series for regional soil moisture is laborious, inaccurate and data demanding. It requires a lot a field data, while its implementation on a regional scale may introduce large errors. The derivation of regional surface moisture time series from Nimbus–7/SMMR passive microwave observations is comparatively easy. The value of the time series for derived surface moisture may, however, only be validated by comparison with measured time series of (regional) topsoil moisture. Since these measurements are generally not available at either the required scale or for the required time period (1978–1987), the time series for topsoil moisture need to be modeled. Accurate validation of the satellite derived surface moisture estimates is therefore hampered. Launch of the Advanced Microwave Scanning Radiometer (AMSR) on board NASA's Earth Observing System (EOS) PM–1 satellite planned in 2000 provides an opportunity to eliminate the problem of historical data and to plan real–time validation campaigns for passive microwave observations. These campaigns should preferably be carried out as long–term observations of soil moisture at shallow depth (< 5 cm) and should be made at the regional scale in areas of low relief with not too much vegetation.Although problems related to the spatial averaging of soil moisture point measurements will remain, they will be reduced due to an improved resolution of ~ 30 km. This will lead to a smaller and more uniform pixel, at least most of the time. The resulting improved surface moisture inversion algorithm may then be applied to the historical SMMR/SMMI data to construct a long–term data base of global surface moisture. Such data sets will be useful for global change detection studies and as an initialization and validation data base for Global Circulation Models (GCM).
An alternative to efforts directed towards validating passive microwave observations may be the derivation of an indicator of surface wetness. The application of constant values for the time–invariant radiative transfer properties provides a possibility to evaluate the changes in time of the derived surface moisture estimates. Although this application does not supply a verified or calibrated value of surface moisture, it may serve as a tool for change or trend detection. Results from such analyses may be used in policy and decision making. In a perspective of the laborious and time–and data demanding character of passive microwave data validation, change detection may serve as a practical alternative.

Summary

The primary objective of the present study is to investigate the potential of satellite passive microwave surface moisture monitoring as a tool for the detection of regional scale climate variability and land use change. This is attempted by a retrospective analysis of long–term time series for meteorological, hydrological and remote sensing data from the West La Mancha region in semi–arid central Spain. The analysis is based on the derivation of regional surface moisture from passive microwave data and regional application of a soil moisture balance model. Time series of hydrological data are used as a control on the soil moisture balance results and, as such, on the satellite derived surface moisture. If the followed approach is successful, then passive microwave observations may be used to assess regional surface moisture and subsequently to estimate individual components in the regional water balance. An assessment of recharge from satellite observations may assist in efforts towards a more sustainable development of the West La Mancha region.

Since the onset of large–scale water abstraction for irrigated cultivation in the early 1970s, the West La Mancha area has experienced a considerable decline in the groundwater level of its main aquifer. Coinciding with a drought period in the 1980s groundwater fell to a critically low level and rivers and wetlands dried up. The 1978–1987 lifetime of the Scanning Microwave Multichannel Radiometer (SMMR) antenna on board Nimbus–7 corresponds with this drought period. Based on solving the radiative transfer function for vegetation covered areas, relatively dry and wet years are discerned. No drying trend, however, is found in the time series for derived surface moisture and the effects of irrigation and/or land–use change are also not detected.

Since a regional database of historical soil moisture measurements to validate the time series of satellite derived surface moisture is not available, time series of topsoil moisture are modeled using a regional scale soil moisture balance approach. A parameter sensitivity study indicates that the moisture model is most sensitive to a change in soil hydraulic properties, the soil profile depth and precipitation. Transpiration by deep rooted vegetation is not accounted for in the soil moisture model, but is estimated on the basis of reported transpiration rates in the literature and the regional surface cover fraction. This sink–term may therefore be considered as an indication of the error magnitude in the closure of the regional water balance.

Long–term annual recharge in the West La Mancha region is estimated on the basis of river flow at the outlet of the Upper Guadiana Catchment. The modeled annual downward moisture percolation rate at the bottom layer of the soil profile exceeds this estimate by several times. A doubling of the transpiration rate by deep rooted vegetation leads to a more comparable annual percolation rate. Alternatively, an adjustment in the soil moisture balance model soil hydraulic properties by a change in soil type from sandy loam to silt loam and an increase of the soil profile depth also leads to a more comparable annual percolation estimate.

Comparison of soil moisture time series show that the seasonal course of the modeled topsoil moisture far exceeds that for the satellite derived surface moisture. The time series are subsequently matched by optimizing parameter values in the radiative transfer function. The optima for the parameter values are consistent, though they are close to their maximum value. This may be explained by matching the time series for satellite derived surface moisture with the large seasonal course of the modeled topsoil moisture.

In the research approach followed, the recharge estimate from river flow is used as a control on model results. The minimum difference for the satellite derived surface moisture and the time series of modeled topsoil moisture is 6% by volume. The best match is with the time series for modeled topsoil moisture using soil hydraulic properties of a sandy loam soil type. An increase in the transpiration rate by deep rooted vegetation therefore seems the proper adjustment to the model results.

The substantial difference between the time series of satellite derived surface moisture and modeled topsoil moisture may be explained by comparing soil moisture over different depths. The relatively shallow microwave emitting soil depth of ~ 1 cm may account for the larger alternation in satellite derived surface moisture. In summer, however, the satellite derived surface moisture generally exceeds the modeled topsoil moisture content, while in the remainder of the year the modeled topsoil moisture is higher. This reversed relation may be explained by matching the time series of satellite derived surface moisture with the large seasonal course of the time series for modeled topsoil moisture. A decreased seasonal course may improve the match between the soil moisture time series and re–invert the relation between satellite derived and modeled topsoil moisture. A decreased seasonal course is obtained via adjustment of the soil moisture model soil hydraulic properties by a change in soil type to loamy sand or sand. Such an adjustment increases downward percolation to a value in excess of the recharge estimate from river flow. A reliable estimation of regional transpiration by deep rooted vegetation would therefore help in evaluating the feasibility of such an adjustment.

In the research approach followed the validation of time series for satellite derived surface moisture proved to be laborious, inaccurate and data demanding. Additionally, the difference between the time series for satellite derived surface moisture and modeled topsoil moisture is substantial. The potential for validating satellite derived surface moisture by use of a regional water balance approach seems therefore limited.

Samenvatting (in Dutch)

De hier gepresenteerde studie onderzoekt de vraag of satellietwaarnemingen in
het passieve microgolf bereik van het electromagnetisch spectrum gebruikt kun-
nen worden om klimaatsvariabiliteit en landgebruiksverandering waar te nemen
op regionale schaal. Hiertoe zijn retrospectief tijdseries geanalyseerd van me-
teorologische, hydrologische en satellietgegevens, die betrekking hebben op het
semi-aride westelijke La Mancha gebied in centraal Spanje. De analyses zijn
gebaseerd op het bepalen van bodemvocht uit de passieve microgolf satelliet-
waarnemingen en de toepassing van een bodemvochtmodel. De tijdseries van
hydrologische gegevens zijn gebruikt als controle op de berekeningen van het
bodemvochtmodel, en als zodanig op het bodemvocht dat bepaald is uit de satel-
lietgegevens. Bij bewezen geschiktheid van de gevolgde aanpak zouden passieve
microgolf satellietwaarnemingen gebruikt kunnen worden voor het schatten van
bodemvocht op regionale schaal. Deze schatting zou vervolgens een indicatie
kunnen geven voor de regionale grondwateraanvulling. Een schatting van de
grondwateraanvulling m.b.v. satellietgegevens zou een bijdrage kunnen leveren
aan een duurzamere ontwikkeling van het westelijke La Mancha gebied.

Het grondwaternivo in het belangrijkste reservoir van het westelijke La Mancha
gebied is sinds de aanvang van grootschalige grondwateronttrekkingen t.b.v. de
geirrigeerde landbouw begin jaren zeventig aanzienlijk gedaald. Gedurende een
droge periode in de jaren tachtig daalde het grondwater tot een nivo, waarbij
rivieren en moerassen droogvielen. De meetperiode van de 'Scanning Microwave
Multichannel Radiometer' (SMMR) antenne aan boord van de Nimbus–7 satel-
liet van 1978 tot 1987 valt samen met deze droge periode. Op basis van het
oplossen van de stralingstransferfunktie voor gebieden bedekt door vegetatie
kunnen relatief vochtige en droge perioden worden onderscheiden. Een ver-
drogingstrend is echter niet gevonden en aanwijsbare effecten van irrigatie en/of
landgebruiksverandering zijn eveneens afwezig.

Omdat bodemvochtgegevens ontbreken om het bodemvocht bepaald uit de satel-
lietgegevens te valideren, is een bodemvochtmodel gebruikt om tijdseries van
topbodemvocht te simuleren. Een gevoeligheidsanalyse wijst uit, dat het bodem-
vochtmodel gevoelig is voor veranderingen in hydraulische eigenschappen van de
bodem, de dikte van het bodemprofiel en de neerslag. De transpiratie door diep
wortelende vegetatie is niet opgenomen in het bodemvochtmodel, maar geschat
op basis van waarden vermeld in de literatuur en de regionale bodembedekking.

De transpiratieterm mag daarom beschouwd worden als een indicatie van de foutengrootte in de sluiting van de waterbalans.

De jaarlijkse grondwateraanvulling voor het westelijke La Mancha gebied is geschat op basis van de rivierafvoer bij het lozingspunt van het Alto Guadiana stroomgebied. De door het bodemvochrmodel berekende jaarlijkse percolatie door het bodemprofiel is enkele malen groter dan deze schatting. Een verdubbeling van de transpiratie leidt tot een meer vergelijkbare percolatie. Een aanpassing van de hydraulische eigenschappen door een verandering van bodemtype van zandig leem naar siltig leem en een verdikking van het bodemprofiel leidt echter eveneens tot een meer vergelijkbare percolatie.

Een vergelijking van de bodemvochttijdseries wijst uit dat de seizoenale gang van het gemodelleerde bodemvocht veel groter is dan die van het bodemvocht bepaald uit satellietgegevens. De tijdseries van het bodemvocht zijn vervolgens aangepast door optimalisatie van de parameters in de stralingstransferfunktie. De optima van deze parameters zijn constant, alhoewel zij dichtbij de maximale waarde liggen.

In de gevolgde onderzoeksopzet is de schatting van de grondwateraanvulling uit rivierafvoer gebruikt als controle op de modelberekeningen. Het minimale gemiddelde verschil tussen het bodemvocht bepaald uit de satellietgegevens en het gemodelleerde bodemvocht is 6 vol.%. Dit kleinste verschil bestaat met de bodemvochttijdseries, gemodelleerd met de hydraulische eigenschappen van het bodemtype zandig leem. Een vergroting van de transpiratie door diep wortelende vegetatie lijkt daarom de juiste aanpassing aan het resultaat van het bodemvochtmodel.

Het relatief grote verschil tussen het gemodelleerde bodemvocht en het bodemvocht bepaald uit satellietgegevens wordt mogelijk veroorzaakt door de vergelijking van bodemvocht over verschillende diepten. De microgolfstraling uitzendende toplaag is slechts $\sim$ 1 cm dik, wat mogelijk de grotere afwisseling in bodemvocht verklaart. In de zomer is het bodemvocht bepaald uit satellietgegevens echter hoger dan het gemodelleerde bodemvocht, terwijl in de rest van het jaar het gemodelleerde bodemvocht hoger is. Deze omgekeerde relatie wordt mogelijk verklaard door de grote seizoenale gang van het gemodeleerde bodemvocht. Een kleinere seizoenale gang betekent een kleinere aanpassing van de bodemvochttijdseries bepaald uit de satellietgegevens. Deze wordt verkregen door een aanpassing van de hydraulische eigenschappen door een verandering van bodemtype naar lemig zand of zand. Een dergelijke aanpassing vergroot de bodemvochtpercolatie t.o.v. de schatting van grondwateraanvulling op basis van de rivierafvoer. Een betrouwbare schatting van de regionale transpiratie zou meer houvast geven bij de bepaling van de waarschijnlijkheid van een dergelijke aanpassing.

Uit de gevolgde onderzoeksopzet blijkt dat de validatie van de tijdseries van bodemvocht bepaald uit satellietgegevens een arbeidsintensief proces is, dat veel gegevens vraagt. Het verschil tussen tijdseries van gemodelleerd bodemvocht en bodemvocht bepaald uit satellietgegevens is daarbij relatief groot. De mogelijkheden voor validatie van bodemvocht bepaald uit passieve microgolf satellietwaarnemingen m.b.v. de regionale waterbalans lijken daarom beperkt.

Acknowledgements

References

Aase, J.F., and S.B. Idso, A comparison of two formula types for calculating long wave radiation from the atmosphere, *Water Resour. Res.*, pp. 623–625, 1978.

Allen, C.T., and F.T. Ulaby, Modelling the polarization dependence of the attenuation in vegetation canopies, in *IGARRS '84*, pp. 119–124, 1984.

Beljaars, A.C.M, J.-F. Mahfouf, and J. Noilhan, Sequential assimilation of soil moisture from atmospheric low-level parameters, Part iii: Implementation in a mesoscale model, *J. Appl. Meteor.*, pp. 1352–1364, 1993.

Betts, A.K., J.H. Ball, M.J. Beljaars, M.J. Miller, and P. Viterbo, Coupling between land-surface, boundary-layer parameterizations and rainfall on local and regional scales: lessons from the wet summer of 1993, in *Fifth Conf. on Global Change Studies, Amer. Meteor. Soc. 74th Annual Meeting, Jan. 23–28, 1994, Nashville, TN*, pp. 174–181, 1994.

Bolle, H.-J., and B. Streckenbach, *EFEDA First annual report*, EFEDA Secretariat, Berlin, 1992.

Bolle, H.-J., and B. Streckenbach, *EFEDA Final Report*, EFEDA Secretariat, Berlin, 1993.

Bolle, H.-J., et al., EFEDA: European Field Experiment in a Desertification-threatened Area, *Ann. Geophysicae*, pp. 173–189, 1993.

Bromley, J., M. Hodnett, J.D. Cooper, A.J. Dixon, and A. Young, Hydrological response to land use change and over-exploitation of water resources in a semi-arid area of Spain, in *EFEDA 2, Final report of the hydrology group*, edited by J. Bromley, chap. 1, pp. 1–18, Institute of Hydrology, 1996.

Brunfeldt, D.R., and F.T. Ulaby, Measured microwave emission and scattering in vegetation canopies, *IEEE Trans. Geosci. Remote Sensing*, *GE–22(6)*, 520–524, 1984.

Brutsaert, W.H., *Evaporation into the Atmosphere: Theory, History and Applications.*, Reidel, Boston, 1982.

Camillo, P.J., R.J. Gurney, and T.J. Schmugge, A soil and atmospheric boundary layer model for evapotranspiration and soil moisture studies, *Water Resourc. Res.*, *19*, 371–380, 1983.

Cervantes Saavedra, M. de, *De vernuftige edelman Don Quichot van La Mancha. Vertaling Barber van de Pol van: El Ingenioso Hidalgo Don Quixote de la Mancha*, Athenaeum-Polak en Van Gennep (2 dln), Amsterdam, 1605.

Choudhury, B.J., T.J. Schmugge, R.W. Newton, and A. Chang, Effect of surface roughness on the microwave emission from soils, *J. Geophys. Res.*, pp. 3660–3666, 1979.

Clapp, R.B., and G.M. Hornberger, Empirical relations for some soil hydraulic properties, *Water Resource Res.*, pp. 371–380, 1978.

Cruces, J., M.R. Llamas, M. Casado, and J.L. Barosso, Assesment of hydrology and hydrogeology of the EFEDA-project, in *EFEDA, Annex to final report*, edited by B. Streckenbach, chap. 9, pp. 1–40, EFEFA Secretariat, Freie Universitaet Berlin, 1992.

Davies, J.A., and C.D. Allen, Equilibrium, potential and actual evapotranpiration from cropped surfaces in southern Ontario, *J. Appl. Meteorol.*, *12*, 649–657, 1973.

Dobson, M.C., F.T. Ulaby, M.T. Hallikainen, and M.A. El Rayes, Microwave dielectric behavior of wet soil-part II: dielectric mixing models, *IEEE Trans. Geosc. Remote Sensing*, *GE–23(1)*, 35–46, 1985.

Droogers, P., D. Van de Abeele, J. Cobbaert, P. Kim, R. Roesslerova, M. Soet, and J.N.M. Stricker, Basic data sets description and preliminary results of EFEDA-Spain, *Tech. rep.*, Dept. of Water Resources, WAU, 1993.

Fienig, J., and B.T. Gouweleeuw, Estimation of local average annual recharge rate using chloride profiling in the West La Mancha area, central Spain, *Tech. rep.*, Faculty of Earth Sciences, Vrije Universiteit Amsterdam, 1996.

Gloersen, P., and F.T. Barath, A Scanning Multichannel Microwave Radiometer for Nimbus-G and Seasat-A, *IEEE I. of Oceanic Engineering*, *OE-2(2)*, 172–178, 1977.

Gouweleeuw, B.T., Movement of infiltrated water in the Llanura Manchega aquifer in central Spain as indicated by tritium profiles, *Tech. rep.*, Faculty of Earth Sciences, Vrije Universiteit Amsterdam, 1994.

Gouweleeuw, B.T., H. Timmer, and B. Meibos, Some hydrogeological aspects of the area around Tomelloso with respect to groundwater recharge, hydrogeological report HAPEX–EFEDA 1991, Master's thesis, Faculty of Earth Sciences, Vrije Universiteit Amsterdam, 1992.

Gouweleeuw, B.T, A.A. Van de Griend, and M. Owe, Estimation of 'effective' soil hydraulic properties by topsoil moisture and evapotranspiration modelling applied to an arable site in central Spain, *Water Resourc. Res.*, *32*, 1387–1392, 1996.

Holben, B.N., and C.O. Justice, An examination of spectral band rationing to reduce the topographic effect on remotely sensed data, *Int. J. Remote Sensing*, *2*, 115–133, 1981.

Huete, A.R., A soil adjusted vegetation index (SAVI), *Remote Sensing of the Environment*, *25*, 295–309, 1988.

Idso, S.B., and R.D. Jackson, Thermal radiation from the atmosphere, *J. Geophys. Res.*, pp. 5397–5403, 1969.

IGME, Mapa tectonico de la Peninsula Iberica y Baleares, 1:1000.000, 1972.

IGME, Sotuellamos, in *Mapa Geologico de Espana, 1:50.000*, vol. 673, Segunda serie, Primera edicion ed., Iinstituto Geologico y Minero de Espana, 1975.

IGME, Llanos del Caudillo, in *Mapa Geologico de Espana, 1:50.000*, vol. 671, Segunda serie, Primera edicion ed., Instituto Geologico y Minero de Espana, 1976a.

IGME, El Bonillo, in *Mapa Geologico de Espana, 1:50.000*, vol. 788, Segunda serie, Primera edicion ed., Instituto Geologico y Minero de Espana, 1976b.

IGME, Tomelloso, in *Mapa Geologico de Espana, 1:200.000*, vol. 62, segunda edicion ed., Instituto Geologico y Minero de Espana, 1976c.

IGME, Plan nacional de investigacion de aguas subterraneas, Investigacion hidrogeologica de la cuenca alta y media del Guadiana, Collecion informe, *Tech. rep.*, Instituto Geologico y Minero de Espana, 1980a.

IGME, Calidad de las aquas subterraneas en la cuenca alta del Guadiana, Program Nacional de Gestion y Conservacion de los Aquiferos, Collecion informe, Primer informe, *Tech. rep.*, Instituto Geologico y Minero de Espana, 1980b.

IGME, Sintesis hidrogeologica de Castilla-La Mancha, Collecion informe, *Tech. rep.*, Instituto Geologico y Minero de Espana, 1985.

IGME, La Gineta, in *Mapa Geologico de Espana, 1:50.000*, vol. 765, segunda serie, Primera edicion ed., Instituto Geologico y Minero de Espana, 1988.

Imeson, A.C., and G. Bergkamp, Soil profile drainage under semi-natural vegetation, in *EFEDA 2, Final report of the hydrology group*, edited by J. Bromley, chap. 4, pp. 1–26, Institute of Hydrology, 1996.

IROE, Dielectric constant measurements of five soil samples by means of an L band working probe, *Tech. rep.*, IROE, 1995.

Jackson, T.J., and P.E. O'Neill, Microwave dielectric model for aggregated soils, *IEEE Trans. Geosci. Remote Sensing*, *GE-24(6)*, 920–929, 1986.

Jackson, T.J., and P.E. O'Neill, Attenuation of soil microwave emission by corn and soybeans at 1.4 and 5 GHz, *IEEE Trans. Geosci. Remote Sensing*, *GE–28(50)*, 978–980, 1990.

Justice, C.O., J.R.G. Townsend, B.N. Holben, and C.J. Tucker, Analysis of the phenology of global vegetation using meteorological satellite data, *Int. J. Remote Sensing*, *6*, 1271–1318, 1985.

Kimes, D.S., B.N. Holben, C.J. Tucker, and W.W. Newcomb, Optimal directional view angles for remote sensing missions, *Int. J. Remote Sensing*, *5*, 887–908, 1984.

Kirdiashev, K. P., A. A. Chikhlantsev, and A. M. Shutko, Microwave radiation of the Earth's surface in the presence of vegetation cover, translation of: SVCH-IZLUCHENIYE ZEMNOY POVERKHNOSTI PRI NALICHII RASTITEL' NOGO POKROVA, *Radiotekhnika i Elektronika*, *24*, 256–264, 1979.

Lerner, D.N., A.S. Issar, and I. Simmers, Groundwater recharge, a guide to understanding and estimating natural recharge, in *International contributions to hydrology*, vol. 8, pp. 101–109, Verlag Heinz Heise GmbH, Hannover, 1990.

List, R.J., *Smithsonian Meteorological Tables*, 6th ed., Smithsonian Institution Press, City of Washington, 1971.

Llamas, M.R., Wetlands and groundwater: new constraints in groundwater management, in *Groundwater management: Quality and quantity. Proceedings of the Benidorm symposium*, 188, IAHS, 1989.

Llamas, M.R., M. Casado, A. De la Hera, J. Cruces, and L. Martinez, El desarollo sostenible de la cuenca alta del rio guadiana: apectos socio-economicos y ecologicos, *Medio Ambiente*, *5*, 66–74, 1996a.

Llamas, M. R., J. Cruces, M. Casado, A. De la Hera, and L. Martinez, Groundwater modelling and estimation of recharge using one-dimensional soil water models, in *EFEDA 2, Final report of the hydrology group*, edited by J. Bromley, chap. 2, pp. 1–44, Institute of Hydrology, 1996b.

Loss, S.O., Calibration adjustment of the NOAA AVHRR Normalized Vegetation Index without recourse to component channel 1 and 2 data, *Int. J. Remote Sensing*, *14*, 1907–1917, 1993.

Marquardt, D.W., An algorithm for least-squares estimation of nonlinear parameters, *SIAM J. Appl. Math.*, pp. 431–441, 1963.

Maul, G.A., *Introduction to satellite oceanography*, Martinus Nijhoff Publishers, Dordrecht, 1985.

Mo, T, B.J. Choudhury, T.J. Schmugge, and T.J. Jackson, A model for microwave emission from vegetated-covered fields, *J. Geophys. Res.*, *87*, 11229–11237, 1982.

NASA/GSFC, The Nimbus 7 users' guide, *Tech. rep.*, The Landsat/Nimbus Project, Goddard Space Flight Center, National Aeronautics and Space Administration, Greenbelt, Maryland, 1978.

Newton, R., Q.R. Black, S. Makanvand, A.J. Blanchard, and B.R. Jean, Soil moisture information and thermal microwave emission, *IEEE Trans. Geosci. Remote Sensing*, *GE–21*, 300–307, 1982.

Njoku, E.G., and J.A. Kong, Theory for passive microwave remote sensing of near-surface soil moisture, *J. Geophys. Res.*, *82(20)*, 3108–3118, 1977.

Ogink-Hendriks, M.J., P. Kabat, J.A. Elbers, W.G.M. Bastiaansen, and H.G.M Van der Elsen, Contribution to the EFEDA field campaigns in 1991 and 1994, *Tech. Rep. 112*, SC-DLO, Wageningen, 1995.

Oliver, H.R., and K.J. Sene, Energy and water balances of developping vines, *Agric. For. Meteorol.*, *61*, 167–185, 1992.

Owe, M., and A.A. Van de Griend, Daily surface moisture model for large area semi-arid land application with limited climate data, *Journal of Hydrology*, pp. 119–132, 1990.

Owe, M., A.A. Van de Griend, and A.T.C. Chang, Surface soil moisture and satellite passive microwave observations in semi-arid southern Africa, *Water Resourc. Res.*, pp. 829–839, 1992.

Penman, H. L., Natural evaporation from open water, bare soil, and grass, *Proc. Roy. Soc. London*, pp. 120–146, 1948.

Perez–Trejo, F., *Enivironment and quality of life, Desertification and land degradation in the European Mediterranean*, EUR 14850 EN, European Commision Directorate-General XII, Science, Research and Development, Luxembourg, 1994.

Prescott, J. A., Evaporation from a water surface in relation to solar radiation, *Trans. Roy. Soc. South. Aust.*, pp. 114–125, 1940.

Priestley, C.H.B., and R.J. Taylor, On the assessment of surface heat flux and evaporation using large-scale parameters, *Mon. Wheater Rev.*, *100*, 81–92, 1972.

Reutov, E.A., and A.M. Shutko, Estimation of the depth to a shallow water table using microwave radiometry, *Int. J. Remote Sensing*, *13*, 2223–2232, 1992.

Richards, L.A., Capillary conduction of liquids through porous mediums, *J. Phys.*, *1*, 318–333, 1931.

Schmugge, T.J., Remote sensing of soil moisture, in *Hydrological Forecasting*, edited by M. Anderson and T. Burt, John Wiley, New York, 1985.

Sene, K.J., Parameterisations for energy transfer from a sparse crop, *Agr. For. Met.*, *71*, 1–18, 1994.

SGDGOH, Evolucion de las extracciones y niveles piezometricos en el aquifero de la Llanura Manchega, Informe 06/88, *Tech. rep.*, Servicio Geologico de la Direccion General de Obras Publicas, Madrid, 1988.

Thiessen, A. H., Precipitation for large areas, *Mon. Weath. Rev.*, pp. 1082–1084, 1911.

Thornes, J. B., S. Burke, A. Harrison, and A. Lopez Bermudez, Regional estimation of groundwater recharge and the role of changing landuse, in *EFEDA 2, Final report of the hydrology group*, edited by J. Bromley, chap. 3, pp. 1–32, Institute of Hydrology, Wallingford, 1996.

Thornthwaite, C.W., Report of the Committee on transpiration and evaporation, *Trans. Am. Geophys. Union.*, pp. 683–693, 1944.

Tucker, C.J., Red and photographic infrared linear combinations for monitoring vegetation, *Remote Sensing of the Environment*, *8*, 127–150, 1979.

Ulaby, F.T., R.K. Moore, and A.K. Fung, *Microwave remote sensing: Active and Passive, Vol. I, Microwave Remote Sensing Fundamentals and Radiometry*, Addison–Wesley, Reasing, MA, 1981.

Ulaby, F.T., R.K. Moore, and A.K. Fung, *Microwave remote sensing: Active and Passive, Vol. II, Radar Remote Sensing ans Surface Scattering and Emission Theory*, Artech House, Norwood, MA, 1982.

Ulaby, F.T., R.K. Moor, and A.K. Fung, *Microwave remote sensing: Active and Passive, Vol. III, From Theory to Application*, Artec House, Norwood, MA, 1986.

UNEP, World Atlas of Desertification, *Tech. rep.*, UNEP, London, 1992.

Van de Griend, A.A., and M Owe, Microwave vegetation optical depth and inverse modelling of soil emissivity using Nimbus/SMMR satellite observations, *Meteorol. Atmos. Phys.*, pp. 225–239, 1994a.

Van de Griend, A.A., and M. Owe, The influence of polarization on canopy transmission properties at 6.6 GHz and implications for large-scale moisture monitoring in semi-arid environments, *IEEE Trans. Geosci. Remote Sensing*, *GE-32(2)*, 409–415, 1994b.

Van de Griend, A.A., M. Owe, J. de Ruiter, and B.T. Gouweleeuw, Measurement and behavior of dual-polarization vegetation optical depth and single scattering albedo at 1.4- and 5-GHz microwave frequencies, *IEEE Trans. Geosci. Remote Sensing*, *GE-34(4)*, 957–965, 1996.

Van den Hurk, B.J.J.M., Sparse canopy parameterizations for meteorological models, PhD thesis, Agricultural University Wageningen, Wageningen, 1996.

Van Genuchten, M.T, A closed-form equation for predicting the hydraulic conductivity of unstaurated soil, *Soil. Sci. Soc. Am. J.*, *44*, 892–898, 1980.

Wang, J.R., The dielectric properties of soil water mixtures at microwave frequencies, *Radio Sci.*, *5*, 977–985, 1980.

Wang, J.R., and T.J. Schmugge, An empirical model for the complex dielectric permittivity of soils as a function of water content, *IEEE Trans. Geosci. Remote Sensing*, pp. 288–295, 1980.

Ward, R.C., *Principles of hydrology*, 2nd ed., McGraw Book Company, 1974.

Wilheit, T.T., Radiative transfer in a plane stratified dielectric, *IEEE Trans. Geosci. Remote Sensing*, *GE–16*, 138–143, 1978.

Young, A. R., Surface water studies, in *EFEDA 2, Final report of the hydrology group*, edited by J. Bromley, chap. 2, pp. 31–62, Institute of Hydrology, Wallingford, 1996.

Appendix A

Acronyms and symbols

Acronymns

AVHRR	Advanced Very High Resolution Radiometer
BAHC	Biosheric Aspects of the Hydrological Cycle
DAAC	Distributed Active Archive Center
DOY	Day Of Year
ECHIVAL	European international project on Climatic and Hydrological Interactions between Vegetation, Atmosphere and Land-surfaces
EFEDA	ECHIVAL Field Experiment in a Desertification-threatened Area
EU	European Union
GSFC	Goddard Space Flight Center
IGBP	International Geosphere-Biosphere Program
IGME	Instituto Geologico y Minero de España
LT	Local Time
MSL	Mean Sea Level
NASA	National Aeronautics and Space Administration
NDVI	Normalized Difference Vegetation Index
NOAA	National Oceanic and Atmospheric Administration
RMSD	Root Mean Square Difference
RMSE	Root Mean Square Error
SMMR	Scanning Multichannal Microwave Radiometer
UTC	Universal Time Coordinated

Symbols

Γ_{P}	Microwave vegetation transmissivity at P-polarization angle	–
Δ	Slope of the saturated vapour pressure curve	–

Δ_{gw}	Change in groundwater storage	m
Δ_{sm}	Change in soil moisture storage	m
ΔT_{a}	Air temperature adjustment to soil surface temperature	K
ΔT_{ab}	Air temperature adjustment to bare soil surface temperature	K
ΔT_{ac}	Air temperature adjustment to canopy surface temperature	K
ΣX	Sum of X /Cumulative X	–
Θ	$(\theta - \theta_{\text{r}})/(\theta_{\text{s}} - \theta_{\text{r}})$ in *Mualem-Van Genuchten* parameterization of soil hydraulic properties	–
α_{ef}	Evaporative fraction	–
$\alpha_{\text{ef}_{\text{max}}}$	Maximum value of the evaporative fraction	–
α_{mvg}	Empirical parameter in *Mualem-Van Genuchten* parameterization of soil hydraulic properties	–
α_{s}	Soil surface albedo	–
γ	Psychrometer constant (0.66)	mbarK^{-1}
ϵ_{ac}	Longwave atmospheric emissivity under clear skies	–
ϵ_{s}	Longwave soil surface emissivty	–
θ	Soil moisture content	m^3m^{-3}
θ_{5cm}	5 cm depth topsoil moisture content	m^3m^{-3}
θ_{fc}	Soil moisture content at field capacity	m^3m^{-3}
θ_{r}	Residual soil moisture content	m^3m^{-3}
θ_{s}	Soil moisture content at saturation	m^3m^{-3}
θ_{sat}	Satellite derived surface moisture content	m^3m^{-3}
θ_{top}	Topsoil moisture content	m^3m^{-3}
θ_{wp}	Soil moisture content at wilting point	m^3m^{-3}
λ	Wavelength	m
λ_{v}	Latent heat of vaporization	Jm^{-1}
μ	Incidence angle	° from nadir
σ	Stefan-Boltzmann constant ($5.67\text{x}10^{-8}$)	$\text{Wm}^{-2}\text{K}^{-1}$
τ_{P}	Microwave vegetation optical depth at ᴘ–polarization angle	–
τ_{cor}	Factor to correct for differences in optical depth of two experimental plots with different vegetation biomass	
ψ	Matric potential	m
ψ_{s}	Matric potential at saturation	m
ω_{P}	Microwave vegetation single scattering albedo at ᴘ–polarization angle	–
A	$\Gamma_{\text{H}}/\Gamma_{\text{V}}$	–
A"	$\tau_{\text{H}}/\tau_{\text{V}}$	–
B	$\omega_{\text{H}}/\omega_{\text{V}}$	–
$C_{\text{NDVI,P}}$	Slope coefficient of linear Γ_{P}-NDVI relation	–
D_{top}	Thickness of the topsoil	m

ET	Evapotranspiration	ms^{-1}
F	Fraction of P	–
G	Soil heat flux	Wm^{-2}
$_\text{H}$	Horizontal polarization angle	–
I	Irrigation	ms^{-1}
K	Complex dielectric constant	Fm^{-1}
K_h	Hydraulic conductivity	ms^{-1}
K_mvg	Hydraulic conductivity in *Mualem-Van Genuchten* parameterization of soil hydraulic properties	cmhr^{-1}
K_s	Hydraulic conductivity at saturation	ms^{-1}
$K_\text{s−mvg}$	Hydraulic conductivity at saturation in *Mualem-Van Genuchten* parameterization of soil hydraulic properties	cmhr^{-1}
L	Empirical parameter of *Mualem-Van Genuchten* parameterization of soil hydraulic properties	–
M	Multiplication factor in computation of R_{n_hour}	–
N_s	Number of daylight hours	–
P	Precipitation	ms^{-1}
P_d	Precipitation duration	hr
$_\text{P}$	Polarization angle ($_\text{H}$ or $_\text{V}$)	–
Q	Discharge	ms^{-1}
R	Recharge/downward moisture percolation	ms^{-1}
R_ld	Downward longwave radiation	Wm^{-2}
R_ldc	Downward longwave radiation under clear skies	Wm^{-2}
R_lu	Upward longwave radiation	Wm^{-2}
R_n	Net radiation	Wm^{-2}
R_nlc	Net longwave radiation under clear skies	Wm^{-2}
R_{n_hour}	Hourly net radiation	Wm^{-2}
R_s	Global shortwave radiation	Wm^{-2}
R_se	Global shortwave radiation for a given latitude and a time of the year based on calculations of Milankovitch	Wm^{-2}
S	Standard deviation	–
T_a	Average daily air temperature	K
T_{a_max}	Maximum daily air temperature	K
T_{a_min}	Minimum daily air temperature	K
T_bp	Brightness temperature at $_\text{p}$-polarization angle	K
T_c	Temperature of the canopy	K
T_s	Temperature of the soil surface	K
T_se	Estimated soil surface temperature	K
T_sm	Measured soil surface temperature	K
$_\text{V}$	Vertical polarization angle	–
$\bar{\text{X}}$	Arithmetic mean	–
$\bar{\text{X}}_\text{w}$	Weighted arithmetic mean	–
$a,\ b,\ c,\ d,\ e$	Fitting parameters in $\alpha_\text{ef} - \theta_\text{top}$ relation	–
$\bar{b}$	Fitting parameter in *Clapp and Hornberger* classification of soil hydraulic properties	–

e_s	Microwave soil surface emissivity	–
e_rs	Microwave emissivity of a rough soil surface	–
f	Frequency	Hz
h	Soil surface roughness	–
j	Constant in $(R_\mathrm{nl}/R_\mathrm{nlc}) = (\mathrm{n_s}/\mathrm{N_s})$ relation	-
$k,\ l$	Fitting parameter in $(R_\mathrm{s}/R_\mathrm{se}) = (\mathrm{n_s}/\mathrm{N_s})$ relation	–
$\mathrm{m_{mvg}}$	Empirical parameter in *Mualem-Van Genuchten* parameterization of soil hydraulic properties	–
n	Number of observations	–
$\mathrm{n_s}$	Number of bright sunshine hours	–
$\mathrm{n_{mvg}}$	Empirical parameter in *Mualem-Van Genuchten* parameterization of soil hydraulic properties	–
r_s	Microwave soil surface reflectivity	–
t	Time	s
t_h	Point of time ([UTC] or [LT])	hr
z	Altitude/Depth	m
z_s	Sampling depth	m